

ADA 279409

REPORT DOCUMENTATION PAGE

Form Approved
OMB No. 0704-0188

Public reporting burden for this collection of information is estimated to average 1 hour per response, including the time for reviewing instructions, searching existing data sources, gathering and maintaining the data needed, and completing and reviewing the collection of information. Send comments regarding this burden estimate or any other aspect of this collection of information, including suggestions for reducing this burden, to Washington Headquarters Services, Directorate for Information Operations and Reports, 1215 Jefferson Davis Highway, Suite 1204, Arlington, VA 22202-4302, and to the Office of Management and Budget, Paperwork Reduction Project (0704-0188), Washington, DC 20503.

1. AGENCY USE ONLY (Leave blank)		2. REPORT DATE 15 April 1994		3. REPORT TYPE AND DATES COVERED Final technical report 2/15/91-2/14/94	
4. TITLE AND SUBTITLE Growth and Electrical and Far-Infrared Properties of Wide Electron Wells in Semiconductors				5. FUNDING NUMBERS G-AFOSR-91-0214	
6. AUTHOR(S) Professor Arthur C. Gossard					
7. PERFORMING ORGANIZATION NAME(S) AND ADDRESS(ES) Materials Department University of California, Santa Barbara Santa Barbara, CA 93106				8. PERFORMING ORGANIZATION REPORT NUMBER AFOSR-TR- 94 0285 UCSB 08-075892	
9. SPONSORING/MONITORING AGENCY NAME(S) AND ADDRESS(ES) Prog. Mgr. Gerald L. Witt AFOSR/NE, Building 410 Bolling AFB, DC 20332-6448 Tel. (202)767-4931				10. SPONSORING/MONITORING AGENCY REPORT NUMBER 2305 CS	
11. SUPPLEMENTARY NOTES					
12a. DISTRIBUTION/AVAILABILITY STATEMENT Unlimited, approved for public release				12b. DISTRIBUTION CODE	
13. ABSTRACT (Maximum 200 words) SEE NEXT PAGE.					
14. SUBJECT TERMS wide electron wells, parabolic wells, electron resonators, molecular beam epitaxy, Terahertz properties				15. NUMBER OF PAGES 57	
				16. PRICE CODE	
17. SECURITY CLASSIFICATION OF REPORT Unclassified	18. SECURITY CLASSIFICATION OF THIS PAGE Unclassified	19. SECURITY CLASSIFICATION OF ABSTRACT Unclassified	20. LIMITATION OF ABSTRACT UL		

**Best
Available
Copy**

ABSTRACT

The thrust of the research carried out under this grant has been the development and study of wide, specially shaped graded quantum wells for electrons in semiconductors, as synthesized by high-precision epitaxial growth. In basic characterization of the wide wells, fundamental measurements of charge density, energy levels, and electron motions in the wells were pursued. The achievement of *high-Q solid state electron resonators* at Terahertz frequencies in the wide wells was stressed. Highly resonant cavities with electron scattering times nearly two orders of magnitude larger than for electrons in high-purity uniformly doped wells of comparable electron concentration have been grown. Structures were also achieved in which the resonant frequency of the electrons could be changed by application of a potential to a control electrode. Modification of the parabolic potential by superposition of periodic potentials and the extension of the parabolic well concept to remotely doped hole wells were also emphasized.

Accession For	
NTIS GRA&I	<input checked="" type="checkbox"/>
DTIC TAB	<input type="checkbox"/>
Unannounced	<input type="checkbox"/>
Justification	
By	
Distribution/	
Availability Codes	
Dist	Avail and/or Special
A-1	

SUBJECT: Final Technical Report, February 15, 1991 - February 14, 1994
Grant Nr. AFOSR-91-0214 (UCSB 08-075892)
"Growth and Electrical and Far-Infrared Properties of Wide Electron
Wells in Semiconductors"

TO: Air Force Office of Scientific Research

ATTN: Dr. Gerald L. Witt
AFOSR
Bolling AFB, DC 20332

FROM: Professor Arthur C. Gossard
Materials and ECE Departments
University of California, Santa Barbara
Tel. 805-893-2686, Fax 805-893-8502
e-mail gossard@engrhub.ucsb.edu

DATE: April 14, 1994

OBJECTIVES

The basic thrust of our research was the development and study of wide, specially shaped wells for electrons in semiconductors, as synthesized by high-precision epitaxial growth. In general, our work has attempted to exploit the flexibility in well design and the advantages of modulation doping in order to achieve new electrical and optical phenomena, especially in the Terahertz frequency regime, where these materials can form highly resonant and controllable solid state electron resonators. Our growth effort is aimed to be closely coupled with the UC Santa Barbara Quantum Institute, which has developed a strong capability in the Terahertz frequency region. It is also closely coupled with the Joint Services Electronic Program laboratories at Harvard University for specialized low temperature and high magnetic field electrical and optical measurements and for theoretical consultation. Collaboration with researchers at Wright-Patterson Laboratories has also been initiated under this contract to study cyclotron resonance in graded quantum wells as well as the application of dielectric mirrors based on digital-alloy growth. As indicated in the publication list, this has been a productive effort during the past three years, with the publication of over thirty papers and additional manuscripts in press or in preparation.

TABLE OF CONTENTS

Growth and characterization of parabolic wells

Introduction to parabolic wells	1
Growth techniques (digital and analog alloys)	3
Beam flux monitoring	5

Electrical properties

CV Subband depopulation and profiling	8
Electron mobility in PBW's (size effect scattering)	11
Quantum Hall Effect in PBW's	14

Optical properties

PL, PLE, Raman scattering	16
Nonlinear properties	18
Surface plasmons (PBW and bi-metallic well)	20
FIR absorption in PBW (Tilted B field, Voigt geometry, grating coupler)	22
FIR absorption in PBW with deviations from parabolicity (hard walls)	24

Additional Graded Structures

3DHG (growth and characterization)	27
Superlattice in a PBW (growth and characterization)	30
Tunable electron resonator	33
Parabolically graded mirror stacks in VCSEL's	36

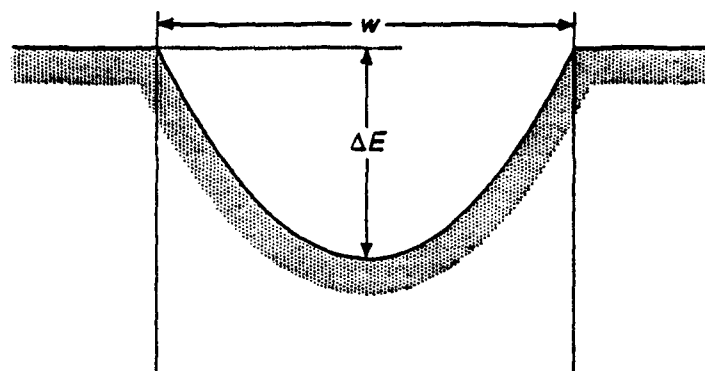
Other Heterostructures	38
-------------------------------	-----------

GROWTH OF WIDE PARABOLIC WELLS

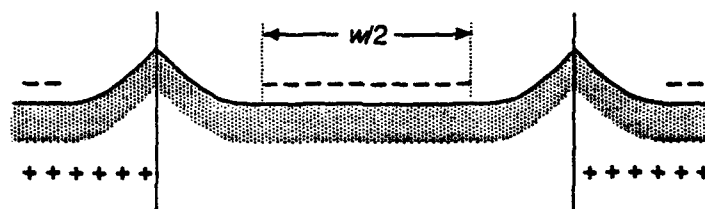
Concept

The concept of achieving a nearly three-dimensional electron gas while reducing electron-impurity interactions was introduced by Gossard and Halperin¹ who proposed the growth of remotely doped wide parabolic quantum well structures as a means of achieving the nearly ideal electron gas. In such wells, the conduction band edge potential $V(z) = Az^2$ of the undoped well mimics the potential of a uniform positive slab of material of positive charge density $n_0 = A\epsilon/2pe^2$, where ϵ is the dielectric constant of the material and e is the electron charge. The band profiles in the doped and undoped parabolic well are illustrated in Figure 1. In the AlGaAs system, the conduction band edge potential is nearly proportional to the aluminum content in the alloy. This allows the creation of a parabolic potential by quadratic variation of aluminum content in the growth direction in an AlGaAs heterostructure. Electrons are introduced into the system by remotely doping the wide parabolic well structure with donor atoms in the barrier layer regions outside the well. The electrons from the donors fall into the well, where they screen the parabolic potential of the well and distribute themselves in a nearly uniform layer of density equal to the positive charge density that would produce the original unscreened parabolic potential. Electron mobilities in this system are roughly two orders of magnitude higher than bulk GaAs due to separation of free carriers from the ionized impurities. In addition, densities below the metal-insulator transition can be achieved with this method since carrier freezeout is not a concern.² Mobilities in excess of 100,000 cm²/Vs (and as high as 350,000 cm²/Vs for a 3DEG with density $\approx 10^{16}$ cm⁻³) have been obtained in a variety of 3DEGs with densities ranging from as low as 4×10^{15} cm⁻³ up to 10^{17} cm⁻³.^{3,4}

Zero-Charge Band Diagram of Parabolic Well:



Matched True Doping Added Outside Parabolic Well:



$$N_D^{**} = \frac{\epsilon}{q^2} \cdot \frac{d^2 \Omega_C}{dx^2} = \frac{8\epsilon}{q^2} \cdot \frac{\Delta E}{w^2}$$

Figure 1. Band profile in undoped and doped parabolic well where doping is added outside the well.

Growth Techniques

Wide parabolic quantum wells have now been grown both by a high precision grading technique that involves computer-controlled chopping of the aluminum molecular beam in a short period (~ 20 Å) graded superlattice² and by a temperature-controlled aluminum oven deposition technique that varies the aluminum oven temperature during growth⁵.

The digital alloy technique is shown schematically in Figure 2. A superlattice with a constant period of 20 Å is grown. The duty cycle of the Al in each period is varied in the desired fashion, for instance, parabolic, by computer control of the Al oven shutter in the MBE machine. The carrier 'sees' an average Al mole fraction, in effect an analog alloy. Using the fact that the bandgap of $\text{Al}_x\text{Ga}_{1-x}\text{As}$ is directly proportional to the Al mole fraction over a large range of x values (0 to 0.45), the result is a graded bandgap directly proportional to the graded alloy composition. To synthesize a uniformly quasi-doped semiconductor with a carrier density of $\sim 2 \times 10^{16} \text{ cm}^{-3}$ would require a 2000 Å wide parabolic well in which the Al mole fraction went quadratically from zero at the center to 0.2 at the edges.

In comparison, the analog alloy technique involves the changing of the temperature of the aluminum molecular beam furnace to create a variation of the beam flux over time. Although this method produces a potential without the sharp variation in local potential created in the digital alloy, several problems exist. Due to thermal time constants, thermal gradients, and heat capacities of the furnaces, there will be time delays between the set point of the furnaces and the actual desired flux rate from the effusion cells, although these delays can be partially compensated for by using iteratively learned control loops for the furnaces.⁶ Additionally, this method requires precise calibration of the aluminum flux over a wide range of temperatures in comparison to the relatively simple RHEED oscillation growth rate measurement used in the digital alloy technique.

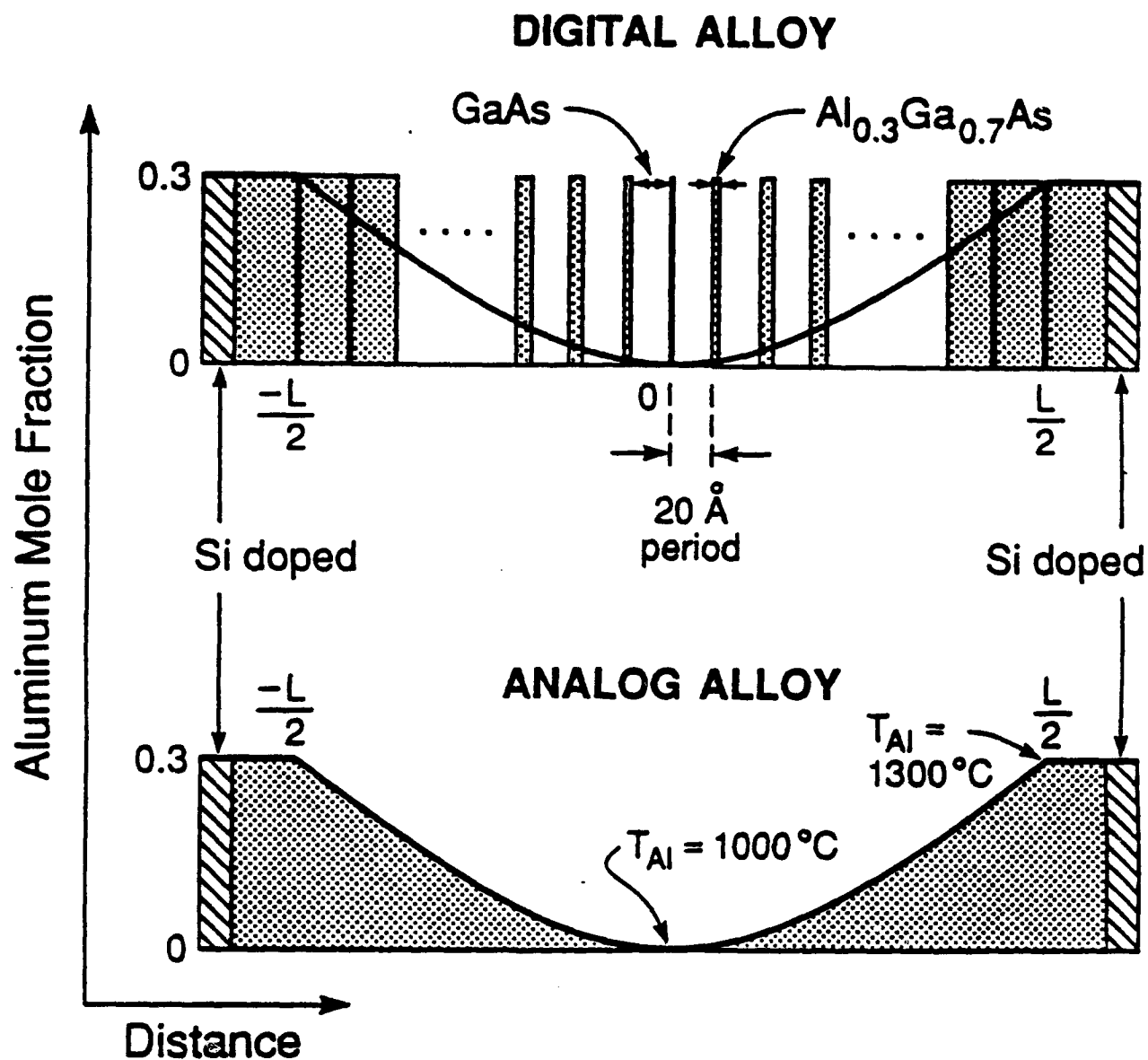


Figure 2. Digital alloy and analog alloy parabolic well compositional profiles.

Composition Determination by Flux Profiling

In order to determine epitaxial growth rates and composition profiles for wide parabolic wells and other graded heterostructures, we developed a sensitive and fast method for pre-growth calibration of our graded structures⁷. The profiles are measured in calibration runs by using a fast picoammeter to track the ion-collector current of the beam flux monitor ion-gauge (facing the ovens) and by integrating the ion current with time to calibrate the profile of Al mole fraction vs. depth deposited in growth of graded $\text{Al}_x\text{Ga}_{1-x}\text{As}$ alloys. A computer is used to either ramp the Al oven temperature (analog alloy), or pulse the Al beam (digital alloy), with a fractional monolayer depth resolution that permits a wide range of averaged alloy profiles to be obtained. Parabolic quantum wells have been grown by both techniques and the corresponding measured profiles compared to each other and to the design profile. The ability of the digital-alloy technique to generate arbitrary graded-alloy profiles is illustrated in Figures 3 and 4. Figure 3 shows the measured flux profiles in comparison with a target sinusoidal flux profile for beam flux control by oven temperature variation (analog alloy) and for beam flux control by periodic molecular beam shuttering (digital alloy) control. It is our contention that the degree of attainable accuracy in composition profile is greater with the digital alloy control especially for structures with rapidly varying potentials. It is also evident that the degree of measurement accuracy for the flux profile is greater by our ion gauge measurement than it is by post-growth profiling by, for example, sputter Auger or sputter SIMS profiling⁸. For electron gases in wide parabolic potential wells the design parameter of interest is the well curvature, inasmuch as the carrier density profile is controlled by it. Curvature vs. depth profiles calculated from digital and analog alloy profiles are shown in Fig. 4 and compared to the constant design curvature. The development of this technique has been extremely useful for pregrowth calibrations. The curvature of the composition is still more sensitive to the accuracy of the graded alloy compositional profile than the composition itself. Our experimental results on measurements of the electron density profile confirm that the uniformity of the three dimensional gas is very sensitive to the uniformity of the curvature of the wells. Again, the precision of the digital shuttering technique and the accuracy of the fast ionization gauge profile measurement are evident in comparison with analog alloy and sputter profiling techniques.

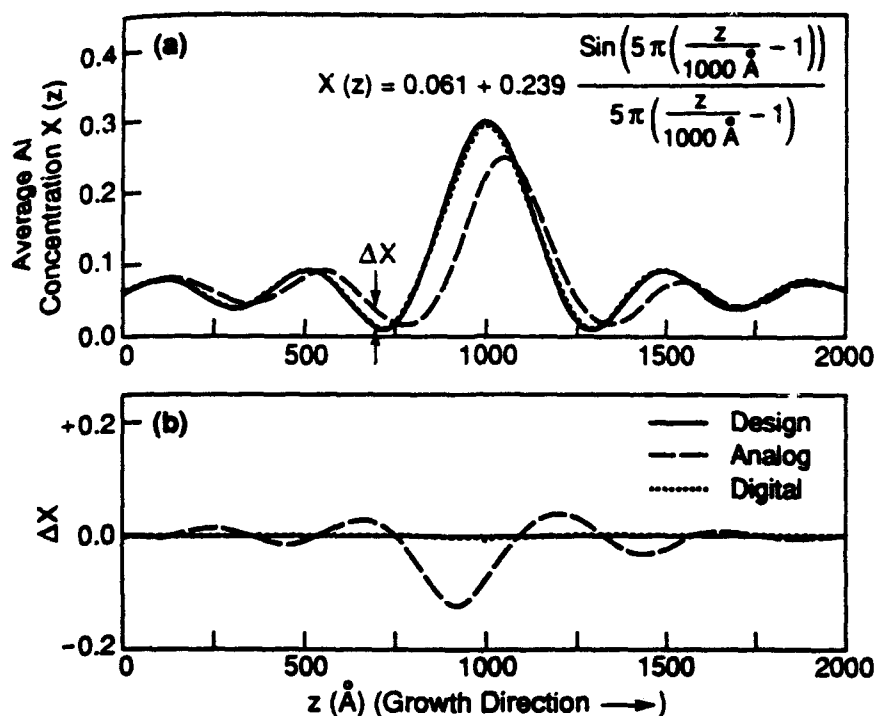


Figure 3. a) Measured aluminum molecular beam flux composition profiles $x(z)$ in comparison with a target sinusoidal flux profile (solid curve) for beam flux control by oven temperature variation (analog alloy, dashed curve) and for beam flux control by computer-controlled molecular beam shuttering (digital alloy, dotted curve) control. b) Deviations Δx in average aluminum concentration $x(z)$ between measured molecular beam flux profiles and the target sinusoidal flux profile.

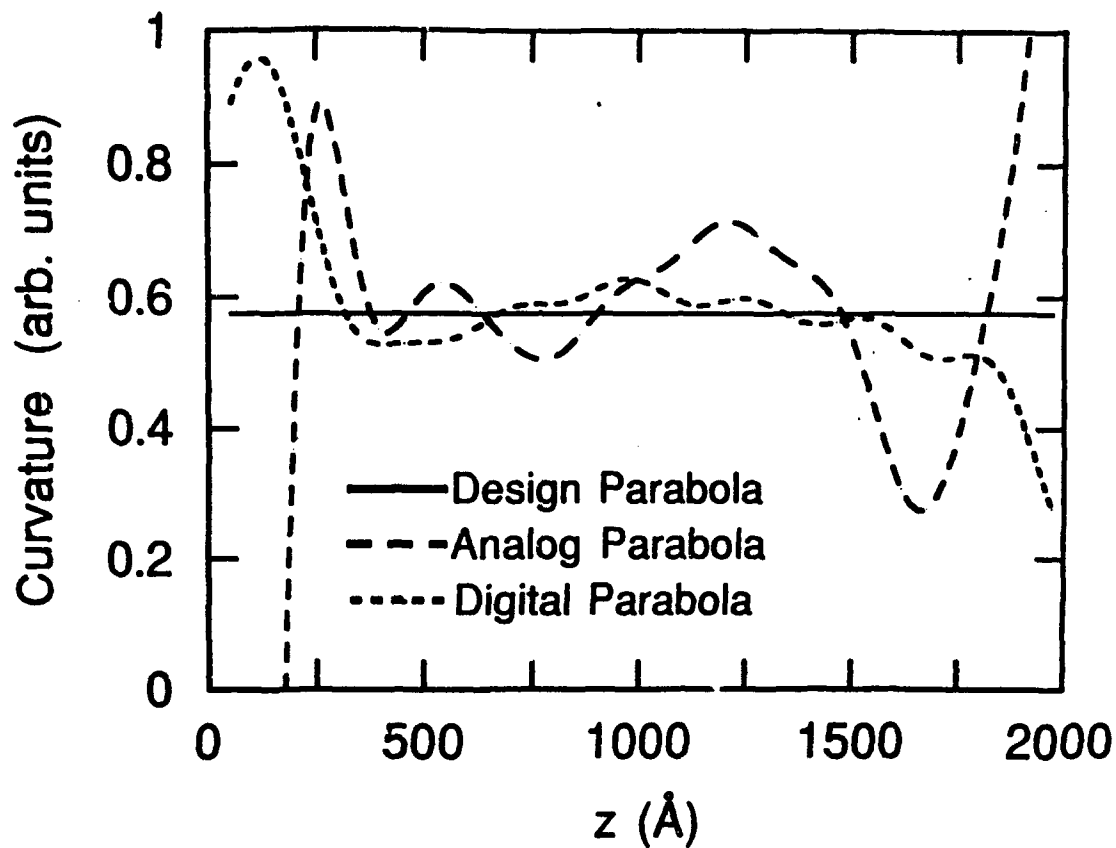


Figure 4. Curvature vs. depth profiles calculated from measured digital alloy (dotted line) and analog alloy (dashed line) beam flux composition profiles for parabolic wells compared to the constant design curvature (solid curve).

ELECTRICAL PROPERTIES

Capacitance-Voltage Profiling

In conjunction with the Harvard group, measurement of the capacitance between a front gate and the electron gas in a wide parabolic well was used to study the subband structure and the uniformity of the electron gas layer in the wells⁹. Performing these measurements in an in-plane magnetic field allows features that arise as a result of subband depopulation to be differentiated from those due to charge density fluctuations as a result of potential perturbations. Features in the C-V profiles that do not shift with magnetic field are attributable to non-uniform features in the electron distribution, whereas observed features in the C-V profiles that shift with magnetic field (as illustrated in Figure 6 for fields between zero and 8 tesla) are attributable to the filling and emptying of quantum-confined subbands in the wide quantum wells. Figure 7 shows both the capacitance and resistance of the same sample as a function of in-plane magnetic field. The resistance features caused by depopulation of the subbands coincide with the occurrence of capacitance features.

Capacitance-voltage profiling is now a standard tool to measure the width, density, and modulation of the electron gas in wide graded structures (see sections on hole gas and wide electron gas with periodic density modulation). A thorough theoretical and experimental study of C-V profiling on several types of graded heterostructures has been done in which carrier profiles extracted from capacitance data are compared to theoretical carrier distributions¹⁰. This method has also been used to measure the conduction band offsets in the $\text{Al}_x\text{Ga}_{1-x}\text{As}$ system for different values of aluminum mole fraction, x . It was found that $\text{DE}_c(\text{meV}) = 720 x_{\text{Al}}$, in good agreement with existing measurements.

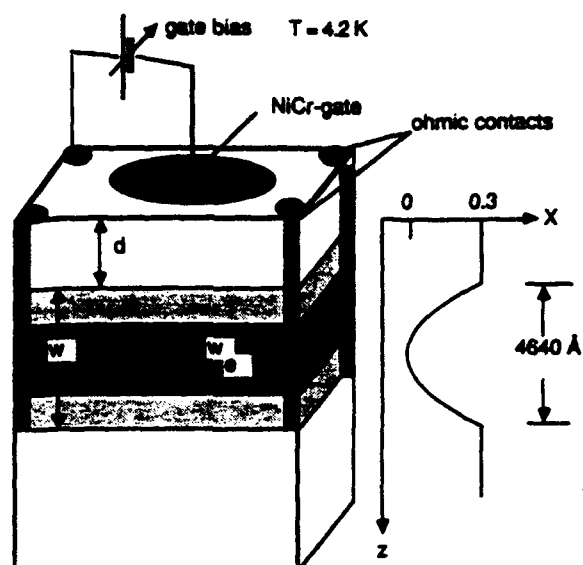


Figure 5. Contacting and gate bias configuration for measurements of capacitance between gate electrode and electron gas in a graded well.

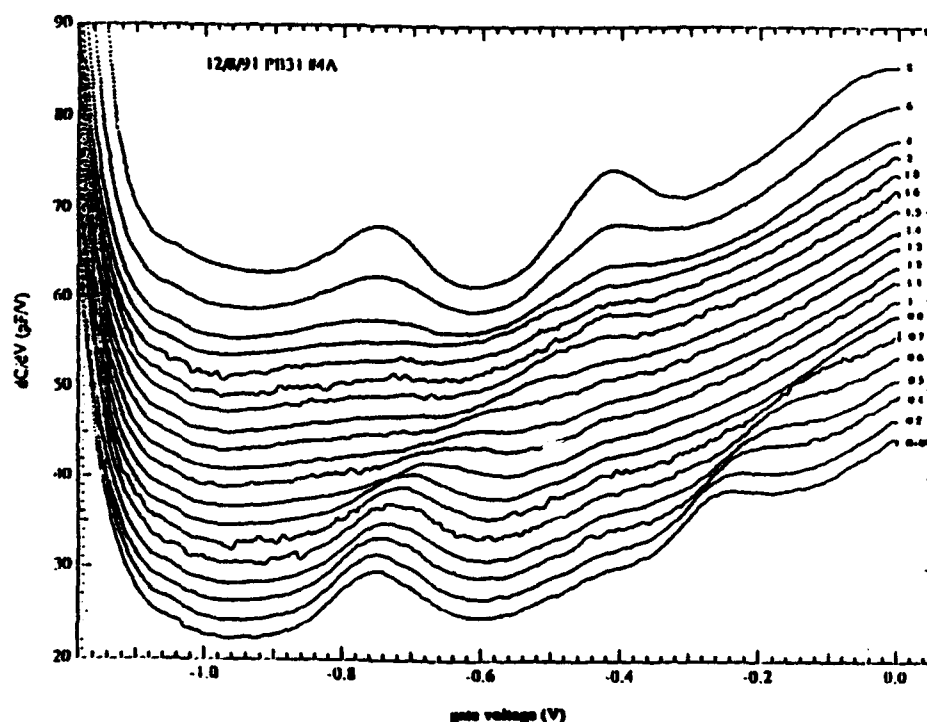


Figure 6. Derivative of capacitance (dC/dV) between gate electrode and electron well as a function of gate voltage for a parabolic potential well in magnetic fields between 0 tesla (bottom trace) and 8 tesla (top trace). Features that move with applied magnetic field are due to subband filling, while features in high field that do not move are due to non-parabolicities in the potential profile.

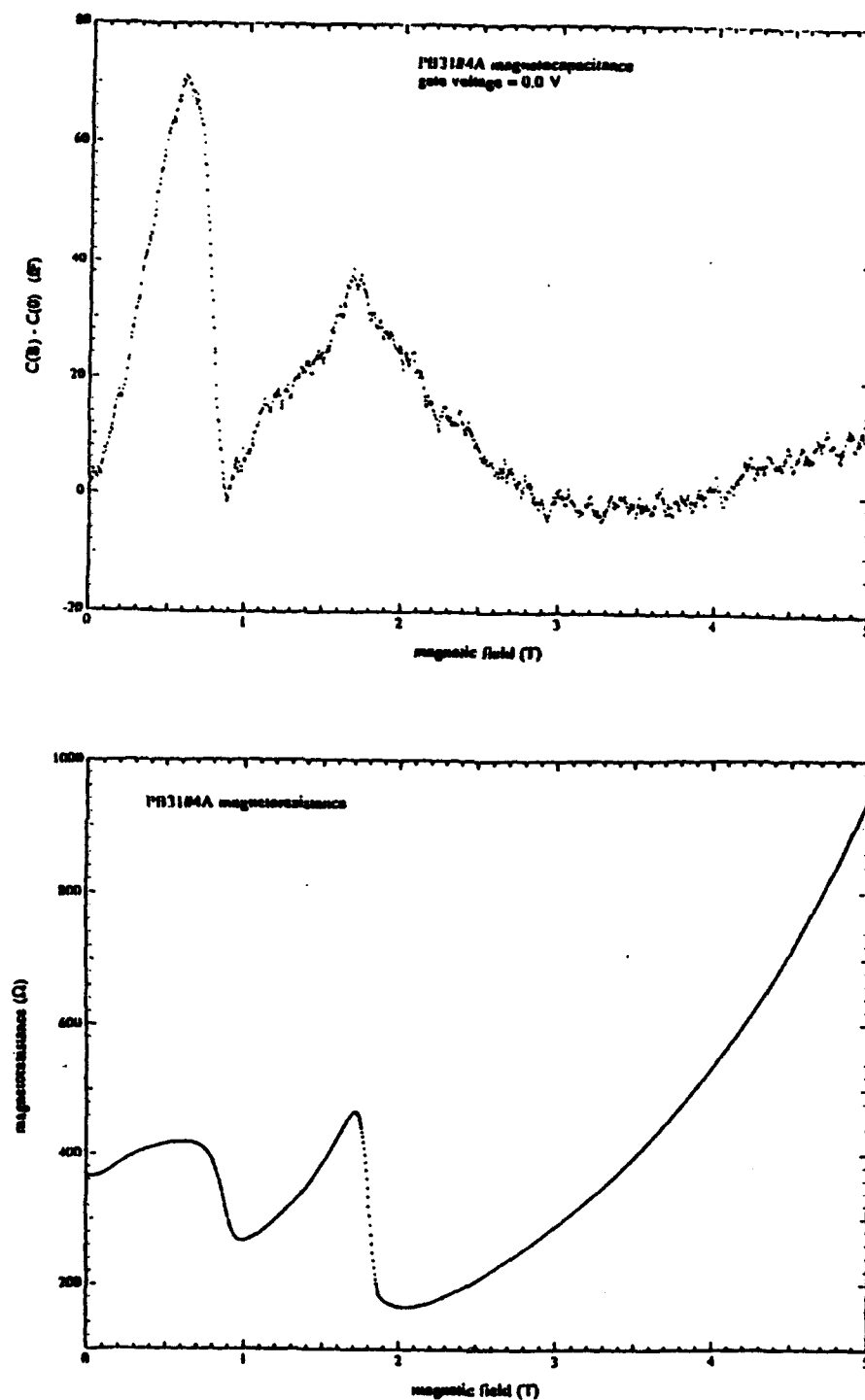


Figure 7. Curve at top shows capacitance between gate and electrons in wide parabolic well as a function of magnetic field at zero gate voltage. Peaks at 0.6 tesla and 1.8 tesla are caused by depopulation of new subbands and occur at nearly the same magnetic fields as the corresponding peaks in the electrical resistance as a function of magnetic field that are shown in the lower half of the figure.

Electron mobility

Wide parabolic wells offer new insights into the electron scattering that determines the electrical conductivity of semiconductors. The principal sources of electron scattering are potential fluctuations due to impurities, alloy fluctuations, and lattice vibrations.

Another source of scattering has been proposed and calculated by Wladislaw Walukiewicz at Lawrence Berkeley Laboratories¹¹, in response to experimental data from our wide parabolic wells. This new source of scattering is size effect scattering of high-mobility electrons at the edges of the electron gas. It occurs when the potentials at the edges of the gas are not uniform, allowing the edge of the electron gas to expand in regions of potential fluctuations (Figure 8). This allows non-specular electron scattering from the soft walls of the parabolic potential. With this mechanism, Walukiewicz has been able to explain, for the first time, the magnitude and temperature dependence of the electron mobility in the three-dimensional electron gas in wide parabolic wells (Figure 9). A similar effect had been proposed for thin semiconductor films¹², and for silicon inversion layers¹³, but had not been identified experimentally because of the relatively hard edges and steeply sloping potentials for the two-dimensional electron gas in MOSFET's. The effect could be important in graded heterostructures, though, where the edges of the electron gas are softer. It had not been observed in uniformly-doped semiconductors because of the short mean free paths of carriers. In the uniformly doped case, the path lengths are generally much shorter than sample dimensions.

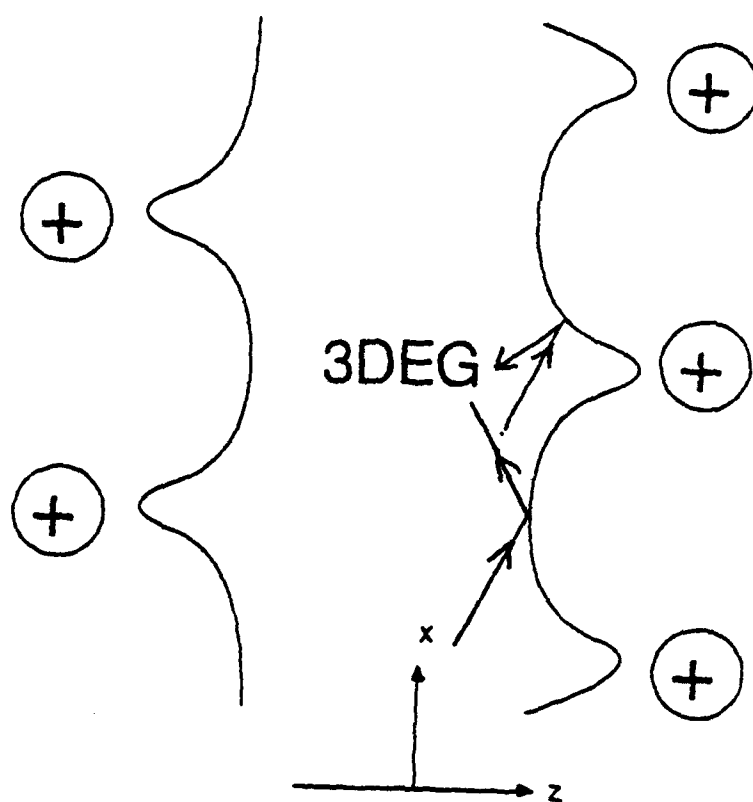


Figure 8. Schematic illustration of scattering of electrons at fluctuations in edges of an electron gas.

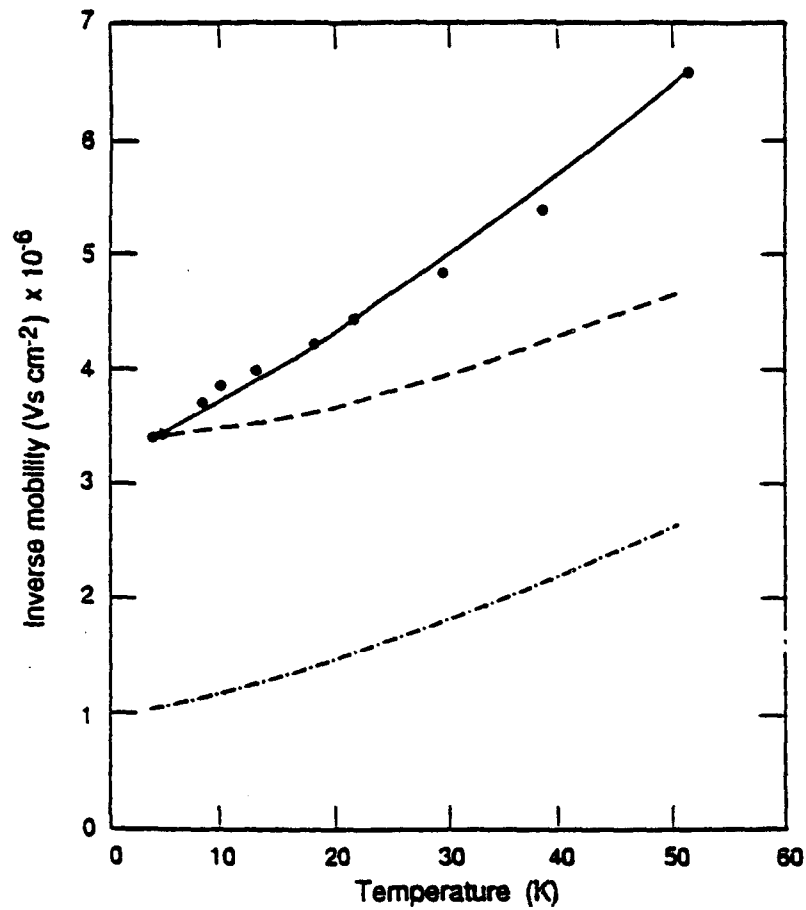


Figure 9. Calculated inverse mobility versus temperature for wide parabolic GaAs quantum well with ionized impurity concentration $n_{ii} = 2.3 \times 10^{14} \text{ cm}^{-3}$ and no size effect scattering (bottom curve), $n_{ii} = 1.0 \times 10^{15} \text{ cm}^{-3}$ and no size effect scattering (middle curve), and $n_{ii} = 2.3 \times 10^{14} \text{ cm}^{-3}$ with size effect scattering. Points show experimental data (for sample PBW 31).

Quantum Hall effect

At high magnetic fields, the integral quantum Hall effect was observed in parabolic wells (Fig 10)¹⁴. The data show how the integral quantum Hall effect makes a transition from two-dimensional toward three-dimensional behavior as electrons are added to the well via the persistent photoconductivity effect. As the thickness of the electron layer increases on filling of the well, the magnetic field position of the $\nu = 1$ filling factor Hall step remains fixed, indicating a nearly constant Fermi energy; positions of Hall steps at higher filling factors change due to the decreasing subband energy spacings as the electron layer gets wider.

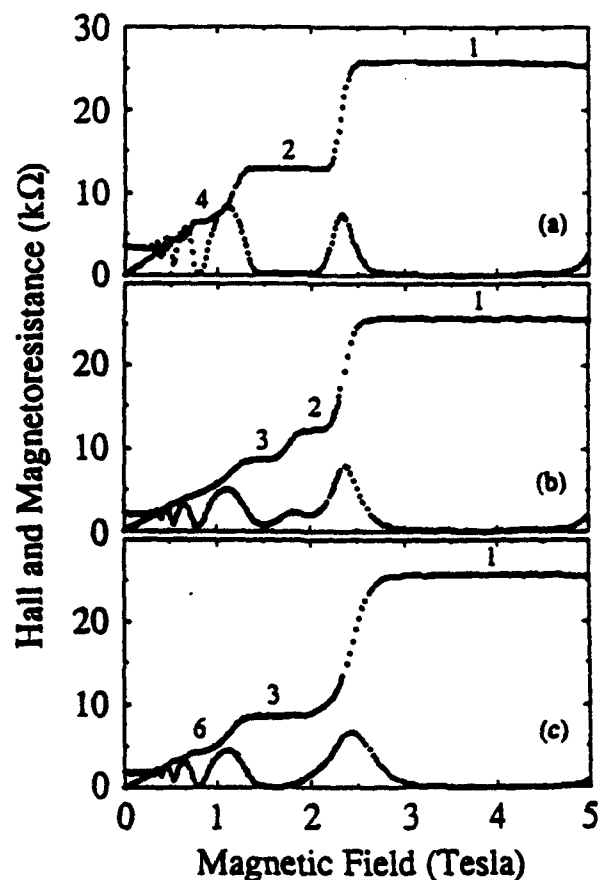


Figure 10. Quantum Hall effect and magnetoresistance versus magnetic field in a 4000 Å wide parabolic well: (a) before illumination, (b) and (c) after increasing periods of illumination, which raise the number of electrons from $0.78 \times 10^{11} \text{ cm}^{-2}$ to $1.12 \times 10^{11} \text{ cm}^{-2}$.

Electron transport in parabolic wells has also been studied under the influence of a gate bias applied to a semitransparent (Ti/Au) front gate¹⁵. For certain orientations of the magnetic field with respect to the sample, even integer quantum Hall states were observed to be suppressed and recovered as a function of gate bias. Figure 11 shows Hall resistance for several gate biases showing clearly the suppression and recovery of the $\nu = 4$ plateau. This effect can be explained quantitatively by a self-consistent calculation that considers the interplay of occupied Landau levels belonging to different subbands. In addition, a double minimum structure for the $\nu = 3$ has been observed, reflecting the different exchange enhancement of the spin splitting of the two lowest subbands. Parabolic well samples have also been studied in the fractional quantum hall regime where very different signatures have been seen compared to a standard high mobility 2DEG³.

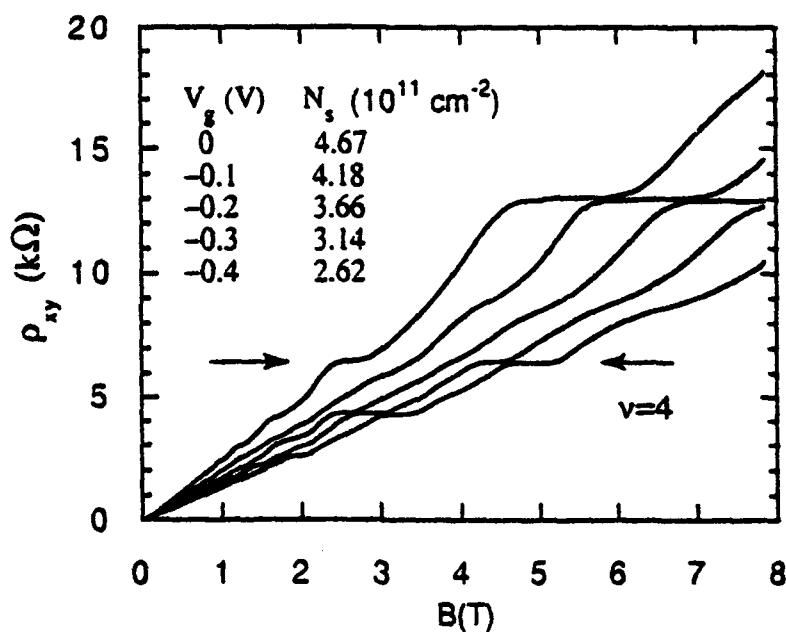


Figure 11. Hall resistance ρ_{xy} for different carrier densities. The arrows indicate the $\nu=4$ plateau which vanishes and reappears in this range of N_s .

OPTICAL PROPERTIES

Photoluminescence and Photoluminescence Excitation

To verify the parabolicity of the conduction and valence bands in the parabolic wells grown by digital alloy, PL and PLE experiments were performed on a sample consisting of ten undoped 520Å wide parabolic wells with Al content going from 0 at the center to 0.3 at the edges as shown in Fig. 12¹⁶. The peaks in the excitation spectrum reflect the harmonic oscillator like transitions between electron and hole states and confirm the electron and hole energy level spacing for parabolic wells.

Our collaborators at Harvard have measured PL and PLE on undoped parabolic wells as well as p-type and n-type modulation doped wells¹⁷. The modulation doped parabolic wells no longer show a simple harmonic oscillator ladder spacing. As electrons (holes) fill the well, a uniform quasi-3D gas is created which screens the parabolic potential leaving a flat conduction (valence) band profile. The valence (conduction) band in this case is still parabolic, but with an increased curvature. Although this becomes a very complicated problem with exchange and correlation effects making significant contributions to the absolute energies, data show that energy levels are qualitatively consistent with the picture of a uniform density slab of carriers screening a parabolic potential.

Also in collaboration with the Harvard group, the hydrostatic pressure dependences of the harmonic oscillator spacings of an AlGaAs parabolic well were measured by photoluminescence excitation spectroscopy¹⁸. The pressure dependence of the conduction band offset for GaAs/AlGaAs heterojunctions could be determined from these results, and it was shown that the band gap difference in the conduction band may increase with pressure by as much as 10% at pressures of 25 kbar. Thus previous determinations of conduction band offsets by use of pressure data are shown to be subject to an overestimation by up to ten percent.

Resonant inelastic light scattering, performed by the Harvard group¹⁹, was used to probe the excitations of wide parabolic quantum wells. In each sample, a series of spectra for excitations near the spin-orbit split-off band gap showed two strongly resonant light scattering peaks. The resonance curves for the peaks were separated by an energy equal to the scattering peak separation, and are consistent with a model in which the electron gas in the well is distributed as a uniform density slab, giving rise to a square

well effective potential, in confirmation of the theoretical behavior of an ideal modulation doped parabolic well.

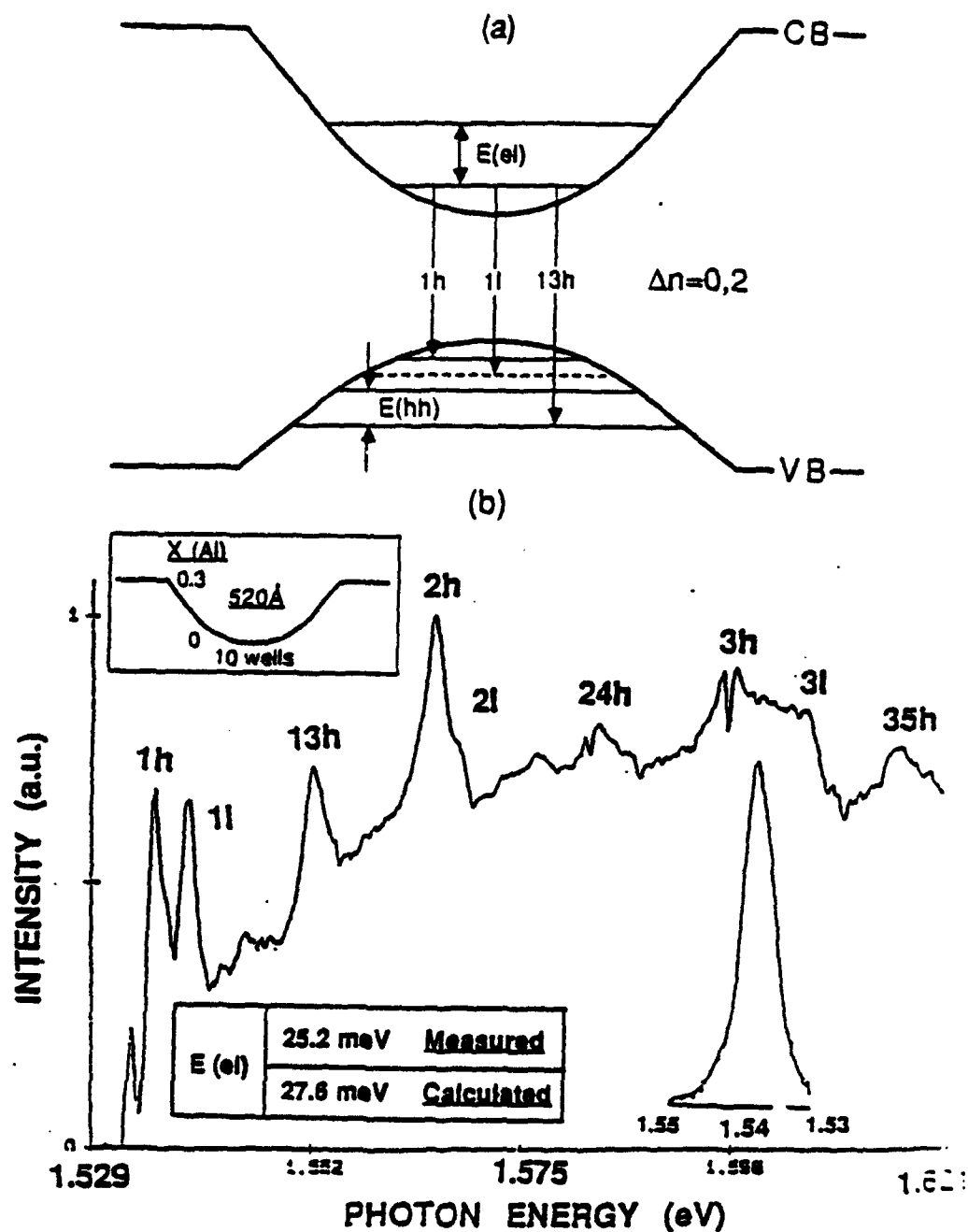


Figure 12. Energy levels and optical interband transitions in an undoped 520 Å parabolic quantum well are shown at top. Observed photoluminescence excitation spectrum and emission peak are shown at bottom.

Nonlinear Properties

Second harmonic generation at infrared frequencies requires an asymmetric crystal structure and offers another application for the parabolic well family that has been explored. The second harmonic generation should be greatly enhanced in asymmetric parabolic potential wells, especially the half parabolic well, as compared to certain bulk materials which themselves are highly non-linear (Fig. 13). This structure was proposed by our collaborator, Professor Mark Sherwin, in the UCSB Physics Department. The first non-linear susceptibility coefficient, $\chi(2)$ for half parabolic wells has been calculated and it was found to be more than four orders of magnitude greater than lithium tantalate and more than six orders of magnitude greater than for gallium arsenide.

These structures have been grown and examined in the intense pulsed far-infrared beam of the UCSB free electron laser²⁰. Strong second harmonic response was seen from the half parabolic wells as well as from single heterojunctions and measured as a function of incident beam intensity for incident photon energies in the 30 to 50 cm^{-1} range (Fig. 14). In addition, ionization of carriers from the wells by the intense FEL beam was achieved. From the persistence of the carrier decrease after irradiation, it was deduced that the electrons that are removed from the wells are bound at DX centers in the AlGaAs barriers.

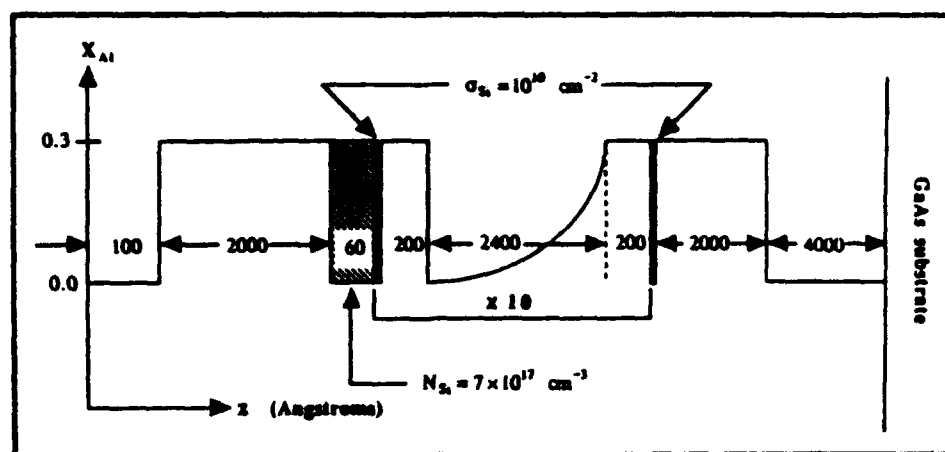


Figure 13. Design of the structure containing ten half-parabolic electron wells for study of harmonic generation. Aluminum content versus distance is plotted, and location of doping layers is shown.

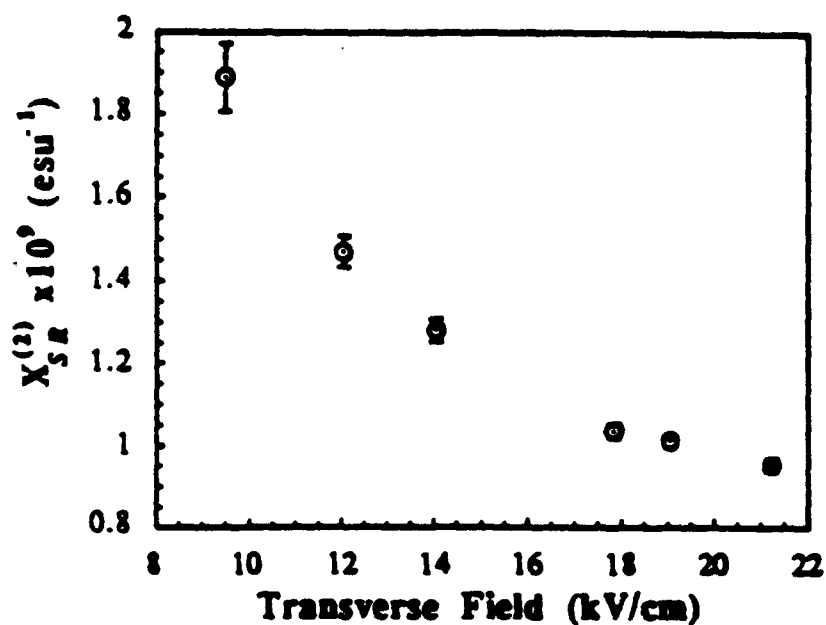


Figure 14. Second order susceptibility $\chi^{(2)}$ as a function of transverse component of electromagnetic electric field for half parabolic wells at $T = 7 \text{ K}$ at a fundamental frequency of 29.5 cm^{-1} .

Surface Plasmons

Coupled surface plasmons in high mobility three dimensional electron gases in parabolic wells were observed for the first time in collaboration with Professor Beth Gwinn in the UCSB Physics Department and her graduate students Paul Pinsukanjana, Esther Yuh, and Naggi Asmar²¹. The parabolic well electron gas gives a unique opportunity to observe such modes because 1) the electrons are spaced further apart than in a metal, 2) the electron scattering is small in the modulation doped parabolic well, and 3) the width of the electron gas in the parabolic well can be varied by means of a gate electrode. This has allowed Professor Gwinn and her group to study and gain access to the parts of the dispersion relation between the zone boundaries and the zone centers that could not be reached in previously available materials. Using this technique, coupled plasmon modes having the configurations shown in Figure 15a were observed. The predicted frequencies of the modes with increasing width w of the electron gas are shown in Fig. 15b; the studied well is shown in Fig. 15c; and the grating coupler/gate and configuration of the parabolic well are shown in Fig. 15d. Transmission spectra at two different gate biases are shown in Figure 16. The two lowest frequency resonances are coupled surface plasmons with the stronger one corresponding to a plasmon with wavevector parallel to the surface and equal to the grating wavevector. The weaker mode corresponds to a surface plasmon with wavevector equal to twice the wave vector of the grating. The high frequency resonance occurs near the plasma frequency ω_p of the sloshon mode and is assumed to arise from the positively coupled surface modes of frequency ω^+ . These surface plasmon modes shift with changing width of the occupied region as gate bias is changed. This occurs because the surface modes on opposite sides of the electron slab are coupled with each other and the coupling changes as the slab width changes. The system is particularly tractable to analyze because the parabolic potential continues beyond the edges of the occupied slab.

Coupled surface plasmons have also been studied in more complicated heterostructures such as a bi-metallic well²². This structure consists of two parabolic regions of different curvature which meet smoothly creating an electron distribution with a step in the electron density. Additional structure in the absorption spectra was seen due to the additional interface between regions of different electron density. These studies have provided information as to how excitations of a thin metal with internal density gradients evolve into surface plasmons of a three dimensional layer.

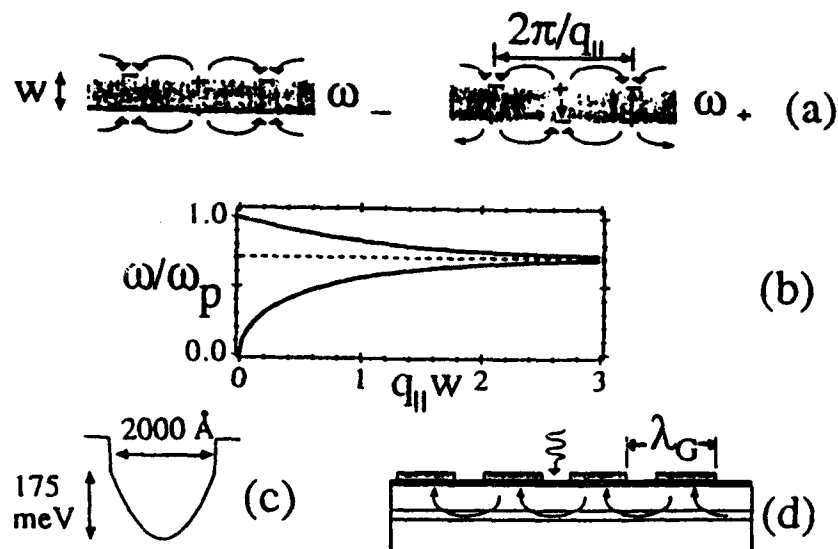


Figure 15. a) Charge and electric fields of coupled plasmon modes of electrons in wide parabolic potential wells. b) Predicted frequencies of the modes as a function of the width w of the electron gas slab. c) Dimensions and composition and potential profile (for empty well) of the modulation doped well in which the coupled plasmon modes were observed. d) The grating coupler and well configuration, the grating wavelength λ_G , the incident photon direction (sine wave arrow) and the internal electric field distributions (curved arrows) for measurement of the coupled plasmon modes.

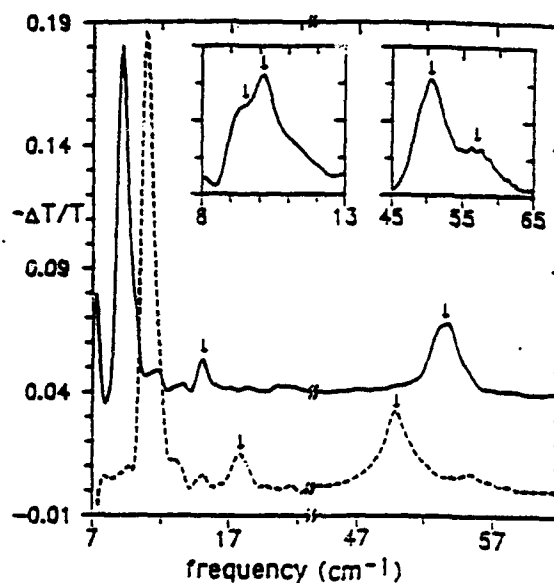


Figure 16. Relative transmission $-\Delta T/T$ of modulation doped parabolic well as a function of frequency. Dashed and solid lines show transmission spectra before illumination for gate voltages $-0.2V$ and $+0.2V$ respectively. The baseline for the solid curve has been offset. Inset shows illumination-induced splitting of the low and high frequency modes for gate voltage $-0.5V$.

Far-infrared Spectroscopy of Wide Parabolic Wells

Sharply resonant behavior of electrons in wide graded wells has now been seen using several different coupling techniques²³. Working with Professor Elizabeth Gwinn in the UCSB Physics Department and with Dr. Achim Wixforth, we have made structures in which resonant electron behavior has been seen in a) cyclotron resonance, b) hybrid cyclotron-plasma resonances and c) in pure plasma resonances²⁴. Observation of sharp resonances in the wide graded structures is made possible by the enhanced carrier scattering times (τ) due to the high mobilities in the structures. To observe clear resonant behavior requires that $\omega\tau \gg 1$. This condition implies that a mobility near $1000 \text{ cm}^2/\text{Vs}$ is required at submillimeter wavelength frequencies. Low temperature mobilities typically two orders of magnitude greater than this limit in our structures enable the first enhanced-Q electron resonators in this frequency range to be built for electrons in semiconductors.

A plot of the observed plasma frequencies as a function of gate voltage for a 2000 \AA wide well in a magnetic field tilted with respect to the sample surface is shown in Figure 17. When the gate on the sample is biased, the total number of electrons in the well is changed, but the observed plasma frequency, as shown in Figure 17, is found to be independent of the total charge density, in confirmation of the so-called Kohn theorem for the parabolic well²⁵. The Kohn theorem²⁶ states that electrons in a perfect parabolic well with a magnetic field in an arbitrary direction will absorb long wavelength light only at the two frequencies (plasma and cyclotron or admixtures thereof) corresponding to the motion of the center of mass of the electron system. The striking feature is that the intersubband resonance remains constant in frequency as the well is filled with electrons even though the single particle levels are changing dramatically from evenly spaced harmonic oscillator energy levels to square well like quadratically spaced levels. The Kohn theorem is applicable to all systems with parabolic confinement, the most notable being electrons in electrostatically defined potentials (i.e quantum dots)²⁷.

In addition to observation of the hybrid plasma/cyclotron resonance for magnetic fields tilted and parallel with respect to the surface, the plasma resonance has also been observed directly with normally incident radiation without the use of a magnetic field (Wixforth et al., 1991) by using a grating coupler to couple to the plasma resonances.

Parabolic wells with widths 75 nm and 200 nm in which the number of electrons in the well was controlled and varied by a semitransparent front gate electrode have been studied. The resonance positions for the fundamental absorption mode are also independent of gate voltage and carrier densities within the precision of the measurement. Thus, the determined value of the plasma frequency was in agreement for the different measurement techniques, as shown in Figure 18.

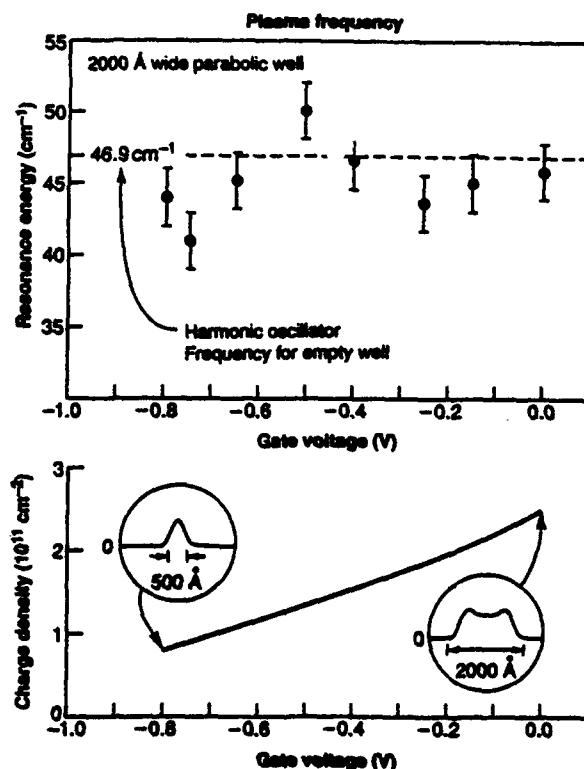


Figure 17. Observed resonance frequencies as a function of gate voltage (upper plot) for a 2000 Å wide well in a magnetic field tilted with respect to the sample surface. The total charge density per unit area in the well and the charge density profile in the well are shown for the same range of gate voltages in the bottom half of the figure.

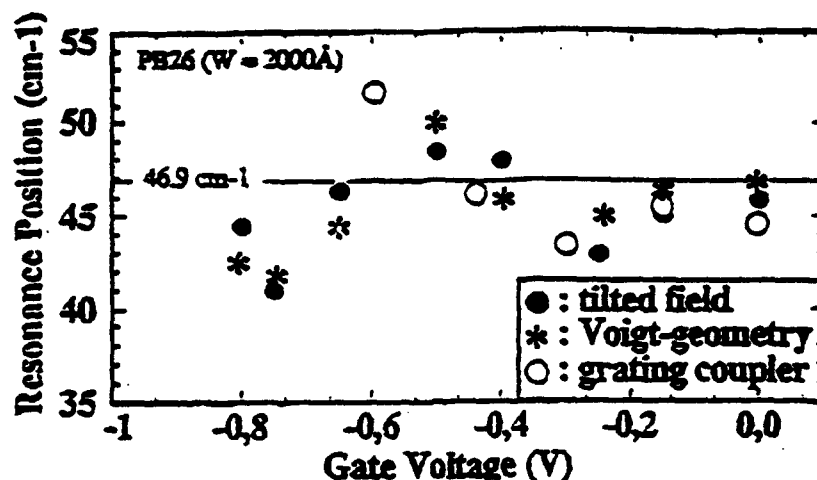


Figure 18. Resonance frequencies as a function of gate voltage for a modulation doped parabolic well measured by three different techniques. Filled circles represent frequencies measured in tilted magnetic field, stars represent resonant frequencies determined from measurements with magnetic field parallel to the surface, and open circles show resonant frequencies measured by direct absorption measurement with a grating coupler.

We have also grown a number of structures in which the potential profile differs from a pure parabola, either due to intentional nonparabolicities or due to the effect of the edges of the potential. Because of the simplicity of the Kohn theorem result (that the fundamental absorption frequency in parabolic wells is independent of the total number of electrons in the well), the absorption spectrum of the conduction electrons in a wide well becomes a sensitive test of the shape of potential wells with small deviations from parabolicity. For wells that are not purely parabolic, the plasma and cyclotron frequencies are shifted and transitions between other states of the electron system are allowed. In our experiments on wells of 750 Å width with sharp external barriers, the energies of the fundamental plasmon excitations were shifted only slightly from those of the perfect wells, but satellite resonant absorption lines were observed (Figure 19). There are many modes close to the cyclotron frequency, and this accumulation of modes shows up as a heavy line at the cyclotron frequency in the 23 degree orientation of Fig. 20. The

observability of modes with frequencies (square points) different from the center of mass modes occurs because the parabolic symmetry is broken by the edges of the well and the influence of the gate electrode that controls the carrier concentration in the well. The theory calculation of the frequencies and intensities of these modes has been carried out by our Harvard theory collaborators²⁸. The agreement between the theory and the experimental points suggests that the experimentally observed modes are closely related to the calculated magnetoplasmon modes. The small satellite resonances observed at zero magnetic field demonstrate the coupling of the far infrared radiation to the internal oscillations of the electron system.

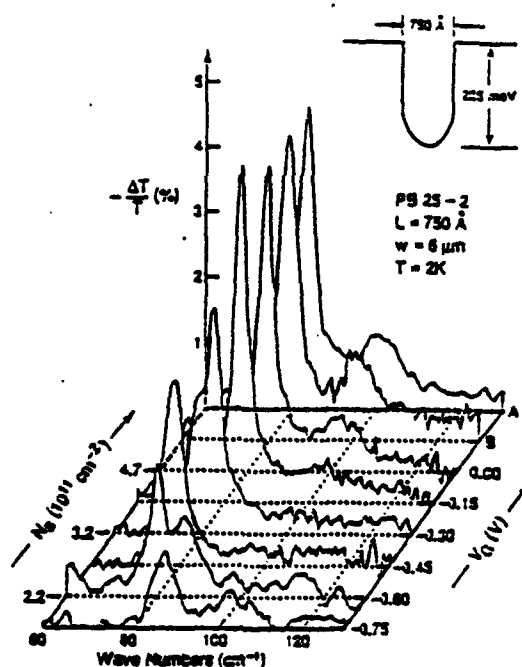


Figure 19. Relative transmission spectra of $-\Delta T/T$ versus frequency for electron resonances measured experimentally at different gate voltages in parabolic wells of 750 \AA width with sharp external barriers. Traces A and B were taken after illumination of the sample, which further increased the carrier density in the well. In both the limits of high and low electron concentration, deviations from the harmonic oscillator behavior are observed as satellite absorption lines are observed.

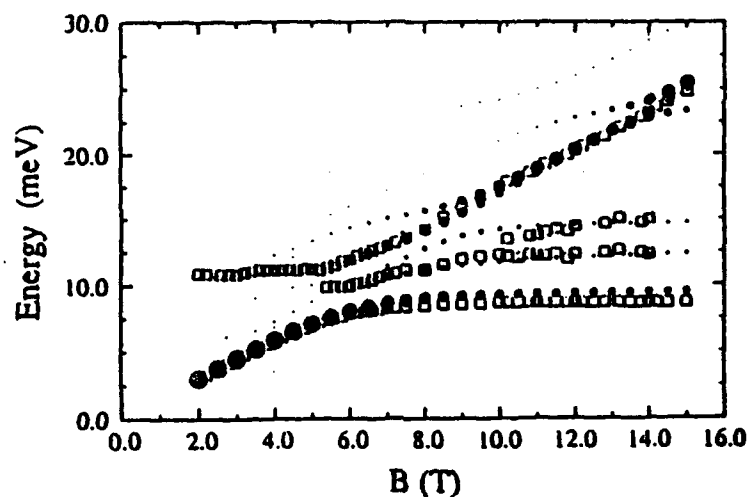


Figure 20. Electron resonance frequencies as a function of magnetic field in the sample of Figure 19. Open points are experimentally observed resonance positions and closed circles are theoretically calculated resonance energies. The diameters of the closed circles represent the theoretically calculated relative intensities of the resonances. The observability of modes with frequencies (square points) different from the center of mass modes occurs because the parabolic symmetry is broken by the edges of the well and the influence of the gate electrode that controls the carrier concentration in the well.

ADDITIONAL GRADED HETEROSTRUCTURES

Three Dimensional Hole Gas

The concept of creating a wide, uniform density layer of electrons by modulation doping of a parabolic well with Si donors can be extended to create a three dimensional, high mobility hole gas²⁹. A schematic diagram of the valence band and conduction band edges and the energy levels in the p-type modulation doped parabolic wells is shown in Figure 21. The materials used for making the three dimensional hole gases were digital alloy AlGaAs wells with beryllium doping in the barriers. The hole concentrations in the wide parabolic wells, unlike hole concentrations in uniformly doped materials, do not freeze out at the lowest temperatures, and hole mobilities that are strongly enhanced with respect to uniformly doped p-type layers have been observed (Fig. 23). Thus, they offer the first opportunity to observe quantum effects in the electrical resistance of three-dimensional holes and to produce hole resonators. Clear oscillations of the magnetoresistance with multiple periods have been observed as well as plateaus in the Hall resistance (Fig. 24).

These $\text{Al}_x\text{Ga}_{1-x}\text{As}$ parabolic wells were formed by the digital alloy technique, and it was not fully understood whether the holes with their substantially heavier effective mass would be able to effectively screen the fine period superlattice. Analysis of the charge distribution and energy levels in the digital alloy parabolic well were carried out by a simple perturbation theory treatment. The result of this treatment is that a sinusoidal superlattice potential superimposed on a uniform electron gas changes the electron effective mass from m_0^* for a uniform potential to $m_0^* \{1 + 0.5[U(G)/E_0(G/2)]^2\}$ for a potential to which a sinusoidal potential of magnitude $2U(G)\cos(Gz)$ has been added. $E_0(G/2)$ is the energy for carriers with the bulk effective mass at wavevector $G/2 = \pi/d$, where d is the period of the perturbation. The change in mass of the carriers for motion perpendicular to the digital alloy superlattice is thus proportional to the fourth power of the superlattice period. At a superlattice period of 20 Å, a hole of mass 0.50 m_e is increased to electron mass 0.513 m_e , while the energy of the band is shifted by an amount 4.6 meV. Although the hole charge density has ripples of size about $\pm 23\%$ for this structure, the electron motion is not significantly perturbed at this period of digital alloy superlattice.

Be modulation doped parabolic well

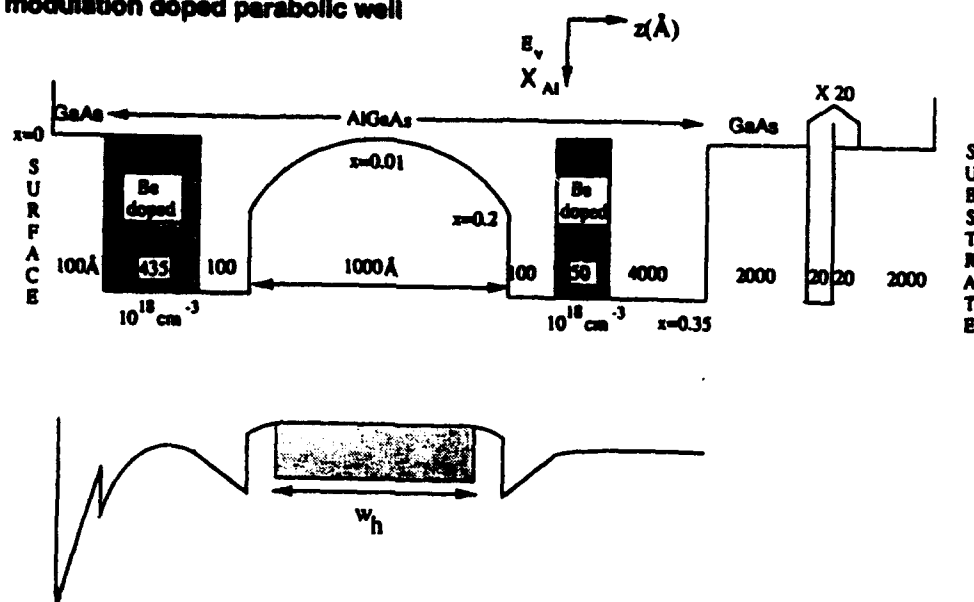


Figure 21. Schematic diagram of the composition profile and the valence band edge profile in p-type modulation doped parabolic well.

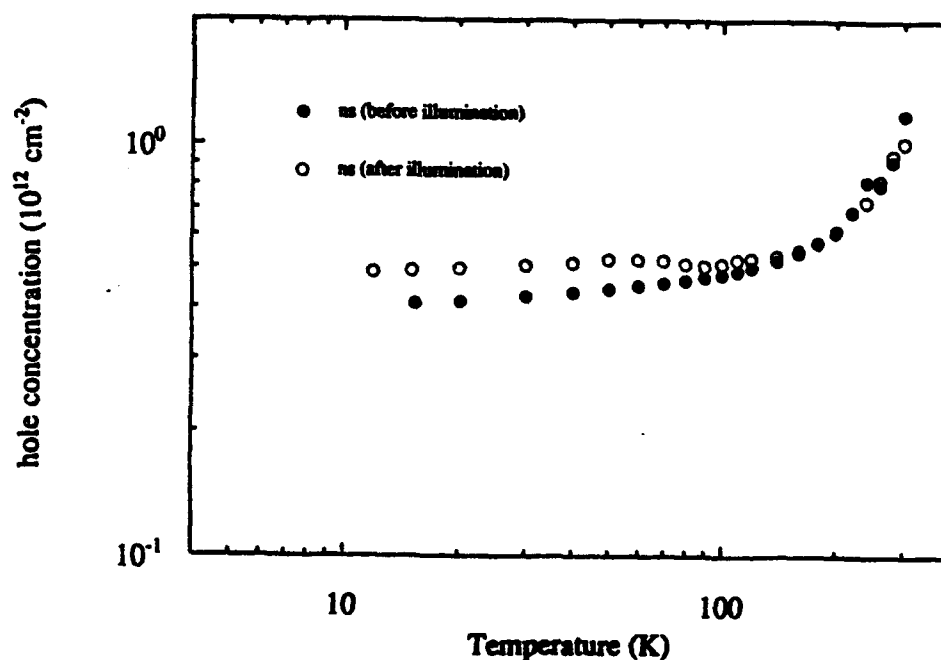


Figure 22. Hole concentration per cm^2 as a function of temperature measured by Hall effect in parabolic well hole gas before (crosses) and after (circles) illumination. The design curvature of the parabola corresponds to a uniform hole concentration of 4×10^{16} holes per cm^3 .

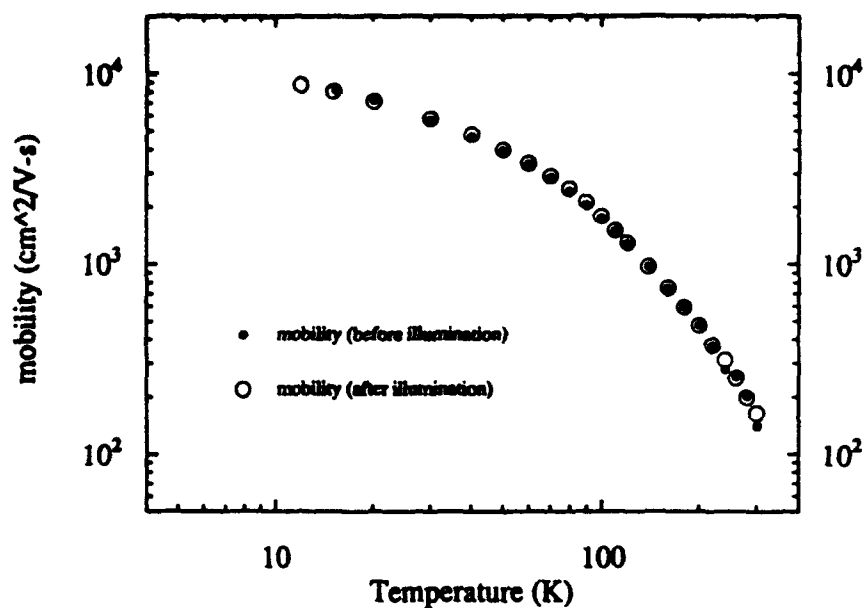


Figure 23. Hole mobility from Hall effect measurements as a function of temperature in parabolic well hole gas before (closed circles) and after (open circles) illumination.

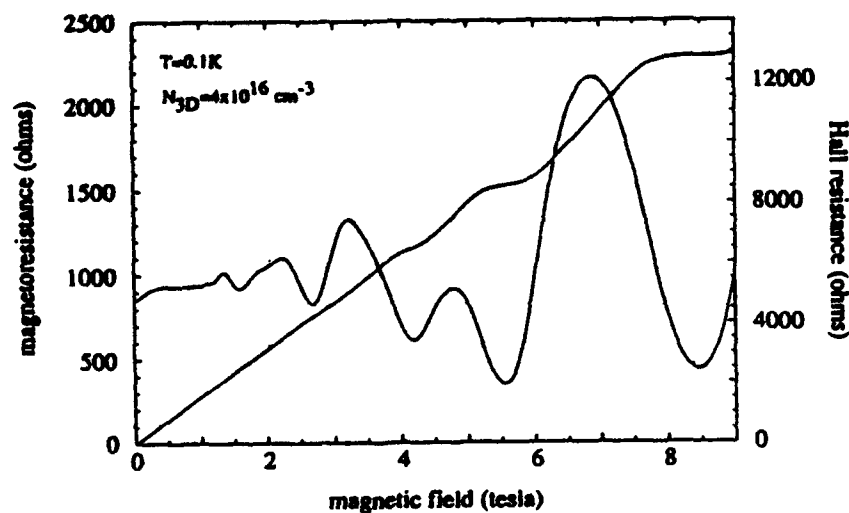


Figure 24. In-plane electrical resistance and Hall resistance as a function of transverse magnetic field for holes in wide parabolic well.

Superlattice in a Parabolic Well

The growth of parabolic wells containing superlattices has been shown to produce a wide, high-electron mobility, periodically modulated electron gas^{30, 31}. This technique allows the realization of layered electron gases with far higher mobility than ever before for layers that are close enough to each other for significant coupling between the electrons. The principle of the structure is illustrated in Figures 25 and 26. Figure 25 compares structures for producing coupled sheets of electron gases. The top figure illustrates band edges before transfer of electrons from donors to the wells and the bottom figure shows band edges and carrier distributions after electrons transfer to the wells for a) the modulation doped superlattice and b) a superlattice in a parabolic well with only the exterior barriers doped. Reduced ionized impurity scattering at low temperatures due to the removal of donors from superlattice barriers gives mobilities almost an order of magnitude higher for the superlattice in the parabolic well. Figure 26 shows the electron densities and effective potential profiles calculated quantum mechanically by a self-consistent Poisson-Schrodinger equation solver for a superlattice in a parabolic well having the dimensions and compositions of a sample that we have grown, as well as the corresponding electron densities and effective potential calculated for a parabolic well without a superlattice.

Two samples, similar to the ones for which calculations were presented in Fig. 26, were grown. Mobilities as high as $1.8 \times 10^5 \text{ cm}^2/\text{Vs}$ at a sheet density of $2.5 \times 10^{11} \text{ cm}^{-2}$ for the bare parabolic well, and $1.1 \times 10^5 \text{ cm}^2/\text{Vs}$ at a carrier density of $2.0 \times 10^{11} \text{ cm}^{-2}$ for the parabolic well with superimposed superlattice were observed³². The low-temperature mobility measured in the plane of the layers for the density-modulated 3DEG is an order of magnitude higher than is available in a standard modulation-doped superlattices of the type shown in Fig. 25.

Capacitance versus voltage (CV) measured between the surface gate and the electron gas in the graded well for both samples are shown in the inset in Fig. 27. Whereas the capacitance falls off smoothly with voltage for the bare parabolic well (PB31), the CV trace for the parabolic well with a superlattice (PB32) displays ripples superimposed on the decrease. These ripples are associated with the sweeping of the leading edge of the electron gas through successive periods of the superlattice with more

negative bias. From the CV measurement one can extract an apparent electron distribution versus depth shown in Fig. 9 for both samples. A modulation of the apparent electron density is readily seen for the electron gas in the parabolic well with superimposed SL; no such modulation is seen for the 3DEG in the bare parabolic well. We believe this to be the most direct evidence to date of the density-modulation produced in such structures. Theoretical studies of this system³³ predict novel electrical and optical properties which are currently being investigated.

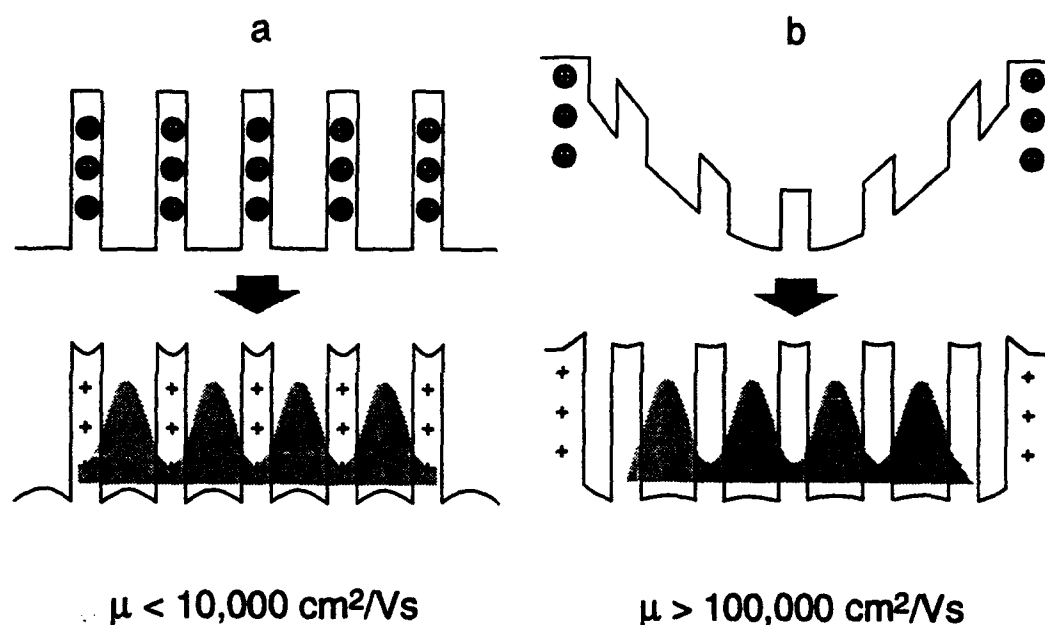


Figure 25. Comparison of structures for producing coupled sheets of electron gases. The top sketches of band edge profiles and location of dopant atoms shows band edges before transfer of electrons from donors to the wells. The bottom sketches show band edges and carrier distributions after electrons transfer to the wells for a) the modulation doped superlattice and b) a superlattice in a parabolic well with only the exterior barriers doped. The larger spacing between the dopants and the electron gases gives far higher mobility (more than ten times larger) in case b) (superlattice in a parabolic well).

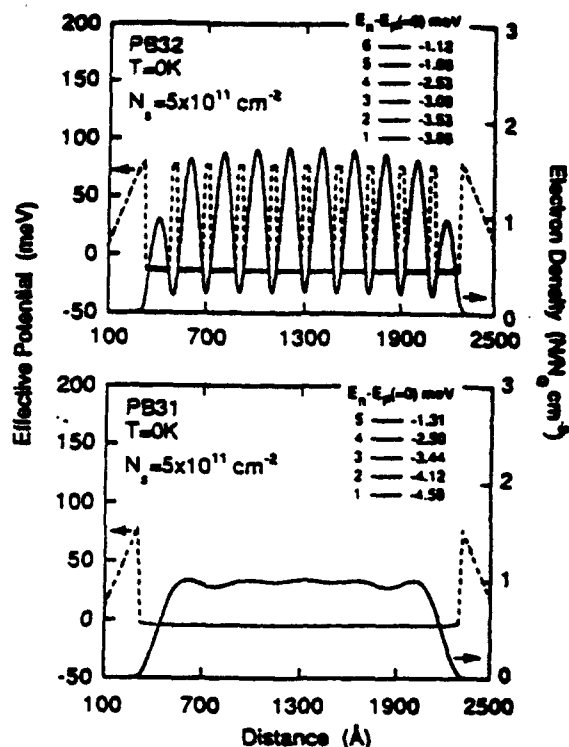


Figure 26. Electron densities (solid lines) and effective potential profiles (dashed lines) for a superlattice in a parabolic well having the dimensions and compositions of a sample that we have grown (top curve), as well as the corresponding electron densities and effective potential calculated for a parabolic well without a superlattice (bottom curve). Energies E_n of the edges of subbands are also shown.

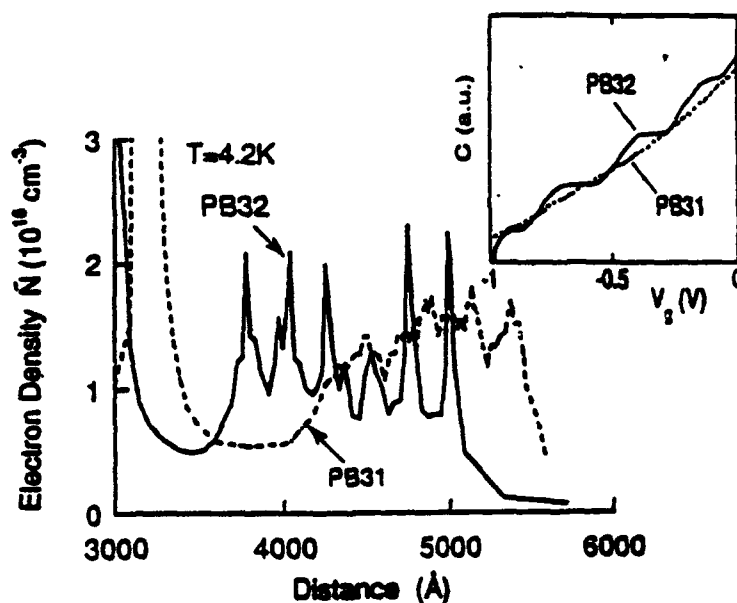


Figure 27. Electron density profile as a function of distance measured by capacitance profiling between a surface gate electrode and the electron gas in a graded well for samples containing a superlattice in a parabolic well (solid curve) and a parabolic well with no superlattice (dashed curve). Inset shows capacitance versus voltage measured for the same samples.

Tunable Electron Resonator

Another example of a graded heterostructure based on the parabolic well is a widely tunable high-Q Terahertz-frequency electron resonator³⁴. These modulation-doped asymmetric wide wells have been shown to give electric field-induced shifts of the electron resonances of more than 200% (from resonant absorption frequencies of 1.1 THz to 3.7 THz, i. e. from 35 cm^{-1} to 125 cm^{-1}) for modest gate voltages³⁵. By contrast, purely parabolic wells have resonant absorption frequencies that are remarkably independent of electron occupation of the wells and independent of applied electric fields. Thus the new resonators operate in an interesting regime between a purely parabolic well (in which an applied electric field or a depletion of the well causes no shift whatsoever in resonance frequency) and in square wells (in which only much smaller shifts can be produced). The resonances are strong and do not require magnetic field or exotic low temperatures.

The devices are based on a wide graded "logarithmic" well structure with the shape illustrated in Figure 28. Using a surface gate, an epitaxially grown back gate, and a contact to the electron gas, we produce the shift in the far infrared collective electronic resonant response by moving the electron gas through the asymmetric well. By controlling the electron density in the well, we can separately tune the absorption strength. In comparison, previous work on narrower ($\sim 100 \text{ \AA}$) asymmetric step wells has yielded much weaker shifts in the frequency of the intersubband optical absorption. Narrow band detectors and emitters based on cyclotron resonance have comparable tunability, but require strong magnetic fields.

We synthesized a bare well potential $V(z)$ in which the harmonic oscillator frequency ω_0 at the potential minimum varies linearly with applied electric field $E(z) = E$ across the well:

$$\omega_o(z_{\min}) = \left\{ \frac{1}{m^*} \left[\frac{\partial^2 V_T(z_{\min})}{\partial z^2} \right] \right\}^{1/2} = \frac{1}{\sqrt{m^*}} (aeE + b) \quad (1)$$

where a and b are constants, e is the electronic charge, $V_T(z) = V(z) + eEz$ is the total potential in the absence of electrons in the well, and the second derivative is evaluated at the minimum point of $V_T(z)$. We studied the solution of Eq. (1), $V(z) = -a^*$

$2\ln(abz+1) + zb/a$, in which we give the empty well a tunability $\frac{1}{2\pi c} \frac{\partial \omega_0}{\partial E} = 2.0 \text{ cm}^{-1}/(\text{kV/cm})$ by setting $a = 0.0751 (\text{meV})^{-1/2}$ and $b = 0.0263 (\text{meV}/\text{\AA}^2)^{1/2}$. The well edges are $z = -450 \text{ \AA}$ and $z = 1005 \text{ \AA}$.

GaAs/ $\text{Al}_x\text{Ga}_{1-x}\text{As}$ samples were grown by molecular beam epitaxy to simulate the potential $V(z)$ shown above. Far-infrared transmission measurements were made using a stripline geometry (inset of Fig. 29) with radiation coupled into the edge of the sample. The large tunable absorption in the logarithmic well is demonstrated in Fig. 29, which shows the observed absorption spectra for a series of V_{fg} at fixed V_{bg} . Compiled in Fig. 30 are the frequencies of the dominant absorption peaks versus V_{bg} for equally spaced V_{fg} . The filled data points have approximately the same $n_s(V_{fg}, V_{bg}) \sim 5 \pm 2 \times 10^{10} \text{ cm}^{-2}$, and demonstrate that it is possible to Stark shift the single sharp absorption peak from 35 cm^{-1} to 125 cm^{-1} by moving the electron gas through the logarithmic well, while maintaining approximately constant n_s and integrated absorption strength. These collective electronic resonances make this structure a $B = 0$ voltage-tunable modulator. Similar graded well structures could form the basis for tunable, narrow band, Terahertz solid state oscillators and harmonic generators.

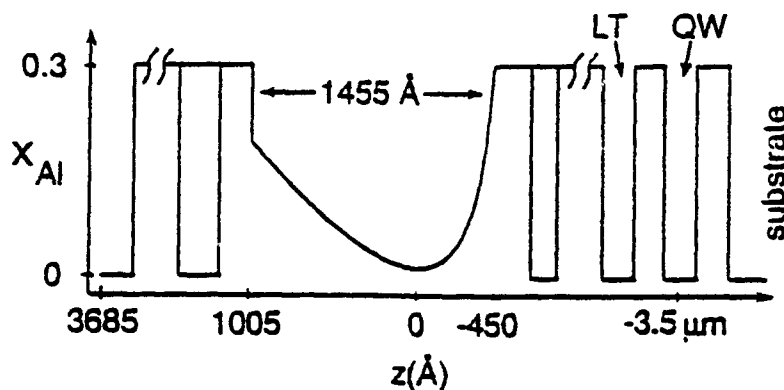


Figure 28. Compositional structure x_{Al} of $\text{Al}_x\text{Ga}_{1-x}\text{As}$ graded tunable potential well with quantum well back gate (QW), low temperature GaAs insulating barrier (LT), and modulation doping (shaded layers) on either side of the tunable well.

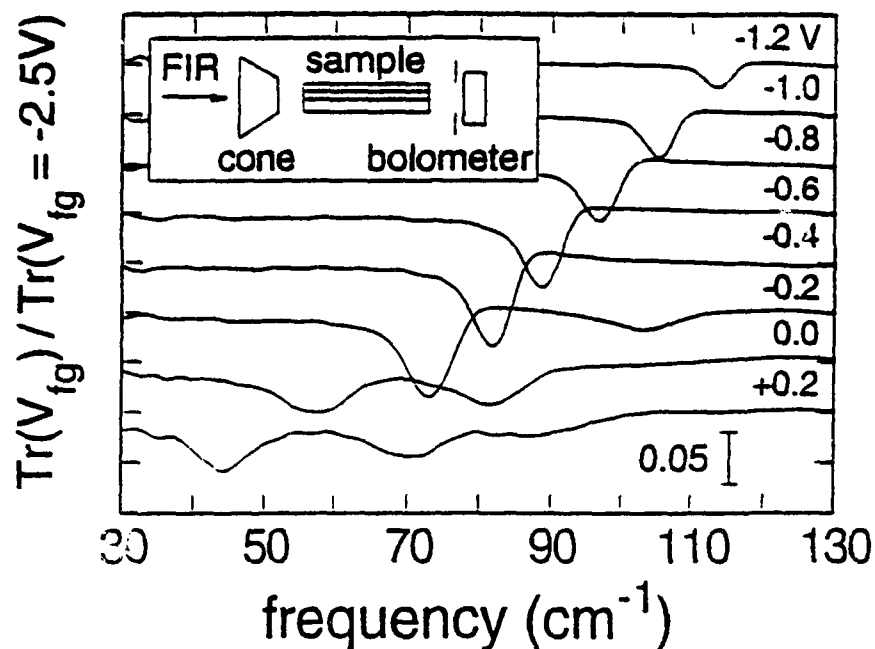


Figure 29. Experimentally observed transmission spectra for far-infrared Terahertz radiation passing through tunable well in a parallel direction at a series of front gate applied potentials from -1.2 Volts to +0.2 Volts. Back gate potential is 0.0 Volts.

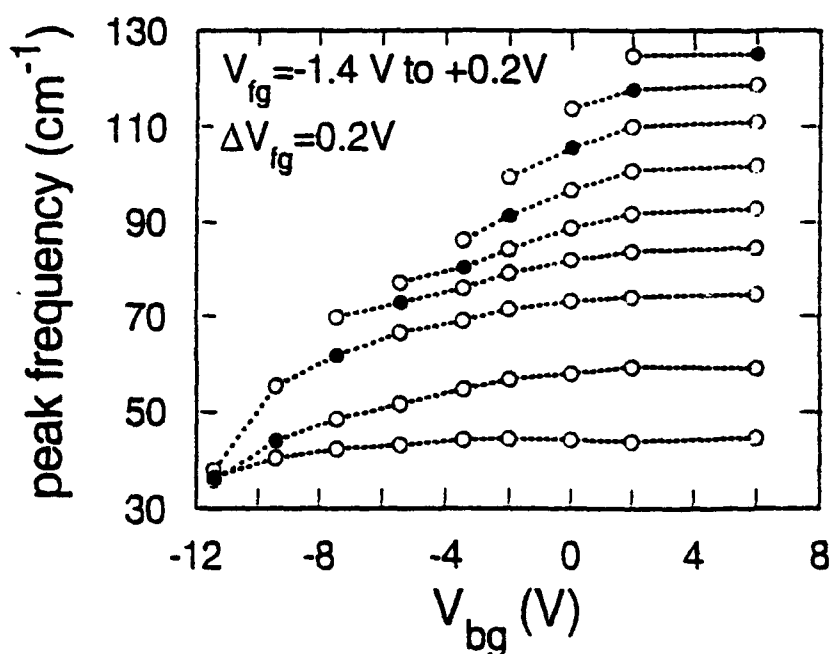


Figure 30. Frequencies of peak absorption for tunable well as a function of back gate voltage V_{bg} for a series of front gate voltages from -1.4 to +0.2 Volts. Filled circles correspond to conditions at which the electron occupation of the tunable well are all approximately equal.

Parabolically Graded Mirror Stacks in VCSEL's

In collaboration with Professor Larry Coldren at UCSB, we have successfully applied the design and synthesis techniques that we developed for wide graded wells to the design and synthesis of improved interfaces between the layers of doped multi-layer Bragg mirrors for vertical cavity surface emitting lasers (VCSEL's)³⁶. The techniques of high precision compositional grading, modulation doping, and digital-alloy growth developed so far under this AFOSR program have opened a path to improvement in growth and performance of VCSEL's. Such lasers rely heavily on high reflectivity Bragg mirror stacks through which it is necessary to inject laser current with low loss and low voltage drop. We have recently shown that modulation-doped precision-graded structures based on the techniques developed under this AFOSR program can accomplish this current injection through the mirrors far more efficiently than the former brute-force approaches that simply used massive doping and uncontrolled grading profiles to try to beat down the mirror series electrical resistance. The concept is shown in Figure 31, which illustrates the flattening of the valence band profile in a parabolically graded interface achieved by excess acceptor ions and holes introduced by modulated doping. The new approach achieves a substantially *higher* mirror conductivity with a substantially *lower* carrier concentration and thus gives the important added advantage of reduced optical losses due to light absorption by the free carriers in the mirror. This in turn has the further important advantage that laser mirrors can be made with materials components such as higher aluminum-content alloys that were previously considered to be insufficiently dopable for good electrical performance. This in turn will let structures with higher optical performance be used, leading to yet greater laser operating efficiency and speed. The mirror improvement has already been demonstrated experimentally. The improved interfaces are producing substantially reduced series electrical resistance and improved optical properties in test structures as well as in surface emitting lasers, where record high efficiencies and low operating voltages are being obtained.

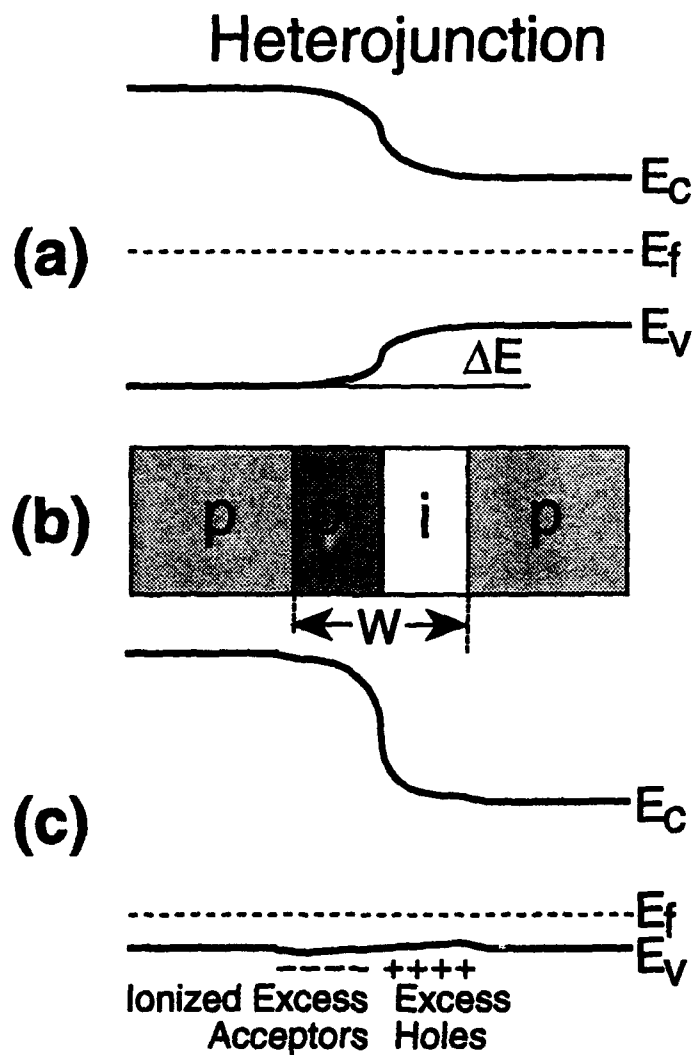


Figure 31. Band edge diagram for engineered high-conductivity interface between wide-gap and narrow-gap p-type materials. The interface is composed of parabolically graded, modulation-doped regions as indicated. a) shows band edges for undoped case; b) shows doping profile; and c) shows band edges in the modulation-doped parabolically graded structure.

OTHER HETEROSTRUCTURES

In addition to the work performed on graded heterostructures, a large amount of research has been carried out on a number of high quality 2-dimensional electron gas (2DEG) systems. Much of this work was carried out in collaboration with researchers from the Center for Free Electron Laser Studies (CFELS) here at UCSB (Dr. Beth Gwinn, Dr. Mark Sherwin, and Dr. Jim Allen). Here we briefly mention several such projects.

Measurements have been performed of the in-plane dc conductivity of a 2DEG subject to electric fields in the 0.25 to 3.5 THz range provided by radiation from a free electron laser (FEL)³⁷. This experiment allows a measurement of the energy relaxation time of hot carriers in a 2DEG as well as providing information as to the mechanisms for carrier relaxation (phonon emission) at different frequencies of the applied electric field.

Another research thrust involves resonant harmonic generation in asymmetric double quantum well structures³⁸. This system approximates a quantum mechanically simple two level system with level spacing near 10 meV. A resonance in the second (third) harmonic generation was measured when the depolarization-shifted absorption peak is tuned by the application of a front gate bias (Stark effect) to 2 (3) times the pump frequency of the FEL. This shows the importance of many body effects due to the fact that the resonance is associated with the depolarization-shifted, instead of the bare, intersubband energy.

Work on superlattice transport in intense terahertz fields has also been carried out using the free electron laser³⁹. The I-V characteristics of a GaAs/AlGaAs superlattice were measured while the strong electric fields generated by the FEL were concentrated on the sample. The low voltage superlattice conductance was found to have an oscillatory dependence on the terahertz field strength as predicted⁴⁰ and the I-V characteristic showed steps indicative of photon mediated sequential tunneling occurring when neighboring levels differ in energy by an integer number of photon energy quanta ($\pm n\hbar\omega$).

In collaboration with the Westervelt group at Harvard, experiments on high quality near surface 2DEG samples have been performed. In particular, micron scale heterostructures have been fabricated using electron-beam lithography for the study of chaotic scattering in ballistic microstructures⁴¹. In these devices, the mean free path of electrons is larger than the device size so that motion of electrons is ballistic. This means that essentially all large-angle scattering takes place as specular reflection from the electrostatically defined potential walls. Low-temperature magnetoconductance measurements (20mK) on a circle of sub-micron diameter (0.88 μm) and a "chaotic" stadium show large, aperiodic, conductance fluctuations as a function of perpendicular magnetic field and a zero-field resistance peak indicating geometry-dependent enhanced backscattering.

- ¹ B. Halperin, *Jpn. J. Appl. Phys. (Suppl. 26-3)* **26**, 1913 (1987).
- ² M. Sundaram, A. C. Gossard, J. H. English, and R. M. Westervelt, *Superlattice and Microstructures* **4**, 683 (1988).
- ³ M. Shayegan, J. Jo, W. Suen, M. Santos, and V. J. Goldman, *Phys., Rev. Lett.* **65**, 2916 (1990).
- ⁴ M. Sundaram, A. C. Gossard, and P. O. Holtz, *J. Appl. Phys.* **69**, 2375 (1991).
- ⁵ M. Shayegan, T. Sajoto, M. Santos, and C. Silvestre, *Appl. Phys. Lett.* **53**, 791 (1988).
- ⁶ J. Harbison, L. D. Peterson, and J. Levkoff, *J. Cryst. Growth* **81**, 34 (1987).
- ⁷ M. Sundaram, K. Ensslin, A. Wixforth, and A. C. Gossard, *Superlattices and Microstructures* **10**, 157 (1991).
- ⁸ K. Karrai, M. Stopa, X. X. Ying, H. D. Drew, S. D. Sarma, and M. Shayegan, *Phys. Rev. B* **42**, 9732 (1990).
- ⁹ A. J. Rimberg, S. Yang, J. Dempsey, J. H. Baskey, R. M. Westervelt, M. Sundaram, and A. C. Gossard, *Appl. Phys. Lett.* **62**, 390 (1993).
- ¹⁰ M. Sundaram and A. C. Gossard, *J. Appl. Phys.* **73**, 251 (1993).
- ¹¹ W. Walukiewicz, P. F. Hopkins, M. Sundaram, and A. C. Gossard, *Phys. Rev. B* **44**, 10909 (1991).
- ¹² F. S. Ham and D. C. Mattis, *IBM J. Res. Dev.* **4**, 143 (1960).
- ¹³ J. R. Schrieffer, *Phys. Rev.* **97**, 641 (1955).
- ¹⁴ E. G. Gwinn, R. M. Westervelt, P. F. Hopkins, A. J. Rimberg, M. Sundaram, and A. C. Gossard, *Phys. Rev. B* **39**, 6260 (1989).
- ¹⁵ K. Ensslin, M. Sundaram, A. Wixforth, J. H. English, and A. C. Gossard, *Phys. Rev. B* **43**, 9988 (1991).
- ¹⁶ R. C. Miller, A. C. Gossard, D. A. Kleinman, and O. Munteanu, *Phys. Rev. B* **29**, 3740 (1984).
- ¹⁷ J. H. Burnett, H. M. Cheong, W. Paul, P. F. Hopkins, A. J. Rimberg, R. M. Westervelt, E. G. Gwinn, M. Sundaram, and A. C. Gossard, *Bull. Amer. Phys. Soc.* **35**, 683 (1990).
- ¹⁸ J. H. Burnett, H. M. Cheong, W. Paul, P. F. Hopkins, and A. C. Gossard, *Jpn. J. Appl. Phys.* **32**, 75 (1992).
- ¹⁹ J. H. Burnett, H. M. Cheong, R. M. Westervelt, W. Paul, P. F. Hopkins, M. Sundaram, and A. C. Gossard, *Phys. Rev. B* **48**, 4524 (1993).
- ²⁰ W. W. Bewley, (University of California, Santa Barbara, 1992),
- ²¹ P. R. Pinsukanjana, E. L. Yuh, N. G. Asmar, E. G. Gwinn, M. Sundaram, and A. C. Gossard, *Phys. Rev. B* **46**, 7284 (1992).
- ²² E. L. Yuh, E. G. Gwinn, P. R. Pinsukanjana, W. L. Schaich, and P. F. Hopkins, *Phys. Rev. Lett.* **71**, 2126 (1993).
- ²³ K. Karrai, H. D. Drew, M. W. Lee, and M. Shayegan, *Phys. Rev. B* **39**, 1426 (1989).
- ²⁴ A. Wixforth, M. Sundaram, K. Ensslin, J. H. English, and A. C. Gossard, *Phys. Rev. B* **43**, 10000 (1991).
- ²⁵ L. Brey, N. F. Johnson, and B. I. Halperin, *Phys. Rev. B* **40**, 10647 (1989).
- ²⁶ W. Kohn, *Phys. Rev.* **123**, 1242 (1961).
- ²⁷ P. A. Maksym and T. Chakraborty, *Phys. Rev. Lett.* **65**, 108 (1990).

- 28 L. Brey, J. Dempsey, N. F. Johnson, and B. Halperin, *Phys. Rev. B* **42**, 1240 (1990).
- 29 P. F. Hopkins, K. L. Campman, and A. C. Gossard, *Journal of Crystal Growth* **127**, 798 (1993).
- 30 M. Sundaram, A. Wixforth, P. F. Hopkins, and A. C. Gossard, *J. Appl. Phys.* **72**, 1460 (1992).
- 31 M. Santos, J. Jo, M. Shayegan, and A. M. Lanzillotto, *J. Cryst. Growth* **111**, 366 (1991).
- 32 J. H. Baskey, A. J. Rimberg, S. Yang, R. M. Westervelt, P. F. Hopkins, and A. C. Gossard, *Appl. Phys. Lett.* **61**, 1573 (1992).
- 33 L. Brey, N. F. Johnson, and J. Dempsey, *Phys. Rev. B* **42**, 2886 (1990).
- 34 J. Maserjian and A. C. Gossard, *NASA Tech Briefs* **14**, 26 (1990).
- 35 P. F. Hopkins, K. L. Campman, G. Bellomi, A. C. Gossard, M. Sundaram, E. L. Yuh, and E. G. Gwinn, *Appl. Phys. Lett.* **64**, 348 (1993).
- 36 M. G. Peters, B. J. Thibeault, D. B. Young, J. W. Scott, F. H. Peters, A. C. Gossard, and L. A. Coldren, *Appl. Phys. Lett.* **63**, 3411 (1993).
- 37 N. G. Asmar, A. G. Markelz, E. G. Gwinn, P. F. Hopkins, and A. C. Gossard, *Proc. of 6th MSS*, 1993.
- 38 J. N. Heyman, K. Craig, B. Galdrikian, M. S. Sherwin, K. Campman, P. F. Hopkins, S. Fafard, and A. C. Gossard, *Phys. Rev. Lett.* **72**, 2183 (1994).
- 39 B. J. Keay, P. S. S. Guimaraes, J. Kaminski, J. S.J. Allen, M. Holthaus, P. F. Hopkins, A. C. Gossard, L. T. Florez, and J. P. Harbison, *Proc. of 2nd International Conference on New Phenomena in Mesoscopic Structures*, Maui, Hawaii 1992.
- 40 M. Holthaus, *Phys. Rev. Lett.* **69**, 351 (1992).
- 41 C. M. Marcus, A. J. Rimberg, R. M. Westervelt, P. F. Hopkins, and A. C. Gossard, *Phys. Rev. Lett.* **69**, 506 (1992).

PUBLICATION LIST

Growth and characterization of wide parabolic wells

"MODULATION-DOPED GRADED STRUCTURES: GROWTH AND CHARACTERIZATION", by M. Sundaram, A. C. Gossard, and P. O. Holtz. *Journal of Applied Physics* 69, pp. 2370-2375 (1991).

"MOBILITY AND UNIFORMITY OF THE ELECTRON GAS IN WIDE PARABOLIC GAAS/ALGAAS WELLS", by P.F. Hopkins, A.J. Rimberg, E.G. Gwinn, R.M. Westervelt, M. Sundaram, and A.C. Gossard. *Superlattices and Microstructures* 9, pp. 127-131 (1991).

"A DIRECT METHOD TO PRODUCE AND MEASURE COMPOSITIONAL GRADING IN $\text{Al}_x\text{Ga}_{1-x}\text{As}$ ALLOYS", by M. Sundaram, A. Wixforth, R. S. Geels, A. C. Gossard, and J. H. English. *Journal of Vacuum Science and Technology B* 9, pp. 1524-1529 (1991).

"NEW QUANTUM STRUCTURES", by M. Sundaram, S.A. Chalmers, P.F. Hopkins, and A.C. Gossard. *Science* 254, pp. 1326-1335 (1991).

"WIDE GRADED POTENTIAL WELLS", by A.C. Gossard, M. Sundaram, and P.F. Hopkins. *Semiconductors and Semimetals* 40, pp. 153-217 (1993).

Electrical properties

"MAGNETO-CAPACITANCE-VOLTAGE MEASUREMENTS OF ELECTRONS IN WIDE PARABOLIC QUANTUM WELLS", by M. Sundaram, K. Ensslin, A. Wixforth, and A. C. Gossard. *Superlattices and Microstructures* 10, pp.157-165 (1991).

"CAPACITIVE DETECTION OF SUBBAND STRUCTURE IN THE ELECTRON GAS IN A WIDE PARABOLIC $\text{GaAs}/\text{Al}_x\text{Ga}_{1-x}\text{As}$ QUANTUM WELL", by A. J. Rimberg, S. Yang, J. Dempsey, J. H. Baskey, R. Westervelt, M. Sundaram, and A. C. Gossard. *Applied Physics Letters* 62, pp. 390-392 (1993).

"CAPACITANCE-VOLTAGE PROFILING THROUGH GRADED HETEROJUNCTIONS - THEORY AND EXPERIMENT", by M. Sundaram and A. C. Gossard. *Journal of Applied Physics* 73, pp. 251-260 (1993).

"SIZE EFFECT IN PARABOLIC $\text{GaAs}/\text{Al}_x\text{Ga}_{1-x}\text{As}$ QUANTUM WELLS", W. Walukiewicz, P. F. Hopkins, M. Sundaram, A. C. Gossard, and R. M. Westervelt, *Physical Review B* 44, pp. 10909-10912 (1991).

"SUPPRESSION AND RECOVERY OF QUANTUM HALL PLATEAUS IN A PARABOLIC QUANTUM WELL", by K. Ensslin, M. Sundaram, A. Wixforth, J. H. English, and A. C. Gossard. *Physical Review B* 43, pp. 9988-9991 (1991).

"SUPPRESSION OF QUANTUM HALL PLATEAUS AND NONLINEAR LANDAU LEVEL FAN DIAGRAM IN A PARABOLIC QUANTUM WELL", K. Ensslin, M. Sundaram, A. Wixforth, and A. C. Gossard, *Surface Science* 267, pp. 553-557 (1992).

"DIRECT OBSERVATION OF RESONANT SUBBAND-LANDAU-LEVEL COUPLING IN A TRANSPORT EXPERIMENT", K. Ensslin, C. Pistitch, A. Wixforth, M. Sundaram, P. F. Hopkins, and A. C. Gossard. *Physical Review B* 45, pp. 11407-11410 (1992).

"SINGLE-PARTICLE SUBBAND SPECTROSCOPY IN A PARABOLIC QUANTUM WELL VIA TRANSPORT EXPERIMENTS", by K. Ensslin, A. Wixforth, J. P. Kotthaus, M. Sundaram, P. F. Hopkins, and A. C. Gossard. *Physical Review B-Condensed Matter* 47, pp 1366-1378 (1993).

Optical properties

"PHOTOLUMINESCENCE EXCITATION SPECTROSCOPY OF WIDE PARABOLIC GaAs/AlGaAs QUANTUM WELLS", by J. H. Burnett, H. M. Cheong, W. Paul, P. F. Hopkins, A. J. Rimberg, R. M. Westervelt, M. Sundaram, and A. C. Gossard. *Superlattices and Microstructures* 10 pp. 167-170 (1991).

"PHOTOLUMINESCENCE EXCITATION SPECTROSCOPY OF BE REMOTELY-DOPED WIDE PARABOLIC GAAS/ALGAAS QUANTUM WELLS", by J. H. Burnett, H. M. Cheong, W. Paul, P. F. Hopkins, and A. C. Gossard. *Physical Review B* 48, pp. 7940-7943 (1993).

"RESONANT INELASTIC LIGHT SCATTERING IN REMOTELY DOPED WIDE PARABOLIC GAAS/ALGAAS QUANTUM WELLS", by J. H. Burnett, H. M. Cheong, R. M. Westervelt, W. Paul, P. F. Hopkins, M. Sundaram, and A. C. Gossard. *Physical Review B* 48, pp. 4524-4529 (1993).

"PRESSURE DEPENDENCE OF THE HARMONIC OSCILLATOR LEVELS OF ALGAAS PARABOLIC QUANTUM WELLS", by J. H. Burnett, H. M. Cheong, W. Paul, P. F. Hopkins, and A. C. Gossard. *Japanese Journal of Applied Physics* 32, Suppl. 32-1, pp. 75-77 (1993).

"DIMENSIONAL RESONANCES IN WIDE PARABOLIC QUANTUM WELLS", by A. Wixforth, M. Sundaram, K. Ensslin, J. H. English, and A. C. Gossard. *Physical Review, Rapid Communications* B43, pp. 10000-10003 (1991).

"ELECTRON PLASMA RESONANCES IN WIDE PARABOLIC QUANTUM WELLS", A. Wixforth, M. Sundaram, K. Ensslin, J. H. English, and A. C. Gossard, *Surface Science* 267, pp. 523-527 (1992).

"RESONANT COUPLING OF COLLECTIVE INTRASUBBAND AND INTERSUBBAND EXCITATIONS IN A PARABOLICALLY CONFINED ELECTRON SYSTEM", by M. Kaloudis, K. Ensslin, A. Wixforth, M. Sundaram, and A. C. Gossard. *Physical Review B-Condensed Matter* 46, pp. 12469-12472 (1992).

"ANISOTROPIC BAND STRUCTURE OF A PARABOLICALLY CONFINED ELECTRON SYSTEM SUBJECTED TO AN IN-PLANE MAGNETIC FIELD", by A. Wixforth, M. Kaloudis, M. Sundaram, and A. C. Gossard. *Solid State Communications* 84, pp. 861-864 (1992).

"SURFACE COLLECTIVE MODES OF NON-NEUTRAL JELLIUM", by P. R. Pinsukanjana, E. G. Gwinn, J. F. Dobson, E. L. Yuh, N. G. Asmar, M. Sundaram, and A. C. Gossard. *Physical Review B* 46 pp. 7284-7287 (1992).

"ONSET OF 3D COLLECTIVE RESPONSE IN BIMETALLIC JELLIUM FILMS: SURFACE AND MODE SENSITIVITY", by E.L. Yuh, E.G. Gwinn, P.R. Pinsukanjana, W.L. Schaich, P.F. Hopkins, and A.C. Gossard. Physical Review Letters 71, pp. 2126-2130 (1993).

Additional graded structures

"GROWTH AND CHARACTERIZATION OF Be MODULATION DOPED WIDE PARABOLIC GaAs/Al_xGa_{1-x}As WELLS", by P. F. Hopkins, K. L. Campman, and A. C. Gossard. Journal of Crystal Growth 127, pp. 798-802 (1993).

"MAGNETOTRANSPORT CHARACTERIZATION OF REMOTELY-DOPED SUPERLATTICES IN WIDE PARABOLIC GaAs/Al_xGa_{1-x}As QUANTUM WELLS", by A.J. Rimberg, J. H. Baskey, R.M. Westervelt, P.F. Hopkins, M. Sundaram, and A. C. Gossard. Superlattices and Microstructures 11, pp. 317-319 (1992).

"WIDE ELECTRON GAS WITH PERIODIC DENSITY MODULATION", M. Sundaram, A. Wixforth, P. F. Hopkins, and A. C. Gossard, Journal of Applied Physics 72, pp.1460-1463 (1992).

"REMOTELY-DOPED SUPERLATTICES IN WIDE PARABOLIC GaAs/Al_xGa_{1-x}As QUANTUM WELLS", J. H. Baskey, A. J. Rimberg, S. Yang, R. M. Westervelt, P. F. Hopkins, and A. C. Gossard. Applied Physics Letters 61, pp. 1573-1575 (1992).

"LOGARITHMICALLY GRADED QUANTUM WELL FAR-INFRARED MODULATOR", P. F. Hopkins, K. L. Campman, G. Bellomi, A. C. Gossard, M. Sundaram, E. L. Yuh, and E. G. Gwinn. Applied Physics Letters 64, pp. 348-351 (1993).

"BAND-GAP ENGINEERED DIGITAL ALLOY INTERFACES FOR LOWER RESISTANCE VERTICAL-CAVITY SURFACE-EMITTING LASERS", M.G. Peters, B.J. Thibeault, D.B. Young, J.W. Scott, F.H. Peters, A.C. Gossard, and L.A. Coldren. Applied Physics Letters 63, pp. 3411-3413 (1993).

Additional Heterostructures

"PHOTON-MEDIATED SEQUENTIAL RESONANT TUNNELING IN INTENSE TERAHERTZ ELECTRIC FIELDS", by P. S. S. Guimaraes, Brian J. Keay, Jann Kaminski, S. J. Allen, Jr., P. F. Hopkins, A. C. Gossard, L. T. Fiore, and J. P. Harbison. Physical Review Letters 70, pp. 3792-3795 (1993).

"PHOTOLUMINESCENCE FROM Al_xGa_{1-x}As/GaAs QUANTUM WELLS QUENCHED BY INTENSE FAR-INFRARED RADIATION" by S. M. Quinlan, A. Nikroo, M. S. Sherwin, M. Sundaram, and A. C. Gossard. Physical Review B 45, pp. 9428-9431 (1992).

"FAR-INFRARED CAPTURE OF ELECTRONS BY DX CENTERS", by J.J. Plombon, W. W. Bewley, C.L. Felix, M.S. Sherwin, P.F. Hopkins, M. Sundaram, and A.C. Gossard. Applied Physics Letters 60, pp. 1972-1974 (1992).

"CONDUCTANCE FLUCTUATIONS AND CHAOTIC SCATTERING IN BALLISTIC MICROSTRUCTURES", by C. M. Marcus, A. J. Rimberg, R. M. Westervelt, P. F. Hopkins, and A. C. Gossard. Physical Review Letters 69, pp. 506-509 (1992).

INTERACTIONS (COUPLING ACTIVITIES)

PAPERS PRESENTED:

"MBE DIGITAL ALLOY GROWTH OF SOLID STATE ELECTRON RESONATORS", by K. L. Campman, P. F. Hopkins, and A. C. Gossard. 1993 Electronic Materials Conference, Santa Barbara, CA, June 25, 1993.

"TUNABLE FAR INFRARED ABSORPTION IN LOGARITHMICALLY GRADED QUANTUM WELLS", by P. F. Hopkins, M. Sundaram, K. L. Campman, G. Bellomi, E. L. Yuh, S. J. Allen, Jr., and A. C. Gossard. Sixth International Conference on Modulated Semiconductor Structures, Garmisch-Partenkirchen, Germany, August 26, 1994.

"DC TRANSPORT IN INTENSE, IN-PLANE TERAHERTZ ELECTRIC FIELDS IN $\text{Al}_x\text{Ga}_{1-x}\text{As}$ HETEROSTRUCTURES at 300 K", by N. G. Asmar, A. G. Markelz, E. G. Gwinn, P. F. Hopkins, and A. C. Gossard. Sixth International Conference on Modulated Semiconductor Structures, Garmisch-Partenkirchen, Germany, August 23, 1994.

"TRANSITION FROM 2D TO 3D COLLECTIVE RESPONSE: SURFACE SENSITIVITY", by E. L. Yuh, P. R. Pinsukanjana, E. G. Gwinn, P. F. Hopkins, and A. C. Gossard. Tenth International Conference on the Electronic Properties of Two-Dimensional Systems", Newport, Rhode Island, June, 1994.

"RESONANT INELASTIC LIGHT SCATTERING IN REMOTELY DOPED WIDE PARABOLIC $\text{GaAs}/\text{Al}_x\text{Ga}_{1-x}\text{As}$ QUANTUM WELLS IN A MAGNETIC FIELD", by J. H. Burnett, H. M. Cheong, R. M. Westervelt, W. Paul, P. F. Hopkins, and A. C. Gossard. Tenth International Conference on the Electronic Properties of Two-Dimensional Systems", Newport, Rhode Island, June, 1994.

"TERAHERTZ FREQUENCY, HOT ELECTRON TRANSPORT IN $\text{Al}_x\text{Ga}_{1-x}\text{As}$ HETEROSTRUCTURES", by N. G. Asmar, A. G. Markelz, E. G. Gwinn, P. F. Hopkins, and A. C. Gossard. American Physical Society March Meeting, Seattle, WA, 22 March, 1993.

"SUPERLATTICE TRANSPORT IN INTENSE TERAHERTZ ELECTRIC FIELDS", by B. J. Keay, P.S.S. Guimaraes, J. P. Kaminski, S. J. Allen, P. F. Hopkins, A. C. Gossard, L.T. Florez, and J. P. Harbison. American Physical Society March Meeting, Seattle, WA, 22 March, 1993.

"ELECTRONIC EXCITATIONS IN A BIMETALLIC FILM", by E. L. Yuh, P. R. Pinsukanjana, E. G. Gwinn, P. F. Hopkins, A. C. Gossard, and W. L. Schaich. American Physical Society March Meeting, Seattle, WA, 24 March, 1993.

"TWO-DIMENSIONAL ELECTRON GAS HALL ELEMENTS AS LOW TEMPERATURE MAGNETOMETERS", by S. Gider, D. D. Awschalom, K. L. Campman, A. C. Gossard, and S. Von Molnar. American Physical Society March Meeting, Seattle, WA, 24 March, 1993.

"MAGNETOTRANSPORT MEASUREMENTS ON A TUNABLE BALLISTIC QUANTUM BOX", by M. J. Berry, J. A. Katine, R. M. Westervelt, P. F. Hopkins, and A. C. Gossard. American Physical Society March Meeting, Seattle, WA, 25 March, 1993.

"CAPACITIVE MEASUREMENTS OF SUBBAND STRUCTURE OF SUPERLATTICES IN WIDE PARABOLIC $\text{GaAs}/\text{Al}_x\text{Ga}_{1-x}\text{As}$ QUANTUM WELLS", by J. H. Baskey, R. M Westervelt, P. F. Hopkins, and A. C. Gossard. American Physical Society March Meeting, Seattle, WA, 26 March, 1993.

"FAR-INFRARED ABSORPTION IN A SINGLE LIGHTLY DOPED SQUARE QUANTUM WELL", by C. L. Felix, K. Craig, M. S. Sherwin, P. F. Hopkins, and A. C. Gossard. American Physical Society March Meeting, Seattle, WA, 26 March, 1993.

"RESONANT RAMAN SCATTERING STUDY OF INTER-LANDAU AND INTERSUBBAND TRANSITIONS IN A WIDE PARABOLIC QUANTUM WELL", by L. B. Liao, D. Heiman, P. F. Hopkins, and A. C. Gossard. American Physical Society March Meeting, Seattle, WA, 26 March, 1993.

"SPLITTING OF PLASMON RESONANCES IN A QUASI 3-D ELECTRON GAS INDUCED BY PERIODIC SPATIAL MODULATION", by P. R. Pinsukanjana, E. L. Yuh, N. G. Asmar, E. G. Gwinn, P. F. Hopkins, and A. C. Gossard. American Physical Society March Meeting, Seattle, WA, 26 March, 1993.

"JOSEPHSON JUNCTIONS USED AS A TUNABLE MILLIMETER WAVE SOURCE TO STUDY 2DEG IN MESOSCOPIC SYSTEMS", by Scott Yang, C. M. Marcus, A. S. Adourian, M. J. Berry, J. A. Katine, R. M Westervelt, A. C. Gossard, and M. Sundaram. American Physical Society March Meeting, Seattle, WA, 26 March, 1993.

"ARTIFICIAL QUANTUM WELLS FOR THREE-DIMENSIONAL PHYSICS", by Arthur C. Gossard. Physics Department Colloquium, Ohio State University, 20 April, 1993.

"MODULATION-DOPED GRADED SEMICONDUCTOR STRUCTURES: DESIGN, GROWTH AND PROPERTIES", by Arthur C. Gossard. Materials Department Colloquium, University of Southern California, 19 November 1993.

"EPITAXIAL GROWTH AND HETEROSTRUCTURES", by Arthur C. Gossard. Quantum Structures Colloquium, Los Alamos National Laboratory, 14 October 1993.

CONSULTATIVE AND ADVISORY FUNCTIONS WITH OTHER LABORATORIES

Harvard University:

We have continued close interactions with researchers at Harvard University throughout the period of this contract. Professor Westervelt spent the Fall, 1992 semester with us at Santa Barbara. He and his students worked on transport in our wide graded wells, with special emphasis on capacitance studies of the subband filling and on the transport and capacitance in the presence of a superlattice potential. Professor William Paul's graduate student John Burnett also worked on the optical properties of the wide parabolic wells at Harvard.

UCSB Quantum Institute:

We also continued to collaborate with several researchers in the UCSB Quantum Institute and Center for Free Electron Laser Studies. The arrival of Professor Jim Allen as director of the Quantum Institute increases its strength in the submillimeter wave field and adds a special interest in the behavior of electronic devices in intense Terahertz fields. Work with Professor Mark Sherwin in studies of non-linear and chaotic infrared properties of our materials also continued. Professor Beth Gwinn extended her research in the studies of the infrared plasmon properties of the new materials. Mani Sundaram, who was the first graduate student supported under this AFOSR program, worked as a postdoctoral fellow in the Quantum Institute making extensive infrared measurements in our materials.

Wright-Patterson Laboratories:

During the period of this contract, we have initiated collaboration with several researchers at Wright-Patterson Labs. Cyclotron resonance and electronic properties of wide graded structures grown at UCSB are being studied by Omar Manasreh. Ron Caspi and K.R. Evans are looking at structures grown by the digital alloy technique at UCSB to compare that growth technique to the mass desorption spectrometry technique developed at Wright-Patterson. In addition, Lorene Samoska, a student of Professor Gossard and Professor Herbert Kroemer from the UCSB MBE laboratories is cooperating with Gail Brown on the growth and properties of arsenide/antimonide short period strained superlattices for infrared detection.

University of Munich, Germany:

Professor Jorg Kotthaus from the University of Munich continued to interact extensively with us. We grew several new structures with Professor Kotthaus that involve multiple layers in three-dimensional systems and that are currently under investigation in his laboratories. Former UCSB postdoctoral fellow Klaus Ensslin is now a faculty member at Munich and is making further magnetotransport investigations, particularly on coupled wells, with our materials. We are also extending our work on far infrared properties of our materials in collaboration with our former postdoctoral researcher Dr. Achim Wixforth who is also now a faculty member in Professor Kotthaus' laboratory in Germany.

Other Interactions:

Our results on sub-millimeter wave second harmonic generation from wide, specially shaped quantum wells have formed the basis for a fledgling company that two former students of Professor Mark Sherwin have formed. The goal of the company is to develop submillimeter wave parametric oscillators and mixers based on wide, asymmetric wells.

We continued a collaboration with Professor Gottfried Dohler of the University of Nurnberg and Erlangen in Germany. We have grown two n-i-p-i doped graded well structures and work is now underway at Erlangen to investigate the properties of these alternately doped structures.

We also initiated a collaboration with Dr. Don Heiman at the MIT Francis Bitter Magnet Laboratory in which Dr. Heiman is investigating the optical properties of relatively narrow, n-type modulation doped parabolic wells in the high magnetic fields at the Bitter Magnet Laboratory.

In other advisory and organizational contributions not directly involved with the work of this contract, but benefiting it indirectly, Professor Gossard was active in national and international professional activities. He completed his term on the editorial board of the Journal of Applied Physics and Applied Physics Letters. He has also completed a review chapter on wide graded wells and digital alloys that will appear in a volume on Epitaxial Microstructures that he is editing for the Willardson and Beer Academic Press series, "Semiconductors and Semimetals", edited by R. Willardson, A. Beer. He served on the review board for the University of Utah Materials Science and Engineering Department. He was a member of the selection committee for the American Physical Society International Prize for New Materials, and was named chairman of the committee for this year. He was one of the most highly cited authors of the 1980's, with over 9900 citations

in the 1980's to papers of his that were published in the 1980's. This placed him as the second most highly cited author in the physical sciences for this period.

PERSONNEL

Professor Arthur C. Gossard (Principal Investigator)

Dr. Gossard received his PhD degree in Physics from University of California, Berkeley in 1960. His PhD thesis title was "Nuclear Magnetic Resonance in Ferromagnetic Materials". He was at AT&T Bell Laboratories from 1960 to 1987, with the exception of a year of research at the Centre d'Etudes Nucleaires, Saclay France from 1962 to 1963. He has been Professor of Materials and of Electrical and Computer Engineering in the University of California, Santa Barbara from July, 1987 to the present. His special interests are in the field of growth and properties of new artificially structured materials. He has 12 patents in this area and over 490 publications. He is a member of the National Academy of Engineering, a Fellow of the American Physical Society, and a former Distinguished Member of Technical Staff in Bell Laboratories.

Dr. Mani Sundaram, Graduate Student, Research Assistant

Dr. Sundaram received his Bachelors Degree in Electrical Engineering from the Indian Institute of Technology, Madras, in 1985. He came to UCSB in 1985 and did research with Professor Steve Long on high speed GaAs field effect transistor devices before starting his research on the fabrication and properties of high quality three-dimensional electron gases. He earned his Ph.D. in September of 1991 and continued to work at UCSB as a postdoctoral researcher in the Physics department with Dr. Jim Allen. Currently he is a member of the technical staff at Jet Propulsion Laboratory.

Dr. Peter F. Hopkins, Postdoctoral Research Engineer.

Postdoctoral researcher, Dr. Peter F. Hopkins, joined the UCSB research program in June, 1990 immediately after receiving his Ph.D. degree in Physics from Harvard University, where he worked under Professor Robert Westervelt on electrical and optical measurements of wide parabolic well materials generated at UCSB under this program. In his work at Harvard, he observed the quantum Hall effect and associated magnetotransport phenomena in the parabolic well structures and participated in the discovery of the new features in the optical spectra of the doped wells. He previously received his B.S. degree in Engineering Physics from University of California, Berkeley with highest honors. His appointment at UCSB ended in September of 1993.

Mr. Kenneth L. Campman, Graduate Student, Research Assistant.

Kenneth Campman is a graduate student research assistant who has been working under this contract since June, 1991. He received the B.S. degree from Caltech in May, 1991 in Engineering Physics. He had an outstanding scholastic record at Caltech and holds an Office of Naval Research Graduate Fellowship. He has been involved in the growth of a number of graded well structures for observation of electron resonances in single and coupled wells and with setting up the new enhanced-performance molecular beam epitaxy system. He has also been working on the quantum mechanical simulation of charge distributions and energy levels in graded superlattices.

Mr. Kevin Maranowski, Graduate Student, Research Assistant.

Mr. Maranowski received his Bachelors Degree in Electrical Engineering from Carnegie Mellon University, Pittsburgh, in June, 1993. He joined Professor Gossard's current AFOSR program on the growth and electrical and far-infrared properties of wide electron wells in semiconductors in July, 1993. Kevin is an outstanding student and graduated

from Carnegie Mellon in only three years, while achieving an overall 3.97 grade point average and holding technical industrial positions during summers. He was highly recruited for graduate school, and we feel fortunate to have him in this program.

DISCOVERIES AND INVENTIONS

No further patent applications were filed during the period of this report.

OTHER STATEMENTS

The work supported under this grant has high visibility and is attracting interest from leading researchers from a number of institutions around the world. It has led to an unusually large number of publications, key ones of which are attached to this report.

Technically, the research is pushing our control of electrons in semiconductors from the optical frequency range toward the millimeter wave-frequency range and is compressing the range of difficulty between the two frequency regimes. The work has my highest interest and priority, and has been my only single-investigator grant.

Reprinted from

Applied Physics Letters

Volume 63

20 December 1993

Number 25

Band-gap engineered digital alloy interfaces for lower resistance vertical-cavity surface-emitting lasers

M. G. Peters, B. J. Thibeault, D. B. Young, J. W. Scott, E. H. Peters, A. C. Gossard,
and L. A. Coldren

*Department of Electrical and Computer Engineering, University of California, Santa Barbara,
California 93106*

(Received 2 August 1993; accepted for publication 18 October 1993)

pp. 3411-3413

a publication of the American Institute of Physics

Band-gap engineered digital alloy interfaces for lower resistance vertical-cavity surface-emitting lasers

M. G. Peters, B. J. Thibeault, D. B. Young, J. W. Scott, F. H. Peters, A. C. Gossard, and L. A. Coldren

Department of Electrical and Computer Engineering, University of California, Santa Barbara, California 93106

(Received 2 August 1993; accepted for publication 18 October 1993)

We report on a technique of grading the heterobarrier interfaces of a p -type distributed Bragg reflector mirror to reduce the operating voltages of vertical-cavity surface-emitting lasers (VCSELs). We report VCSELs with lower operating voltages (2–3 V) and record continuous-wave room-temperature power-conversion efficiencies (17.3%). We experimentally demonstrate that by using a parabolic grading and modulating the doping correctly, a flat valence band is generated that provides low voltage hole transport. The low resistance mirrors are achieved using low Be doping, digital-alloy grading and 600 °C growth temperatures.

Vertical-cavity surface-emitting lasers (VCSELs) are promising candidates for computer interconnections and optical communication because of their ability to be integrated as arrays on a single chip, high efficiency coupling to fibers, and single longitudinal mode operation. The VCSEL structure shown in Fig. 1 has the advantage of uniform current injection and simple processing that requires no regrowths, critical alignments, or implants. This type of structure has yielded record results for VCSELs in many areas.^{1–4} The dominant limitation of this structure's performance is the interface potential barriers of the p -type distributed Bragg reflector (DBR) mirror which the current must be driven through. The high resistance causes power loss and joule heating of the device, and operating voltages are typically higher than logic level drive specification (> 5 V).

Several solutions to lower the resistance of the p -type mirror have been developed. The early attempts used digital alloy linear grading and heavy doping ($\sim 5 \times 10^{18} \text{ cm}^{-3}$) at the AlAs/GaAs interface which lowered the VCSEL threshold voltage to less than 3 V.¹ Growing DBR stacks with lower barrier combinations, such as $\text{Al}_{0.67}\text{Ga}_{0.33}\text{As}/\text{GaAs}$ instead of AlAs/GaAs, also with heavy doping ($\sim 6 \times 10^{18} \text{ cm}^{-3}$) produced threshold voltages less than 2 V with differential resistances of $3.6 \times 10^{-4} \Omega \text{ cm}^2$ for a $45 \mu\text{m}$ square device.⁵ Recently, total resistances as low as $1.9 \times 10^{-4} \Omega \text{ cm}^2$ have been reported for $\text{Al}_{0.1}\text{Ga}_{0.9}\text{As}/\text{Al}_{0.9}\text{Ga}_{0.1}\text{As}$ mirrors grown with heavy doping ($\sim 3 \times 10^{18} \text{ cm}^{-3}$) and piecewise continuous grading formed by group III cell temperature variation.⁶ A more elegant approach of valence band engineering was reported by Shubert *et al.*⁷ The method uses parabolic grading and modulation doping in the interfaces to create a flat valence band. Their implementation relies on the precision control of alloy composition by Group III cell flux variation to grade between GaAs and AlAs.

Theoretically, with an absolute control of doping and composition, there are an infinite variety of DBR mirror interface designs that would flatten the valence band, but VCSEL performance and technical limitations must be considered. For better VCSELs, lower doping is required to reduce free-carrier loss and improve VCSEL efficiency, so

the average doping level is kept low in our design. To reduce the total potential barriers, instead of an AlAs/GaAs stack, $\text{Al}_{0.67}\text{Ga}_{0.33}\text{As}/\text{GaAs}$ mirrors are used. Also, since the p -type doping source is beryllium, which is known to redistribute in AlAs,⁸ by using AlGaAs/GaAs continuous alloy layers, better Be doping control is achieved. The other consideration is the speed and control of changing material flux through the cell temperature. This requires feedback to control the group III (Ref. 6) or group v (Ref. 9) cells. However, using digital alloys, accurate grading profiles over a few hundred angstroms can be generated without the need for cell temperature feedback control. Since the Be doping rate also depends on the cell temperature variation, a series of constant steps is chosen for the doping profile.

From Poisson's law, constant space charge creates parabolic band bending, so by compensating a parabolic grade with constant space-charge regions, a flat valence band can be theoretically generated. Figure 2 is a graphical explanation of the grading profile used. On the left-hand side of Fig. 2 is a GaAs abrupt p - n homojunction. At the interface, within the depletion region, the bands bend parabolically following Poisson's law. The energy discontinuity (ΔE) and the width of the depletion layer (W) are determined

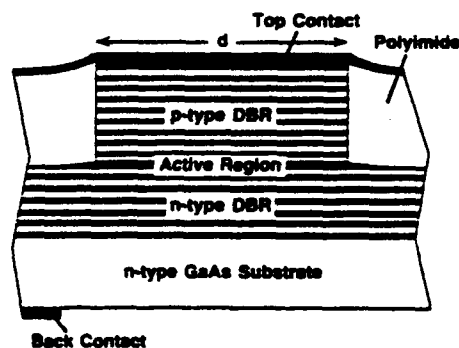


FIG. 1. Schematic of VCSEL structure, which is a circular pillar. Current is driven through the DBR mirrors and light is emitted out the substrate. The active region consists of three 80 Å $\text{In}_{0.2}\text{Ga}_{0.8}\text{As}$ quantum wells lasing at 980 nm.

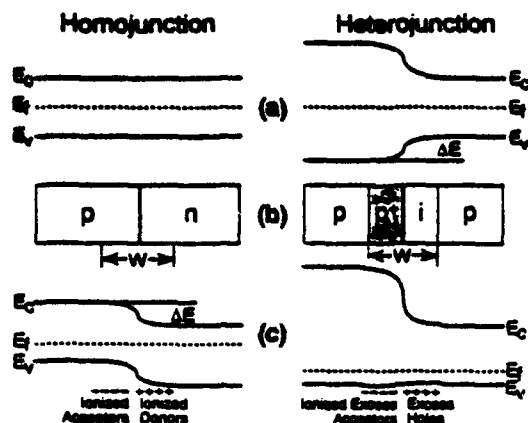


FIG. 2. Explanation of parabolic grading concept: the parabolic band bending of an abrupt p - n junction is created by using a p - i interface. The parabolic band bending compensates for the parabolic grade to create a nearly flat valence band. Part (a) is the intrinsic band diagram, (b) is the intended doping profile, and (c) is the result.

by the doping concentrations and can be derived from Eq. (1) for the abrupt diode:¹⁰

$$W = \sqrt{\left[\frac{2\epsilon_s \Delta E}{q} \left(\frac{N_A + N_D}{N_A N_D} \right) \right]}, \quad (1)$$

where N_D and N_A are the n and p doping levels, q is the electron charge, and ϵ_s is the dielectric permittivity. The p - n homojunction equation is reprinted here because it is used as a first approximation to design the p -type heterojunction interfaces.

The $\text{Al}_{0.67}\text{Ga}_{0.33}\text{As}/\text{GaAs}$ heterojunction, shown on the right-hand side in Fig. 2, has a valence-band discontinuity which is well known¹¹ and is graded parabolically between compositions. If this is doped with a p - n like abrupt junction, the parabolic band bending and the parabolic grading will cancel, yielding an approximately flat valence band. The estimation of the grading and doping required goes as follows. First, for efficient hole transport the average carrier concentration, after band bending and compensation, must be p type. In addition, for a flat valence-band E_f — E_v must be kept constant at all points, therefore the hole concentration must be constant in every section of the mirror, ignoring small material differences. Second, to reduce free-carrier loss, the average number of holes should be kept low, so we choose $\sim 1 \times 10^{18} \text{ cm}^{-3}$. Third, to obtain the proper band bending within the parabolic region there must be an excess of holes on the AlGaAs side of the graded region and a deficit of holes (or excess of electrons) on the GaAs side. To have an average of $1 \times 10^{18} \text{ cm}^{-3}$ holes in the grading region after redistribution requires $N + 1 \times 10^{18} \text{ cm}^{-3}$ acceptors on the AlGaAs side and $N - 1 \times 10^{18} \text{ cm}^{-3}$ donors on the GaAs side. The value of N affects the width of the grading region; a larger N equals a narrower grading width from Eq. (1). Other considerations are that high values of N (e.g., $5 \times 10^{18} \text{ cm}^{-3}$) requires changing the Be cell temperature dramatically at the interface and high doping in the grading region will cause optical loss from ionized impurity scattering. If N is chosen to be equal to the average concentration, $1 \times 10^{18} \text{ cm}^{-3}$,

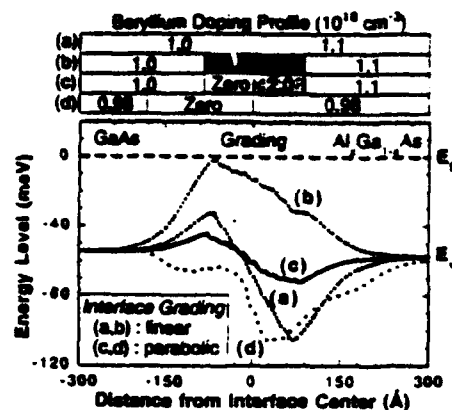


FIG. 3. Iterative Poisson solution of the valence band E_v bending for four different DBR interfaces. Simulations (a) and (b) are linearly graded $\text{Al}_{0.67}\text{Ga}_{0.33}\text{As}/\text{GaAs}$ DBRs with 1×10^{18} and $5 \times 10^{18} \text{ cm}^{-3}$ doping at the interfaces. Simulation (d) is a parabolically graded AlAs/GaAs DBR undoped on the GaAs side of the interface (see Ref. 7). Simulation (c) is the latest design $\text{Al}_{0.67}\text{Ga}_{0.33}\text{As}/\text{GaAs}$ DBR, with parabolic grading and an abrupt step of doping at the interface, which demonstrates both a low energy barrier for holes and low free-carrier loss.

then the GaAs side of the interface will be nonintentionally doped (NID) and the AlGaAs side will be doped with $2 \times 10^{18} \text{ cm}^{-3}$ acceptors, eliminating all donor atoms. Equation (1), using GaAs material parameters, provides a first estimation for the heterojunction grading required for the given doping. For an $\text{Al}_{0.67}\text{Ga}_{0.33}\text{As}/\text{GaAs}$ DBR mirror, ΔE is $\sim 146 \text{ meV}$,¹¹ and for $N_A = N_D = N = 1 \times 10^{18} \text{ cm}^{-3}$, Eq. (1) yields a depletion width of 224 \AA . Therefore, 224 \AA is the thickness of the graded region which bends parabolically between GaAs and $\text{Al}_{0.67}\text{Ga}_{0.33}\text{As}$.

To self-consistently solve for the band bending across the interface, a computer program which solves the Poisson equation iteratively is used. The digital alloy is grown with a 10 \AA period, so in the program it is modeled as a series of 10 \AA steps of varying composition. The program output, shown in Fig. 3, is the calculated valence band energy using different interface designs. In cases (a), (b), and (c), the doping is $1 \times 10^{18} \text{ cm}^{-3}$ in the pure GaAs and $1.1 \times 10^{18} \text{ cm}^{-3}$ in the $\text{Al}_{0.67}\text{Ga}_{0.33}\text{As}$ region so E_f — E_v is equal in both regions. Curves (a) and (b) are interfaces linearly graded over 180 \AA with 1×10^{18} and $5 \times 10^{18} \text{ cm}^{-3}$ doping, respectively. Curve (d) is the interface design proposed by Shubert *et al.*⁷ between GaAs and AlAs . In case (d) the GaAs side of the interface is a NID region, but the AlAs side does not have twice as much doping as the average, so the bands do not flatten out optimally. Curve (c) is our parabolically graded interface as described previously without any changes to the first approximation design except to raise the $\text{Al}_{0.67}\text{Ga}_{0.33}\text{As}$ doping due to the different material parameters. Our parabolic interface design has the smallest voltage barrier and approaches the ideal flat valence band.

DBR mirror stacks were grown to test the prediction and Fig. 4 shows the experimental current density versus voltage (J - V) characteristics. Since high mirror reflectivity is a requirement for VCSEL operation, the number of alternating layers in each growth was chosen to yield equal

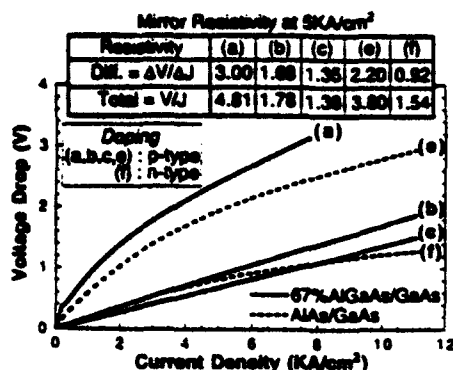


FIG. 4. Measured current density vs voltage for different MBE grown DBR mirror stacks (with contact, substrate, etc. effects subtracted out). Curves (a) and (b) are the $\text{Al}_{0.67}\text{Ga}_{0.33}\text{As}/\text{GaAs}$ linearly graded DBR mirrors, with 1×10^{18} and 5×10^{18} doping at the interfaces and curve (c) is the parabolically graded $\text{Al}_{0.67}\text{Ga}_{0.33}\text{As}/\text{GaAs}$ DBR mirror. Dashed curves (e) and (f) are linearly graded p- and n-type AlAs/GaAs stacks with $5 \times 10^{18} \text{ cm}^{-3}$ doping at the interfaces for comparison. The differential and total resistivity ($\times 10^{-4} \Omega \text{ cm}^2$) of the stacks are shown at 5 kA/cm^2 drive.

reflectivity ($> 99.9\%$). Curves (a), (b), and (c) are the $\text{Al}_{0.67}\text{Ga}_{0.33}\text{As}/\text{GaAs}$ (30 period) DBR mirrors corresponding to simulations (a), (b), and (c) in Fig. 3. Mirrors (b) and (c) have linear J - V characteristics, and there is a noticeable improvement in the resistance between curves (b) and (c). More importantly, the average p-type doping drops by one-half for the parabolically graded mirror. The lower doping decreases the optical loss by half and should improve the external differential efficiency, η_d , (photons-out/electrons-in) of a typical VCSEL from $\eta_d \approx 40\%$ to $\eta_d \approx 50\%$. For comparison, curves (e) and (f) are p- and n-type AlAs/GaAs stacks (18 periods) with 180 Å linear graded interfaces and $5 \times 10^{18} \text{ cm}^{-3}$ doping at the interfaces. Notably, n-type mirrors have not been a problem because of the lower resistance and lower free-carrier loss for electrons.

To truly test the parabolic grading concept, VCSEL material must be grown using the new mirror design. The cw experimental characteristic of a 20 μm VCSEL using the improved DBR mirror is shown in Fig. 5. The I - V characteristics are improved^{1,2} yielding a threshold voltage of 1.86 V and operating voltages of 2–3 V with a differential resistance of $1.32 \times 10^{-4} \Omega \text{ cm}^2$. These VCSELs demonstrate a differential efficiency of $\sim 45\%$, and a record unmounted cw peak power of 36 mW (for a 70 μm device). A comprehensive parameter for laser performance is

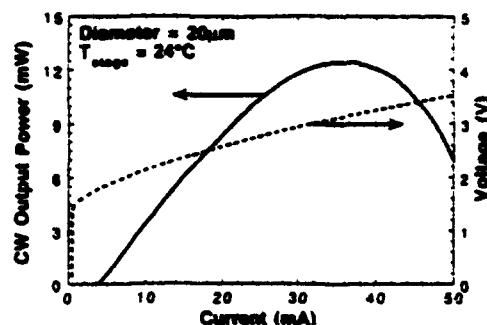


FIG. 5. Light-current-voltage curves of an example VCSEL using the DBR mirror with the parabolic interfaces. A peak wall plug efficiency of 17.3% is observed.

the wall plug efficiency (defined as total optical power out divided by total electrical power in) which reaches a record 17.3% (improved from 14%⁴) for the 20 μm device.

In conclusion, by applying simple modeling to the problem of high-barrier p-type DBR mirror interfaces, a flatter valence-band discontinuity has been generated. The parabolic grading technique requires no extra effort or growth time than a linear grade, and yields lower loss and lower resistance DBR mirrors. The VCSELs fabricated using material grown with the new mirror are the best devices to date with up to 17.3% wall plug efficiency.

This work was supported by the Office of Naval Research through the Optoelectronics Technology Center.

- ¹R. S. Geels, S. W. Corzine, and L. A. Coldren, *IEEE J. Quantum Electron.* **27**, 1359 (1991).
- ²D. B. Young, J. W. Scott, F. H. Peters, B. J. Thibault, S. W. Corzine, M. G. Peters, S.-L. Lee, and L. A. Coldren, *IEEE Photon. Tech. Lett.* **5**, 129 (1993).
- ³F. H. Peters, M. G. Peters, D. B. Young, J. W. Scott, B. J. Thibault, S. W. Corzine, and L. A. Coldren, *Electron. Lett.* **29**, 200 (1993).
- ⁴M. G. Peters, F. H. Peters, D. B. Young, J. W. Scott, B. J. Thibault, and L. A. Coldren, *Electron. Lett.* **29**, 170 (1993).
- ⁵J. D. Walker, D. M. Kuchta, and J. S. Smith, *Appl. Phys. Lett.* **59**, 2079 (1991).
- ⁶K. L. Lear, S. A. Chalmers, K. P. Kileen, and J. Zolper, *CLEO '93 Technical Digest*, Baltimore, MA, 1993, paper CTuD2.
- ⁷E. F. Schubert, L. W. Tu, G. J. Zydzik, R. F. Kopf, A. Benvenuti, and M. R. Pinto, *Appl. Phys. Lett.* **60**, 466 (1992).
- ⁸R. F. Kopf, E. F. Schubert, S. W. Downey, and A. B. Emerson, *Appl. Phys. Lett.* **61**, 1820 (1992).
- ⁹K. R. Evans, R. Kaspi, C. R. Jones, R. E. Sheriff, V. Jogai, and D. C. Reynolds, *J. Cryst. Growth* **127**, 523 (1993).
- ¹⁰S. M. Sze, *Semiconductor Devices, Physics and Technology*, Wiley, New York, 1985, pp. 70–108.
- ¹¹H. C. Casey, Jr. and M. B. Panish, *Heterostructure Lasers Part A* (Academic, New York, 1978), pp. 191–194.

Reprinted from

Journal of APPLIED PHYSICS

Volume 72

15 August 1992

Number 4

Wide electron gas with periodic density modulation

M. Sundaram, A. Wixforth,^{ab} P. F. Hopkins, and A. C. Gossard

*Department of Electrical and Computer Engineering, and Materials Department, University of California,
Santa Barbara, California 93106*

pp. 1460-1463

a publication of the American Institute of Physics

AIP

Wide electron gas with periodic density modulation

M. Sundaram, A. Welforth,²⁾ P. F. Hopkins, and A. C. Gossard

Department of Electrical and Computer Engineering, and Materials Department, University of California, Santa Barbara, California 93106

(Received 9 September 1991; accepted for publication 11 May 1992)

We report the growth and characterization of a high-quality wide (~ 2000 Å) three-dimensional electron gas (3DEG) with periodic density modulation (period ~ 200 Å) in a modulation-doped wide parabolic potential well with a superimposed superlattice. Computer-controlled molecular beam epitaxy is used to synthesize the potential well as a graded $\text{Al}_x\text{Ga}_{1-x}\text{As}$ digital alloy. The density-modulated 3DEG is compared to a uniform 3DEG of the same average density and width in a parabolic well without the superlattice. The Al mole fraction profiles for the two samples are measured in calibration runs immediately prior to actual growths. The density-modulated 3DEG has a low-temperature in-plane mobility in excess of 10^5 cm^2/Vs , compared to $\sim 2 \times 10^5$ cm^2/Vs for the uniform 3DEG. Capacitance-voltage measurements directly reveal the modulation of the density of the electron gas in the parabolic well with superimposed superlattice, and the absence of any density modulation for the gas in the bare parabolic well.

I. INTRODUCTION

Applying a periodic potential to an electron gas gives rise to novel electrical properties arising from the creation of a superlattice (SL) band structure in the SL direction.¹ Periodic modulation of the density of an electron gas offers a system for the systematic study of collective excitations and interactions between electrons in different periods as the strength of the modulation is turned up from zero to a value high enough to break the continuous gas into unconnected layers of two-dimensional electron gases (2DEGs). Interactions between two 2DEGs in neighboring quantum wells separated by a thin barrier have recently been investigated.^{2,3} An externally tunable periodic potential is usually applied in the plane of a 2DEG by lithographically or holographically patterning a periodic one-dimensional or two-dimensional array of connected metal gates on the sample surface.⁴ Feature sizes in *e*-beam lithography and holography are currently limited to dimensions of several hundred Å, with the level of uncertainty and nonuniformity being of the same order of magnitude. Also, inasmuch as the patterned surface gate is spatially removed from the 2DEG by at least a few hundred Å, the induced lateral periodic potential is smoothed on the same length scale as this spatial separation.⁴ The amplitude of this potential is therefore smaller than when the periodic potential is directly immersed in the electron gas itself. Smaller periods (~ 100 Å) can be obtained by incorporating a lateral superlattice (LSL) in or near a 2DEG at a GaAs/AlGaAs single interface grown on a vicinal GaAs surface.⁵ The resulting periodic potential has manifested itself in anisotropic electron transport of the 2DEG parallel and perpendicular to the LSL,⁵ but terrace-width nonuniformity and intermixing between the GaAs and AlGaAs components of the LSL⁶ remain serious blocks to applying potentials of

uniform period and large amplitude. Recently, cleaved edge overgrowth (CEO) has been used to realize a periodic potential (with small and uniform period) on a 2DEG, grown on the cleaved edge of an in-plane SL, and grown by conventional molecular beam epitaxy (MBE).⁷ With a low-temperature mobility of $\sim 4 \times 10^4$ cm^2/Vs , this, like other CEO structures, offers exciting possibilities for the study of novel electronic properties arising from additional confinement and/or applied periodic potentials with length scales determined by MBE to atomic precision, but processing on 150 μm cleaved edges is nontrivial at this time. Direct immersion of a periodic potential in an electron gas has also been attempted in a SL with barriers that are selectively doped and thin enough that the electron states are extended in the growth direction [Fig. 1(a)].⁸ But the scattering of electrons by the ionized donors in the barriers reduces the low-temperature in-plane mobility drastically.

Immersing the SL in a thick electron gas of high mobility produced by some other means than doping the SL barriers themselves suggests itself as a means of getting a high-mobility electron gas with a strong periodic potential. Such thick (~ 2000 Å) three-dimensional electron gases (3DEGs) have been produced in modulation-doped wide parabolic potential wells, in which the 3D density is controlled by the curvature of the parabola.^{9,10} A SL added to the parabolic well, as schematically illustrated in Fig. 1(b), is expected to modulate the density of the uniform 3DEG produced by the slowly varying parabolic potential.

A self-consistent solution of the Poisson-Schrödinger equation for this structure confirms this scenario [Fig. 2(a)]. The solution for a 2000 -Å-wide parabolic well is shown for comparison [Fig. 2(b)], and is seen to produce a wide electron gas in the well fairly uniform at the curvature density $N_0 \sim 2.6 \times 10^{16}$ cm^{-3} . With the addition of a SL, the electron density is modulated by as much as 50%. However, the energy spectrum for a single electron in the bare parabolic well is only slightly perturbed, for the SL period shown.

²⁾Present address: Universität München, Sektion Physik, Geschw.-Scholl-Platz 1, D-8000 München 22, Germany.

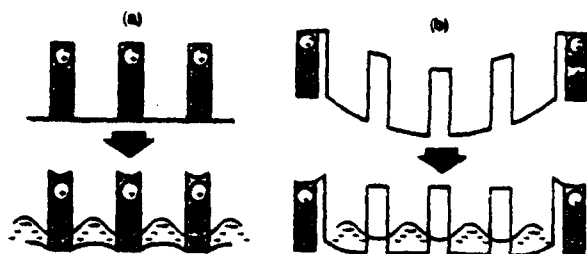


FIG. 1. (a) Modulation-doped superlattice (SL) with thin doped barriers used to produce an extended electron gas with periodic potential. (b) SL superimposed on a modulation-doped wide parabolic well to produce the same density modulation as in (a) on a wide electron gas of uniform density determined by the curvature of the parabola.

Such structures have been grown and their low-temperature transport properties measured,^{11,12} and some of their electrical and optical properties calculated.¹³ These transport measurements yield the energy spectrum, but afford only an indirect measure of the electron-density modulation. A more direct signature of this effect is needed. Such a measurement is presented below, along with other characterizations of the sample that highlight features of this design technique.

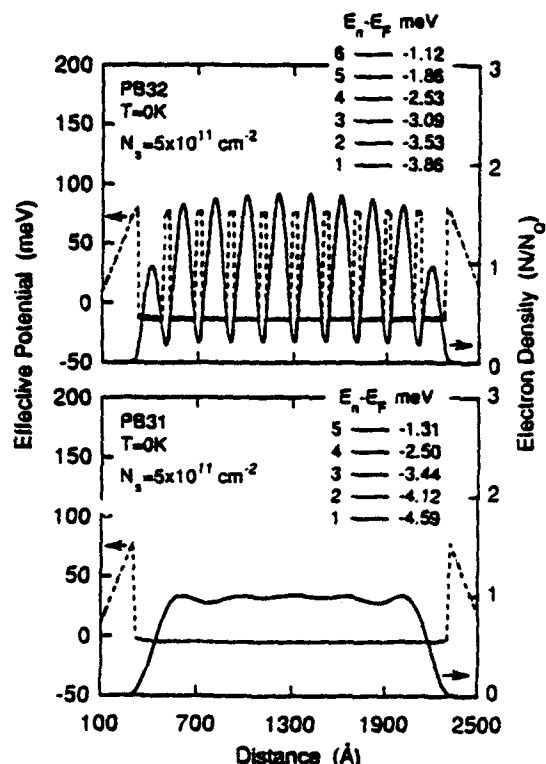


FIG. 2. Self-consistent potential and electron distribution for a wide parabolic well with SL (top) and without (bottom), showing the density-modulating effect of the SL. $N_0 = 2.61 \times 10^{16} \text{ cm}^{-3}$ is the curvature of the parabola. While the uniform electron distribution (bottom) is strongly modified (top) by the SL, the energy eigenvalues are not substantially changed for the SL period shown. The Fermi energy E_F is the zero reference energy on the potential energy scale.

II. EXPERIMENTS AND DISCUSSION

Two samples, similar to the ones for which calculations were presented in Fig. 2, were grown by solid-source MBE: PB31, a modulation-doped 2000-Å-wide parabolic well, and PB32, a modulation-doped 2000-Å-wide parabolic well with a SL of 200 Å period superimposed. The two samples were identical in every respect, save for the density-modulating SL in PB32, and were grown one after the other to minimize system variations. The potential wells were realized as graded $\text{Al}_x\text{Ga}_{1-x}\text{As}$ digital alloys,¹⁴ i.e., by controlled pulsing of the Al beam in the presence of constant Ga and As beams incident on a semi-insulating GaAs substrate, which was held at 580 °C. The digital alloy is therefore itself composed of a fine SL, whose period was selected to be 20 Å, a value small enough for an electron to see a local average Al mole fraction x . The complete layer sequence for both samples is: 5000 Å GaAs buffer/2000 Å $\text{Al}_{0.3}\text{Ga}_{0.7}\text{As}$ buffer/40 Å $\text{Al}_{0.3}\text{Ga}_{0.7}\text{As}$ Si doped at $1.1 \times 10^{18} \text{ cm}^{-3}$ /200 Å $\text{Al}_{0.3}\text{Ga}_{0.7}\text{As}$ spacer/graded potential well/200 Å $\text{Al}_{0.3}\text{Ga}_{0.7}\text{As}$ spacer/40 Å $\text{Al}_{0.3}\text{Ga}_{0.7}\text{As}$ Si doped at $1.1 \times 10^{18} \text{ cm}^{-3}$ /170 Å $\text{Al}_{0.3}\text{Ga}_{0.7}\text{As}$ Si doped at $5 \times 10^{17} \text{ cm}^{-3}$ /2000 Å $\text{Al}_{0.3}\text{Ga}_{0.7}\text{As}$ cap/100 Å GaAs cap. The $\text{Al}_x\text{Ga}_{1-x}\text{As}$ in the 2000-Å-wide parabolic wells of PB31 and PB32 was varied quadratically from GaAs at the well center to $\text{Al}_{0.2}\text{Ga}_{0.8}\text{As}$ at the well edges, jumping abruptly to the barrier $\text{Al}_{0.3}\text{Ga}_{0.7}\text{As}$ there. The bigger SL in the parabolic well of PB32 has a period of 200 Å, composed of a 160-Å-wide well and a 40-Å-wide barrier, with Δx_{Al} between the well and barrier being 0.1. All widths of the big SL are integer multiples of the finer digital-alloy SL period of 20 Å.

The variation of Al mole fraction versus depth in the graded potential wells was measured in a calibration run immediately prior to actual sample growth. The variation of the collector current of an ion gauge used in place of the substrate was monitored as a function of time as the Al beam was pulsed with the same controlled sequence as for the subsequent actual growth.¹⁵ The Al mole fraction profiles for both samples (Fig. 3) show fairly small deviations from the design profiles and testify to the level of control achievable in digital alloys to obtain these complex potentials.

Cloverleaf pattern Van der Pauw mesas were etched on both samples, and indium was alloyed to the ohmic-contact pads. Hall measurements were performed in a cold-finger cryostat from 300 to 10 K, and in liquid He (4.2 K). The variation of the in-plane mobility (μ) and electron sheet density (N_s) with temperature is shown for both samples in Fig. 4. The reduced ionized-impurity scattering at low temperatures resulting from the spatial separation of the electrons in the well from the donors in the barriers surrounding the parabolic well results in $\mu(4.2 \text{ K})$ as high as $1.8 \times 10^5 \text{ cm}^2/\text{Vs}$ at $N_s(4.2 \text{ K}) = 2.5 \times 10^{11} \text{ cm}^{-2}$ for the bare parabolic well, and $\mu(4.2 \text{ K}) = 1.1 \times 10^5 \text{ cm}^2/\text{Vs}$ at $N_s(4.2 \text{ K}) = 2.0 \times 10^{11} \text{ cm}^{-2}$ for the parabolic well with superimposed SL. The low-temperature mobility for the density-modulated 3DEG is an order of magnitude higher than was obtained in a modulation-doped SL of the type shown in Fig. 1(a).⁸ Since the samples were grown

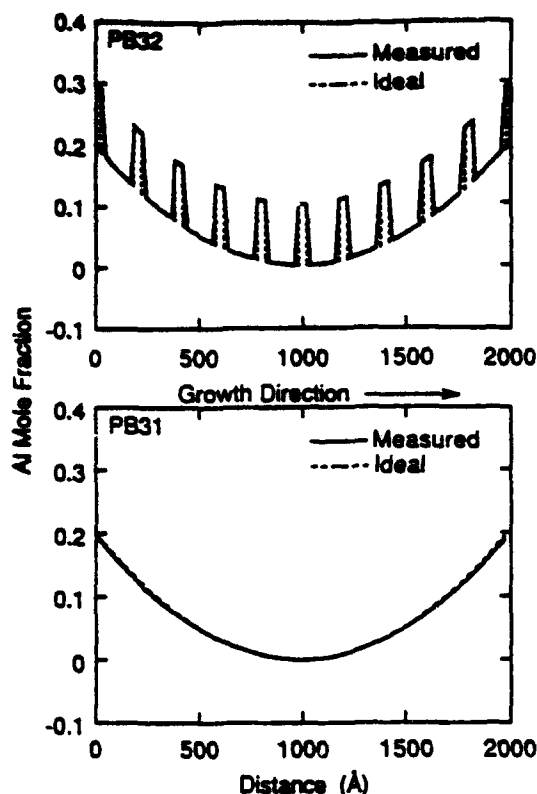


FIG. 3. Ion-gauge measured Al mole fraction profiles for wide parabolic well with SL (top) and without (bottom), for a MBE-grown digital AlGaAs alloy composed of a fine SL of 20 Å period. The slight tilt of the walls of the SL (top) is due to the 20 Å resolution of the measurement, and not an intrinsic limitation.

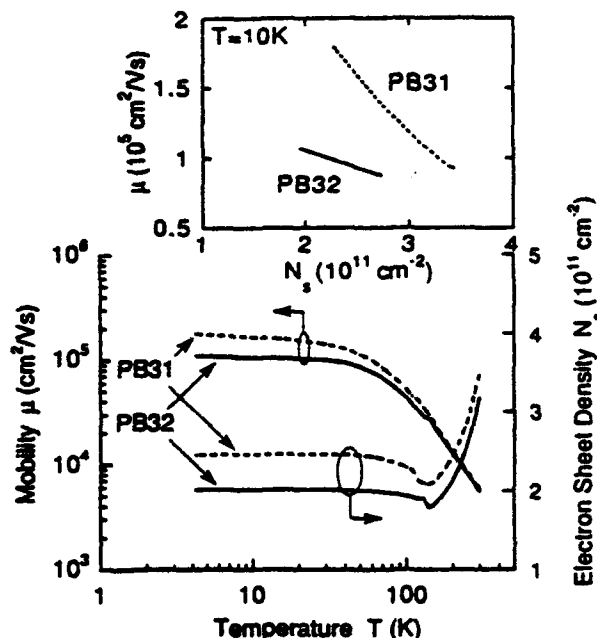


FIG. 4. Mobility vs temperature for both samples, showing the benefits of modulation doping at low temperature. Inset shows mobility of both samples decreasing with increasing electron sheet density at $T=10$ K.

one right after the other, and the densities N_s (4.2 K) are comparable, the difference in μ (4.2 K) must be attributed at least partly to the greater Al content in PB32 with its attendant enhanced alloy-disorder scattering. $\mu_{\text{alloy-disorder}}$ being inversely proportional to $\int x(1-x)dx$,¹⁶ the higher x_{avg} of 0.037 for PB32 over the extent of the electron gas, when compared to 0.017 for PB31 over the same extent, implies a reduction in mobility by a factor of ~ 1.7 on addition of the SL to the bare parabolic well just from this effect. The roughness of the walls of the 160-Å-wide wells in the SL is an important issue.¹⁷ For a single quantum well of this width and infinite potential depth, the interface-roughness scattering limited mobility is in excess of 10^6 cm²/V s.¹⁷ The coupling between the SL wells through the 40-Å-wide barriers should increase this estimate even further, and suggests that for this structure, interface roughness is not a critical issue. The mobility for both samples decreases with increasing electron sheet density (inset in Fig. 4) at a fixed temperature $T=10$ K, probably a result of the spread of the electron distribution from the center into regions of more Al mole fraction at the well edges with the attendant enhanced alloy-disorder scattering there.

Ti/Au (200 Å/2000 Å) was then evaporated on the mesas and the small-signal capacitance versus voltage (C - V) measured between the surface gate and the electron gas in the graded well, for both samples, using standard lock-in techniques. The results were found to be independent of ac-voltage frequency, dc-voltage-bias sweep rate, and sweep direction. C - V profiles ($T=4.2$ K) for both samples are shown in the inset in Fig. 5. Two features are apparent in these profiles. First, the capacitance falls off, with more negative gate bias, from zero bias to threshold (where all the electrons are depleted from the well), for both samples. This decrease is mainly attributed to the increased spacing between the two plates of the parallel-plate capacitor formed by the surface metal gate and the electron gas in the well, respectively, as the leading edge of the gas is pushed deeper toward the substrate with more negative voltage bias at the gate.¹⁸ Furthermore, whereas the capacitance falls off smoothly with voltage for the bare parabolic well (PB31), the C - V profile for the parabolic well with SL (PB32) displays ripples superimposed on the decrease. These ripples are associated with the sweeping of the leading edge of the electron gas through successive periods of the SL with more negative bias. In both cases, there is concurrent depopulation of the subbands occupied by the electron gas, but the ripples expected in the C - V traces from this effect are calculated to be small,¹⁹ a fact that is experimentally underscored by the relative absence of ripples in the C - V trace for the parabolic well. From the C - V measurement, one can extract an apparent electron distribution versus depth using $\bar{N}(z) = 2/q\epsilon_s[d(1/C^2)/dV]^{-1}$ as the apparent electron density at the apparent depth $z = \epsilon_s/C$, where C is the capacitance per unit area between surface gate and electron gas at voltage bias V , and ϵ_s is the uniform permittivity assumed.²⁰ Using $\epsilon_s = 12.2$ (of the Al_{0.3}Ga_{0.7}As cap), we arrive at the apparent electron profiles shown in Fig. 5 for both samples. A modulation of the apparent electron density is readily seen for the electron

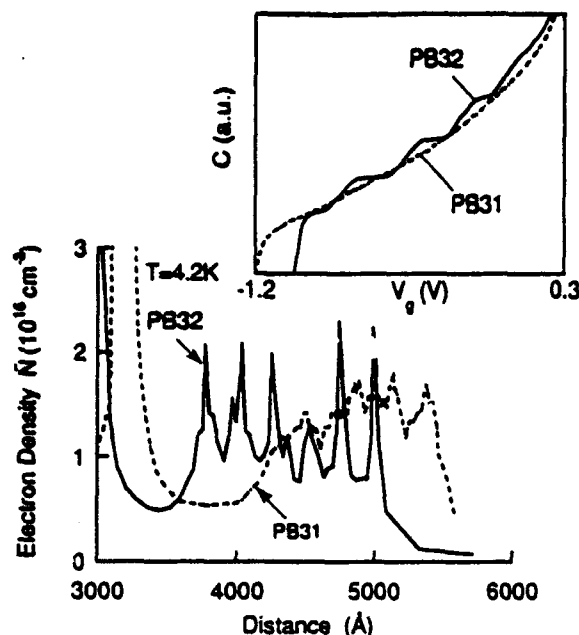


FIG. 5. 4.2 K apparent-electron-density distributions extracted from the C - V traces (inset) show strong density modulation of the electron gas in the parabolic well with SL (PB32) and the relative absence of modulation for the parabolic well without SL (PB31) (the sensitivity of the technique allowing us to measure the unintentional nonuniformities in the well curvature at the level that can be achieved with current MBE technology). The effect of the SL on electron distribution is most directly seen in the C - V traces in inset. Threshold gate voltage for both samples ~ -1 V.

gas in the parabolic well with superimposed SL; no such modulation is seen for the 3DEG in the bare parabolic well. The average periodicity of the apparent-electron-density modulation in the C - V measurement is ~ 230 Å, in reasonable agreement with the nominal SL period of 200 Å. We believe this to be the most direct evidence to date of the density modulation produced in such structures.

III. CONCLUSIONS

In summary, we have fabricated a high-mobility 3DEG with periodic density modulation using computer-controlled MBE to make a digital AlGaAs alloy with accurate Al mole fraction variation. This variation is directly measured with an ion gauge, and the resulting periodic modulation of the electron density is directly seen in a simple capacitance-voltage measurement. An attractive feature of this technique is the possibility of applying peri-

odic potentials to high-mobility electron gases of different shapes. The average-density profile is defined by the curvature of a wide potential well; density modulation is achieved with a SL of narrower period inserted in this wide well. More complex electron density distributions can, of course, be achieved with the appropriate Al mole fraction profiles in digital $\text{Al}_x\text{Ga}_{1-x}\text{As}$ alloys.

ACKNOWLEDGMENTS

We thank J. H. English, M. S. Sherwin, E. G. Gwinn, G. Snider, and K. Campman of UCSB, R. M. Westervelt, A. J. Rimberg, and J. Baskey of Harvard University, and K. Ensslin of Universität München, for valuable discussions. This research was supported by the United States Air Force Office of Scientific Research.

- ¹L. Esaki and R. Tsu, *IBM J. Res. Develop.* **14**, 61 (1970).
- ²J. P. Eisenstein, L. N. Pfeiffer, and K. W. West, *Appl. Phys. Lett.* **58**, 1497 (1991).
- ³A. H. MacDonald, P. M. Platzman, and G. S. Boebinger, *Phys. Rev. Lett.* **65**, 775 (1990).
- ⁴See, for example, *Nanostructure Physics and Fabrication*, Proc. Int. Symp., College Station, Texas, edited by M. A. Reed and W. P. Kirk (Academic, Boston, 1989).
- ⁵J. Motohisa, M. Tanaka, and H. Sakaki, *Appl. Phys. Lett.* **55**, 1214 (1989).
- ⁶S. A. Chalmers, A. C. Gossard, P. M. Petroff, and H. Kroemer, *J. Vac. Sci. Technol. B* **8**, 431 (1990).
- ⁷H. L. Stormer, L. N. Pfeiffer, K. W. Baldwin, K. W. West, and J. Spector, *Appl. Phys. Lett.* **58**, 726 (1991).
- ⁸H. L. Stormer, J. P. Eisenstein, A. C. Gossard, W. Wiegmann, and K. Baldwin, *Phys. Rev. Lett.* **56**, 85 (1986).
- ⁹M. Sundaram, A. C. Gossard, J. H. English, and R. M. Westervelt, *Superlattices and Microstructures* **4**, 683 (1988).
- ¹⁰M. Shayegan, T. Sajoto, M. Santos, and C. Silvestre, *Appl. Phys. Lett.* **53**, 791 (1988).
- ¹¹J. Jo, M. Santos, M. Shayegan, Y. W. Suen, L. W. Engel, and A. M. Lanzillotto, *Appl. Phys. Lett.* **57**, 2130 (1990).
- ¹²A. J. Rimberg, J. H. Baskey, R. M. Westervelt, P. F. Hopkins, M. Sundaram, and A. C. Gossard, *Proc. Int. Symp. Nanost. and Mesoscop. Syst.*, Santa Fe, New Mexico, 1991.
- ¹³L. Brey, N. F. Johnson, and J. Dempsey, *Phys. Rev. B* **42**, 2886 (1990).
- ¹⁴A. C. Gossard, *IEEE J. Quantum Electron.* **22**, 1649 (1986).
- ¹⁵M. Sundaram, A. Wixforth, R. S. Geel, A. C. Gossard, and J. H. English, *J. Vac. Sci. Technol. B* **9**, 1524 (1991).
- ¹⁶W. Walukiewicz, H. E. Ruda, J. Lagowski, and H. C. Gatos, *Phys. Rev. B* **30**, 4571 (1984).
- ¹⁷H. Sakaki, T. Noda, K. Hirakawa, M. Tanaka, and T. Matsusue, *Appl. Phys. Lett.* **51**, 1934 (1987).
- ¹⁸A. Wixforth, M. Sundaram, K. Ensslin, J. H. English, and A. C. Gossard, *Appl. Phys. Lett.* **56**, 454 (1990).
- ¹⁹M. Sundaram, K. Ensslin, A. Wixforth, and A. C. Gossard, *Superlattices and Microstructures* **10**, 157 (1991).
- ²⁰H. Kroemer, Wu-Yi Chien, J. S. Harris, Jr., and D. D. Edwall, *Appl. Phys. Lett.* **36**, 295 (1980).

Remotely-doped superlattices in wide parabolic GaAs/Al_xGa_{1-x}As quantum wells

J. H. Baskey, A. J. Rimberg, Scott Yang, and R. M. Westervelt
*Division of Applied Sciences and Department of Physics, Harvard University,
 Cambridge, Massachusetts 02138*

P. F. Hopkins and A. C. Gossard
*Department of Electrical and Computer Engineering and Materials Department,
 University of California, Santa Barbara, California 93106*

(Received 27 April 1992; accepted for publication 24 July 1992)

Using the digital alloy technique, a series of high-mobility remotely doped GaAs/AlGaAs coupled multiple quantum well structures have been produced by the superposition of a wide parabolic quantum well and a square superlattice potential. Structures containing up to twenty superlattice periods with low temperature Hall mobilities from 23 000 to 100 000 cm²/V s have been produced. Fourier analysis of low field Shubnikov-de Haas oscillations, capacitance-voltage and Hall measurements of a 200 Å period superlattice in a 1600 Å wide parabolic well indicate the occupation of four superlattice periods with subband spacings in good agreement with theory.

Semiconductor superlattices have been studied for many years for their interesting physical properties and applications.^{1,2} The electron mobility in these structures at low temperatures is typically limited by ionized impurity scattering.³ A large improvement in mobility was achieved by modulation doping in which the donors are placed in the superlattice barriers.⁴ Considerably larger mobilities have recently been achieved by removing the dopant atoms from the superlattice altogether using a wide parabolic well (WPBW) superimposed with a superlattice, as shown in Fig. 1(a). The finite width of the parabolic potential restricts the number of superlattice periods forming the coupled multiple quantum well structure. Parabolic structures with both sinusoidal⁵ and square⁶ superlattices were recently reported. In this letter we present a quantitative comparison of Shubnikov-de Haas oscillation data with theory and capacitance-voltage profiles, which demonstrate high quality remotely doped square superlattices.

In WPBWs, the parabolically varying band edge, by Poisson's equation, mimics a uniform positive charge distribution of three dimensional density $n_{3D} = 8\epsilon\Delta/\epsilon^2w^2$, where w and Δ are the width and height of the parabolic potential, ϵ is the dielectric constant, and e is the electronic charge. The electrons from dopants placed outside the parabola move to screen this fictitious charge forming a uniform electron gas of width $w_e = n/n_{3D}$ and sheet density n_s inside the parabolic well.^{7,8} When a superlattice of sufficiently short period is superimposed on the parabolic background, the electrons can screen the parabolic potential but not that of the superlattice,⁹ producing a self-consistent potential as shown in Fig. 1(b): the electron density is spatially modulated by the superlattice potential, but the average electron density is approximately n_{3D} .

The samples were grown via molecular beam epitaxy (MBE) using the digital alloy technique.⁷ The average Al concentration along the growth direction was varied by computer-controlled shuttering of the Al furnace, allowing control of the band edge profile during growth of the WPBW with superlattice. Before well growth, the Al con-

centration versus position in the well was measured with an ion gauge substituted for a wafer in the MBE chamber. This information was used to correct for the shutter response time, improving control of barrier width and height, and minimizing deviations from parabolicity.

In this letter we discuss one sample SL6, with 83 meV high, 80 Å wide superlattice barriers inside a parabolic well of width $w=1600$ Å and height $\Delta=210$ meV. These parameters were chosen so that the Fermi level lies in the gap between the first and second minibands of the superlattice potential. Carriers were supplied by Si dopants set back 105 Å from the well edges, in delta-doped sheets on either side of the well in a fine AlAs/GaAs superlattice with a period 21 Å and average Al concentration $x=0.35$. From the depth of the donors below the conduction band edge¹⁰ the well was expected to be only partially full at liquid He temperatures. This well was one of a series of superlattice structures also investigated. Samples containing 8–20 periods with a range of characteristics were grown and tested. For all, the bandwidth of the lowest miniband was maintained at 2 meV and the superlattice period was fixed at $d=200$ Å. Barrier widths b ranged from 40 to 80 Å and barrier heights h from 83 to 175 meV. The parabolic well width w ranged from 1600 to 4000 Å and height Δ from 87.5 to 210 meV (see Fig. 1), corresponding to a range of electron density from $n_{3D}=4.0\times 10^{15}$ to 4.6×10^{16} cm⁻³.

The sample was cooled in the dark inside a top-loading

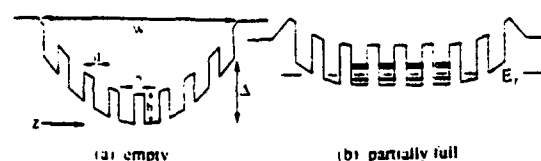


FIG. 1. Schematic diagram of (a) an empty and (b) a partially full wide parabolic well with superlattice. The Fermi level for the partially full well is indicated to lie between the two lowest energy bands represented by the hatched regions.

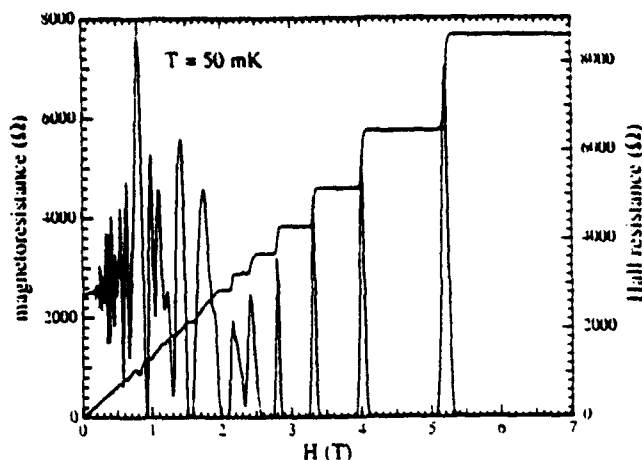


FIG. 2. Magnetoresistance and Hall effect data for sample SL6.

Oxford Model 200 dilution refrigerator. Using standard low frequency lock-in techniques, magnetotransport measurements were made at $T=50$ mK. Low currents (less than 1 nA) and slow magnetic field sweeps (less than 0.04 T/min) were used to avoid sample heating. The magnetoresistance and Hall effect data are shown in Fig. 2 from which a Hall sheet density of $n_s=4.3 \times 10^{11} \text{ cm}^{-2}$ and mobility $\mu=23\,000 \text{ cm}^2/\text{V s}$ were obtained. This mobility is several times greater than that achieved in standard modulation doped superlattices which typically have mobilities less than $10\,000 \text{ cm}^2/\text{V s}$.² The integer quantum Hall effect is observed with the location of the magnetoresistance zeros consistent with the low field Hall sheet density. Hall steps up to $\nu=20$ can be identified in the data. In strong magnetic fields above 3 T, a simple estimate predicts that only the lowest Landau level of the lowest miniband states is occupied. In weaker magnetic fields below 3 T, higher Landau levels are also occupied and a complex series of level crossings occurs, resulting in missing or weak Hall plateaus as shown in Fig. 2. Characteristic missing quantum Hall steps also occur in wide parabolic wells without superlattices in which several subbands are occupied.¹¹

Multiply periodic Shubnikov-de Haas (SdH) oscillations in the magnetoresistance data were used to measure the Fermi level and subband energies of the superlattice sample. The magnetoresistance oscillation associated with a given occupied subband is periodic in inverse magnetic field $1/H$ with period $\hbar e/m_e(E_f - E_i)$, where $m_e=0.067 m_0$ is the electron effective mass, E_i is the bottom of the i th subband, and E_f is the Fermi energy, both in zero field. We assume that the two spin states of each subband are not

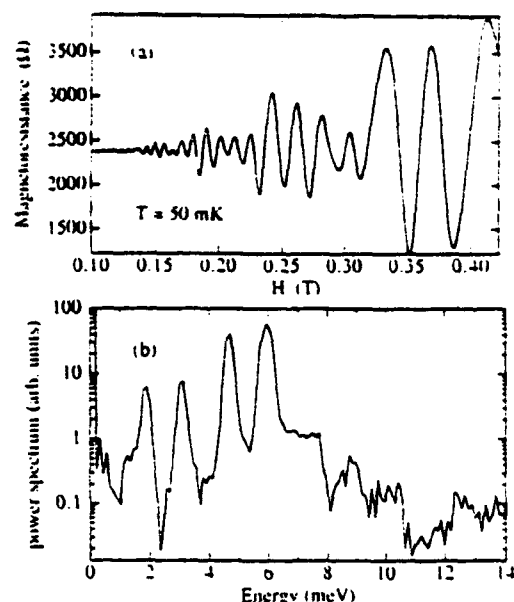


FIG. 3. (a) Multiply periodic low field SdH oscillations for sample SL6 indicating the occupation of several subbands and (b) the power spectrum of the SdH oscillations over the field range $H=0.03\text{--}0.35$ T.

resolved at the low magnetic fields used for this measurement. Using this expression, the separations $(E_f - E_i)$ between the Fermi level and the subband bottoms can be calculated by Fourier analysis of the SdH oscillations, and the total sheet density n_s can be determined by summing the contributions from each subband $n_s = \sum m_e(E_f - E_i)/\pi\hbar^2$. Magnetoresistance data for magnetic fields less than 0.4 T at $T=50$ mK are shown in Fig. 3(a) together with the corresponding SdH power spectrum in Fig. 3(b) computed from interpolated magnetoresistance data spaced equally in $1/H$. For convenience, the horizontal axis of the power spectrum in Fig. 3(b) has been given in electron energy $(E_f - E_i)$ using the expression for the SdH period given above. Four peaks are clearly visible in the power spectrum, indicating that four subbands of the superlattice are occupied, each with two spin states. The total sheet density obtained by summing subbands is $n_s=4.4 \times 10^{11} \text{ cm}^{-2}$, in excellent agreement with the Hall sheet density $n_s=4.3 \times 10^{11} \text{ cm}^{-2}$. Table I lists the measured Fermi level E_f and the energies E_i of the occupied subbands, all given relative to the lowest subband E_1 .

To compare these experimental results with theory, a self-consistent solution of Schrödinger's and Poisson's equation, including the exchange-correlation potential in

TABLE I. Comparison of Shubnikov-de Haas measurements of the Fermi energy and subband energies with theory; all energies are in meV.

	Experiment	Theory-Superlattice	Theory-Parabola	
		(1370 Å)	(1370 Å)	(1600 Å)
$E_f - E_1$	5.93 ± 0.06	5.89	7.98	6.56
$E_2 - E_1$	1.22 ± 0.10	1.23	2.34	1.36
$E_3 - E_1$	2.79 ± 0.14	2.78	5.71	3.43
$E_4 - E_1$	4.03 ± 0.14	4.17	...	6.10

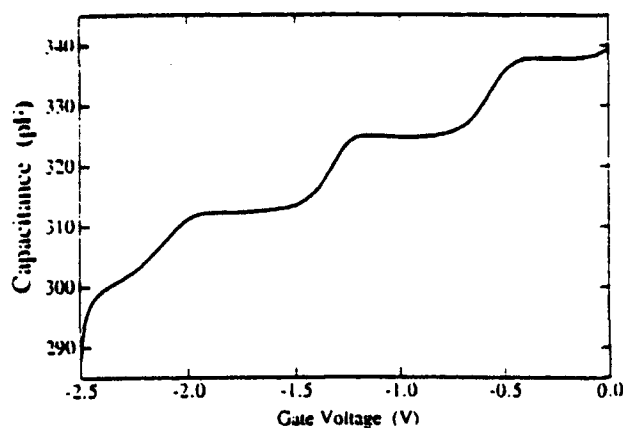


FIG. 4. Capacitance vs gate voltage at $T=0.43$ K. Each step corresponds to an occupied period of the superlattice system. As the electron layer in the period nearest the gate is depleted the capacitance shifts to the value associated with the occupied period next nearest the gate.

the local density functional approximation,¹² was calculated using the experimentally determined sheet density as input, assuming symmetric filling about the well center. The parabolic well width is position dependent because the source guns are angled with respect to the wafer, and the wafer is not rotated during growth to avoid aliasing effects, resulting in a uniform gradation in well width across the sample. A 20% gradient in the growth rate of GaAs across unrotated test wafers was measured via RHEED oscillations. Using the parabolic well width as the only adjustable parameter we found excellent agreement, shown in Table I, between experiment and theory for a well which is 1370 Å wide, well within the range of growth parameters. Table I also shows theoretical energy level spacings for WPBW's identical to SL6 with widths 1370 and 1600 Å but no superlattice. It is clear the measured energy levels are not those of a plain WPBW; the level of agreement cannot be significantly improved by altering the well width. The spacing of the observed subband energies is relatively uniform, and the Fermi energy is reduced relative to a simple WPBW, as expected for a superlattice.⁹

The electron density profile in the superlattice was directly probed using capacitance-voltage measurements.¹³ The sample was cooled in the dark to 0.43 K in a pumped He-3 immersion system. The capacitance between a Cr/Au front gate evaporated on the sample and the electron gas in the parabolic well was measured using lock-in techniques with a superimposed ac voltage (20 mV_{rms} @ 402 Hz) and dc voltage applied between the gate and the electron gas as the width of the gas was swept to depletion. Experimental results were checked for several different frequencies and amplitudes of the applied ac signal with good agreement. The measured $C-V$ profile shown in Fig. 4 has four well-defined plateaus, indicating that the electron density profile has four well-defined layers in agreement with the calculated number of occupied superlattice wells for the measured sheet density and parabolic well width $w=1370$ Å. From the steps in capacitance between plateaus in Fig. 4, we determined that the electron layers were uniformly

spaced at 175 ± 10 Å consistent with the spacing obtained from SdH data above.

Combining the number of occupied superlattice periods from $C-V$ data with the number of occupied subbands from SdH data, we find that one subband with two spin states is occupied for each of four superlattice periods. It is interesting to interpret these results in terms of a simple tight-binding model. In the absence of electrons, the individual square wells of the superlattice are not aligned in energy as they are superimposed on a parabolic potential. In a full well the parabolic potential is approximately cancelled by the electrostatic potential of the electron layer, bringing all superlattice wells into energy alignment. For the sample studied here the WPBW is half full so only four superlattice periods are occupied and in approximate energy alignment. The lowest miniband of a tight binding model for this case is full, with four energy levels and two spin states per level. This configuration is consistent with the design of the structure, for which the Fermi energy lies in the gap above the lowest miniband (see Fig. 1).

In summary we have produced and characterized remotely doped high-mobility multiple quantum well structures with a range of three-dimensional electron densities from $n_{3D}=4.0 \times 10^{15}$ to 4.6×10^{16} cm⁻³. Magnetotransport and $C-V$ measurements for one structure show a spatially modulated electron density profile occupying four periods of a square superlattice potential, demonstrating control of both the electron density profile and energy subband structure of a wide electron gas.

We thank Jed Dempsey for valuable comments. One of the authors (J.H.B.) acknowledges support from the Natural Science and Engineering Research Council of Canada. Work at Harvard was supported in part by the National Science Foundation and by the Harvard Materials Research Laboratory under Grants DMR-91-19386 and DMR-89-20490; work at Santa Barbara was supported by the Air Force Office of Scientific Research under Grant AFOSR-91-021.

¹ L. Esaki and R. Tsu, IBM J. Res. Dev. 14, 61 (1970).

² H. L. Störmer, J. P. Eisenstein, A. C. Gossard, W. Wiegmann, and K. Baldwin, Phys. Rev. Lett. 56, 85 (1986).

³ See, for example, K. Seeger, *Semiconductor Physics* (Springer, New York, 1973), p. 170.

⁴ R. Dingle, H. Stormer, A. C. Gossard, and W. Wiegmann, Appl. Phys. Lett. 33, 665 (1978).

⁵ J. Jo, M. Santos, M. Shayegan, Y. W. Suen, L. W. Engel, and A. M. Lanzilotto, Appl. Phys. Lett. 57, 2130 (1990).

⁶ A preliminary report of this work appears in Proc. NanoMES'91, Santa Fe, New Mexico, Superlatt. Microstruct. 11, 317 (1992).

⁷ M. Sundaram, A. C. Gossard, J. H. English, and R. M. Westervelt, Superlatt. Microstruct. 4, 683 (1988).

⁸ M. Shayegan, T. Sojoto, M. Santos, and C. Silvestre, Appl. Phys. Lett. 53, 791 (1988).

⁹ L. Brey, N. F. Johnson, and J. Dempsey, Phys. Rev. B 42, 2886 (1990).

¹⁰ N. Chand, T. Henderson, J. Klem, W. T. Masselink, R. Fischer, Y. Chang, and H. Morkoç, Phys. Rev. B 30, 4481 (1984).

¹¹ E. G. Gwinn, R. M. Westervelt, P. F. Hopkins, A. J. Rimberg, M. Sundaram, and A. C. Gossard, Phys. Rev. B 39, 6250 (1989); K. Ensslin, M. Sundaram, A. Wixforth, J. H. English, and A. C. Gossard, Phys. Rev. B 43, 9988 (1991).

¹² A. J. Rimberg and R. M. Westervelt, Phys. Rev. B 40, 3970 (1989).

¹³ M. Sundaram, A. Wixforth, P. F. Hopkins, and A. C. Gossard, J. Appl. Phys. (to be published).

Growth and characterization of Be modulation doped wide parabolic GaAs/Al_xGa_{1-x}As wells

P.F. Hopkins, K.L. Campman and A.C. Gossard

Materials Department and Department of Electrical and Computer Engineering, University of California, Santa Barbara, California 93106, USA

Remotely-doped, p-type wide (~ 1000 Å) parabolic GaAs/Al_xGa_{1-x}As quantum wells grown on (100) substrates were used to create high mobility, low density, wide layers of hole gas. Low temperature capacitance-voltage and magnetotransport measurements were used to characterize these structures. Hole gas widths ~ 700 Å, sheet densities $> 3 \times 10^{11}$ cm⁻², and mobilities $> 23,000$ cm²/V·s at $T = 0.1$ K have been achieved in wells with a curvature corresponding to a three-dimensional density $\sim 4 \times 10^{16}$ cm⁻³. These mobilities are more than three orders of magnitude higher at low temperature than bulk p-type GaAs with similar three-dimensional density.

By parabolically tailoring the conduction band edge of an undoped GaAs/Al_xGa_{1-x}As heterostructure along the growth direction z , the conduction band potential $\Phi(z)$ is, by Poisson's equation, equivalent to a uniform density n_+ of background positive charge: $d^2\Phi/dz^2 = en_+/\epsilon$, where e is the electronic charge and ϵ is the dielectric constant [1]. When remotely n-doped, the electrons from the dopant fall into the parabolic well, and are expected to form a thick slab of nearly uniform density $n(z) \approx n_+$. Quantum mechanical calculations of the electron density profile in these wide (≥ 1000 Å) structures confirm this classical idea [2]. Using these concepts, high quality structures with a variety of electron density profiles have been constructed by appropriate tailoring of the band edge potential [3,4].

Because the dopant atoms are spatially removed from the well, high electron mobilities and low carrier densities that do not freeze out at low temperatures have been achieved [5]. n-Type modulation doped wide parabolic wells (WPBW's) have been used previously to create high mobility (to $> 200,000$ cm²/V·s), wide electron layers (to ~ 2000 Å) of low, nearly uniform density (down to $< 10^{16}$ cm⁻³) providing access to new elec-

tronic and optical phenomena [1,3,6]. In this paper, we extend this work to p-type structures and report on the growth and characterization of Be doped WPBW's; we have obtained wide (~ 700 Å), high mobility ($> 23,000$ cm²/V·s at $T = 0.1$ K) hole gas layers in wells with curvature corresponding to a 3D density $p(z) \sim 4 \times 10^{16}$ cm⁻³. This 3D density is below the critical metal-insulator transition density for p-type doped bulk GaAs, providing unprecedented access for investigations of the electronic and optical properties of low density wide hole gas layers at low temperatures.

There have been two techniques used to grow wide parabolic GaAs/Al_xGa_{1-x}As wells by molecular beam epitaxy: (1) controlling the temperature [4] of the Al furnace so that the Al flux is varied with time (analog alloy technique) and (2) dividing the wide well into a fine period superlattice (of period d , typically ~ 20 Å) of GaAs and Al_xGa_{1-x}As and controlling the shuttering of the Al furnace so that the average Al composition x per period varies parabolically (digital alloy technique) [7,8]. The first technique has the advantage that a more uniform alloy is obtained, but has the disadvantage that precise calibration of thermal time lags of the Al flux and

precise control of the flux versus furnace temperature are needed. The second technique has the advantage that the Al furnace temperature can be kept constant throughout the growth, but has the disadvantage that the periodic potential modulation caused by the fine superlattice may affect the relevant properties of the well that we wish to study [9]. The superlattice must be fine enough to allow sufficient tunneling of the carriers between layers. However, as the period of the superlattice is made finer, shuttering times of the Al source (at typical growth rates) can become small (< 100 ms), requiring precise calibration of the Al shutter opening and closing times and/or designing wells with nonzero Al composition at the center of the parabolic well. This suggests that there is an optimal range of superlattice periods to use which depends on the well structure, carrier effective mass, height of the Al_xGa_{1-x}As barriers, growth rates, etc. We believe that with careful choice of these parameters, the digital alloy technique allows more exact control of the average composition profiles than the analog alloy technique, especially for profiles too rapidly changing in time during the growth for the Al furnace to track precisely [8].

To determine the optimal range of superlattice periods to use, we use simple second order Rayleigh-Schrödinger perturbation theory to estimate the change in the effective mass, energy levels, and charge distribution for free carriers in a sinusoidal potential perturbation $2U(G)\cos(Gz)$. The perturbed effective mass m^* in the growth direction and at the zone center ($E(k=0)$) is:

$$m^* = m \left\{ 1 + 0.5 [U(G)/E_0(G/2)]^2 \right\}, \quad (1)$$

where $E_0 = \hbar^2(G/2)^2/2m$ is the energy for carriers with bulk effective mass m at wavevector $G/2 = \pi/d$, where d the period of the perturbation; note that the correction term is proportional to d^4 . The Fourier transform power spectra for our digital alloy potential show a peak at the frequency $f = 1/d$ corresponding to the superlattice period, and smaller amplitude peaks at the higher harmonics $f = n/d$, where $n = 2, 3, 4, \dots$. Because of the strong dependence on d , we approximate our superlattice potential as a single

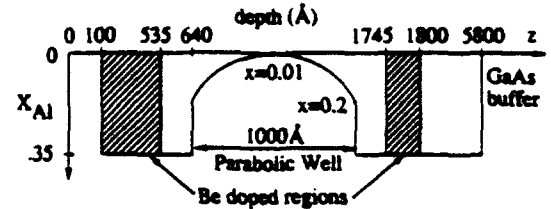


Fig. 1. Aluminum mole fraction x_{Al} (also valence band edge energy) versus depth of WPBW structure. The 1000 Å wide digital alloy well was constructed from a 20 Å period GaAs/Al_{0.35}Ga_{0.65}As superlattice.

wavevector perturbation; the correction in eq. (1) due to the n th harmonic is smaller by more than a factor of n^{-4} . To model the actual structure presented in this paper, we use $d = 20$ Å, $U(G) = \Delta E_v/\pi = 41.6$ meV and $m = 0.500 m_0$, and obtain an estimate $m^* = 0.513 m_0$. The energy spectrum of the valence band $E(k)$ is shifted up into the bandgap by 4.6 meV, although the lowest energy level spacings change only by $\sim 2.5\%$. The first order change in the ground state wavefunction creates 20 Å period ($= d$) ripples in the charge density $p(z)$ of size $(p_{peak} - p_{ave})/p_{ave} \sim 23\%$ due to localization of the carriers in the GaAs wells. The approximation given by eq. (1) breaks down sharply for superlattice periods d above ~ 40 Å (see also ref. [9]).

The design of one of a series of samples made is shown in fig. 1 and was grown by MBE on a semi-insulating GaAs (100) substrate. The 1000 Å wide parabolic well was constructed from a 20 Å period digital alloy superlattice of GaAs and Al_{0.35}Ga_{0.65}As. The average Al concentration x in the well is $x = 0.2$ at the edges and $x = 0.01$ in the center; the shortest time that the DC operated Al shutter is open is > 100 ms, much larger than the uncertainty (~ 10 ms) in the shutter opening and closing times. Using the conduction band/valence band offset ratio for Al_xGa_{1-x}As of 0.7/0.3 gives $\Delta E_v = 131$ meV and the equivalent background charge density for the parabolic well $p_{3D} = 4 \times 10^{16} \text{ cm}^{-3}$. Holes were introduced into the well from Be δ -doped regions ($2 \times 10^{11} \text{ cm}^{-2}$ per δ -doped sheet, 18 Å spacing) set back 105 Å on either side. The RHEED measured growth rates for GaAs and AlAs were 1.0 and 0.54 $\mu\text{m/h}$, respectively. The substrate was kept

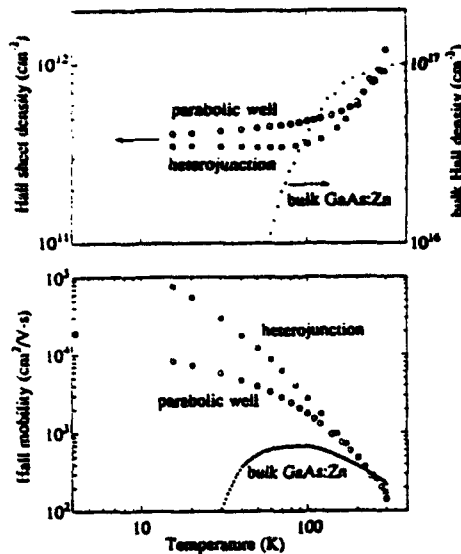


Fig. 2. Hall density and the Hall mobility for the range $T = 4.2\text{--}300\text{ K}$ for the p-type modulation doped WPBW and a Be-doped heterojunction, and $T = 25\text{--}300\text{ K}$ for bulk Zn-doped p-type GaAs from ref. [10].

at a pyrometer-measured temperature of 580°C , except for the Be δ -doped regions which were grown at 520°C to reduce dopant migration. To avoid effects due to the incommensurability of the rotation period and the varying Al shutter timing, the substrate was not rotated during the growth of the digital alloy well resulting in a calculated change in the well density p_{3D} of $< 3\%$ for a typical sample taken $< 1\text{ cm}$ from the wafer center. Hall bar ($2.5\text{ mm} \times 0.26\text{ mm}$) samples were photolithographically defined and ohmic contacts were made by annealing In/Zn at 410°C for 60 s. For the capacitance measurements, a $50\text{ \AA}/1500\text{ \AA}$ Ti/Au front gate was e-beam evaporated onto the sample.

Fig. 2 shows the temperature dependence of the Hall sheet density p_s and the Hall mobility μ for the range $T = 4.2\text{--}300\text{ K}$ after the Hall bar was illuminated with a red LED. The density was measured from the Hall voltage for the magnetic field B range of $-0.5 < B < 0.5\text{ T}$ and the Hall mobility was obtained with the Hall density and the $B = 0$ resistance values. The Hall factor 1 was used. In comparison, data from a Be modulation-doped normal interface GaAs/Al_{0.3}Ga_{0.7}As heterojunction (700 \AA from the surface) and from a

bulk Zn-doped (p-type) GaAs sample [10] with $p_{3D} = 1 \times 10^{17}\text{ cm}^{-3}$ are also shown. The sheet density p_s for the parabolic well and the heterojunction are nearly constant for $T < 80\text{ K}$, in contrast to the strongly decreasing 3D carrier density for the bulk doped sample for $T < 150\text{ K}$ caused by carrier freeze-out. Similarly, the measured Hall mobility μ for the parabolic well and the heterojunction both monotonically increase with decreasing temperature, while the mobility for the bulk doped sample increases slightly with decreasing temperature and then strongly decreases for $T < 70\text{ K}$. The low temperature ($T < 20\text{ K}$) mobility for the parabolic well with curvature corresponding to a three-dimensional density $p_{3D} = 4 \times 10^{16}\text{ cm}^{-3}$ is over 3 orders of magnitude greater than the mobility of the bulk doped sample with similar density $p_{3D} = 1 \times 10^{17}\text{ cm}^{-3}$. The low temperature mobility of the bulk sample is limited by ionized impurity scattering, while scattering from acoustic phonons and background impurities play a more important role for the remotely-doped heterojunction [11] and the WPBW. Additionally, scattering of holes in the WPBWs due to alloy disorder and size effect [12] is expected.

Capacitance-voltage measurements of the same sample cooled in the dark were made at $T = 0.1\text{ K}$ in a dilution refrigerator and are shown in fig. 3. A DC gate bias and small (10 mV peak-peak) 647 Hz AC signal were applied between the Ti/Au front gate and the ohmic con-

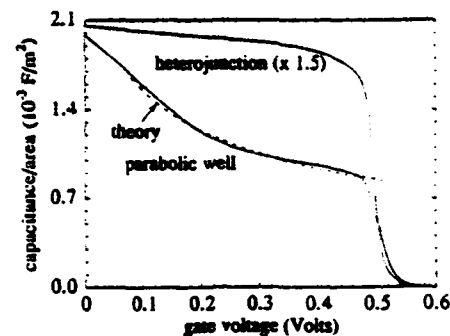


Fig. 3. Low temperature capacitance versus gate voltage for the WPBW and the Be-doped heterojunction taken at 10 mV, 647 Hz excitation. The fit (—) to the WPBW data is described in the text.

tacts to the hole gas. The induced current is measured by a current preamplifier and fed into a phase-sensitive lock-in amplifier. The data show a smooth monotonic decrease in the capacitance with increasing DC gate bias as the depletion edge is moved through the structure. In contrast, the 4.2 K measured capacitance for the p-type heterojunction is essentially flat and then decreases sharply near +0.5 V, as the depth of the hole gas is essentially fixed at the Al_xGa_{1-x}As/GaAs interface. For both structures, the impedance measured was purely capacitive, except at the pinchoff voltage near +0.5 V, and no significant changes in the data were found over the frequency range 200–2000 Hz.

The capacitance data for the parabolic well were fit to a simple geometric formula used to describe the depletion edge moving through a uniformly doped semiconductor:

$$C(V) = [2(V - V_0)/e\epsilon p_{3D} + C^{-2}(V_0)]^{-1/2}, \quad (2)$$

where C is capacitance per unit area, V_0 is the voltage at which the well starts to deplete, and p_{3D} is the 3D hole density in the sample. The values $p_{3D} = 4.5 \times 10^{16} \text{ cm}^{-3}$, GaAs dielectric constant $\epsilon = 13$, and $V_0 = 0.05 \text{ V}$ were used to obtain the fit. Deviations of the capacitance from this fit are believed to be primarily due to nonuniformities in the hole density profile $p(z)$ caused by nonparabolicities in the well potential, with small effects due to subband depopulations [13]. From the capacitance values of $C(V_0)$ and $C(\sim 0.47 \text{ V})$ and assuming $\epsilon = 13$, we estimate the width of the hole gas to be $\sim 700 \text{ \AA}$, or an order of magnitude wider than the expected width of a 2D hole gas at the GaAs/Al_xGa_{1-x}As heterojunction.

Hall and magnetoresistance measurements at $T = 0.1 \text{ K}$ and zero gate bias are shown in fig. 4 for the sample cooled in the dark. Shubnikov-De Haas oscillations are observed in the magnetoresistance and quantized Hall plateaus are forming at the filling factors $\nu = 2, 3$, and 4.

In conclusion, we have extended the concept of modulation doped GaAs/Al_xGa_{1-x}As WPBW's to the case of holes. The inherent qual-

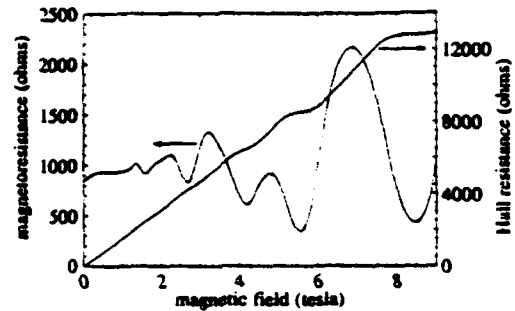


Fig. 4. Magnetoresistance and Hall resistance of the WPBW at $T = 0.1 \text{ K}$ for the magnetic field range 0–9 T.

ity of the wide hole gas in these structures should provide unprecedented access to low temperature electronic and optical properties of 3D hole gas systems; for example, the parameter r_s , which is the interparticle spacing in units of the Bohr radius and which is also the ratio of the unscreened Coulomb repulsion energy to the 3D Fermi energy for the holes, is much larger in the p-type than in the n-type WPBW's, because of the heavier hole mass. This suggests that collective phenomena (e.g. spin density wave or Wigner crystal formation) may be more accessible in the p-type WPBW's [14].

We thank J. English, H. Kroemer and M. Sundaram, for valuable discussions, J. Baskey and A. Rimberg for advice on the capacitance measurements, and E. Gwinn and her group for use of the dilution refrigerator. This work was supported by the Air Force Office of Scientific Research under grant AFOSR-91-0214.

References

- [1] B.I. Halperin, Japan. J. Appl. Phys. Suppl. 26-3 (1987) 1913.
- [2] A.J. Rimberg and R.M. Westervelt, Phys. Rev. B 40 (1989) 3970.
- [3] M. Sundaram, A.C. Gossard, J.H. English and R.M. Westervelt, Superlattices Microstruct. 4 (1988) 683.
- [4] J. Jo, M. Santos, M. Shayegan, Y.W. Suen, L.W. Engel and A.-M. Lanzillotto, Appl. Phys. Letters 57 (1990) 2130.
- [5] P.F. Hopkins, A.J. Rimberg, E.G. Gwinn, R.M. Westervelt, M. Sundaram and A.C. Gossard, Appl. Phys. Letters 57 (1990) 2823.

- [6] K. Karrai, X. Ying, H.D. Drew, M. Santos, M. Shayegan, S.-R.E. Yang and A.H. MacDonald, *Phys. Rev. Letters* 67 (1991) 3428.
- [7] R.C. Miller, A.C. Gossard, D.A. Kleinman and O. Muntenau, *Phys. Rev. B* 29 (1984) 3740.
- [8] M. Sundaram, A. Wixforth, R.S. Geels, A.C. Gossard and J.H. English, *J. Vacuum Sci. Technol. B* 9 (1991) 1524.
- [9] L. Brey, N.F. Johnson and J. Dempsey, *Phys. Rev. B* 42 (1990) 2886.
- [10] F. Ermanis and K. Wolfstirn, *J. Appl. Phys.* 37 (1966) 1963.
- [11] W. Walukiewicz, *J. Appl. Phys.* 59 (1986) 3577;
- E. Mendez and W. Wang, *Appl. Phys. Letters* 46 (1985) 1159.
- [12] W. Walukiewicz, P.F. Hopkins, M. Sundaram and A.C. Gossard, *Phys. Rev. B* 44 (1991) 10909.
- [13] A.J. Rimberg, S. Yang, J. Dempsey, J.H. Baskey, R.M. Westervelt, M. Sundaram and A.C. Gossard, *Appl. Phys. Letters*, submitted;
- A. Wixforth, M. Sundaram, K. Enslin, J.H. English, and A.C. Gossard, *Appl. Phys. Letters* 56 (1990) 29.
- [14] See, for example, M. Santos, Y.W. Suen, M. Shayegan, Y.P. Li, L.W. Engel and D.C. Tsui, *Phys. Rev. Letters* 68 (1992) 1188.

Onset of 3D Collective Response in Bimetallic Jellium Films: Surface and Mode Sensitivity

E. L. Yuh,¹ E. G. Gwinn,¹ P. R. Pinsukanjana,¹ W. L. Schaich,² P. F. Hopkins,³ and A. C. Gossard³

¹Physics Department, University of California at Santa Barbara, Santa Barbara, California 93106

²Physics Department, Indiana University, Bloomington, Indiana 47405

³Electrical and Computer Engineering and Materials Departments, University of California at Santa Barbara, Santa Barbara, California 93106

(Received 15 April 1993)

We use experimental and calculated excitation spectra of bimetallic jellium films with widths of up to a few Fermi wavelengths to explore how excitations of a thin metal with internal density gradients evolve into surface plasmons of a three-dimensional layer. We find that the onset of 3D plasmons is mode specific, and sensitive to surface potentials, even for small surface wave vectors.

PACS numbers: 73.20.Mf, 71.45.Gm, 72.30.+q

The excitations of thin electron gases with widths of up to a few Fermi wavelengths remain incompletely understood. In particular, little is known about how excitations of a thin gas evolve into the plasmons of a 3D metal slab as the gas widens and effects of level quantization diminish [1]. The sensitivity of excitations of thin gases to surface potentials has also been little explored, while for 3D metals the existence of multipole surface plasmons (MSP's) and the dispersion of ordinary surface plasmons (OSP's) are sensitive to surface barrier shapes [2]. Recent studies of alkali films on Al substrates relate to these questions: Submonolayer alkali overlayers clearly modify surface conditions [3]. However, because electrons pass freely from the thin overlayer into the 3D substrate, the role of quantum confinement is unclear.

AlGaAs heterostructures are ideally suited for addressing these questions, because they can realize arbitrarily thin, metallic films. Complex effects arising from crystallinity in elemental metals are also eliminated: The effective positive background in the heterostructure closely approximates the "jellium" limit. Here we study a bimetallic film in a special AlGaAs heterostructure, in which the thicknesses of both metal layers are on the order of a Fermi wavelength or less. The rich excitation spectra we see in experiment and calculations for this two-density system allow us to probe the effects of quantum confinement and nonlocality on the dynamic response of electron layers with quantum dimensions. We find a strikingly mode-dependent onset of OSP's characteristic of a 3D, bimetallic layer, arising from nonlocal effects. Further, we demonstrate that altering surface barrier shapes dramatically changes excitation spectra of thin, bimetallic gases.

Figures 1(a)–1(c) show the ground state of a bimetallic gas in an $\text{Al}_{x(z)}\text{Ga}_{1-x(z)}\text{As}$ heterostructure. The potential well in the conduction band edge, $E_c(z)$, confines the electrons [Fig. 1(a)]. E_c was tailored during molecular-beam-epitaxy growth [4] so that $E_c = n_1 z^2 (e^2 / 2\epsilon_T \epsilon_0)$ for $z < 0$ and $E_c = n_2 z^2 e^2 / 2\epsilon_T \epsilon_0$ for $z > 0$, where $\epsilon_r \approx 13$, and z is along the growth direction. By Poisson's equation, this well stimulates adjacent slabs of positive charge with densities $n_+ = n_1$ for $z < 0$ and $n_+ = n_2$ for

$z > 0$. Our heterostructure has $n_1 = 2.7 \times 10^{16} \text{ cm}^{-3}$ ($r_s = 2.1$) over a width of 1100 Å, and $n_2 = 1.35 \times 10^{16} \text{ cm}^{-3}$ ($r_s = 2.6$) over 1500 Å. Outside the well in Fig. 1(a), the Al fraction $x = 0.26$, giving E_c a 225 meV depth.

To screen n_+ , electrons (from Si donors set back 50 Å from the well edges) form a bimetallic layer with density $n_e \approx n_1$ for $z < 0$ and $n_e \approx n_2$ for $z > 0$. The solid line in Fig. 1(b) shows n_e , and Fig. 1(c) the corresponding single-electron potential U_{tot} , both found in the local-density-functional approximation [5]. The small width of the gas quantizes electron energies into subbands $E_n(q_{\parallel}) = \epsilon_n + \hbar^2 q_{\parallel}^2 / 2m^*$, where ϵ_n [horizontal lines in Fig. 1(c)] are eigenvalues of U_{tot} . Figure 1(b) shows that n_+ (dotted line) is wider than the electron gas, causing a quadratic rise in U_{tot} outside it [Fig. 1(c)]. Thus, the partly filled well in Fig. 1(c) realizes an effectively non-neutral bimetallic film. Figures 1(d)–1(f) illustrate a companion neutral film to be discussed below.

Our experimental spectra are for such non-neutral

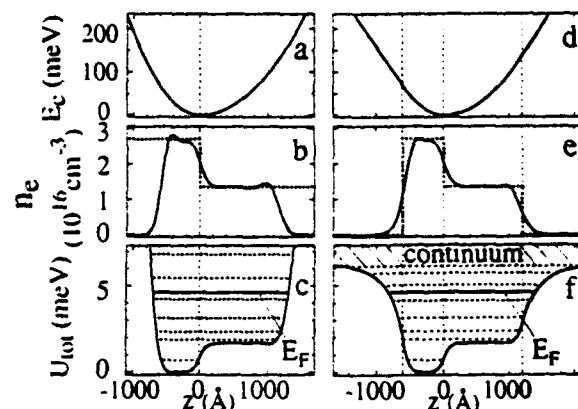


FIG. 1. Bimetallic electron gases: (a)–(c) non-neutral film, and (d)–(f) neutral counterpart. Vertical line at $z=0$ separates low- and high-density regions of n_+ . (a) Potential E_c due to n_+ ; (b) electron density $n_e(z)$ (solid line) and n_+ (dotted line); (c) one-electron potential $U_{\text{tot}}(z)$; dashed horizontal lines are ϵ_n . (b) and (c) are for well in (a) filled to $N_e = 3.2 \times 10^{11} \text{ cm}^{-2}$. (d)–(f) Neutral bimetallic film with the same N_e . Dotted, vertical lines mark outer surfaces of n_+ .

bimetallic films, with electron sheet densities $N_e \leq 2.1 \times 10^{11} \text{ cm}^{-2}$ in the well of Fig. 1(a). We study the dependence of the gas's transmission spectrum on its total width w_{tot} , for $w_{\text{tot}}=0$ to $\sim 1.5(\lambda_F)$ (three occupied subbands), where $(\lambda_F)=765 \text{ \AA}$ is the mean Fermi wavelength of 3D gases with densities n_1 and n_2 . To vary w_{tot} , a dc voltage bias is applied between a semitransparent NiCr gate on the sample's top surface, and an Ohmic contact to the gas [6]. Normally incident, far-infrared radiation couples to excitations of the gas with fixed $q_1=2\pi/\lambda_0$, via an Au grating of period $\lambda_0=2 \mu\text{m}$ that overlies the gate [7]. A Fourier transform spectrometer and He³-cooled detector collect transmission spectra $T(\omega)$ over 20–100 cm^{-1} . Displayed $-\Delta T/T$ spectra are normalized to the transmission T_0 of the empty well: $-\Delta T/T=(T_0-T)/T_0$. The sample was held at 1.5 K, well below $T_F \sim 40 \text{ K}$.

Figures 2(a)–2(d) show $-\Delta T/T$ spectra for increasing w_{tot} . The insets are $n_e(z)$ calculated using N_e and gas widths found from gate-to-gas capacitance measurement [6]. In Fig. 2(a), the gas lies entirely in the region of lower background density $n_+ = n_2$, about 600 \AA from the step in n_+ (at $z=0$), and a single resonance appears near 35 cm^{-1} in $-\Delta T/T$. This peak grows as the low-density gas widens [Fig. 2(b)]. When the edge of the gas crosses the step in n_+ and a second slab with higher density $n_+ \sim n_1$ begins to form, broad absorption appears near 50 cm^{-1} [Fig. 2(c)], and grows strong as the higher-density gas widens. In Fig. 2(d), the gas has well-defined regions of both high and low density, and has resonances peaked at 35 and 50 cm^{-1} . The feature near 50 cm^{-1} is broad, over twice the width of the 35 cm^{-1} peak.

We compare the data in Figs. 2(a)–2(d) to predictions of two models: a *local, macroscopic* "local optics" model, and the full random-phase approximation (RPA), a *microscopic, nonlocal* model that works well for alkali surfaces at small q_1 [2,3]. These models allow us to probe how quantum confinement and nonlocal response affect

the onset of collective excitations characteristic of a macroscopic, bimetallic ("3D") slab.

Local optics ascribes the Drude electric function to adjacent gases with densities n_1 and n_2 . The oscillating charge δn of OSP's is confined to sheets at surfaces of the gas. Applying electrostatic boundary conditions gives three OSP's, with frequencies Ω_{low} , Ω_{mid} , and Ω_{high} . Coupling of the exponentially decaying potentials from δn at the different surfaces causes the Ω 's to vary with slab widths w_1 and w_2 . For $q_1 w_1 \gg 1$ and $q_1 w_2 \gg 1$, surfaces decouple and δn localizes at the outer surface of the low- (high-) density gas for the Ω_{low} (Ω_{mid}) mode, while δn localizes at the interior interface for the Ω_{high} mode. In this limit, the Ω 's give OSP frequencies accurately at $q_1=0$, regardless of surface barrier shapes [8]. Because the q_1 dispersion of OSP modes should have little effect ($\sim 1\%$ shift [9]) for the small q_1 studied here, $q_1/k_F \sim 0.04$, we expect OSP frequencies of the bimetallic gas to converge toward the Ω 's as the gas widens.

Figure 2 compares data [Figs. 2(a)–2(d)] to RPA absorption spectra $A(q_1, \omega)$ [Figs. 2(e)–2(h)] calculated [10] for an external potential that approximates the effect of the grating coupler [11]. Vertical lines in Fig. 2 show Ω_{mid} and Ω_{high} (Ω_{low} is below our range of observation). The solid lines in Figs. 2(e)–2(h) are $A(q_1, \omega)$ calculated for a collision damping time $\tau=2$ psec, comparable to the sample's measured momentum relaxation time; dotted lines are for $\tau=6$ psec. The $A(q_1, \omega)$ with $\tau=2$ psec resemble the experimental $-\Delta T/T$ spectra in Figs. 2(a)–2(d): Prominent resonances in both data and $A(q_1, \omega)$ lie close to Ω_{mid} and Ω_{high} . However, the $\tau=6$ psec calculations reveal that the broad structure in the data near 50 cm^{-1} is *not* a single, well-defined OSP, but rather a cluster of resonances spread by collision damping into a single feature. This accounts qualitatively for the large width of the peak at 50 cm^{-1} in the data, although other damping mechanisms (e.g., due to width-dependent layer roughness) may also contribute.

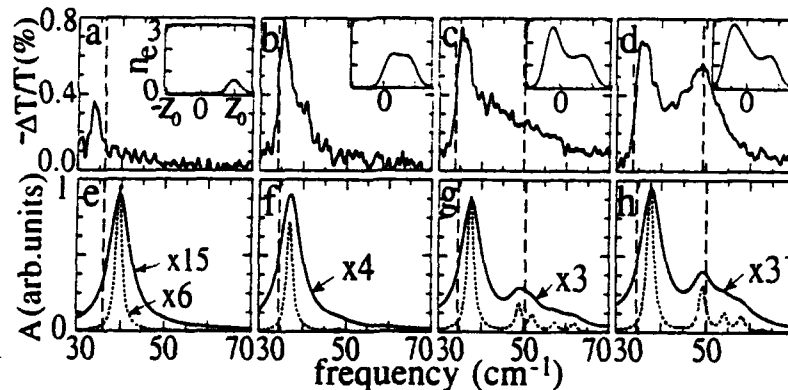


FIG. 2. Dynamic response of effectively non-neutral, bimetallic films. Vertical lines show Ω 's. (a)–(d) Experimental 1.5 K transmission spectra. Insets show calculated $n_e(z)$ based on measured gate-to-gas capacitance ($z_0=600 \text{ \AA}$; n_e is in units of $10^{16} \text{ electrons/cm}^3$). (e)–(h) $A(q_1, \omega)$ at $T=0$, for $\tau=2$ psec (solid line), and for $\tau=6$ psec (dashed line). (a),(e) $N_e=1.7 \times 10^{10} \text{ cm}^{-2}$. (b),(f) $N_e=9.3 \times 10^{10} \text{ cm}^{-2}$. (c),(g) $N_e=1.7 \times 10^{11} \text{ cm}^{-2}$. (d),(h) $N_e=2.1 \times 10^{11} \text{ cm}^{-2}$.

To understand how the resonances in Fig. 2 relate to OSP's characteristic of a 3D gas, we extend our calculations to gas widths greater than obtained experimentally. Figure 3(a) shows dependences of RPA and local optics frequencies on w_{tot} (frequencies are all normalized to ω_1 , the bulk plasma frequency of the higher-density gas; w_{tot} is normalized to $\langle\lambda_F\rangle$, and for the largest w_{tot} shown, $q_1 w_{tot} = 1.9$). For simplicity, in Fig. 3 sheet densities of the adjacent gases are kept equal, so that $w_{tot} = 3N_e/4n_2$. Solid lines in Fig. 3(a) show the Ω 's; \times 's denote resonances with $> 4.3\%$ of the spectral weight, and \circ 's, resonances with weight between 1.8% and 4.3% . Figures 3(b)–3(d) are δn (shaded) [12] and n_e (dashed lines) for resonances marked in Fig. 3(a). Figures 3(e)–3(g) show example $A(q_1, \omega)$ spectra for three values of e_{tot} (dashed lines locate the Ω 's).

Figure 3(a) shows that the approach of RPA resonance frequencies to the Ω 's is *mode dependent*. A resonance lies at Ω_{low} for all w_{tot} . In contrast, resonance frequencies converge to Ω_{mid} and Ω_{high} gradually as w_{tot} increases, in a distinct manner for each mode. For w_{tot} greater than roughly $\langle\lambda_F\rangle$, RPA frequencies approach Ω_{mid} smoothly, while resonances near Ω_{high} are grouped into branches that cut through Ω_{high} at discrete values of w_{tot} . Deviation from the Ω 's is produced by quantum confinement and nonlocal response. Figure 3(a) shows

that the frequency of the RPA resonance at Ω_{low} —an *intrasubband* “2D” plasmon for small w_{tot} —is insensitive to these effects [13]. Also, δn for this mode resembles its local optics counterpart for all w_{tot} ; e.g., for $w_{tot} = 8\langle\lambda_F\rangle$, Fig. 3(d) shows δn localizing at the outer surface of the low-density gas.

Unlike Ω_{low} , resonances near Ω_{mid} and Ω_{high} evolve from *intersubband* excitations of the gas, and for small w_{tot} are sensitive to changes in subband occupation. For w_{tot} less than roughly $1.5\langle\lambda_F\rangle$, the scattered resonance frequencies in Fig. 3(a) reflect the addition of new intersubband absorption channels. (Three subbands are occupied at $w_{tot} = 1.5\langle\lambda_F\rangle$.) For w_{tot} above $\sim 1.5\langle\lambda_F\rangle$, the smooth approach of RPA frequencies toward Ω_{mid} is unaffected by changes in subband occupation, indicating that the resonances have plasmon character. The smoothly decaying offset from Ω_{mid} reflects the diminishing influence of nonlocality as OSP's at different faces decouple. For $q_1 w_{tot} > 1$, the δn approach the expected local optics form, eventually localizing to the outer surface of the denser gas, as Fig. 3(c) shows.

The more complex behavior of resonance frequencies near Ω_{high} results from the two-density form of n_e and nonlocal dispersion. The bulk plasmon (BP) frequency in an infinite electron gas increases as $\omega_2(q_\perp) = \omega_2(0)[1 + \beta^2 q_\perp^2]$, where the dispersion coefficient β would be zero in a *local* response model, and q_\perp is along z . In a bimetallic gas, Ω_{high} is greater than ω_2 (the BP frequency of the lower-density gas), so that the OSP is degenerate with a *bulk* plasmon in the lower density gas, for some q_\perp . In adjacent, semi-infinite gases, coupling between density oscillations at the interior interface and throughout the lower-density gas has been shown to produce plasmons with mixed bulk and surface character, with frequency at $q_\perp = 0$ given by the large-width limit of Ω_{high} [8].

Here the low-density gas has finite width, so one expects a standing-wave condition $q_\perp \sim n\pi/w_2$ to allow discrete BP frequencies $\omega_2(n) = \omega_2(0)[1 + (\beta^2 \pi^2) n^2/w_2^2]$, where w_2 is the width of the lower-density gas. Thus, no BP is degenerate with Ω_{high} for general w_2 . However, Fig. 3(a) and $A(q_1, \omega)$ spectra [Figs. 3(f) and 3(g)] show that a *near* degeneracy with Ω_{high} is sufficient to greatly strengthen modes with bulk character in the lower-density gas: Resonances on the branches in Fig. 3(a) strengthen dramatically as they approach Ω_{high} . Their δn have form consistent with mixed surface-bulk character, as the example in Fig. 3(b) shows. Within each branch, the number of nodes in δn across the low-density gas is constant as the gas widens, while at fixed w_{tot} , the number of nodes changes by 1 between branches. This behavior in δn , the falling frequency along each branch, and the decrease in the branch spacing with increasing gas width, are all as expected for modes with BP standing-wave character in the low-density gas. The δn lose this regular standing-wave form as their frequency moves away from Ω_{high} , indicating that the resonance character

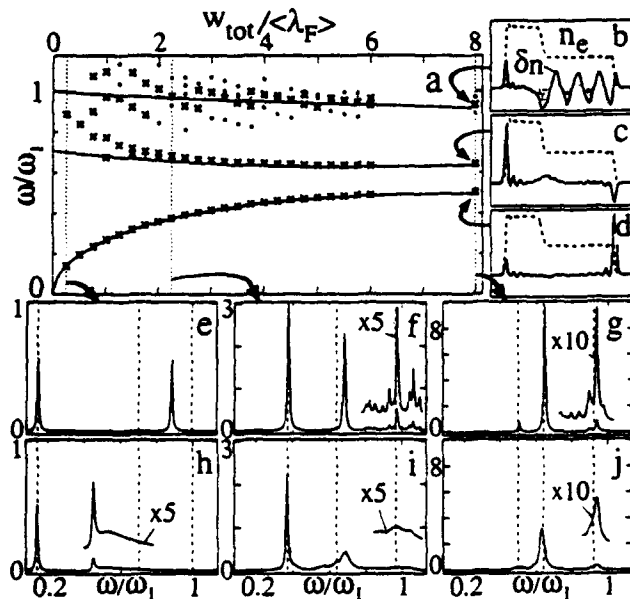


FIG. 3. Mode and surface sensitivity of the onset of macroscopic dynamic response. (a) RPA and local optics resonance frequencies vs w_{tot} , for q_1 ($3.14 \times 10^4 \text{ cm}^{-1}$) used in experiment. Frequencies are normalized to ω_1 ; width, to $\langle\lambda_F\rangle$. RPA resonances are \circ and \times ($> 1.8\%$ and $> 4.3\%$ of spectral weight, respectively). Solid lines are local optics Ω 's. (b)–(d) RPA δn (snapshot of the oscillating charge in a given mode) and n_e (dashed line) for resonances in (a) marked by arrows. (e)–(g) Non-neutral and (h)–(j) neutral RPA spectra for w_{tot} marked by vertical dotted lines in (a). Vertical dashed lines locate Ω_{low} , Ω_{mid} , and Ω_{high} .

is evolving from plasmon- to single-particle-like.

Thus, as the film widens, modes with clear plasmon character evolve from intersubband excitations at the local optics frequencies expected for a 3D plasma. Convergence of excitation frequencies towards Ω_{mid} for $w_{\text{tot}} = 1 - 2(\lambda_F)$ indicates that level quantization ceases to be important for surprisingly small film widths. The more complex behavior near Ω_{high} is primarily due to a coupling of surface and bulklike density oscillations allowed by nonlocal response in this two-density system. Hydrodynamic calculations [14], which are nonlocal but do not include level quantization, support this conclusion: For layer widths above $\sim 1.5(\lambda_F)$, frequencies of RPA and hydrodynamic modes near Ω_{high} are in good agreement.

We now show that the unusual, "non-neutral" surface barriers for the gases discussed above strongly affect our results. Figures 1(d)–1(f) compare a *neutral* bimetallic jellium, the appropriate model for uncharged metal films [2,3], with the non-neutral case. The sheet density of electrons $N_e = \int n_e(z)dz$ for the neutral film is the same as in Figs. 1(b) and 1(c), but termination of n_+ at the dotted vertical lines in Fig. 1(e) makes $N_+ = \int n_+(z)dz = N_e$. This neutrality forces U_{tot} to soften outside the gas and eventually become flat [Fig. 1(f)]. Thus, for the neutral film the ϵ_n above E_F are closely spaced, forming a continuum at high energies. E_F and the occupied ϵ_n are nearly identical in both neutral and non-neutral cases; but the *unoccupied* ϵ_n are quite different, due to the different surface barriers.

The $A(q_1, \omega)$ calculated for the *neutral* film in Figs. 3(h)–3(j) show that surface conditions strongly affect absorption spectra: All features above Ω_{low} are broader than for the non-neutral film [Figs. 3(e)–3(g)]. This is due to the large number of transitions from occupied states to the neutral film's empty continuum. In the non-neutral film, degeneracy of plasmon and surface plasmon excitations is improbable at the small q_1 studied here, due to the discreteness of the ϵ_n for all energies. Thus, Landau damping is suppressed in the non-neutral system [linewidths in Figs. 3(e)–3(g) are primarily due to the $\tau = 20$ psec collision time], but plasmons in the neutral film are Landau damped.

Sensitivity of $A(q_1, \omega)$ to surface conditions is most dramatic for thin layers [Figs. 3(e) and 3(h) and 3(f) and 3(i)]. For larger w_{tot} [Figs. 3(g) and 3(j)], OSP frequencies approach the local optics Ω 's in both neutral and non-neutral films. This is expected for a macroscopic film, because OSP frequencies are rather insensitive to surface conditions at small q_1 . However, Figs. 3(f) and 3(i) and 3(g) and 3(j) show that neutral surface barriers heavily blur the multiple resonances near Ω_{high} in the non-neutral film. Studies of alkali films on Al substrates (in which electrons see a *neutral* surface barrier) [3] have not discussed plasmons near Ω_{high} . Because the density contrast in the alkali/Al system is large ($n_1/n_2 \sim 7$, compared to $n_1/n_2 = 2$ here), these were probably suppressed by Landau damping, as discussed in [8]. The steep sur-

face barriers in our non-neutral system also eliminate [15] MSP's, while δn for some weak resonances of the neutral film have multipole character.

General implications of this work are the following: (1) The plasmons characteristic of a macroscopic metal slab emerge in a strongly mode-dependent manner from excitations of thin electron gases; (2) in thin films with internal density gradients, non-neutral surface barriers enhance plasmons with mixed surface and bulk character; and (3) absorption spectra in thin films are particularly sensitive to surface barrier shapes: Non-neutral surface barriers dramatically narrow absorption features. This narrowing may also be observable in positively charged, elemental metal films or clusters, in which the charging would force the continuum to higher energies.

We thank N. G. Asmar, J. F. Dobson, and W. Kohn for helpful discussions. This work was supported primarily by NSF DMR90-02491 and AFOSR-91-0214. Clean room use was partly supported by NSF DMR91-20007, and FTIR use in part by ONR N00014-92-5-1452. W.L.S. acknowledges support from NSF DMR89-03851.

- [1] W. L. Schaich and A. H. MacDonald, *Solid State Commun.* **83**, 779 (1992); W. H. Backes *et al.*, *Phys. Rev. B* **45**, 8437 (1992).
- [2] K. D. Tsuei, E. W. Plummer, and P. J. Feibelman, *Phys. Rev. Lett.* **63**, 2256 (1989); K. D. Tsuei *et al.*, *Phys. Rev. Lett.* **64**, 44 (1990).
- [3] J. A. Gaspar *et al.*, *Phys. Rev. Lett.* **67**, 2854 (1991); A. Liebsch, *Phys. Rev. Lett.* **67**, 2858 (1991).
- [4] M. Sundaram *et al.*, *Superlattices Microstruct.* **4**, 683 (1988).
- [5] N. G. Asmar and E. G. Gwinn, *Phys. Rev. B* **46**, 4752 (1992).
- [6] E. L. Yuh *et al.* (to be published).
- [7] S. J. Allen, Jr., D. C. Tsui, and R. A. Logan, *Phys. Rev. Lett.* **38**, 980 (1977).
- [8] P. J. Feibelman, *Phys. Rev. B* **3**, 2974 (1971).
- [9] The OSP dispersion measured [2] at small q_1 for alkalis with similar r_s gives only a $\sim 1\%$ shift in the OSP frequency for $q_1/k_F = 0.04$.
- [10] A. G. Eguluz, *Phys. Rev. Lett.* **51**, 1907 (1983); B. N. J. Persson and E. Zaremba, *Phys. Rev. B* **31**, 1863 (1985).
- [11] $A(q_1, \omega)$ is calculated for $\phi_{\text{ext}} \propto \exp[i(q_1 x - \omega t) - q_1 z]$, which approximates the effect of the grating coupler, as $A(q_1, \omega) = -\omega \text{Im}[\int dz e^{-|q_1 z|} \delta n(z; q_1, \omega)]$ [10]. The induced charge $\delta n(z; q_1, \omega)$ is $\int dz' \chi(z, z'; q_1, \omega) \phi_{\text{ext}}(z'; q_1, \omega)$, where χ is found from the LDA ground state using standard expressions [10]. Calculated $-\Delta T/T$ spectra using a detailed model of the grating are very similar to $A(q_1, \omega)$: For the 30–70 cm^{-1} range shown here, there is little change in relative peak strengths and a small, < 1 cm^{-1} frequency shift.
- [12] J. F. Dobson, *Phys. Rev. B* **46**, 10163 (1992).
- [13] J. F. Dobson (to be published) has shown that for $q_1 w_{\text{tot}} \ll 1$, a resonance with frequency equal to Ω_{low} exists for any electron gas slab, regardless of its $n_e(z)$.
- [14] W. L. Schaich *et al.* (to be published).
- [15] P. R. Pinsukanjana *et al.*, *Phys. Rev. B* **46**, 7284 (1992).

Surface collective modes of non-neutral jellium

P. R. Pinsukanjana, E. G. Gwinn, John F. Dobson,* E. L. Yuh, and N. G. Asmar
 Physics Department, University of California, Santa Barbara, California 93106

M. Sundaram and A. C. Gossard

Department of Electrical and Computer Engineering, University of California, Santa Barbara, California 93106

(Received 11 May 1992)

We report studies of the surface plasmon modes of a layer of electron gas that is embedded in a wider, effective positive background, provided by a parabolic $\text{Al}_x\text{Ga}_{1-x}\text{As}$ well. Although conditions in the interior of the electron gas are nearly identical to those in a neutral jellium slab, the more abrupt electronic surfaces in the parabolic well produce a qualitatively different surface plasmon spectrum.

Electron gases in $\text{Al}_x\text{Ga}_{1-x}\text{As}$ heterostructure wells provide experimental access to aspects of metal surface physics that are inaccessible in conventional metals. The principal advantages of the semiconductor system are as follows: the near-surface density profile of the electron gas can be tailored; the effective positive background can be chosen to be smooth; and the thickness of the electron gas is continuously variable from zero to a few Fermi wavelengths, so that the interesting crossover regime between two and three dimensions can be probed.

By their nature, the surface collective modes of an electron gas are sensitive to surface electronic structure.^{1,2} We investigate surface plasmons on an electron gas that is embedded in a wider, effective positive background, provided by a parabolically graded, $\text{Al}_x\text{Ga}_{1-x}\text{As}$ well.^{3,4} The unusual nature of the surfaces in this non-neutral jellium produce a qualitatively different surface plasmon spectrum from that of a neutral jellium slab.³ Although the optical, magneto-optical, and transport properties⁵⁻¹² of parabolic $\text{Al}_x\text{Ga}_{1-x}\text{As}$ wells have been studied previously, this work presents an experimental study to address surface-related phenomena in such structures.

In $\text{Al}_x\text{Ga}_{1-x}\text{As}$ heterostructure wells, varying the Al fraction, x , along the growth direction, z , varies the conduction-band edge, E_c , to realize a potential well for electrons. The well curvature $K = d^2E_c/dz^2$ determines an effective background charge density n_b , which by Poisson's equation is $n_b(z) = eK(z)/e^2$.⁷ Remote donors, which lie in planes that are set back from either side of the well, provide conduction electrons. The nearly uniform, static fields of the planar sheets of ionized donors cancel in the well region between the donor planes, and should have little effect on the dynamic response of the electron gas.¹³

Neutral jellium is realized by adding a sheet density of electrons $N_e = n_b w_b$ to the potential well produced by a slab of positive charge with density n_b and width w_b . The electrostatic potential due to the positive slab is parabolic within the slab, and linear outside, as sketched by the dotted line in Fig. 1(a). The vertical, dashed lines show the slab boundaries, and the solid line shows a parabolic potential, for comparison. Non-neutral jellium is realized when $N_e < n_b w_b$: The layer of electron gas is then embedded in a wider positive background. In both the neutral and non-neutral cases, the electron gas forms a layer with density $n_e \approx n_b$, over a width $w_e \approx w_b$. The nominal width

of the electron gas $w_e = N_e/n_b$. For the parabolic well studied here, the effective positive background extends at least four Thomas-Fermi screening lengths on either side of the electron layer, so the electron gas is well embedded.

In the interior of the electron gas, the parabolic well and neutral jellium are similar: The spacing of occupied single-electron levels are the same to within a fraction of a percent,⁴ and the electron gas is nearly uniform. For temperatures below the Fermi temperature $T_F \sim 50$ K, the ratio of the characteristic potential and kinetic energies is similar to that in simple metals, although the electronic density in the semiconductor structure is ~ 6 orders of magnitude smaller. For the parabolic well studied here, $r_s = 2.07$, where $r_s = r_0/a^*$, $(4\pi r_0^3/3)n_b = 1$, and a^* is the Bohr radius in GaAs.

The conditions at the surfaces of the electron gas in a parabolic well are different from those at neutral jellium surfaces. Figure 1(b) plots the self-consistent potential $V(z)$ that results from adding a sheet density of electrons $N_e = n_b w_b$ to the confining potentials E_c shown in Fig. 1(a), for $n_b = 2.75 \times 10^{16} \text{ cm}^{-3}$ and $w_b = 880 \text{ \AA}$. The extension of the positive background beyond the electron gas

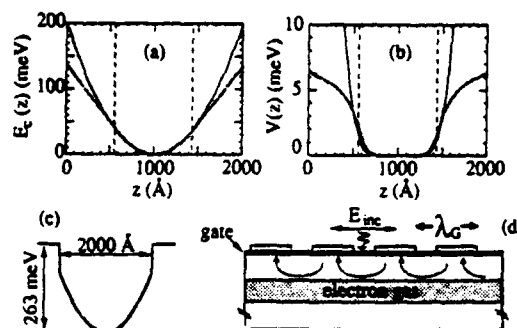


FIG. 1. (a) The dotted line shows electrostatic potential due to a uniform slab of positive charge with width $w_b = 880 \text{ \AA}$ and density $n_b = 2.75 \times 10^{16} \text{ cm}^{-3}$. Dashed, vertical lines show boundaries of positive slab. The solid line shows parabolic potential for $n_b = 2.75 \times 10^{16} \text{ cm}^{-3}$. (b) Total, self-consistent potential $V(z)$ for the wells in (a), for a sheet density of electrons $N_e = n_b w_b$. (c) Conduction-band edge $E_c(z)$ for PB31 (empty). Donor planes (not shown) are set back from the well edges by 200 Å. (d) Grating coupler; here $q_G = 1.60 \times 10^4 \text{ cm}^{-1}$. Vectors sketch fringing field.

in the parabolic well produces a steeper surface potential (solid line in Fig. 1(b)), and a corresponding steeper decay in the density at the surfaces of the electron gas. The different surface conditions shown in Fig. 1(b) have a marked effect on the surface plasmon spectrum.

Extensive investigations of collective electronic excitations in heterojunctions, square wells, and superlattices of square wells have been carried out.¹⁴ All of these structures realize electron gases with density profiles that are sharply peaked in one or more sheetlike layers, and have different plasmon modes from the thick, nearly uniform layer of electron gas explored here.

We have studied a sample from a high-quality, molecular-beam epitaxy (MBE) grown parabolic well structure. Measurements of the Al flux during programmed growth sequences indicate that the well follows the design parabola closely, and extensive magnetotransport studies¹² show that the measured single-electron subband spacings agree with self-consistent calculations at the 3% level. Figure 1(c) sketches the conduction-band edge, E_c , for the empty well. The Al fraction, x , increases quadratically from $x=0$ at the well center to $x=0.2$ at the well edges at $z=2510$ Å and $z=4510$ Å, where z is measured from the sample surface. At the edges of the well, x steps up to 0.3. The design density¹⁵ is $n_b=2.5 \times 10^{16}$ cm⁻³, and corresponds to $\omega_p=50$ cm⁻¹.

We study the dependence of the surface plasmon spectrum on the continuously variable width, w_e , of the electron layer. A negative dc voltage bias V_G applied between a semitransparent gate that covers the sample surface, and an Ohmic contact to the electron gas, reduces w_e by moving the top edge of the electron gas away from the gate. We obtain the sheet density $N_e(V_G)$ and the width $w_e=N_e/n_b$ from the integral of $C(V_G)$, the measured capacitance between the gate and the electron gas. Magnetotransport measurements give $N_e(V_G)$ in agreement with that obtained from the capacitance. We also obtain the separation between the gate and the top surface of the electron gas, from the capacitance.¹⁶

To excite surface plasmons, we used a 3.92- μ m period grating of Au bars to spatially modulate normally incident, far-infrared radiation.¹⁷ Figure 1(d) sketches the fringing fields in the near field of the grating, which excite surface plasmons with wave vectors $q_1=nq_G$, where $q_G=2\pi/\lambda_G$, λ_G is the grating period, and $n=1, 2, \dots$.¹⁷ A 300-mK composite Si bolometer and a Bomem DAC.002 Fourier-transform spectrometer, set at nominal 0.5 cm⁻¹ resolution, were used to collect far-infrared transmission data. The 2.90-mm diam sample was held at 1.5 K for all measurements.

Transmission spectra display both low- and high-frequency resonances, which arise from the coupling of charge fluctuations on opposite faces of the electron layer. Figure 2(a) shows the normalized transmission, $-\Delta T/T=[T_0-T(w_e)]/T_0$, where T_0 is the transmission through the empty well. The solid line corresponds to $w_e=880$ Å, and the dotted line to $w_e=580$ Å. As discussed below, we identify the resonances below 20 cm⁻¹ and near 50 cm⁻¹ as low and high frequency, coupled surface plasmons, ω_- and ω_+ . Because we probe $q_1 \neq 0$ only, we cannot measure $\omega_p^2=n_b e^2/\epsilon m^*$ directly, but estimate that ω_p lies in the

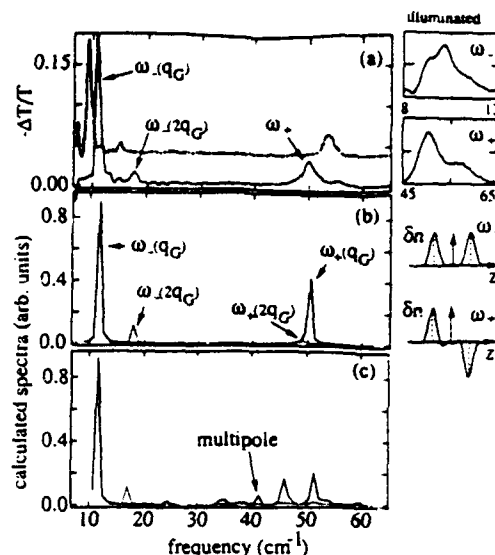


FIG. 2. (a) Solid and dotted lines show $-\Delta T/T$ prior to illumination for $w_e=880$ Å and $w_e=580$ Å (baseline offset), respectively. Insets to the right show illumination-induced splitting of the $\omega_-(q_G)$ resonance (top) and of the ω_+ resonance (bottom), for $w_e=500$ Å. (b) Calculated absorption spectrum for a parabolic well with $n_b=2.75 \times 10^{16}$ cm⁻³, and $w_e=880$ Å for $q_1=q_G=1.6 \times 10^4$ cm⁻¹ (solid line) and for $q_1=2q_G=3.2 \times 10^4$ cm⁻¹ (dotted line). Insets to the right show the calculated, fluctuating surface plasmon charge $\delta n(z, q_1=q_G)$ for the ω_- and ω_+ resonances. (c) Calculated absorption spectrum for a neutral jellium slab with $n_b=2.75 \times 10^{16}$ cm⁻³, and $w_e=880$ Å.

range 51–54 cm⁻¹, based on the observed range of ω_+ with w_e .

For $q_1=0$, the ω_+ resonance becomes the parabolic well sloshing resonance discussed in Ref. 10. Because the confining potential E_c is harmonic, the frequency of the sloshing mode is independent of w_e , and is equal to ω_p .¹⁰ Resonances in parabolic wells at $\omega \approx \omega_p$ have been observed by other groups, and identified as the sloshing resonance.^{5,6} Surface plasmons are a more general type of collective mode, which have frequencies that do depend on w_e .

Surface plasmon spectra for both neutral and non-neutral jellium layers have been calculated in the time-dependent, local-density approximation (TDLDA).³ To simulate the grating coupler, an external potential $\delta\phi_{ext}=\exp(iq_1x-\omega t)\exp(q_1z)$ was used, where q_1 is the wave vector of the surface plasmon, and the electron gas lies at $z < 0$. Surface plasmon resonances appear as peaks in $\text{Im}[M(q_1, \omega)]$, where

$$M(q_1, \omega) = \left\{ \int_{-\infty}^{\infty} dz e^{iq_1z} \delta n(z, q_1, \omega) \right\},$$

and $\delta n(z, q_1, \omega)$ is the induced charge density. The calculations assume $m^*/m_0=0.069$ and $\epsilon/\epsilon_0=13$; a constant $\text{Im}(\omega)=1/\tau$, with $\omega_p\tau=300$; and include an image plane above the electron gas, which mimics the effects of the metallic gate and grating on the surface of the sample.

Figures 2(b) and 2(c) show the absorption spectrum $\omega \text{Im}[M(q_1, \omega)]$ for the parabolic well and for the neutral slab, respectively, for $n_b=2.75 \times 10^{16}$ cm⁻³ ($\omega_p=52.2$

cm^{-1}) and $w_e = 880 \text{ \AA}$. These parameters correspond to the experimental spectrum shown as a solid line in Fig. 2(a). The relative amplitudes of the calculated spectra for $q_1 = q_G$ (solid lines) and $q_1 = 2q_G$ (dashed lines) have been scaled to account for the coupling efficiency of the grating to the low-frequency resonance, in the limit that the electron gas becomes a two-dimensional sheet.¹⁷ The unperturbed electron gas is calculated to occupy three subbands of the self-consistent potential $V(z)$ for $w_e = 880 \text{ \AA}$.

The form of the calculated parabolic well spectrum is simple: only two resonances appear, for fixed q_1 . As shown in the inset to the right of Fig. 2(b), the calculated, fluctuating charge of the surface plasmon, $\delta n(z, \omega_{\pm})$, is localized near the surfaces of the electron layer. In contrast to the parabolic well, the calculated spectrum for the neutral jellium slab has a large number of weak resonances. The resonance near $0.8\omega_p$ ($\sim 42 \text{ cm}^{-1}$) has been identified³ as the thin-layer analog of the multipole surface plasmon. This resonance becomes much stronger for lower electron densities and larger q_1 .

The qualitative differences between the spectra for the parabolic well and the neutral slab are due to the more abrupt electronic surfaces of the embedded electron gas. The multipole mode, for example, occurs only at electronic surfaces that are sufficiently diffuse.¹⁸ This association of the simple spectrum for the parabolic well with its steep electronic surfaces is corroborated by calculated results for electron gases with surfaces that are steeper than in the parabolic well.³ For example, if the central parabolic region occupied by the electron gas is bounded with quartic, rather than by quadratic, extensions, the absorption

$$\omega_{\pm}^2 = \frac{2\omega_p^2}{2 + (\epsilon_1/\epsilon_2)(\coth(q_1 w_e)[1 + \coth(q_1 d)] \pm \{\coth^2(q_1 w_e)[1 + \coth(q_1 d)]^2 - 4\}^{1/2})} \quad (1)$$

In the limit $d \rightarrow \infty$, for $\epsilon_1 = \epsilon_2$ Eq. (1) reduces to $\omega_{\pm}^2 = \frac{1}{2}\omega_p^2[1 \mp \exp(-q_1 w_e)]$, as is appropriate for a symmetric slab.¹⁹ In the limit $w_e \rightarrow 0$, Eq. (1) becomes $\omega_{+} = \omega_p$ and

$$\omega_{-}^2 = \frac{\omega_p^2(q_1 w_e)}{(\epsilon_1/\epsilon_2)[1 + \coth(q_1 d)]} = \frac{e^2 q_1 N_e}{\epsilon_1 m^* [1 + \coth(q_1 d)]} \quad (2)$$

the well-known dispersion relation for the two-dimensional plasmon on an electron sheet of vanishing thickness.¹⁷ For the range of q_1 and w_e used in the experiment, the resonance frequencies calculated for the embedded electron gas in the TDLDA agree with Eq. (1), which becomes inaccurate for larger q_1 and w_e than studied here. In contrast, for the neutral jellium slab, the local optics model fails qualitatively, even for small $q_1 w_e$.

Figure 3(a) shows ω_{-} from Eq. (1) (solid lines) and Eq. (2) (dashed lines), for $q_1 = q_G$ (lower curves), and for $q_1 = 2q_G$ (upper curves). Figure 3(b) shows $\omega_{+}(q_G)$ from Eq. (1). We have used $n_b = 2.75 \times 10^{16} \text{ cm}^{-3}$, $\epsilon_1 = 12.5\epsilon_0$ in the dielectric layers surrounding the electron gas, and $\epsilon_2 = 13.1\epsilon_0$ and $m^* = 0.069m_0$, which are the average values over the part of the well occupied by the electron gas for $w_e = 880 \text{ \AA}$. The observed frequencies deviate

spectrum still shows only two resonances, with resonance frequencies ω_{+} and ω_{-} that are both shifted slightly upwards from those of the parabolic well.³

The experimental transmission spectra for the parabolic well, shown in Fig. 2(a), are similar in form to the calculated spectra in Fig. 2(b). The two low-frequency resonances in the data can be identified from their dependence on w_e as $\omega_{-}(q_G)$, and $\omega_{-}(2q_G)$. The strong resonance near 50 cm^{-1} is the antisymmetric, coupled surface plasmon, ω_{+} . In the spectrum for $w_e = 880 \text{ \AA}$, an additional, small peak appears above the main ω_{+} resonance. This feature is not apparent in spectra for smaller w_e , and is discussed below. Because the damping processes that occur in the physical system are more complex than in the calculations, we do not expect agreement in the resonance strengths for the experimental and calculated spectra.

Figure 3(a) shows the dependence of the experimental ω_{-} on w_e . The vertical lines indicate subband occupation: Self-consistent calculations for $n_b = 2.75 \times 10^{16} \text{ cm}^{-3}$ show that the second subband begins to fill at $w_e = 360 \text{ \AA}$, and the third subband at $w_e = 690 \text{ \AA}$. The dependence of the experimental ω_{+} on w_e is shown in Fig. 3(b). No sharp features associated with subband filling are apparent in the data, for either resonance, in agreement with TDLDA calculations.

The resonance frequencies can also be estimated from a nonretarded, local optics model, in which the dielectric function of the electron gas is taken to be $\epsilon = \epsilon_2(1 - \omega_p^2/\omega^2)$ over its width w_e . Dielectrics with $\epsilon = \epsilon_1$ separate the electron gas from the gate, which is treated as a perfect conductor, and bound the back side of the electron gas. We obtain

from the calculated values by as much as 6%. Possible origins for this discrepancy include variation in the curvature across the well, the abrupt step in the confining potential at its extreme edges [see Fig. 1(c)], and the spatial variation in m^* and ϵ .

Large-scale changes in the curvature of the part of the well occupied by the electron gas should produce extra resonances in the transmission spectra, which are not observed for $w_e \lesssim 880 \text{ \AA}$. Fluctuations in the curvature may be responsible for the larger linewidth of the ω_{+} mode relative to the ω_{-} mode.

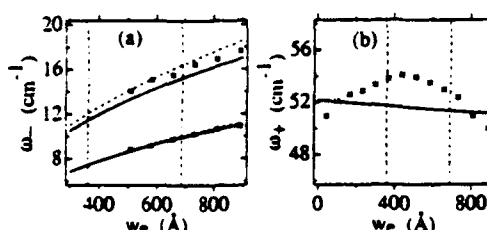


FIG. 3. (a) Dependence of ω_{-} on w_e . The solid lines show ω_{-} calculated from Eq. (1). The horizontal dashed lines show the 2D limit, Eq. (2). (b) Dependence of ω_{+} on w_e . The solid line is $\omega_{+}(q_1 = q_G)$ from Eq. (1).

We (parabo- the elec- the gas- the Th- with n - part of- meV, c- creased- ω_{+} per- This m- the ele- confin- show - nances- The- produc- electro- the sur- electro- may be- gas, w- spectiv- The- perime- observ- lation - ple fro- gold g- weakly

*Preser- Univ- 1P. J. F- 2K. D. Lett- 3J. F. I- 4N. G. 5K. Ka- *ibid.* 6A. W- 7M. Si- E. G- 8T. Sa- Jo, - 9A. J. (198- 10L. B- 106- 11M. (19- 12P. F- 13Une- abor- unif- the- ioni- cau- 14For

We estimate that the step in $E_c(z)$ at the edge of the parabolic well occurs ~ 400 Å from the nearest surface of the electron gas, for $\omega_e = 880$ Å, if the density profile of the gas is idealized as rectangular. This is roughly 4 times the Thomas-Fermi screening length for an electron gas with $n_e = 2.75 \times 10^{16} \text{ cm}^{-3}$. The depth of the parabolic part of the well above the Fermi energy is at least ~ 100 meV, or $\sim 16\hbar\omega_p$, for the data shown here. As ω_e is increased, a weak resonance first appears above the main ω_+ peak in the spectrum for $\omega_e = 880$ Å [see Fig. 2(a)]. This may indicate the onset of the interaction of the tail of the electron density with the step at the edge of the confining potential. For larger ω_e , transmission spectra show a series of several, substantially broadened resonances near 50 cm^{-1} .

The dependence of ϵ and m^* on the local Al fraction²⁰ produces $\sim 2\%$ variation in the average of ϵm^* over the electron layer with ω_e . Because the fluctuating charge of the surface plasmon is concentrated at the edges of the electron gas, the variation of ϵ and m^* at the surfaces may be more relevant. At the top surface on the electron gas, we estimate that m^* and ϵ vary by 9% and 2%, respectively, as the well is depleted.

The effects of static, spatial modulation of ω_e on the experimental spectra are consistent with identification of the observed resonances as surface plasmons. Periodic modulation of ω_e was produced by briefly illuminating the sample from its back side with an infrared LED. Because the gold grating has higher reflectivity than the Ti gate, ω_e is weakly modulated, due to the persistent photoeffect.²¹ Al-

though a detailed analysis of the surface modes of a corrugated electron layer is complex,²² qualitatively one expects that the modulation in ω_e should open gaps in surface plasmon dispersion relations $\omega(q_1)$, for $q_1 = m\pi/\lambda_G$, where $m = (\pm 1, \pm 2, \dots)$.²³ Because the grating coupler excites plasmons with wave vectors $q_1 = 2\pi/\lambda_G$, for $n = 1, 2, \dots$, these gaps should split surface plasmon resonances, as has been observed for two-dimensional plasmons.²³ The insets in Fig. 2(a) show the effect of illumination on ω_+ and ω_- , for $\omega_e \sim 500$ Å. Both resonances split into two peaks, with a fractional splitting $\Delta\omega/\omega \approx 12\%$ and 9% for the ω_+ and ω_- resonances, respectively. If the ω_+ resonance were the parabolic well sloshing mode,¹⁰ which has frequency independent of ω_e , one would expect weak, static modulation of ω_e to have little effect on the line shape.

We have shown that $\text{Al}_x\text{Ga}_{1-x}\text{As}$ heterostructures can be used to realize quasi-three-dimensional metals with unusual surface properties, and that they provide a physical system in which to probe in detail the effects of surface conditions on surface electronic excitations. More detailed calculations are needed to understand the dependence of the observed resonance frequencies on ω_e .

We acknowledge useful conversations with W. Kohn and S. J. Allen. This work was supported in part by NSF Grant No. DMR-9002491. Clean room use was supported in part by the NSF Science and Technology Center for Quantized Electronic Structures, Grant No. DMR88-10430.

*Present address: Division of Science and Technology, Griffith University, Nathan, Queensland 4111, Australia.

¹P. J. Feibelman, *Prog. Surf. Sci.* **12**, 287 (1982).

²K. D. Tsuei, E. W. Plummer, and P. J. Feibelman, *Phys. Rev. Lett.* **63**, 2256 (1989); K. D. Tsuei *et al.*, *ibid.* **64**, 44 (1990).

³J. F. Dobson, *Phys. Rev. B* (to be published).

⁴N. G. Asmar and E. G. Gwinn, *Phys. Rev. B* **45**, 4752 (1992).

⁵K. Karrai *et al.*, *Phys. Rev. B* **39**, 1426 (1989); K. Karrai *et al.*, *ibid.* **40**, 12020 (1989).

⁶A. Wixforth *et al.*, *Phys. Rev. B* **43**, 1991 (1991).

⁷M. Sundaram *et al.*, *Superlattices Microstruct.* **4**, 683 (1988); E. G. Gwinn *et al.*, *Phys. Rev. B* **41**, 10700 (1990).

⁸T. Sajoto *et al.*, *Phys. Rev. B* **39**, 10464 (1989); T. Sajoto, J. Jo, and M. Shayegan, *Appl. Phys. Lett.* **55**, 1430 (1989).

⁹A. J. Rimberg and R. M. Westervelt, *Phys. Rev. B* **40**, 3970 (1989).

¹⁰L. Brey, N. F. Johnson, and B. I. Halperin, *Phys. Rev. B* **40**, 10647 (1989).

¹¹M. P. Stopa and S. Das Sarma, *Phys. Rev. B* **40**, 10048 (1989).

¹²P. F. Hopkins *et al.*, *Appl. Phys. Lett.* **57**, 2823 (1990).

¹³Unequal charge transfer from the donor planes below and above the well can occur. If the donor sheets were perfectly uniform laterally, this would effectively add a linear term to the well in E_c , which would remain parabolic. Because the ionized donor sheets are not perfectly uniform, their fields will cause a small, random modulation of equipotential surfaces.

¹⁴For example, S. Das Sarma and A. Madhukar, *Phys. Rev. B*

23, 805 (1981); D. Olego *et al.*, *ibid.* **25**, 7867 (1982); R. D. King-Smith and J. C. Inkson, *ibid.* **33**, 5489 (1986); T. Zettler, C. Peters, and J. P. Kotthaus, *ibid.* **39**, 3931 (1989); G. Fasol *et al.*, *ibid.* **39**, 12695 (1989); D. Richards, G. Fasol, and K. Ploog, *Appl. Phys. Lett.* **56**, 1649 (1990); and references in Ref. 17, below.

¹⁵To find n_b , we assume $\Delta E_c = 875x(\text{meV})$ and $\epsilon = 13\epsilon_0$. Because the orientation of the Al and Ga sources cause the curvature to vary laterally across the wafer, samples taken from different parts of the wafer will have somewhat different ω_p .

¹⁶ C is well approximated by $C = eAd$, for $\epsilon = 12.5\epsilon_0$, where A is the sample area: The average ϵ between the sample surface and the top edge of the well is $12.3\epsilon_0$, and the average ϵ from the sample surface to the bottom side of the well is $12.6\epsilon_0$ (Ref. 20).

¹⁷S. J. Allen, Jr., D. C. Tsui, and R. A. Logan, *Phys. Rev. Lett.* **38**, 980 (1977); T. N. Theis, *Surf. Sci.* **98**, 515 (1980); E. Batke, D. Heitmann, and C. W. Tu, *Phys. Rev. B* **34**, 6951 (1986).

¹⁸J. F. Dobson and G. H. Harris, *J. Phys. C* **21**, L729 (1988), and references therein.

¹⁹R. Ritchie, *Phys. Rev.* **106**, 874 (1957).

²⁰S. Adachi, *J. Appl. Phys.* **58**, R1 (1985).

²¹R. Fletcher *et al.*, *Phys. Rev. B* **41**, 10649 (1990).

²²H. Raether, *Surface Plasmons* (Springer-Verlag, Berlin, 1988).

²³U. Mackens *et al.*, *Phys. Rev. Lett.* **53**, 1485 (1984).



ANISOTROPIC BAND STRUCTURE OF A PARABOLICALLY CONFINED ELECTRON SYSTEM SUBJECTED TO AN IN-PLANE MAGNETIC FIELD

Achim Wixforth and Michael Kaloudis

Sektion Physik, Universität München, Geschw. Scholl Platz 1, D-8000 München 22, Germany

and

Mani Sundaram and Arthur C. Gossard

Materials Department, University of California, Santa Barbara, CA 93106, U.S.A.

(Received 18 September, 1992 by T.P. Martin)

The anisotropy of the effective mass in a wide electron layer confined in a parabolic potential well has been determined from plasmon resonance experiments for the case of an in plane magnetic field. For this system, the resulting band structure can be described in terms of a hybridization of the electrical and the magnetic confinement and free motion in the plane of the electron system. The effective mass shows a strong anisotropic behavior along the two principal directions with respect to the magnetic field. For a purely parabolic confining potential one can derive analytical expressions for this anisotropy which are in excellent agreement with the experimental results. Similarities to the collective excitation spectra of one-dimensional quantum wires are discussed.

The collective excitation spectrum of an electronic system contains valuable information as it is one of its most fundamental properties. For two-dimensional electron systems (2DES) as realized in space charge layers in semiconductors the study of plasmonic (intrasubband-) excitations as well as intersubband-transitions have proven invaluable in the characterization and understanding of these systems¹. More recently², also the collective excitations in quasi-one-dimensional electron systems (Q1DES, quantum wires)^{3,4} and quasi-zero-dimensional (Q0DES, quantum dots)⁵ have attracted very much attention. On the other hand, the collective intersubband-like excitations of wide electron layers in so-called parabolic quantum wells (PQW) which form a quasi-three-dimensional electron system^{6,9} (Q3DES) has led to the generalization of Kohn's theorem¹⁰. Subsequently, this theorem has been very successfully applied to explain many experimental observations also on Q1DES and Q0DES. It states that in a purely parabolically confined electron system long-wavelength radiation couples only to the center of mass coordinates and its motion. Relative coordinates and thus particularly electron-electron interactions in such systems do not affect the resonance frequency of the observed transitions.

Here, we report on the investigation of the collective excitations of a wide electron system in a PQW at finite wave vector⁹. If such a system is subjected to an in-plane

magnetic field the resulting band structure is very closely related to the one of a 1D quantum wire in a perpendicular magnetic field. The reason is that 1D quantum wires in most cases can be described in good approximation by an external parabolic confining potential. The main advantage of a PQW, however, is the exact knowledge of the shape of the potential which allows to directly deduce analytical expressions for the expected spectrum of the collective excitations. Moreover, the case of an ideal parabolic quantum well in a parallel magnetic field is particularly simple and can be quantized in analytical form^{11,12}.

Referring the reader to a more detailed description of the growth procedure and fundamental properties of a PQW in refs. 6..9, we give here only a short list of the parameters for the sample used in the present experiment: Our sample is a parabolic $\text{Al}_x\text{Ga}_{1-x}\text{As}$ quantum well of width $W=200\text{nm}$ and energetical depth of $\Delta_1=150\text{meV}$. It has additional vertical sidewalls of height $\Delta_2=75\text{meV}$. The curvature of the parabolic part of the well corresponds to the potential of a positive background density $n^+=2.2 \cdot 10^{16}\text{cm}^{-3}$. On top of the sample we have a semitransparent NiCr gate and an Ag grating coupler of periodicity $a=2\mu\text{m}$. Ohmic contacts are made to the electron system by alloying In at $T=430^\circ\text{C}$ in reducing atmosphere. By application of a bias between the gate and the electron system¹³ we can change the carrier density in the well from

$N_S=0$ to $N_S=2.6 \cdot 10^{11} \text{ cm}^{-2}$. The grating coupler provides a plasmon wave vector $q = 2\pi/a = \pi \cdot 10^6 \text{ m}^{-1}$.

As has been shown before^{14,15}, a quasi 3DES confined in a PQW can support intra-subband excitations that for small q resemble the well known surface plasmon¹⁶ of a 2DES. Its dispersion is given by

$$\omega_p^2 = \frac{N_S e^2 q}{2m_p \bar{\epsilon}(q) \epsilon_0} \quad (1)$$

where $\bar{\epsilon}(q)$ denotes an effective dielectric constant containing sample parameters and geometry, and m_p an effective plasmon mass. The other symbols have their usual meaning. For our sample $\hbar\omega_p \approx 15 \text{ cm}^{-1}$, depending on the carrier density in the well. The sample is mounted in Voigt geometry in the center of a superconducting solenoid providing magnetic fields up to 15T parallel to the plane of the electron system. It is held at a temperature of $T=4.2\text{K}$. The experiment are performed in transmission using a rapid scan Fourier transform spectrometer under normal incidence of unpolarized far infrared radiation (FIR). Experimentally we determine the relative change in transmission

$$\frac{\Delta T}{T} = \frac{T(0) - T(N_S)}{T(0)} \quad (2)$$

which is proportional to the real part of the dynamic conductivity $\bar{\sigma}(\omega)$ of the electron system. The geometry of our experiment is depicted in Fig. 1. Here, both principal orientations of the plasmon wave vector with respect to the magnetic field are already sketched. By rotating the sample by $\pi/2$ we can excite surface plasmons with q being either parallel or perpendicular to the magnetic field.

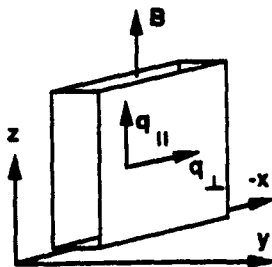


Fig. 1. Sketch of the geometry of the experiment. The unpolarized far-infrared radiation is incident in y-direction, the magnetic field is directing parallel to the electron layer (x-y-plane). The plasmon wave vector q is defined by use of a metal grating on top of the sample, and can direct either parallel or perpendicular to the magnetic field.

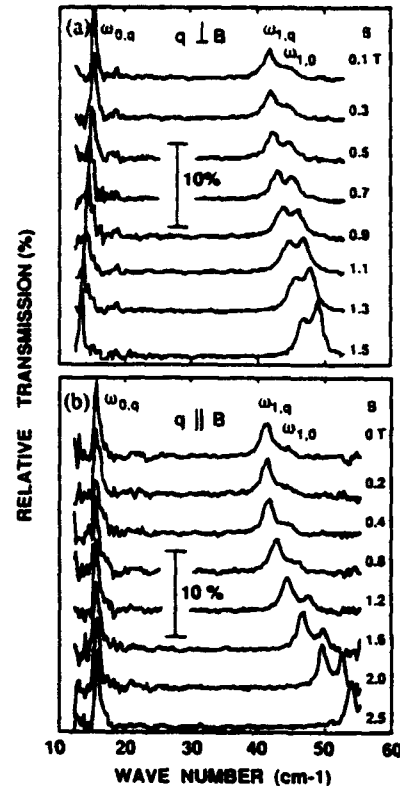


Fig. 2. Typical spectra as obtained in transmission and Voigt geometry for different magnetic fields B . Both cases of q being perpendicular (a) and parallel (b) to B are depicted. In both experiments we observe three resonances, which are related to the intra-subband plasmon at finite wave vector $(0,q)$, the inter-subband plasmon at finite wave vector $(1,q)$, and the inter-subband plasmon at zero wave vector $(1,0)$. The latter is also called plasma shifted cyclotron resonance. In (a) the resonance $(0,q)$ has a characteristic negative magnetic field dispersion, whereas $(1,q)$ and $(1,0)$ follow the dispersion for a magneto-electric hybrid excitation as described in the text. In contrast to (a), for parallel configuration $(0,q)$ has no magnetic field dependence as expected from the simple model (b).

Typical spectra for both orientations of the plasmon wave vector with respect to the magnetic field are shown in Fig. 2. Here, we plot the observed relative change in transmission vs. energy for different magnetic fields. In perpendicular geometry, i.e. the plasmon wave vector being normal to the magnetic field (Fig. 2a) we observe basically three resonances. The lower frequency mode $\omega_{0,q}$ around 16 cm^{-1} at low B is identified with the surface plasmon and exhibits a *negative* dispersion with the magnetic field, which is a unique feature of an edge magnetoplasmon type of oscillation^{17,18}. The higher frequency modes $\omega_{1,q}$ and $\omega_{1,0}$ are the grating coupler

induced intersubband-type excitation⁹ and the plasma shifted cyclotron resonance^{7,8} at $q=0$, respectively. The oscillator strength of the latter is zero for zero magnetic field and then increases as the field increases⁸, which can be clearly seen in the figure. This excitation is formally identical to the magneto-electric subband hybrid in a 1D quantum wire. For parallel geometry (Fig. 2b), we also observe three oscillations, but $\omega_{0,q}$ now has no significant magnetic field dependence. This striking difference contains information about the magnetic field induced anisotropy of the effective band structure that we like to discuss in this Communication.

Using the coordinate system of Fig. 1 and omitting the spin, the initial eigenenergy equation for a PQW subjected to an in-plane magnetic field reads¹²

$$\left[\frac{1}{2m^*} (\vec{p} + e\vec{A})^2 + \frac{m^* \omega_{1,0}^2}{2} y^2 \right] \psi = E \psi \quad (3)$$

where $m^* \omega_{1,0}^2 / 2$ characterizes the parabolic potential in growth (y-) direction. This frequency is given by the bare external potential of the PQW and due to Kohn's theorem independent of the number of electrons in the well. It has been shown before^{6,10} that this frequency $\omega_{1,0}$ for $q=0$ is solely determined by the curvature of the external parabolic potential and is given by

$$\omega_{1,0}^2 = \frac{8\Delta_1}{W^2 m^*} \quad (4)$$

where Δ_1 is the energetical height of the parabolic part of the potential, and W its width in confining direction. At finite wave vector q , the mode exhibits a dispersion^{14,15} which is determined by the quantity qd , d being the width of the electron system in the direction of confinement:

$$\omega_{1,q}^2 = \frac{\omega_{1,0}^2}{2} (1 + e^{-2qd}) \quad (5)$$

Taking $\vec{A} = -(By, 0, 0)$ and separating the variables in the usual way one obtains from (3)

$$\left(\frac{-\hbar^2}{2m^*} \frac{d^2}{dy^2} + \frac{m\Omega^2}{2} \tilde{y}^2 \right) f(\tilde{y}) = \tilde{E} f(\tilde{y}) \quad (6)$$

where $\Omega^2 = \omega_{1,q}^2 + \omega_c^2$ is the effective hybrid frequency, $\tilde{y} = y - y_0$ with $y_0 = \hbar k_x \omega_c / m^* \Omega^2$. The resulting energy dispersion then turns out to be given by

$$E = \hbar \Omega (n + 1/2) + \frac{\hbar^2 k_x^2 \omega_{1,q}^2}{2m^* \Omega^2} + \frac{\hbar^2 k_z^2}{2m^*} \quad (7)$$

This dispersion describes a harmonic oscillator-like quantization in the confining direction of the parabolic potential with a characteristic frequency Ω , representing the intersubband-type collective excitation that obeys Kohn's theorem. The free motion in the plane of the Q3DES is represented by the quasi-momenta k_x and k_z . Eq. (7) has exactly the same form for a 1DES in parabolic approximation (quantum wire) if one replaces the term containing k_z by a 2D subband energy, since it is also confined in this direction. The term containing k_x is then related to so-called one-dimensional plasmons propagating along the wire⁴. The hybrid oscillator term is governed by the 1D intersubband plasmon. The interesting fact for a PQW, however, is the occurrence of an anisotropic band structure in the plane of the electron system with respect to the direction of the magnetic field. The same anisotropy has been observed before, although as a much weaker effect, for high quality 2DES on GaAs/AlGaAs heterostructures¹⁹. The theoretical description in that case, however, is rather complex and not straightforward²⁰. Using eq. (7) one can define a very simple expression for the effective mass for a PQW and the geometry under consideration

$$m_{\perp} = m^* \left(1 + \frac{\omega_c^2}{\omega_{1,q}^2} \right) \quad \text{and} \quad m_{\parallel} = m^* \quad (8)$$

in the plane of the electron system. The subscript symbols for m^* indicate the direction with respect to the magnetic field. With increasing magnetic field the 'perpendicular' effective mass increases quadratically. The effective mass parallel to the magnetic field, respectively, remains unaltered and is given by m^* . Using this expression for the plasmon mass we obtain the magnetic field dispersion of the surface plasmon.

$$\omega_{0,q}^2(q_{\perp}) = \omega_p^2 \left(1 + \frac{\omega_c^2}{\omega_{1,q}^2} \right)^{-1} ; \quad \omega_{0,q}^2(q_{\parallel}) = \omega_p^2 \quad (9)$$

The result is shown in Fig. 3, where we plot the extracted resonance positions of $\omega_{0,q}$ for both principal orientations of q as a function of the magnetic field. For high magnetic fields ($B > 3T$) we are not able to follow the negative dispersion of $\omega_{0,q}(q_{\perp})$ since we are approaching the noise limit of our spectrometer close to 10cm^{-1} . The magnetic field independent resonance $\omega_{0,q}$ for $q \parallel B$, however, does not deviate significantly from its low field behavior up to $B = 15\text{ T}$. This part of the data has been omitted in the plot for clarity. Note that no fit parameter has been used since all quantities can be measured independently. From cyclotron resonance^{7,8} in Voigt-geometry one can

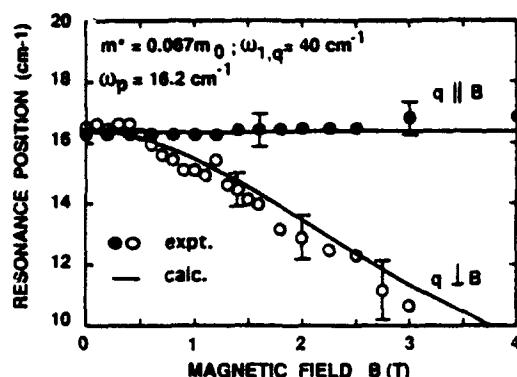


Fig.3. Resonance positions as extracted from Fig. 2 for both orientations of the plasmon wave vector q with respect to B . They reflect the magnetic field induced anisotropy of the plasmon mass. Symbols represent the experimental data, whereas the solid lines are the result of the simple model as described in the text. The parameters used are given in the inset.

extract m^* . Plasmon resonance experiments¹⁴ in Faraday geometry, i.e. the magnetic field directing normal to the sample surface are used to extract $\omega_{0,q}$. The $q=0$ resonance $\omega_{1,0}$ can be determined by tilted field experiments^{3,6,8}, where no grating coupler is needed to excite it.

In summary, we have investigated the collective excitations of a parabolically confined electron system subjected to a magnetic field perpendicular to the gradient of the confinement. The magnetic field induces a strong anisotropy of the effective band structure, which is reflected in the magnetic field dispersion of a finite q plasmon parallel to the electron layer. The resulting band structure is formally identical to the one of a 1DES as confined in a quantum wire in harmonic approximation. The orientation where q is normal to the magnetic field results in an edge magneto-plasmon type excitation that in a 1DES is propagating along the wire and usually is referred to as a 1D plasmon.

ACKNOWLEDGEMENT - We gratefully acknowledge useful discussions with J.P. Kothaus. Financial support for this work has been provided by both the Deutsche Forschungsgemeinschaft and the U.S. Airforce Office of Scientific Research under Contract No. AFOSR-88-099. A.W. wishes to express his gratitude for the hospitality of the QUEST- Center at UCSB during a sabbatical stay.

REFERENCES

1. see, e.g., D. Heitmann, *Two-Dimensional Systems: Physics and New Devices* (ed. G. Bauer, F. Kuchar, and H. Heinrich, Springer, Berlin) p 285 (1986)
2. for a recent review, see, e.g., W. Hansen, U. Merkt, and J. P. Kothaus, in *Semiconductors and Semimetals*, (ed. R. K. Willardson, A. C. Beer, E. R. Weber), Vol. 35, (Academic Press, San Diego 1992) p. 279.
3. K. Kern, D. Heitmann, R.R. Gerhardt, P. Grambow, Y. Zhang, and K. Ploog, *Phys. Rev. B* **44**, 1139 (1989)
4. T. Demel, D. Heitmann, P. Grambow, and K. Ploog *Phys. Rev. Lett.* **66**, 2657 (1990)
5. T. Demel, D. Heitmann, P. Grambow, and K. Ploog, *Phys. Rev. Lett.* **64**, 788 (1990)
6. K. Karrai, H.D. Drew, H.W. Lee, and M. Shayegan, *Phys. Rev. B* **39**, 1426 (1989)
7. K. Karrai, X. Ying, H.D. Drew, and M. Shayegan, *Phys. Rev. B* **40**, 12020 (1989)
8. A. Wixforth, M. Sundaram, K. Ensslin, J.H. English, and A.C. Gossard, *Surf. Sci.* **267**, 523 (1992)
9. A. Wixforth, M. Sundaram, K. Ensslin, J.H. English, and A.C. Gossard, *Phys. Rev. B* **43**, 10000 (1991)
10. L. Brey, N.F. Johnson, and B.I. Halperin, *Phys. Rev. B* **40**, 647 (1989)
11. J.C. Maan, *Two Dimensional Systems: Heterostructures and Superlattices* (ed. G. Bauer, F. Kuchar, and H. Heinrich, Springer, Berlin) p. 183 (1984)
12. W. Zawadzki, *High Magnetic Fields in Semiconductor Physics II* (ed. G. Landwehr, Springer, Berlin), p. 220 (1989)
13. A. Wixforth, M. Sundaram, K. Ensslin, J.H. English, and A.C. Gossard, *Appl. Phys. Lett.* **56**, 454 (1990)
14. M. Kaloudis, K. Ensslin, A. Wixforth, M. Sundaram, J.H. English, and A.C. Gossard, *Phys. Rev. B*, in press
15. P.R. Pinsukanja, E. Yuh, E.L. Ansmar, E.G. Gwinn, M. Sundaram, and A.C. Gossard, *Phys. Rev. B*, in press
16. F. Stern, *Phys. Rev. Lett.* **18**, 546 (1967)
17. G. Eliasson, J.W. Wu, P. Hawrylak, and J.J. Quinn *Sol. St. Comm.* **60**, 41 (1986)
18. D.B. Mast, A.J. Dahm, and A.L. Fetter, *Phys. Rev. Lett.* **54**, 1706 (1985)
19. E. Batke, and C.W. Tu, *Phys. Rev. B* **34**, 3027 (1986)
20. F. Stern, *Phys. Rev. Lett.* **21**, 1687 (1968)

Resonant inelastic light scattering in remotely doped wide parabolic GaAs/Al_xGa_{1-x}As quantum wells

J. H. Burnett, H. M. Cheong, R. M. Westervelt, and W. Paul

Department of Physics and Division of Applied Sciences, Harvard University, Cambridge, Massachusetts 02138

P. F. Hopkins, M. Sundaram, and A. C. Gossard

Materials Department and Department of Electrical and Computer Engineering, University of California, Santa Barbara, Santa Barbara, California 93106

(Received 5 April 1993)

We have used resonant inelastic light-scattering spectroscopy in the depolarized backscattering configuration $z(y',x')z$ to probe the single-particle excitations of two n -type remotely doped wide parabolic GaAs/Al_xGa_{1-x}As quantum wells, with design curvatures corresponding to empty conduction-band harmonic-oscillator spacings of 4.4 and 3.3 meV. For the former sample, a series of spectra, for excitations near the $E_0 + \Delta_0$ gap of the bulk material at the center of the well, reveal two light-scattering peaks with shifts ~ 0.85 and ~ 3.0 meV, which are strongly resonant with resonance widths of ≤ 3 meV. Separate resonance curves were extracted, and the two resonance peaks are found to be separated by an energy approximately equal to the scattering peak separation. For the latter sample, similar spectra were obtained which reveal two strongly resonant light-scattering peaks with energy shifts ~ 0.65 and ~ 2.0 meV, with resonance maxima separated by an energy approximately equal to the scattering peak separation. We have interpreted these results in terms of single-particle transitions between conduction-band subbands and have found them quantitatively consistent with a model for the electron gas in the well distributed as a uniform density slab, giving rise to a square-well-like effective potential, as predicted for this system.

I. INTRODUCTION

Inelastic light scattering has been shown to be a useful technique for measuring electronic intersubband spacings in two-dimensional electron gas (2DEG) systems.^{1,2} Following the proposal by Burstein, Pinczuk, and Buchner³ to measure excitations in 2DEG's using inelastic light scattering and the observation by Pinczuk *et al.*⁴ that both single particle and collective excitations in bulk n -type GaAs are strongly resonant near the $E_0 + \Delta_0$ gap, Abstreiter and Ploog¹ reported evidence for intersubband transitions by carriers in the accumulation layer at a single GaAs/ n -Al_xGa_{1-x}As interface using this technique. Subsequently, Pinczuk *et al.*² reported observation by resonant inelastic light scattering of intersubband excitations of the multilayer 2DEG in modulation-doped GaAs/Al_xGa_{1-x}As heterojunction superlattices. The intersubband energies measured were in good agreement with the calculated values for this structure.

This technique has been applied to other structures. Menéndez *et al.*⁵ reported resonant inelastic light scattering in photoexcited parabolic GaAs/Al_xGa_{1-x}As quantum wells (PBW's) to accurately measure the conduction-band harmonic-oscillator levels, with spacing ~ 25 meV. From these measurements they determined small deviations from parabolicity, and obtained the conduction-band offset. In this paper we report resonant inelastic light scattering in n -type remotely doped wide parabolic GaAs/Al_xGa_{1-x}As quantum wells, a structure with altogether different characteristics from the empty

PBW's investigated by Menéndez *et al.*⁵

Remotely doped wide parabolic GaAs/Al_xGa_{1-x}As quantum wells have generated interest because they have been demonstrated to create relatively thick (> 1000 Å) layers of uniform density, high-mobility electron gas,⁶⁻⁹ and the properties of this electron gas are a subject of active research. As illustrated in Fig. 1(a), PBW's are created in the conduction band Γ_6 (CB), heavy- and light-hole valence bands Γ_8 (VB's), and spin-orbit split-off band Γ_7 (SOB) by varying the average Al concentration in a parabolic profile. For an empty PBW this results ideally in simple-harmonic-oscillator (SHO) energy levels for electrons, heavy holes, light holes, and spin-orbit split-off holes, with energy-level spacings given by $\hbar\omega_e^0$, $\hbar\omega_{hh}^0$, $\hbar\omega_{lh}^0$, and $\hbar\omega_{so}^0$, respectively, where for electrons $\omega_e^0 = (K_{CB}/m_e^*)^{1/2}$. m_e^* is the electron effective mass and K_{CB} is the CB edge curvature given by $K_{CB} = d^2E_{CB}/dz^2 = 8\Delta E_{CB}/L_z^2$, where ΔE_{CB} is the difference between the energies at the center of the PBW and at the edge, and L_z is the width of the well. Analogous definitions apply for the hole levels.¹⁰

When electrons are added to the well by remote doping, for filling beyond single subband occupancy, self-consistent quantum-mechanical calculations¹¹ verify semiclassical arguments, that they become distributed as a slab with roughly uniform three-dimensional (3D) number density, $n^{3D} = 2\Delta E_{CB}\epsilon/\pi e^2 L_z^2$. (Here, ϵ is the electron charge and ϵ is the static dielectric constant.) The potential of this charged slab cancels the parabolic band-edge potential over the slab width w_e , which is propor-

tional to the filling, i.e., the sheet density $n_s (=w_s n^{3D})$. This leaves a flat-bottomed self-consistent potential in the CB over a width $\sim w_s$ and PBW's with greater curvatures $K_{CB} + K_{VB}$ and $K_{CB} + K_{SOB}$ in the VB's and the SOB, respectively, as indicated in Fig. 1(b), where K_{CB} , K_{VB} , and K_{SOB} are the curvatures for the corresponding empty PBW's. Furthermore, the 3D density and Fermi level are roughly independent of n_s , depending only on the bare parabolic curvature, and the occupied subband energy levels behave like a square-well spectrum $E_n \propto n^2/w_{eff}^2$. Here, n_s is the quantum number, and w_{eff} is an effective well width given by w_s plus a constant needed to account for the exponential tail of the wave function.¹¹ These predictions have been given support by transport measurements.^{7,8} In this work we investigated the predicted square-well-like subband spacing in the CB with inelastic light scattering, using the harmonic-oscillator-like subbands in the SOB as resonance levels.

II. EXPERIMENT

The PBW samples were fabricated by molecule-beam epitaxy on (100) GaAs substrates, as described by Sundaram *et al.*⁶ The parabolic band-edge variations were constructed from a 20-Å period superlattice, each period containing a GaAs and an $Al_xGa_{1-x}As$ layer, with the relative width of the two layers varied using a computer-

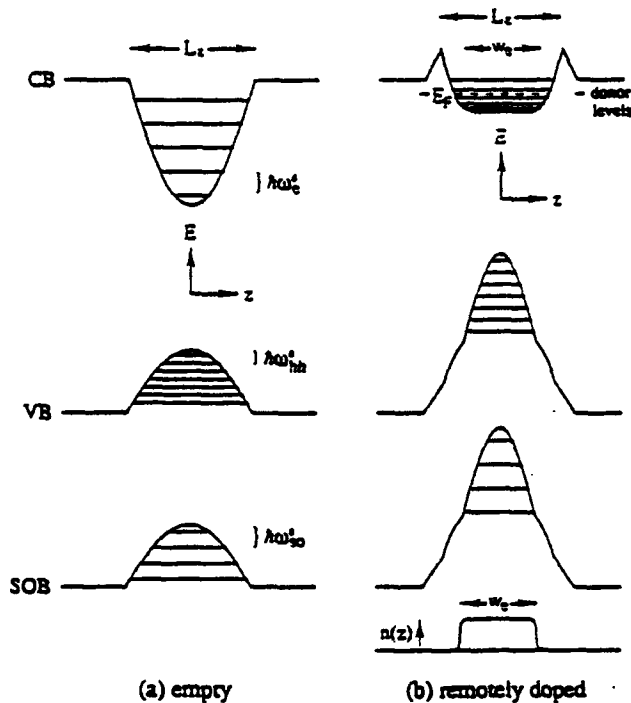


FIG. 1. Schematic diagram of the conduction-band edge, valence-band edge, and spin-orbit split-off band-edge profiles in (a) an empty $Al_xGa_{1-x}As$ parabolic well, with $k_z = k_y = 0$ energy levels being simple-harmonic-like, and (b) an n -type remotely doped $Al_xGa_{1-x}As$ parabolic well, with $k_z = k_y = 0$ energy levels being simple-harmonic-like in the VB and SOB, but square-well-like in the CB. (Only the heavy-hole levels in the VB are shown.) The effective width of the square well is given approximately by the width w_s of the electron slab indicated by the charge-density profile shown at the bottom of (b).

controlled shutter to produce an average Al concentration with a parabolic profile, with x near zero at the center. The electrons were introduced into the CB well from δ -doped layers, set back symmetrically from both sides of the well with spacer layers in the $Al_xGa_{1-x}As$ barriers. We have made measurements on four PBW samples which showed similar effects. We will here discuss measurements on two samples. Sample 1 was grown with a nominal PBW width of $L_z = 2800$ Å, with $x = 0.005$ at the center and $x = 0.2$ at the edge, giving a design density of $n^{3D} = 1.22 \times 10^{16} \text{ cm}^{-3}$. It was symmetrically δ doped with spacer layers of 300 Å. The Hall-effect sheet density and mobility measured in the dark were $n_s = (1.7 \pm 0.2) \times 10^{11} \text{ cm}^{-2}$ and $\mu = 0.8 \times 10^5 \text{ cm}^2 \text{ V}^{-1} \text{ sec}^{-1}$, respectively. The sheet density increased reversibly when exposed to light at low temperature. When illuminated at 2 K it saturated at $n_s = (1.8 \pm 0.2) \times 10^{11} \text{ cm}^{-2}$, corresponding to a fractional filling of 0.53 and an effective well width of $w_{eff} = \sim 1900 \pm 250$ Å. The Fermi level E_F determined by n^{3D} was 2.9 meV.

Sample 2 was grown with a nominal PBW width of $L_z = 4640$ Å, with $x = 0$ at the center and $x = 0.3$ at the edge, giving a design density of $n^{3D} = 6.8 \times 10^{15} \text{ cm}^{-3}$. It was symmetrically δ doped with spacer layers of 400 Å. The sheet density and mobility measured in the dark were $n_s = (1.4 \pm 0.2) \times 10^{11} \text{ cm}^{-2}$ and $\mu = 2.4 \times 10^5 \text{ cm}^2 \text{ V}^{-1} \text{ sec}^{-1}$, respectively, and Shubnikov-de Haas measurements showed that three subbands were occupied. When exposed to light at 2 K the sheet density increased to $n_s = (1.7 \pm 0.2) \times 10^{11} \text{ cm}^{-2}$, corresponding to a fractional filling of the well of 0.54 and an effective well width of $w_{eff} = \sim 2900 \pm 400$ Å. The Fermi level E_F determined by n^{3D} was 1.9 meV.

The samples were cooled to 2 K using a He vapor flow optical cryostat, and excited with a dye laser, pumped by an Ar-ion laser. The inelastic light-scattering spectra were obtained using a double monochromator, with a cooled GaAs photomultiplier tube, photon counting electronics, and a computer-controlled data-acquisition system. The spectra were obtained in the depolarized back-scattering configuration $z(y', x')z$, with the incident photon energy $\hbar\omega_i$ (1.89–1.94 eV) near the $E_0 + \Delta_0$ gap of GaAs. In this configuration the spectra are expected to exhibit electronic single-particle intersubband transitions.¹²

Recently it was shown by Pinczuk *et al.*¹³ that with the depolarized configuration the dominant peaks actually correspond to spin-density excitations, which are shifted from the single-particle transition energies by the exchange Coulomb interaction. We assume, as is done in the other references cited here,^{1-5,12,14-16} that this difference is small compared to the peak energy shift and width. This is especially justified here due to the low 3D densities of electron gases investigated. Thus we interpret the peaks as giving the energy spacing of the quantum well subbands.

III. MEASUREMENTS

Figure 2 shows a series of light-scattering spectra of sample 1, taken at 2 K, for excitation energies ranging

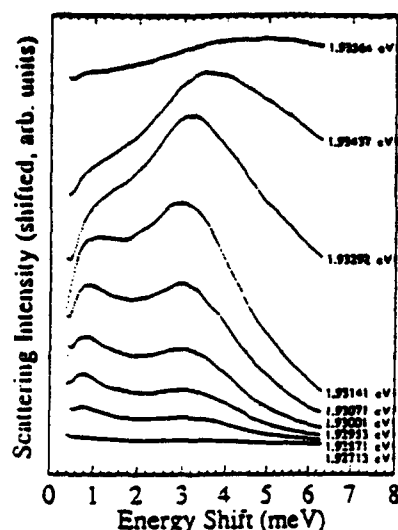


FIG. 2. Light-scattering spectra of sample 1 for various excitation energies shown to the right, taken in the $z(y',x')z$ configuration at 2 K. Instrumental resolution is 0.1 meV. All spectra have the same scale factor and the top four are displaced vertically. The figure shows a peak at an energy shift of ~ 3.0 meV, resonant near 1.932 eV, and a peak at an energy shift of ~ 0.85 meV, resonant near 1.930 eV. The broad peak evident in the top two spectra is due to luminescence across the $E_0 + \Delta_0$ gap.

from 1.927 to 1.936 eV. The focused illumination power density was 5 W/cm^2 and the instrumental resolution was 0.1 meV. The spectra clearly show two peaks resonant at different excitation energies. Deconvolutions of the double peak structure with Lorentzians show that one peak has an energy shift of 3.0 ± 0.3 meV with a full width at half maximum (FWHM) of 3.2 ± 0.4 meV, which is resonant for excitations near 1.932 eV. The other peak has an energy shift of 0.85 ± 0.20 meV with a FWHM of 1.0 ± 0.2 meV, which is resonant for excitations near 1.930 eV. The two peaks are spaced apart by an energy of 2.15 ± 0.4 meV. (The upper three curves are seen to be distorted by a broad peak which has an increasing energy shift with increasing excitation energy. In fact, it has a constant peak energy, and is due to the weak luminescence across the $E_0 + \Delta_0$ gap.) Resonant enhancement curves, showing the excitation energy dependence of the intensities of the two peaks at their maxima, determined from the deconvolution of the double peak structure for the various spectra, are shown in Fig. 3. These curves show a resonance width (FWHM) for the lowest energy shift peak of ~ 2.5 meV, and for the higher-energy shift peak of 3.0 meV. The resonant maxima for the two peaks differ by 2.0 ± 0.4 meV, approximately equal to the spacing between the two scattering peaks.

A series of light-scattering spectra with different excitation energies for sample 2, taken at 2 K, shows behavior similar to that observed for sample 1. The spectra reveal a peak with an energy shift of 2.0 ± 0.2 meV, which has maximum intensity for excitations near ~ 1.902 eV, and a much smaller peak with an energy shift of 0.65 ± 0.10 meV. The maximum intensities for the two peaks occur for excitations separated by an ener-

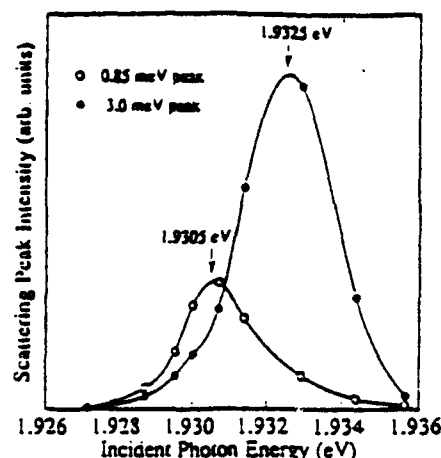


FIG. 3. Normalized scattering intensity for the peak maxima of the two light-scattering peaks of sample 1, as a function of incident photon energy. The solid lines are cubic spline fits to the data.

gy 1.5 ± 0.5 meV, approximately equal to the spacing between the two peaks.

Similar sets of measurements were made on these samples for different angles (from 0° to 45°) between the incident photon direction and the normal to the plane of the sample. For both samples the peak shifts were independent of this angle, eliminating the possibility of the peaks being associated with plasma oscillations.¹² The peak shifts were also independent of power for power densities ranging from 0.03 to 10 W/cm^2 .

IV. DISCUSSION

The $z(y',x')z$ light-scattering spectra of sample 1, shown in Fig. 2, display several noteworthy characteristics: (1) the spectra show peaks with energy shifts near 0.85 and 3.0 meV, which are strongly resonant with excitation energy resonance widths (FWHM) of ≤ 3 meV, (2) the difference in energy between the shifts is approximately equal to the energy difference between the peaks of their respective resonance curves, and (3) the widths of the resonance curves are $\sim E_F \approx 2.9$ meV. These characteristics suggest a model similar to that proposed by Burstein, Pinczuk, and Buchner³ and used by Pinczuk *et al.*² to analyze the inelastic $z(y',x')z$ light-scattering spectra of modulation-doped $\text{GaAs}/\text{Al}_x\text{Ga}_{1-x}\text{As}$ heterojunction superlattices, for which several peaks with energy shifts ≥ 20 meV and resonance widths ≥ 30 meV were observed. However, there are expected to be significant differences for the two cases. For the heterojunction superlattices studied by Pinczuk *et al.*,² the CB levels were relatively widely spaced (≥ 20 meV) due to the narrow accumulation layerlike effective potentials in the CB, while the SOB levels were relatively narrowly spaced. For the case of remotely doped wide PBW's, however, the situation is reversed. The CB levels are expected to be relatively closely spaced (< 1 meV for the first few levels) due to the wide square-well-like effective potentials in the CB, but the SOB levels are expected to be more widely spaced (> 2.5 meV) due to the narrower PBW effective potentials.

In the scattering mechanism proposed by Burstein, Pinczuk, and Buchner³ for the depolarized backscattering geometry $z(y', x')z$, the peaks in the inelastic light-scattering spectra correspond to single-particle transitions from occupied CB subband states below the Fermi level to unoccupied CB subband states above the Fermi level, with opposite spin. These transitions can occur if the occupied intermediate states have mixed spins, due, for example, to the spin-orbit interaction, as in the SOB states. For incident and scattered photon wave vectors perpendicular to the heterostructure plane, the transitions must be vertical, i.e., the initial, intermediate, and final states must have the same value for the in-plane

wave vector k . Two such transitions for the remotely doped PBW structure are illustrated in the E versus k diagram in Fig. 4. Here, the initial and final states are in the square-well-level-like subbands of the CB and the intermediate states are in the harmonic-oscillator-level-like subbands of the SOB.

The matrix elements for these spin-flip intersubband transitions can be obtained from an extension to the case of a 2DEG of the matrix elements for a 3DEG, obtained by Wolf¹⁴ and Hamilton and McWhorter.¹⁵ For the case depicted in Fig. 4, where the intermediate state is a SOB subband state, the matrix element is given by^{12,16}

$$M_{if}(k) = |\hat{e}_i \times \hat{e}_s| |P_{CB,SOB}|^2 \sum_v \frac{\langle \phi_f(z) | e^{ik_f z} | \phi_v(z) \rangle \langle \phi_v(z) | e^{-ik_s z} | \phi_i(z) \rangle}{E(k, v) - \hbar\omega_i} \quad (1)$$

Here, \hat{e}_i , k_i , and ω_i are the unit polarization vector, wave vector, and frequency of the incident photons; \hat{e}_s and k_s are the corresponding quantities for the scattered photons; $\phi_i(z)$ and $\phi_f(z)$ are the square-well-like envelope functions of the initial- and final-state CB subbands; $\phi_v(z)$ are the harmonic-oscillator-like envelope functions of the intermediate-state SOB subbands; k is the two-dimensional in-plane wave vector common to all three states; $P_{CB,SOB}$ is the momentum matrix element between the cell periodic parts of the CB and SOB wave functions; and $E(k, v)$ is the resonant energy given by

$$E(k, v) = E_G + E_f + E_v + \hbar^2 k^2 / 2m_e^* + \hbar^2 k^2 / 2m_{so}^*, \quad (2)$$

where E_G is the $E_0 + \Delta_0$ gap of bulk $Al_xGa_{1-x}As$ at the

PBW minimum, E_f and E_v are the $k=0$ energies of the final- and intermediate-state subbands measured from the CB and SOB edges of bulk $Al_xGa_{1-x}As$ at the PBW minimum, and m_e^* and m_{so}^* are the effective masses of the CB and SOB subbands. The sum over v in Eq. (1) is over all intermediate-state subbands. The total scattering intensity resulting from the transitions $i \rightarrow f$ is proportional to $|M_{if}(k)|^2$ summed over all k which correspond to an occupied initial CB subband state and an unoccupied final CB subband state.

The electric dipole approximation, $e^{ik_f z} - e^{-ik_s z} \rightarrow 1$, can be applied since $k_i \sim k_s \ll 1/L_{WF}$, where L_{WF} is the size of the wave function of the smallest extent in Eq. (1), namely $\phi_v(z)$ with $L_{WF} \sim 400$ Å for $v=1$. In this case, the selection rules are determined by the product of the envelope function overlap integrals,

$$\langle \phi_f(z) | \phi_v(z) \rangle \langle \phi_v(z) | \phi_i(z) \rangle. \quad (3)$$

Since the remotely doped PBW structure depicted in Fig. 1(a) has reflection symmetry about the center of the well, the envelope functions in Eq. (3) have definite parity, and it is clear that for the matrix element to be nonzero all three states must have the same parity. The envelope functions associated with the lowest subbands of the CB, VB, and SOB all have even parity, and alternate parity for higher subbands as indicated in Fig. 4. Thus, for example, the lowest-energy-allowed inelastic scattering intersubband transition is from the first to the third CB subband, CB(1) \rightarrow CB(3), resonant off the lowest SOB subband, SOB(1), and the next lowest-energy transition from CB(1) is CB(1) \rightarrow CB(5), as depicted in Fig. 4. For the assumed square-well-like potentials, the two splittings referred to above have the ratio $(3^2 - 1^2)/(5^2 - 1^2) = \frac{1}{4}$. The transition energies are independent of k assuming parabolic subbands and subband index independent effective masses, assumptions appropriate for the small k 's and low-order subbands considered here. Thus, summing over the contributions from all k obeying the occupancy requirements for the various bands discussed earlier, the two scattering peaks resulting from the two transitions

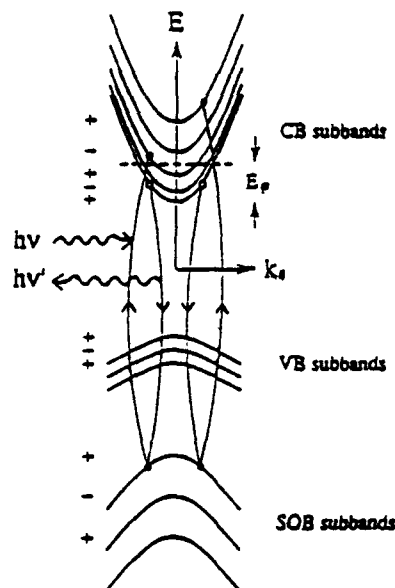


FIG. 4. Schematic diagram of several CB, VB, and SOB subbands for the remotely doped parabolic well shown in Fig. 1(b). Also shown are two vertical allowed inelastic scattering transitions, using a SOB subband state as intermediate state. The + and - signs on the left of the bands indicate the parity of the states.

depicted in Fig. 4 should have energy shifts with a ratio $\frac{1}{3}$.

We will now use this model to analyze our measurements on samples 1 and 2. For sample 1, we assume an effective well width of $w_{\text{eff}} = \sim 1900 \pm 250$ Å, determined from the measured n_s , and an average electron effective mass of $m_e^* = 0.071m_0$, determined by averaging the Al concentration dependent mass over the width of the slab. Then the square-well-like levels are calculated to have splittings of $E_{\text{CB}(3)} - E_{\text{CB}(1)} = 1.1 \pm 0.2$ meV and $E_{\text{CB}(5)} - E_{\text{CB}(1)} = 3.4 \pm 0.6$ meV, compared to the measured energy shifts of 0.85 ± 0.2 and 3.0 ± 0.3 meV, respectively. These measured energy shifts for the two peaks have the ratio $0.85/3.0 = 0.28 \pm 0.07$, consistent within the error bars with the $\frac{1}{3}$ ratio expected for square wells. Equations (1) and (2) predict that for vertical transitions using the same intermediate state, the peaks of the resonance curves for two different final-state subbands CB(f) and CB(f') should have an energy separation of $\Delta E = (E_{\text{CB}(f)} - E_{\text{CB}(f')})$. For sample 1 the scattering peaks are separated by 2.15 ± 0.4 meV, which is approximately equal to the separation of the resonance curve peaks, 2.0 ± 0.4 meV. The resonance curve widths of 2.5 and 3.0 meV are on the order of the calculated Fermi level $E_F = 2.9$ meV for this structure, as expected.

For sample 2, we assume an effective well width of $w_{\text{eff}} = \sim 2900 \pm 400$ Å, determined from the measured n_s , and an average electron effective mass of $m_e^* = 0.070m_0$, determined by averaging the mass over the width of the slab. Then the square-well-like levels are calculated to have splittings of $E_{\text{CB}(3)} - E_{\text{CB}(1)} = 0.52 \pm 0.15$ meV and $E_{\text{CB}(5)} - E_{\text{CB}(1)} = 1.6 \pm 0.5$ meV, compared to the measured energy shifts of 0.65 ± 0.10 and 2.0 ± 0.2 meV, respectively. These measured energy shifts for the two peaks have the ratio $0.65/2.0 = 0.33 \pm 0.06$, approximately equal to the $\frac{1}{3}$ ratio expected for square wells. The peak spacing of 1.35 ± 0.2 meV is consistent with the separation between the resonance maximum excitation energies for the two peaks, 1.5 ± 0.5 meV.

Inelastic scattering involving other intersubband spin-flip transitions are allowed for this structure. For example, for the same lowest-energy SOB subband intermediate state, SOB(1), the transition CB(3) \rightarrow CB(5) is allowed. Also, using SOB(2) (odd parity) as intermediate-state, transitions CB(2) \rightarrow CB(4), CB(2) \rightarrow CB(6), and CB(4) \rightarrow CB(6) are allowed. None of these are evident in the spectra. There are several possible reasons for this. When SOB(2) is used as an intermediate state, by Eqs. (1) and (2), the resonance maxima should be shifted up in energy by an amount $E_{\text{SOB}(2)} - E_{\text{SOB}(1)}$, which is 3.5

meV for sample 1. This results in maximum resonance excitation energies in the range where the photoluminescence starts to dominate the spectra as seen in Fig. 2, and thus this photoluminescence may swamp the scattering peaks. Also, as observed by Pinczuk *et al.*,² peaks associated with higher subband transitions are weaker and broader than those associated with the lower subband transitions. Thus, for example, the peak associated with the transition CB(2) \rightarrow CB(4) might be expected to be small compared to the CB(1) \rightarrow CB(3) and CB(1) \rightarrow CB(5) peaks. Thus, it is not unreasonable that the spectra would be dominated by the CB(1) \rightarrow CB(3) and CB(1) \rightarrow CB(5) transitions, indicated in Fig. 4.

V. CONCLUSIONS

Our measurements of the $z(y', x')\bar{z}$ inelastic light-scattering spectra of n -type remotely doped wide parabolic $\text{Al}_x\text{Ga}_{1-x}\text{As}$ quantum wells have revealed, for two samples, two peaks with energy shifts in the ratio $\sim \frac{1}{3}$. For each sample, a series of spectra, for excitations in a range near the $E_0 + \Delta_0$ gap of the bulk material at the center of the well, shows the peaks to be strongly resonant with resonance widths $\lesssim E_F - 3$ meV. The resonance curves show the resonance maxima have an energy separation approximately equal to the scattering peak separation. Interpreting the peaks in the $z(y', x')\bar{z}$ spectra as single-particle spin-flip vertical transitions between CB subbands,^{2,3,12,16} we have found the observed energy shifts quantitatively consistent with a model for the electron gas in the remotely doped PBW being distributed as a uniform density electron slab, with an effective square-well-like potential, giving rise to square-well-like subbands. This confirms calculations of the energy-level structure for this system, complementing evidence for this behavior from transport measurements,^{7,8} and suggests that this technique could, in principle, be used to give a measure of the electron slab width. The sharpness of the resonances and the small size of the peak shifts discerned also attest to the sensitivity of this technique for measuring precise subband levels in heterostructure systems.

ACKNOWLEDGMENTS

The authors would like to thank John Baskey for his assistance on transport measurements. The work at Harvard University was supported by the Harvard Materials Research Laboratory under Grants Nos. NSF-DMR-89-20490 and NSF-DMR-91-19386. The work at UCSB was supported by the Air Force Office of Scientific Research under Grant No. AFOSR-91-0214.

¹G. Abstreiter and K. Ploog, Phys. Rev. Lett. 42, 1308 (1979).

²A. Pinczuk, H. L. Störmer, R. Dingle, J. M. Worlock, W. Wiegmann, and A. C. Gossard, Solid State Commun. 32, 1001 (1979).

³E. Burstein, A. Pinczuk, and S. Buchner, in *Physics of Semiconductors 1978*, edited by B. L. H. Wilson (The Institute of Physics, London, 1979), p. 1231.

⁴A. Pinczuk, G. Abstreiter, R. Trommer, and M. Cardona, Solid State Commun. 30, 429 (1979).

⁵J. Menéndez, A. Pinczuk, A. C. Gossard, M. G. Lamont, and F. Cerdeira, Solid State Commun. 61, 601 (1987).

⁶M. Sundaram, A. C. Gossard, J. H. English, and R. M. Westervelt, Superlatt. Microstruct. 4, 683 (1988).

⁷T. Sajoto, J. Jo, M. Santos, and M. Shayegan, Appl. Phys. Lett.

- 55, 1430 (1989).
- ⁸E. G. Gwinn, P. F. Hopkins, A. J. Rimberg, R. M. Westervelt, M. Sundaram, and A. C. Gossard, *Phys. Rev. B* 41, 10 700 (1990).
- ⁹P. F. Hopkins, A. J. Rimberg, E. G. Gwinn, R. M. Westervelt, M. Sundaram, and A. C. Gossard, *Appl. Phys. Lett.* 57, 2823 (1990).
- ¹⁰R. C. Miller, A. C. Gossard, D. A. Kleinman, and O. Muntesanu, *Phys. Rev. B* 29, 3740 (1984).
- ¹¹A. J. Rimberg and R. M. Westervelt, *Phys. Rev. B* 40, 3970 (1989).
- ¹²See, for example, G. Abstreiter, M. Cardona, and A. Pinczuk, in *Light Scattering in Solids IV*, edited by M. Cardona and G. Güntherodt (Springer, Berlin, 1984).
- ¹³A. Pinczuk, S. Schmitt-Rink, G. Danaan, J. P. Valladares, L. N. Pfeiffer, and K. W. West, *Phys. Rev. Lett.* 63, 1633 (1989).
- ¹⁴P. A. Wolff, *Phys. Rev. Lett.* 16, 225 (1966).
- ¹⁵D. C. Hamilton and A. L. McWhorter, in *Light Scattering Spectra of Solids*, edited by G. B. Wright (Springer, Berlin, 1969), p. 309.
- ¹⁶A. Pinczuk, J. M. Worlock, H. L. Störmer, R. Dingle, W. Wiegmann, and A. C. Gossard, *Surf. Sci.* 98, 126 (1980).

Photoluminescence excitation spectroscopy of Be-remotely-doped wide parabolic GaAs/Al_xGa_{1-x}As quantum wells

J. H. Burnett, H. M. Cheong, and W. Paul

Department of Physics and Division of Applied Sciences, Harvard University, Cambridge, Massachusetts 02138

P. F. Hopkins and A. C. Gossard

Materials Department and Department of Electrical and Computer Engineering,
University of California, Santa Barbara, California 93106

(Received 30 March 1993)

p-type, remotely doped, wide (~ 1000 Å) parabolic GaAs/Al_xGa_{1-x}As quantum wells were investigated by photoluminescence excitation spectroscopy. For three samples, with valence-band edge curvatures equivalent to the potentials of fictitious uniform slabs of charge with three-dimensional (3D) densities of 0.2 , 3 , and 4×10^{16} cm⁻³, the spectra show uniformly spaced peaks with spacings which scale with these 3D densities. This peak structure is similar to that observed for *n*-type, remotely doped parabolic GaAs/Al_xGa_{1-x}As quantum wells. A simple single-particle model is presented which is quantitatively consistent with the spectra for the three samples, assuming the hole gas forms a wide slab in the valence band with density given by the designed 3D density. These results support the conclusions from transport measurements of the existence of wide hole-gas layers in these structures.

Wide layers (≥ 700 Å) of high mobility, low-density hole gas have recently been created¹ using the technique of parabolic well (PBW) confinement, analogous to that which has been used for electron gases.^{2,3} By varying the Al content in an Al_xGa_{1-x}As heterostructure quadratically in the growth direction, one can create a structure with band-edge PBW's in the conduction band (CB) and valence band (VB), as shown in Fig. 1(a). When electrons are added to the well by remote doping, self-consistent quantum-mechanical calculations⁴ verify semiclassical arguments, that the electrons become distributed as a nearly uniform density slab. The potential of the electron slab cancels the band-edge potential over the width of the slab w_e , which is proportional to the filling, leaving a flat bottomed effective potential in the CB. This behavior has been substantially verified by transport measurements.^{3,5} Investigations of the wide, uniform density electron-gas slab created by this technique have revealed new electronic and optical phenomena.^{6,7}

By analogy, it was speculated that if, instead of electrons, holes are added to this PBW system by remotely doping with Be, a slab of nearly uniform density hole gas would be created, with 3D density given by $p_{3D} = 2\Delta E_{VB}\epsilon/\pi e^2 L_z^2$, determined by the bare parabolic curvature of the VB.¹ Here ΔE_{VB} is the difference between the band-edge energies at the center of the VB PBW and at the edge, ϵ is the dielectric constant, e is the electron charge, and L_z is the width of the well. The potential of the hole gas slab cancels the PBW potential in the VB over the width of the slab w_h , which is proportional to the filling, i.e., $w_h = p_s/p_{3D}$, where p_s is the hole sheet density. This leaves a flat bottomed effective potential well in the VB as shown in Fig. 1(b). This hole-gas system, however, is not entirely analogous to the electron-gas system created in the *n*-type doped PBW

structure because of the valence-band degeneracy, and so the validity of this model is not obvious.

The successful realization of this system would open up new opportunities for investigating the electronic and optical properties of wide, low-density hole-gas layers at low temperatures. Initial magnetotransport and

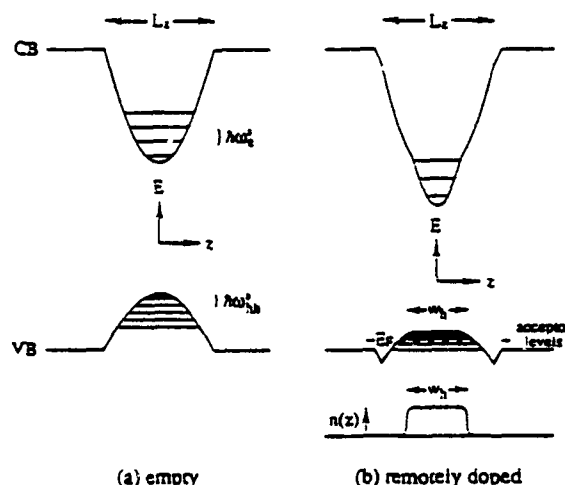


FIG. 1. Schematic illustration of the conduction- and valence-band-edge profiles in (a) an empty Al_xGa_{1-x}As parabolic well, with *z*-confined energy levels simple-harmonic-like (evenly spaced) in the CB and VB, and (b) a *p*-type remotely doped parabolic well, with energy levels simple-harmonic-like in the CB, but square-well-like in the VB. (The square-well level spacings are shown greatly expanded for clarity, and only the heavy-hole levels in the VB are shown.) The effective width of the square well is given approximately by the width w_h of the hole slab indicated by the charge-density profile shown at the bottom of (b).

capacitance-voltage measurements on remotely Be doped PBW's have verified the creation of wide, high mobility hole-gas layers in these structures.¹ Further understanding of this system could be obtained from measurements of the subband energy-level structure. We report here an investigation of this system using photoluminescence excitation spectroscopy (PLE), which gives spectra with peaks at the energies of exciton absorption transitions between occupied VB subbands and unoccupied CB subbands.⁴

The PBW samples were fabricated by molecular-beam epitaxy on GaAs (100) substrates, as discussed by Hopkins, Campman, and Gossard.¹ The parabolic band-edge variations were constructed from 20-Å period superlattices, each period containing a GaAs and an $\text{Al}_x\text{Ga}_{1-x}\text{As}$ layer, with the relative width of the two layers varied using a computer controlled shutter to produce an average Al concentration with a parabolic profile, with x near zero at the center. The holes were introduced in the VB well from Be δ -doped regions set back 100 Å on each side.

Three structures with different design densities p_{JD} and sheet densities p_s were studied, and are labeled samples 1, 2, and 3 in the order of increasing p_{JD} . Sample 1 had $L_z = 5200$ Å, with a design density of $p_{\text{JD}} = 0.2 \times 10^{16} \text{ cm}^{-3}$. It was made with GaAs/ $\text{Al}_{0.3}\text{Ga}_{0.7}\text{As}$ layers with the average x given by $x = 0.005$ at the center of the well and $x = 0.233$ at the edge. It had a measured sheet density and mobility of $p_s = 0.75 \times 10^{11} \text{ cm}^{-2}$ and $\mu = 18000 \text{ cm}^2 \text{ V}^{-1} \text{ sec}^{-1}$, respectively, determined by the Hall effect at 4.2 K. Sample 2 had $L_z = 2400$ Å, with a design density of $p_{\text{JD}} = 3 \times 10^{16} \text{ cm}^{-3}$. It was made with GaAs/ $\text{Al}_{0.65}\text{Ga}_{0.35}\text{As}$ layers with the average x given by $x = 0.015$ at the center of the well and $x = 0.69$ at the edge. It had a measured sheet density and mobility of $p_s = 2.3 \times 10^{11} \text{ cm}^{-2}$ and $\mu = 15000 \text{ cm}^2 \text{ V}^{-1} \text{ sec}^{-1}$, respectively, measured by the Hall effect at 4.2 K. Sample 3 was extensively studied.¹ It had $L_z = 1000$ Å, with a design density of $p_{\text{JD}} = 4 \times 10^{16} \text{ cm}^{-3}$. It was made with GaAs/ $\text{Al}_{0.35}\text{Ga}_{0.65}\text{As}$ layers with the average x given by $x = 0.01$ at the center of the well and $x = 0.2$ at the edge. The sheet density and mobility were $p_s = 3 \times 10^{11} \text{ cm}^{-2}$ and $\mu = 23000 \text{ cm}^2 \text{ V}^{-1} \text{ sec}^{-1}$ respectively, measured by the Hall effect at 0.1 K. Low-temperature ($T \leq 4.2$ K) capacitance-voltage measurements indicated that the hole gas had roughly uniform density and a width of $w_h \sim 700$ Å, in rough agreement with the expected width of $w_h = p_s / p_{\text{JD}}$.

Figure 2 shows PLE spectra for the three samples at 2.2 K, taken in the backscattering configuration with power density of 0.1 W/cm^2 and instrumental resolution of 0.1 meV . Each of the three spectra is seen to have a relatively sharp peak (compared to the higher-energy structures) at the band edge. For higher energies each spectrum is dominated by a series of uniformly spaced peaks, with spacings which scale with the design density p_{JD} . The uniform spacings are not the result of optical interference in the sample or apparatus. For all samples the peak positions were independent of the angle of the sample with respect to the incident and scattered light,

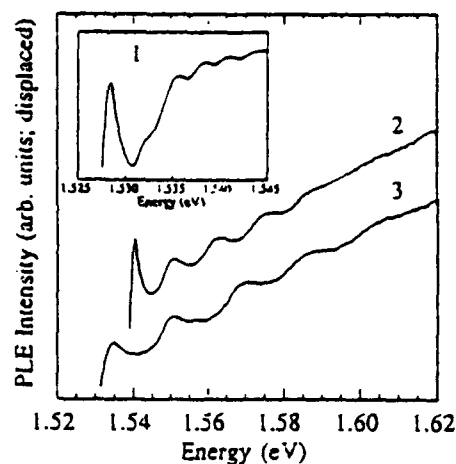


FIG. 2. PLE spectra, taken in the backscattering configuration at 2.2 K, of three remotely Be doped $\text{Al}_x\text{Ga}_{1-x}\text{As}$ parabolic wells. Sample 1 (inset), sample 2, and sample 3 have design densities of $p_{\text{JD}} = 0.2, 3,$ and $4 \times 10^{16} \text{ cm}^{-3}$ respectively, and sheet densities of $p_s = 0.75, 2.3,$ and $3 \times 10^{11} \text{ cm}^{-2}$, respectively. The spectra were scanned at a constant power density of 0.1 W/cm^2 . The resolution is 0.1 meV .

and the peaks were observed to shift rigidly with temperature with the temperature dependence of the GaAs band gap. Also, PLE measurements on empty PBW's and remotely Be doped single heterojunctions with similar sheet densities did not show the uniformly spaced peaks observed in the doped PBW's. Thus this behavior seems to be related to the presence of a hole gas in a PBW potential.

The structure of the PLE spectra for remotely Be doped PBW's is similar to that observed for remotely n -type doped PBW's, for which uniformly spaced peaks with spacings scaling with the CB design density were reported.⁷ For the remotely n -type doped PBW system a simple model based on single-particle transitions between the VB and CB subband levels determined by the effective potentials was suggested.⁷ A related model can account for the uniformly spaced peaks in the remotely Be doped PBW PLE spectra. Due to the hole slab in the VB, the self-consistent effective potential for the holes is not parabolic, but square-well-like, giving a nonuniform energy-level spacing [see Fig. 1(b)]. However, a uniform spacing survives in the CB, since the self-consistent effective potential in the CB is still parabolic, but with the spacing determined by the sum of the bare band-edge curvatures of the CB and VB. This gives a CB subband energy-level spacing given by

$$\Delta E = \hbar \left[\frac{K_{\text{CB}} + K_{\text{VB}}}{m_e^*} \right]^{1/2}, \quad (1)$$

where $K_{\text{CB}, \text{VB}} = d^2 E_{\text{CB}, \text{VB}} / dz^2 = 8 \Delta E_{\text{CB}, \text{VB}} / L_z^2$ and m_e^* is the electron effective mass in the CB. Due to the large size of the heavy-hole mass ($m_{\text{hh}}^* \approx 0.51 m_0$) and the wide (≥ 700 Å for all three samples) flat bottomed effective well in the VB, for the first several occupied (by electrons) VB subbands, the subband spacing is very small ($\ll 1 \text{ meV}$). Thus allowed transitions from the low-energy,

nearly degenerate occupied subbands of the VB to the more widely spaced CB subbands are expected to be separated by approximately ΔE . A plot of the measured peak spacing vs the calculated ΔE for the three samples is shown in Fig. 3, with the line representing the prediction of the model. The figure shows that this simple model fits the data well within the error bars for samples 1 and 2, and just within the vertical error bar for sample 3. The vertical error bars come primarily from the uncertainty in the well width L_z , which is $\sim 20\%$ for sample 3 due to the measurement being taken from a sample near the edge of the nonrotated wafer. The fit occurs with no adjustable parameters for the samples with design densities ranging in magnitude by a factor of ~ 20 .

Though this single-particle model for the uniformly spaced PLE peaks for this p -type doped PBW structure is certainly not proved, it is remarkable that closely related single-particle models quantitatively account for uniformly spaced peaks in the spectra for both the n -type and p -type doped PBW structures, in spite of the different potentials and effective masses of the two bands, CB and VB, containing the particle gas in the two cases.⁷ For the n -type doped PBW structure the potentials are the reverse of that shown in Fig. 1(b), with the square-well-like effective potential in the CB and the PBW-like effective potential in the VB. The single-particle model offered as an explanation of the uniformly spaced peaks in these PLE spectra gives a peak spacing ΔE given by Eq. (1), but with m_e^* replaced with m_{hh}^* and with an additional factor 2 multiplying the right-hand side of the equation.⁹ The factor 2 occurs because in this case, due to the much lighter electron mass, the square-well-like levels in the CB are spaced by energies on the order of 1 meV and thus cannot be considered degenerate. Therefore, comparing a particular strongly allowed transition (one between VB and CB subbands with the same quantum number) with other strongly allowed transitions, the energy differences are not spaced by the VB harmonic-oscillator spacing. However, for a given final CB state (with definite parity), allowed transitions occur from VB states of the same parity, i.e., from alternate VB harmonic-oscillator levels, thus giving rise to peak separations of *twice* the VB harmonic-oscillator spacing. Transitions to other CB states have the same energy separations, thus preserving the periodicity in the PLE spectra. What the two models for the two complementary structures have in common is that the slab of charge in one of the two bands in each case results in an effective potential in the other band which remains parabolic, and this gives rise to strong periodic oscillations in the PLE spectra (or equivalently the absorption spectra⁸).

This model for the optical transitions in p -type doped PBW structures, if valid, has several implications for the Be doped PBW samples investigated here. The uniform spacing of the peaks and their quantitative agreement with ΔE give further verification of the creation of wide

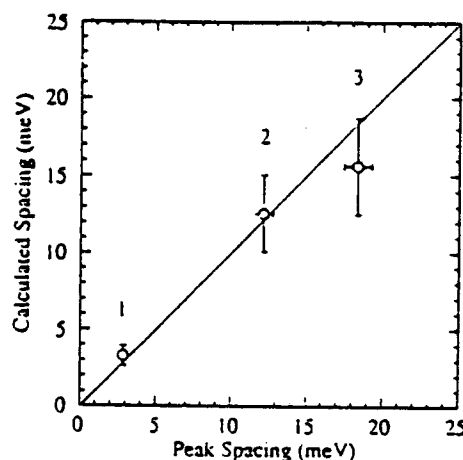


FIG. 3. Comparison of the measured peak spacing vs the calculated CB effective parabolic well energy-level spacing ΔE , Eq. (1), for three remotely doped PBW's. Samples 1, 2, and 3 have VB band-edge curvatures corresponding to three-dimensional densities of 0.2, 3, and $4 \times 10^{16} \text{ cm}^{-3}$.

hole-gas slabs in these structures. The extent to which the uniformly spaced peaks range in energy above the low-energy edge of each spectrum gives a lower bound for the width of the slab for that sample. This is because, as seen in Fig. 1(b), for transitions to CB states near or above the band-edge energy corresponding to the edge of the hole slab, the energy-level spacing changes. For example, the extent of the uniformly spaced peaks in sample 3 implies a uniform slab width of $\geq 500 \text{ \AA}$, compared to a value of 700 \AA determined by capacitance-voltage measurements. The uniformity of the peak spacing in principle gives some measure of the uniformity of the hole-gas density over the layer width, although this is difficult to quantify. Nevertheless, large deviations from uniform density can be ruled out by the peak spacing uniformity, in this model.¹⁰

In conclusion, PLE measurements of three Be-remotely-doped PBW's show uniformly spaced peaks whose uniform spacing scales with valence-band-edge PBW curvature, or 3D design density p_{3D} . This behavior is similar to that observed for n -type remotely doped PBW's, for which a simple single-particle model was found quantitatively consistent with the measurements. For the Be doped PBW's a related single-particle model is found quantitatively consistent with the spectra for the three samples, assuming the hole gas forms a roughly uniform density slab with density given by the design density p_{3D} .

The work at Harvard University was supported by the MRL under Grant No. NSF-DMR-89-20490. The work at UCSB was supported by the Air Force Office of Scientific Research under Grant No. AFOSR-91-0214.

- ¹P. F. Hopkins, K. L. Campman, and A. C. Gossard, *J. Cryst. Growth* 127, 798 (1993).
- ²M. Sundaram, A. C. Gossard, J. H. English, and R. M. Westervelt, *Superlatt. Microstruct.* 4, 683 (1988).
- ³T. Sajoto, J. Jo, M. Santos, and M. Shayegan, *Appl. Phys. Lett.* 55, 1430 (1989).
- ⁴A. J. Rimberg and R. M. Westervelt, *Phys. Rev. B* 40, 3970 (1989).
- ⁵E. G. Gwinn, P. F. Hopkins, A. J. Rimberg, R. M. Westervelt, M. Sundaram, and A. C. Gossard, *Phys. Rev. B* 41, 10 700 (1990).
- ⁶K. Karrai, X. Ying, H. D. Drew, M. Santos, M. Shayegan, S.-R. E. Yang, and A. H. MacDonald, *Phys. Rev. Lett.* 67, 3428 (1991).
- ⁷J. H. Burnett, H. M. Cheong, W. Paul, P. F. Hopkins, E. G. Gwinn, A. J. Rimberg, R. M. Westervelt, M. Sundaram, and A. C. Gossard, *Phys. Rev. B* 43, 12 033 (1991).
- ⁸G. Bastard, *Wave Mechanics Applied to Semiconductor Heterostructures* (Les Éditions de Physique, Les Ulis, France, 1988).
- ⁹We have verified the quantitative agreement between the calculated ΔE and the uniformly spaced PLE peak separations for the *n*-type doped PBW system for samples with a wider range of band-edge curvatures than reported previously (Ref. 7), and we have also observed the uniform peak spacing in the photocurrent spectra of the samples. [J. H. Burnett, H. M. Cheong, W. Paul, P. F. Hopkins, R. M. Westervelt, and A. C. Gossard (unpublished)].
- ¹⁰For example, a first-order perturbation-theory calculation shows that deviations from uniform density of 50% or more due to a quadratic variation in the density profile would give rise to observable deviations from peak spacing uniformity, which are not seen in the spectra.

Single-particle subband spectroscopy in a parabolic quantum well via transport experiments

K. Ensslin and A. Wixforth

Sektion Physik, Universität München, Geschwister-Scholl Platz 1, 8000 München 22, Germany

M. Sundaram, P. F. Hopkins, J. H. English, and A. C. Gossard

Materials Department, University of California, Santa Barbara, California 93106

(Received 4 May 1992)

The transport properties of a parabolic quantum well are investigated at low temperatures $0.5 \text{ K} < T < 4 \text{ K}$. A front-gate voltage is used to tune the carrier density and hence the subband structure over a wide range. Various orientations of a magnetic field B with respect to the normal of the sample $0^\circ \leq \alpha \leq 90^\circ$ are investigated. For $\alpha = 0^\circ$, where B is oriented along the surface normal of the sample, quantum Hall states can be suppressed and recovered depending on the carrier density of the sample. This effect is explained quantitatively by a self-consistent calculation that considers the interplay of occupied Landau levels belonging to different subbands. A suppressed quantum Hall state can also be recovered via a tilted magnetic field. The resonant-subband-Landau-level coupling leads to a repulsion of the levels and, therefore, to the creation of an energy gap. For $T \leq 0.5 \text{ K}$ the spin splitting of the Landau levels appears in the magnetoresistance. In the regime of carrier densities where the quantum Hall plateau corresponding to filling factor $\nu = 4$ is suppressed, a double minimum structure for $\nu = 3$ is observed, reflecting the different exchange enhancement of the spin splitting of the two lowest subbands. For magnetic fields oriented in the plane of the sample, a band structure arises that leads to an anisotropic conductivity for current flow perpendicular and parallel to the magnetic-field orientation.

I. INTRODUCTION

Subband spectroscopy in low-dimensional semiconductors is usually accomplished with optical experiments.¹ Transitions from occupied to empty states in a two-dimensional electron (2DEG) have been studied by Raman spectroscopy² and by far-infrared (FIR) spectroscopy in a strip-line configuration.³ In tilted magnetic fields the resonant-subband-Landau-level coupling (RSLC) was used⁴⁻⁹ to determine the subband separations from the coupling of the cyclotron resonance and the intersubband resonance. These powerful experimental techniques suffer from the fact that the energies they determine are influenced by collective effects.^{10,11} This is especially true in parabolic quantum wells where there exists the unique situation that the RSLC indeed occurs between the plasma frequency and the respective Landau levels. This has been shown theoretically¹² and confirmed experimentally.^{9,13}

In this paper we present a series of magnetotransport experiments that allow the direct determination of the single-particle subband separations in a parabolic quantum well. For magnetic fields oriented perpendicular to the sample a series of equidistant Landau levels develops on each subband. The carrier density and therefore the subband structure can be controlled reproducibly via a front-gate voltage. For a given set of parameters two Landau levels belonging to different subbands can be degenerate at the Fermi energy. In this case the corresponding quantum Hall state is suppressed. It can be recovered by lifting the degeneracy of these Landau levels via a suitable gate voltage. If the magnetic field is tilted with respect to the normal of the sample these Landau

levels repel each other and the degeneracy is also lifted. In both cases the corresponding quantum Hall state is recovered. These experiments depend sensitively on the subband structure and allow a detailed comparison of experiment and calculation. At low temperatures, $T \leq 0.5 \text{ K}$, the Zeeman splitting of the Landau levels is resolved. An especially interesting situation occurs when the quantum Hall state for filling factor $\nu = 4$ is suppressed, while a double minimum structure in the vicinity of $\nu = 3$ is observed in the magnetoresistance. This behavior is explained by the subband dependent exchange enhancement, that leads to an effective charge transfer between the two subbands. An anisotropic band structure arises for magnetic fields oriented in the plane of the sample. This is caused by the fact that the effective mass as well as the scattering time depend on the direction of the field within the sample plane. This is strongly apparent in the conductivity for current flow parallel and perpendicular to the magnetic-field orientation. The features in the magnetoresistance arising from the magnetic depopulation of subbands are much more pronounced for current flow perpendicular to the magnetic-field orientation compared to the parallel orientation. This independent method of determining the single-particle subband energies in a transport experiment gives results that are in good agreement with the experiments described before.

The paper is arranged as follows: Section II describes in detail the self-consistent confining potential and subband occupation of the sample, Sec. III presents magnetotransport experiments for $\alpha = 0$, where α is the angle between the normal of the sample and the magnetic-field orientation. In this case transport is dominated by the formation of Landau levels.¹⁴ Section IV shows that the spin splitting of Landau levels dramatically influences the

magnetoresistance. Section V focuses on the tilted field case $0 \leq \alpha \leq 60^\circ$ with emphasis on the manifestation of resonant-subband-Landau-level coupling.¹⁵ Section VI contains results from the in-plane field case $\alpha = 90^\circ$, where the magnetic depopulation of the subbands dominates the transport properties. Section VII summarizes the results.

II. CONFINING POTENTIAL AND OCCUPATION OF SUBBANDS

The GaAs- $\text{Al}_x\text{Ga}_{1-x}\text{As}$ parabolic quantum well (PQW) is grown by molecular-beam epitaxy. On top of the semi-insulating substrate there is a 400-nm GaAs buffer layer, followed by 200-nm $\text{Al}_{0.3}\text{Ga}_{0.7}\text{As}$, 16-nm $\text{Al}_{0.3}\text{Ga}_{0.7}\text{As}$ with Si doping ($N_D = 2.5 \times 10^{17} \text{ cm}^{-3}$), 20-nm $\text{Al}_{0.3}\text{Ga}_{0.7}\text{As}$ spacer, the 75-nm-wide parabolic well with varying $0 < x < 0.1$. The Al content x is varied through a defined sequence of shutter openings and closings producing a 2-nm period superlattice to achieve a parabolic variation of the conduction band.¹⁶ The cap is formed by a 20-nm $\text{Al}_{0.3}\text{Ga}_{0.7}\text{As}$ spacer and a 101-nm Si-doped $\text{Al}_{0.3}\text{Ga}_{0.7}\text{As}$ ($N_D = 2.5 \times 10^{17} \text{ cm}^{-3}$) layer. The well is designed to have a symmetric electron distribution within the well. At $T = 4.2 \text{ K}$ and $V_g = 0$ the total carrier density is $N_s = 5 \times 10^{11} \text{ cm}^{-2}$ and the mobility of the electron gas in the well is $\mu = 100,000 \text{ cm}^2/\text{Vs}$. The mesa structure consists of two Hall bars that are oriented perpendicular to each other. The width of the current path is $50 \mu\text{m}$ and the spacing between the voltage probes is $150 \mu\text{m}$. Ohmic contacts are made by annealing AuGe/Ni and a front gate (Ti/Au) is evaporated onto the sample. This allows us to tune the carrier density in the parabolic well and with it the width of the electron layer and the number of occupied subbands.¹⁷ The low-frequency ($\nu \approx 30\text{-Hz}$) transport experiments are performed in a superconducting magnet (0–12 T) and the samples are cooled by He exchange gas at temperatures $0.5 \text{ K} < T < 4.2 \text{ K}$. For this section the magnetic field is oriented perpendicular to the plane of the electron gas. The samples are cooled down in the dark.

Figure 1 presents the results of a self-consistent calculation for the conduction-band edge, the occupied subbands, and the wave functions of the investigated sample. The carrier density is $N_s = 5 \times 10^{11} \text{ cm}^{-2}$. The surface of the sample is on the left-hand side of the figure. The inset shows the region of the potential where the electrons actually reside. The symmetry of the wave functions indicates that the hard-wall potential on the right-hand side of the potential does not affect the electron density or the energy levels strongly. The flatness of the potential over a wide region (almost 40 nm) as well as the total carrier distribution shows the quasi-3D nature of the filled parabolic potential. According to the generalized Kohn's theorem¹² an optical intersubband spectroscopy experiment will always detect the plasma frequency of the electron system^{8,9,13} independent of the electron-electron interaction and therefore the number of electrons. A transport experiment will rely on the single-particle energy levels and therefore depend on the energies and wave

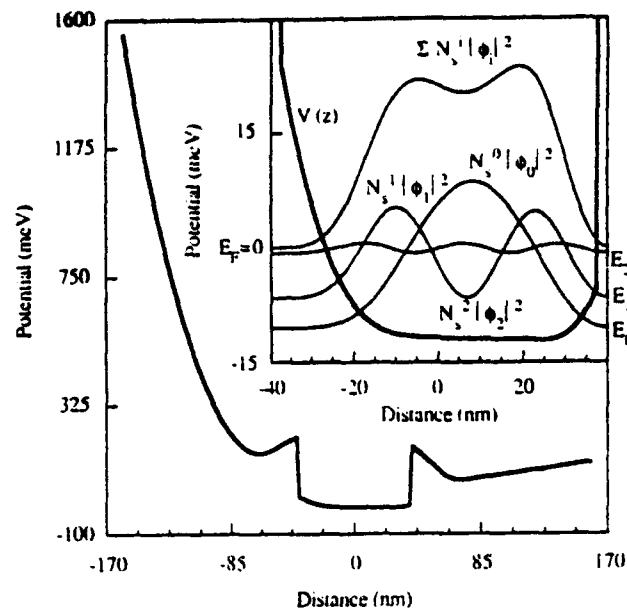


FIG. 1. Self-consistent calculation of the potential of the parabolic well with the surface of the sample (front gate) on the left-hand side of the figure. The inset is an enlarged scale of the potential well and the wave functions weighted by their corresponding subband carrier densities.

functions as depicted in Fig. 1.

Figure 2 presents experimental results on the mobility of the electrons as a function of carrier density. The evaluation of the mobility from the magnetoresistance is usually not a straightforward procedure for systems with more than one occupied subband.^{18–25} In cyclotron resonance^{26,27} the scattering time of a subband can directly be deduced from the linewidth of the respective resonance. In a transport experiment a model has to be used to extract scattering times of various subbands.^{18,20,23} Van

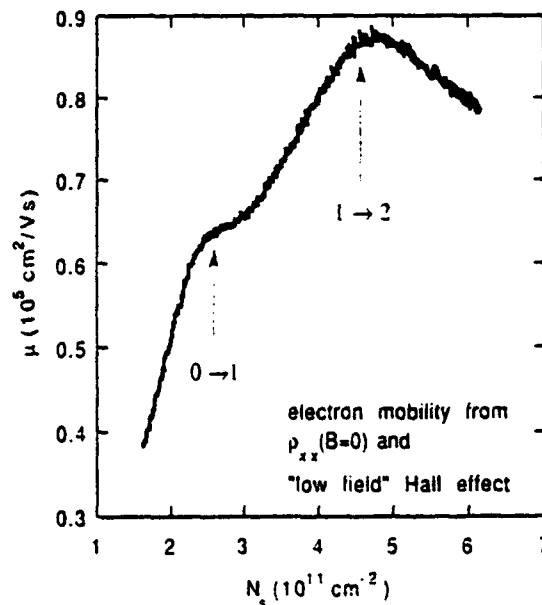


FIG. 2. Mobility at $T = 4.2 \text{ K}$ as a function of carrier density tuned by a gate voltage. The arrows indicate where the E_1 and E_2 subbands become populated and consequently a channel for intersubband scattering opens up.

Houten *et al.* (Ref. 24) showed that for a high-mobility 2DEG with two occupied subbands a positive magnetoresistance ΔR occurs, with $\Delta R/R \propto (\mu_0 - \mu_1)^2$, μ_i being the Drude mobility of the carriers in subband i . The measurement of the magnetoresistance ρ_{xx} on the presented PQW reveals a flat behavior, i.e., ρ_{xx} does not depend on B for very small magnetic fields $B < 0.2$ T and for all temperatures and gate voltages investigated. We thus assume that the scattering time in all occupied subbands is nearly the same and we can therefore simplify the analysis of the mobility as presented in Fig. 2. The Hall effect ρ_{xy} has been measured for a low magnetic field as a function of gate voltage. A linear relation between the carrier density N_i and the gate voltage V_g is obtained in agreement with the evaluation of the $1/B$ periodicity of the Shubnikov-de Haas oscillations at high magnetic fields. The data in Fig. 2 clearly show a nonmonotonic behavior for the mobility μ as a function of carrier density. For two-dimensional electron gases with only one occupied subband a power-law dependence of $\mu(N_i)$ has been observed²⁸ and explained by ionized impurity scattering. The same is observed in our sample below $N_i = 2.5 \times 10^{11} \text{ cm}^{-2}$. For higher carrier densities a second subband becomes populated which opens up an additional scattering channel, i.e., intersubband scattering occurs. This explains the structure in Fig. 2 marked by the first arrow. Similar effects have been observed in GaAs heterostructures (Refs. 18 and 24). A much more pronounced structure however occurs in our data around $N_i = 4.5 \times 10^{11} \text{ cm}^{-2}$, where the mobility has a maximum and then drops for increasing N_i . At this value of the carrier density a third subband becomes populated leading to a further increased intersubband scattering rate. The wave-function overlap which determines the strength of intersubband scattering is especially large between the lowest (denoted by quantum number $i=0$) and the third ($i=2$) subband. This explains the drop of μ as a function of increasing N_i , as soon as the third subband becomes occupied. This sets the limits for the experimentally accessible parameters of this parabolic quantum well.

III. SUPPRESSION AND RECOVERY OF QUANTUM HALL STATES

We will now concentrate on the transport properties of the electron gas under high magnetic fields B that are oriented perpendicular to the surface of the sample. Figure 3 presents data for the Hall resistance ρ_{xy} as a function of magnetic field at a low temperature $T=0.45$ K. Three specific values of N_i are selected. The quantum Hall plateau for filling factor $\nu=2$ ($\nu = hN_i/eB$) is very wide and almost independent of the value of N_i . The well-defined plateau for $\nu=3$ at $N_i = 4.6 \times 10^{11} \text{ cm}^{-2}$ becomes weaker and finally vanishes for decreasing N_i . This is explained by the decrease of the mobility which leads to an overlap of the broadened spin-split Landau levels. A more detailed discussion on the intriguing behavior of the spin states follows in Sec. IV. The interesting filling factor in this figure is however $\nu=4$. The corresponding quantum Hall plateau is well developed for $N_i = 4.6 \times 10^{11} \text{ cm}^{-2}$, completely suppressed for an inter-

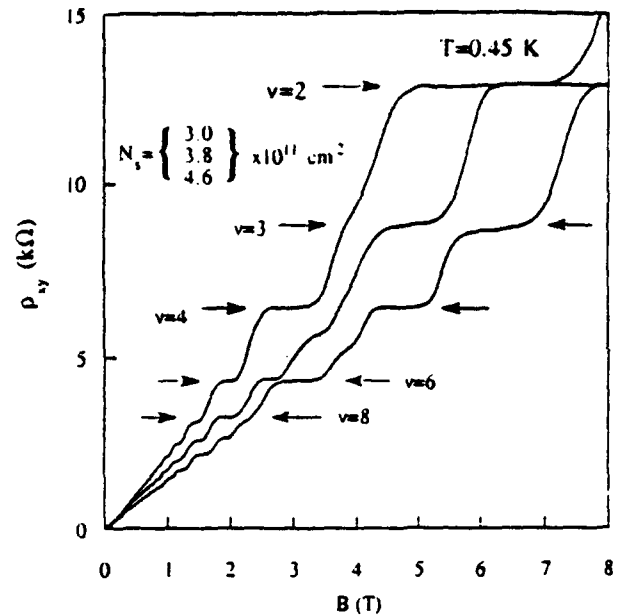


FIG. 3. Hall resistance curves for three different carrier densities measured at low temperatures $T=0.45$ K. The quantum Hall plateau corresponding to $\nu=4$ vanishes and reappears in this range of N_i .

mediate value of $N_i = 3.8 \times 10^{11} \text{ cm}^{-2}$, and entirely recovered for $N_i = 3.0 \times 10^{11} \text{ cm}^{-2}$. A similar behavior is observed for filling factors $\nu=8$ and 12, whereas the suppression of quantum Hall plateaus for $\nu=2$ and 6 is never observed experimentally. The magnetoresistance ρ_{xx} is always correlated with the Hall resistance ρ_{xy} : a pronounced minimum in ρ_{xx} leads to a quantum Hall plateau in ρ_{xy} , a suppressed minimum in ρ_{xx} consequently results in a suppressed quantum Hall plateau in ρ_{xy} . We will concentrate in the following discussion on the behavior of ρ_{xx} , because it can more easily be compared with a theoretical calculation. We will neglect spin splitting in this section, because it is not resolved in the presented measurement.

Figure 4(a) presents a series of magnetoresistance measurements at $T=2$ K. The curves are vertically offset for clarity. The positions of filling factor $\nu=4$ are marked by arrows. In this range of carrier densities two subbands are occupied (see Fig. 1) at $B=0$, so that a minimum in ρ_{xx} does not necessarily coincide with the position of an integer filling factor. For intermediate carrier densities there is actually a maximum in Fig. 4(a) for $\nu=4$. In the following we denote the total filling factor of the PQW by ν ; the filling factor of the subband i is given by $\nu^i = hN_i^i/eB$, N_i^i being the carrier density of subband i . In high magnetic fields carriers may be redistributed among the different subbands but the total carrier density N_i does not depend on B . To understand the data as presented in Fig. 4(a), we solved self-consistently Schrödinger's and Poisson's equation in the presence of a magnetic field. All parameters for the calculation are given by the structure design. The Landau levels are modeled by a Gaussian density of states²⁹ (DOS) with full width at half maximum $\Gamma[\text{meV}] = 0.5 \times (B[T])^{1/2}$. These parameters described reasonably well previous

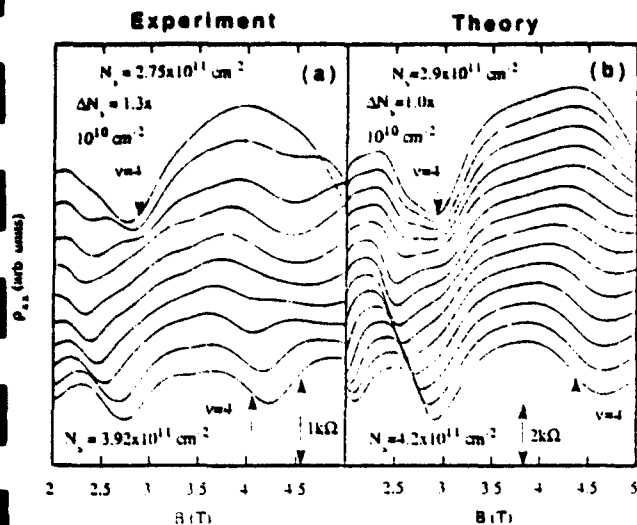


FIG. 4. (a) Experimental magnetoresistance traces for a series of carrier densities at $T=2$ K. The arrows indicate the position of filling factor $\nu=4$. The curves are vertically offset for clarity. The vertical scale is indicated by an arrow. (b) Calculated magnetoresistance traces as described in the text. Note the similarity to the data of 4(a).

magnetocapacitance measurements^{30,31} on samples with similar mobilities. Consequently, there are no adjustable parameters. We did not take into account complications such as spin splitting of the Landau levels, a constant-background DOS (Ref. 32) or a filling-factor-dependent DOS.³⁰ The results are not qualitatively changed by a more refined model of the DOS. From the DOS we calculate the magnetic-field-dependent conductivity $\sigma_{xx}(B)$.²⁹ Since the Hall resistance behaves almost classically in the interesting regime due to the suppression of the Hall plateaus it is reasonable to assume $\sigma_{xy} = -eNs/B$ for the Hall conductivity. This allows us to calculate $\rho_{xx}(B)$ as presented in Fig. 4(b). The overall agreement between experiments [Fig. 4(a)] and theory [Fig. 4(b)] is very good, especially the position of $\nu=4$ with respect to the minima and maxima of ρ_{xx} . The same method of calculating the magnetoresistance but using a magnetic-field-independent subband structure was applied by Gobsch, Schulze, and Paasch³³ to explain the data of Guldner *et al.*³⁴ on heterostructures with two occupied subbands.

An interesting feature in Figs. 4(a) and 4(b) is the double minimum structure in the range $2.5 \text{ T} < B < 3 \text{ T}$. The top part of Fig. 5 presents a calculated magnetoresistance trace for $N_s = 3.2 \times 10^{11} \text{ cm}^{-2}$. The three figures of the lower part show the DOS for three magnetic fields that correspond to the regions on the ρ_{xx} trace as marked by the arrows. Note that the DOS of each subband as well as the total DOS are plotted below and above the Fermi energy E_F . The Landau levels will be denoted in the following by $|i, n\rangle$, where i is the subband index and n the Landau-level index. In going from $B=2.4 \text{ T}$ to $B=2.9 \text{ T}$ the state $|0, 1\rangle$ (dashed line) approaches $|1, 0\rangle$ (dotted line) because, $|0, 1\rangle$ shifts up from the bottom of $i=0$ subband E_0 with $\frac{1}{2}\hbar\omega_c$ while $|1, 0\rangle$ moves up by $\frac{1}{2}\hbar\omega_c$ from E_1 . For an intermediate field $B=2.65 \text{ T}$ the $|1, 0\rangle$

state is just in between the $|0, 1\rangle$ and $|0, 2\rangle$ state making the total DOS at the Fermi energy small. In this way the double minimum structure in ρ_{xx} can be explained.

For low carrier densities $N_s = 3.0 \times 10^{11} \text{ cm}^{-2}$ (see Fig. 3) the upper subband is just barely populated (Fig. 2) at $B=0$. For high magnetic fields the upper subband becomes depopulated at integer filling factors and therefore $\nu=4 = \nu^0 + \nu^1 = 4 + 0$. At high carrier densities $N_s = 4.6 \times 10^{11} \text{ cm}^{-2}$ the upper subband can gain carriers at the cost of the lower one and $\nu=4 = 2 + 2$ will be realized. This results in a quantum Hall state and $N_s^0 = N_s^1$. Such a situation cannot be realized in a triangular shaped potential because there the carrier density in an upper subband N_s^1 will always be much lower than N_s^0 . Consequently the upper subband will be depopulated at $\nu=4$. For intermediate carrier densities $N_s = 3.8 \times 10^{11} \text{ cm}^{-2}$ the influence of the magnetic field on the subband structure is not strong enough to either depopulate the upper subband or match the carrier densities of the two subbands. Two Landau levels originating from different subbands $|0, 1\rangle$ and $|1, 0\rangle$ can be degenerate at the Fermi energy and the quantum Hall state corresponding to $\nu=4$ is suppressed (see Fig. 3).

The question arises whether the degeneracy of Landau

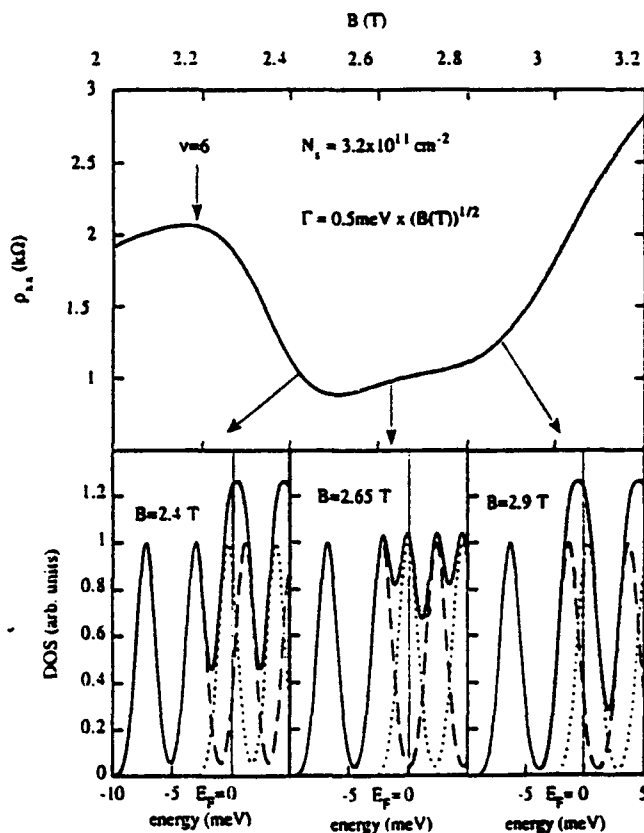


FIG. 5. Calculated magnetoresistance trace presented with an enlarged scale compared to Fig. 5. The lower part of the figure presents three situations for the density of states as marked by the arrows. The dashed line marks the DOS of the lower E_0 subband; the dotted line marks the DOS correspondingly of the E_1 subband, and the solid line indicates the total DOS. The thin solid vertical line represents the position of the Fermi energy $E_F=0$.

levels can also lead to the suppression of quantum Hall states for samples with very high mobility at very low temperatures. We therefore calculate the magnetoresistance ρ_{xx} for very narrow Landau levels $\Gamma[\text{meV}] = 0.005 \times (B[T])^{1/2}$ at $T=0$. The subband structure is calculated self-consistently in the presence of a magnetic field and ρ_{xx} is then obtained as described before. Fig. 6(a) presents the results in an enlarged scale compared to Fig. 4(b). The features are much sharper due to the narrow Landau levels but at intermediate carrier densities $N_s = 3.6 \times 10^{11} \text{ cm}^{-2}$ the position of $\nu=4$ is situated in a maximum of ρ_{xx} . Thus there exists a carrier density even for high mobility samples at very low temperatures where Landau levels will be degenerate and the corresponding quantum Hall state is expected to be suppressed.

For a comparison we calculate the subband structure self-consistently for $B=0$ and modeled the Landau levels on top of these subbands. The effects of the magnetic field on the subband structure are intentionally neglected. The results for ρ_{xx} are presented in Fig. 6(b). The narrow Landau level moves through the ρ_{xx} trace leaving the $\nu=4$ minimum almost unchanged. We conclude that the influence of the magnetic field on the subband structure itself is especially important for samples with very high mobility. The Hartree interaction tends to pin Landau levels of different subbands together to avoid a jump of the Fermi energy from a Landau level from subband $i=0$ to another Landau level from subband $i=1$. The pinning of Landau levels has also been observed via optical spectroscopy in high-density $\text{In}_x\text{Ga}_{1-x}\text{As-InP}$ quantum wells.³⁵

It is interesting to discuss which even integer quantum

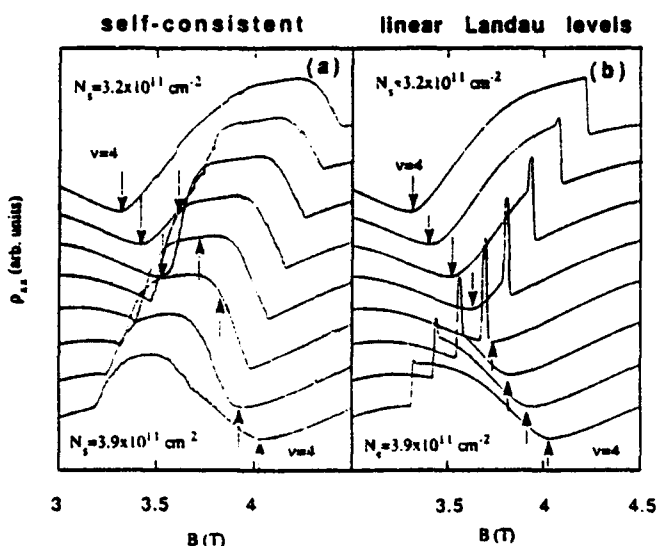


FIG. 6. (a) Self-consistent calculation of the magnetoresistance traces for very narrow Landau levels and $T=0$. The vertical arrows mark the position of filling factor $\nu=4$. It is important to note that for intermediate carrier density $N_s = 3.5 \times 10^{11} \text{ cm}^{-2}$ the position of the arrows sits in a maximum of ρ_{xx} . (b) Calculated magnetoresistance with a constant subband separation E_{10} , independent of magnetic field. The position of filling factor 4 as marked by the arrows is always in a minimum of ρ_{xx} .

Hall state can be suppressed. We again neglect spin splitting for this discussion. Filling factor $\nu=2$ is realized when only one Landau-level and therefore only one subband is occupied. This is true as long as the Landau-level width Γ is smaller than the subband separation E_{10} which is practically the case for all 2DEG's in GaAs heterostructures. Consequently the quantum Hall state corresponding to $\nu=2$, i.e., the quantum lines, can never be suppressed. The $\nu=4$ state can be suppressed as presented in Fig. 3 and discussed above. In our experiments we never observed a situation where the quantum Hall state corresponding to $\nu=6$ is suppressed. The width of the plateau may change, but the plateau is always well developed. The $\nu=8$ state can again be suppressed as discussed in Ref. 15. In general, an even integer quantum Hall state can be suppressed if odd filling factors can occur simultaneously in the respective subbands. This means that an even number has to be represented by the sum of two odd numbers, implying a similar ratio for the carrier densities in the two subbands, since the electrical confinement will always dominate the magnetic-field-induced energy changes. To suppress a quantum Hall state at even ν , this filling factor has to be the sum of odd ν^0 and odd ν^1 . The carrier density within a subband, in general, depends upon the magnetic field. To suppress a quantum Hall state two Landau levels have to be degenerate at the Fermi energy resulting in a large DOS at the Fermi energy. In such a "relaxed" situation the carrier densities in the two subbands have to be close to their $B=0$ values. Otherwise carriers could be easily distributed between the subbands due to the large DOS at E_F without changing E_{10} very much. We conclude that two conditions are important to observe the suppression of an even-integer quantum Hall state: (1) two odd filling factors ν^0 and ν^1 with $\nu^0 + \nu^1 = \nu$ have to be realized in the respective subband; (2) the ratio of the carrier densities at $B=0$ should be close to $N_s^0/N_s^1 \approx \nu^0/\nu^1$. Furthermore ν^0 and ν^1 should be as close as possible to each other. Otherwise the magnetic field depopulates the higher subband and no quantum Hall state can be suppressed.

For example, the $\nu=4$ state is suppressed if $\nu=4 = \nu^0 + \nu^1 = 3 + 1$. With the same argument we find two possibilities for the $\nu=6$ state: $\nu=6 = \nu^0 + \nu^1 = 1 + 5$ and $\nu=6 = \nu^0 + \nu^1 = 3 + 3$. The latter condition does not exist because it implies $N_s^0 = N_s^1$ and therefore a vanishing subband separation. The first condition $\nu=1 + 5$ corresponds to the already discussed situation. The carrier density in the upper subband N_s^1 is much smaller than N_s^0 and high magnetic fields will therefore depopulate the upper subband. We do not exclude that in very specially designed samples the $\nu=6$ state can also be suppressed, but we argue that it is much easier to suppress the $\nu=4$ state. Using the same reasoning we find two conditions to suppress the $\nu=8$ state: $\nu=8 = \nu^0 + \nu^1 = 5 + 3$ or $\nu=8 = \nu^0 + \nu^1 = 1 + 7$. The latter condition is again not favorable because high magnetic fields will depopulate the higher subband. The condition $\nu=5 + 3$ can however easily be realized leading to a suppression of the $\nu=8$ state. Figure 7 presents a schematic illustration for the suppression conditions of $\nu=4, 8, 12$. The Landau levels of the lower (upper) subband are indicated on the left-

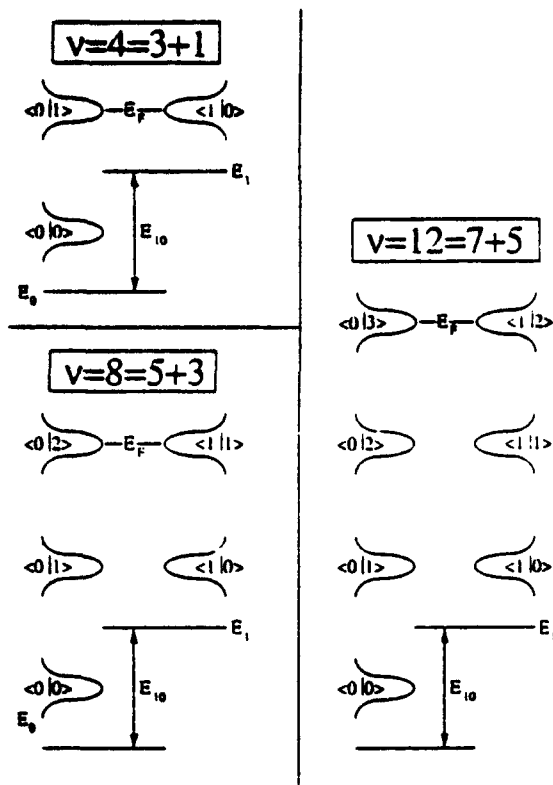


FIG. 7. Schematic illustration of three situations of the energy levels as observed in the experiments. On the left- (right-) hand side the Landau levels of the lower (upper) subband are indicated. Spin splitting is not considered in this picture.

(right-) hand side of the diagram. Along the same line we find for $\nu=10$ three possibilities: $\nu=10=9+1$, $\nu=10=7+3$, and $\nu=10=5+5$. The last case is excluded because it implies degeneracy of the electrical subband energies. The first two cases suggest again a situation where $N_i^1 \ll N_i^0$ which leads to a depopulation of the upper subband in a magnetic field. We note that we do not observe a suppression of the $\nu=10$ in the experiment in agreement with the presented argument. For filling factor $\nu=12$ again three possible scenarios are imaginable: $\nu=12=7+5$, $\nu=12=9+3$, and $\nu=12=11+1$. The last possibility is not realistic due to the above-presented arguments, the first condition $\nu=12=7+5$ can be realized in the experiment. The situation $\nu=12=9+3$ implies $N_i^0 \approx 3N_i^1$ at $B=0$ and therefore coincides with the suppression of $\nu=4$ with $\nu=4=3+1$. Indeed we do observe a simultaneous suppression of the $\nu=4$ and 12 state. However the precise evaluation of the data for large filling factors is difficult because of the many overlapping Landau levels in this case. We conclude that there is a good understanding why and in which range of N_i and B a given even integer quantum Hall state can or cannot be suppressed.

IV. DEGENERACY OF SPIN SPLIT LEVELS

So far the Zeeman spin splitting of Landau levels in a magnetic field has been neglected. Nevertheless it should be possible to study the situation where spin-split levels originating from different subbands are degenerate at the

Fermi energy. We restrict the following discussion to the intriguing behavior of the $\nu=3$ state. It is the best developed spin-split state in the presented experiment and theoretically it allows for a transparent discussion. Figure 8 presents a series of ρ_{xx} data measured at low temperatures $T=0.45$ K for a range of carrier densities where the suppression of the $\nu=4$ state occurs. For high carrier densities and $V_g = -150$ mV (lowest-lying curve) pronounced minima are observed for $\nu=2, 3, 4, 5, 6$ and so on. The uppermost curve with $V_g = -390$ mV shows well-developed ρ_{xx} minima at $\nu=1, 2, 4, 6$ and a weak minimum at $\nu=3$. The curves for intermediate carrier densities $-390 \text{ mV} < V_g < -150 \text{ mV}$ indicate many competing minima for $\nu=3$ and 4. The minima do not lie on the precise position of the respective filling factor.

Figure 9 presents the corresponding ρ_{xy} data for the same range of gate voltages. Well-developed quantum Hall plateaus are observed for $\nu=1$ and 2. For filling factors $\nu=3$ and 4 the quantum Hall plateaus display a variety of features. Especially interesting is the case where ρ_{xy} drops for increasing B and then rises again. This situation cannot be observed at high temperatures where spin splitting is not resolved. The fact that strong spin splitting can be observed in the magnetoresistance ρ_{xx} of GaAs heterostructures³⁶ is based on the exchange enhanced g factor.³⁷ For odd filling factors a filled Landau level at the Fermi energy is fully spin polarized because all occupied states are filled with electrons of the same spin orientation. According to Ando and Uemura (Ref. 37) the exchange enhanced g factor can be written as

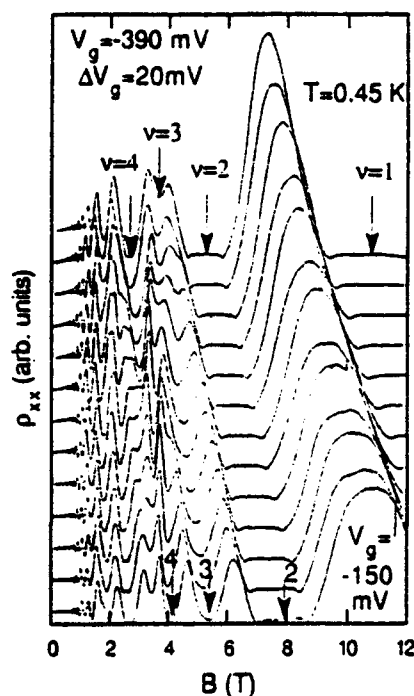


FIG. 8. Experimental magnetoresistance traces for a series of gate voltages at low temperatures $T=0.45$ K. The arrows mark the position of filling factors. The curves are vertically offset for clarity. An interesting double minimum structure occurs for intermediate carrier densities around filling factor $\nu=3$.

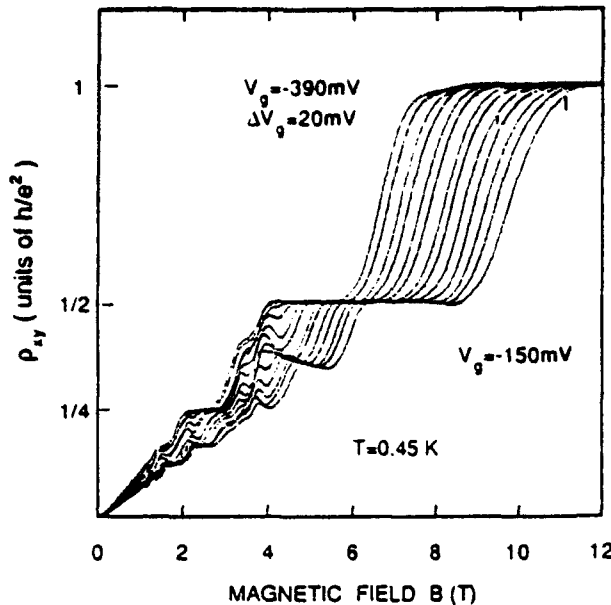


FIG. 9. Hall effect ρ_{xy} for the same range of carrier densities as in Fig. 10. Overshoots of the Hall plateau occur for $\nu=3$ and 4.

$$g^* = g \left[1 + \frac{1}{g\mu B} \sum_N \sum_q \frac{V(q)}{\epsilon(q,0)} (n_{N\uparrow} - n_{N\downarrow}) J_{NN'}^2(q) \right].$$

Here $V(q)$ is the effective two-dimensional Coulomb potential of the electrons, $\epsilon(q,0)$ the dielectric function, and $J_{NN'}^2(q)$ the matrix element of the interaction between electrons in Landau levels N and N' . The population difference of the two spin-split levels is denoted by $n_{N\uparrow} - n_{N\downarrow}$. The value of $n\downarrow$ ($n\uparrow$) is the number of all spin down (up) electrons in all occupied Landau levels of subband i . In a simplified form this can be written as

$$g^* = g[1 + \alpha_{ex}(n\uparrow - n\downarrow)],$$

where α_{ex} now depends on the exchange interaction and also on the subband quantum number i : The important consequence for our experiment is that the energy separation of spin-split Landau levels depends on the filling of these levels ($n\uparrow, n\downarrow$) as well as on the subband quantum number. We will therefore denote the bare g factor in subband i by g_i , the enhanced g factor by g_i^* . To realize filling factor $\nu=3$ there are, in principle, two possibilities that are indicated schematically in Fig. 10. If the $|i=0, n=1\rangle$ and $|1,0\rangle$ levels are degenerate the exchange enhancement may lead to a situation where the spin down (\downarrow) level of the $|0,1\rangle$ state drops in energy and $\nu=3$ is realized by $\nu=\nu^0 + \nu^1 = 3+0$. Alternatively the enhanced spin splitting may occur in the higher-lying subband resulting in $\nu=3=2+1$. These two cases differ dramatically in the carrier densities they assign to the two electrical subbands. The exchange enhancement in the second case will be larger because the upper subband is completely spin polarized ($n\uparrow=0$) whereas the situation as sketched on the left hand side of Fig. 10 occurs due to the spin splitting of the $n=1$ Landau level in the lower subband. The enhanced g factor g_0^* will be smaller because of the spin-unpolarized Landau level $n=0$ below

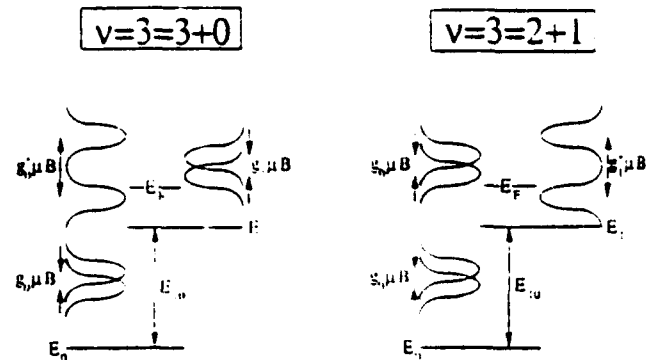


FIG. 10. Schematic representation of two situations that result in three occupied Landau levels. The bare g factor of the system is marked by g_0 and g_1 , the enhanced g factor of the upper and lower subband by g_0^* and g_1^* , respectively.

the spin-polarized state in the $n=1$ Landau level. We conclude that the interesting double minimum structure in Fig. 8 around $\nu=3$ occurs because the enhancement of the g factor is different in the two subbands.

This effect will also influence the suppression behavior of the $\nu=4$ state, since, for resolved spin splitting, $\nu=4$ can be expressed as $\nu=4+0$ or $\nu=3+1$. Again these two situations result in a completely different ratio of carriers in the two subbands (4:0 vs 3:1). Overshoots of quantum Hall plateaus have also been observed for spin-split states³⁸ in GaAs heterostructures with one occupied subband. The temperature and geometry dependence of this effect implies an explanation that relies on the magnetic-field-induced decoupling of the two edge states associated with the topmost spin-split Landau level. In our experiment here on a parabolic quantum well with two occupied subbands we observe similar effects around $\nu=3$ as presented in Fig. 9. In addition to the explanation presented in Ref. 38, we think that the subband dependent enhancement of the g factor as sketched in Fig. 10 further influences the detailed shape of a quantum Hall plateau. In a system with two occupied subbands the spin splitting of Landau levels can also account for features of even integer quantum Hall states.

V. TILTED FIELD EXPERIMENTS: MANIFESTATION OF RESONANT-SUBBAND-LANDAU-LEVEL COUPLING

The magnetotransport data presented so far in this paper were obtained for magnetic fields oriented perpendicular to the plane of the sample. In this case the Hamiltonian can be separated into two terms, one describing the in-plane motion of the carriers and the other the electrostatic confinement in the perpendicular direction.³⁹ The energy-level structure then consists of an equidistant ladder of Landau levels on each electrical subband. The Landau levels associated with different subbands may cross each other without any interaction because the Hamiltonian is separable. In this section we concentrate on the case of tilted magnetic fields where the Hamiltonian can no longer be separated. Consequently Landau levels belonging to different subbands are coupled. This coupling has been observed by far-infrared spectroscopy

ρ_{xx} but is difficult to tackle in a transport experiment. Figure 11(a) presents magnetoresistance data for a series of tilt angles α between the sample normal and the orientation of the magnetic field. The curves are vertically offset for clarity. The measurement temperature is $T=2.2$ K so that spin effects are only weakly pronounced. We will consequently neglect the spin splitting of the Landau levels in the following discussion of RSLC. The gate voltage in Fig. 11(a) is chosen such that the ρ_{xx} minimum and with it the corresponding quantum Hall state for $\nu=4$ is suppressed at $\alpha=0$. The weak minimum between the arrows marking $\nu=4$ and 2 corresponds to the $\nu=3$ state. For increasing tilt angle the minimum for $\nu=4$ starts to reappear and is finally fully recovered for $\alpha=35.9^\circ$. At the same time the neighboring minimum for the $\nu=6$ suffers the opposite fate. For perpendicular magnetic fields, $\alpha=0$, the $\nu=6$ state is well pronounced. As the tilt angle is increased the minimum for $\nu=6$ is completely suppressed at $\alpha=35.9^\circ$. The recovery of the $\nu=8$ state for tilted magnetic fields is described in detail in Ref. 15. The essential features of the magnetoresistance traces in Ref. 15 look very similar as in Fig. 11(a), which shows the recovery of the $\nu=4$ state. In order to understand this remarkable observation in more detail we have solved Schrödinger's and Poisson's equation for $B=0$. The results of Sec. III indicate that the electrical subband energies depend on a perpendicular ($\alpha=0$) magnetic field. The magnitude of these effects is comparable to the typical width (0.5 meV) of a Landau level. For tilted magnetic fields however, $\alpha \neq 0$, the level repulsion is the decisive quantity being larger than typical effects of the magnetic field on the subband structure itself. This justifies the use of a harmonic approximation for the evaluation of the level anticrossing even though the self-consistent potential is no longer parabolic. We therefore

use the subband separation $E_{10}=E_1-E_0$ as obtained from the self-consistent calculation to model a parabolic potential with characteristic frequency $\hbar\omega_0=E_{10}$. The case of a parabolic potential in a tilted magnetic field can be solved analytically^{40,41} and the level repulsion can be obtained. With $\omega_c=eB/m^*$ being the cyclotron frequency the Hamiltonian can be rewritten after a rotation of the coordinate system and one obtains two decoupled harmonic oscillators with frequencies

$$\omega_{1/2}^2 = \frac{1}{2}(\omega_c^2 + \omega_0^2) \pm \frac{1}{2}[\omega_c^4 + \omega_0^4 + 2\omega_0^2\omega_c^2(\sin^2\alpha - \cos^2\alpha)]^{1/2}.$$

The energy spectrum is then given by

$$E_{km} = \hbar\omega_1(k + \frac{1}{2}) + \hbar\omega_2(m + \frac{1}{2}).$$

According to the procedure as described in Sec. III the magnetoresistance ρ_{xx} is calculated. This calculation is based on the subband quantum number i and the Landau-level quantum number n . For tilted magnetic fields hybrid electric magnetic subbands are formed and i and n are no longer good quantum numbers. Consequently the carrier density of a given subband is not a well-defined quantity anymore, especially in the vicinity of a resonant level anticrossing. Nevertheless we associate the new quantum number k and m with the old ones i and n even for $\alpha \neq 0$ as far as the transport calculations are concerned, to accomplish a transparent picture of the experimental situation. A minimum in ρ_{xx} will always correspond to a position of the Fermi energy between two energy levels. The position of the calculated ρ_{xx} minima will therefore not suffer from our assumption. The heights and positions of the maxima are more problematic, since they depend more sensitively on the subband carrier densities and the quantum numbers. The results of this calculation are plotted in Fig. 11(b) in the same way as the experimental data in Fig. 11(a) is presented. The reappearance of the $\nu=4$ minimum for increasing tilt angle as well as the suppression of the $\nu=6$ minimum are very well described by this calculation justifying the approximations that were made. The detailed shape of the oscillations especially in the vicinity of the maxima in ρ_{xx} differs slightly between experiment and theory.

Figure 12 presents the calculated level structure for the typical tilt angles. For $\alpha=0$ the levels are decoupled and the $|0,1\rangle$ and $|1,0\rangle$ states are degenerate at the Fermi energy resulting in the suppression of the $\nu=4$ state. For increasing tilt angle $\alpha=15.4^\circ$ these levels start to repel each other showing a well-defined energy gap at $\alpha=35.9^\circ$ for $\nu=4$. Simultaneously the jump of the Fermi level at $\nu=6$ gets smeared out for increasing tilt angle in agreement with the suppression of the $\nu=6$ state as observed in the experiment [Fig. 11(a)]. The $|0,2\rangle$ and $|1,0\rangle$ state will repel each other at higher tilt angles leading then to a recovery of the $\nu=6$ state. We conclude that the level repulsion caused by the tilted magnetic field strongly manifests in the ρ_{xx} spectra and is well explained by the calculation. Transport experiments can therefore be used to determine the single-particle subband separation of a 2DEG. In analogy to optical experiments the results of

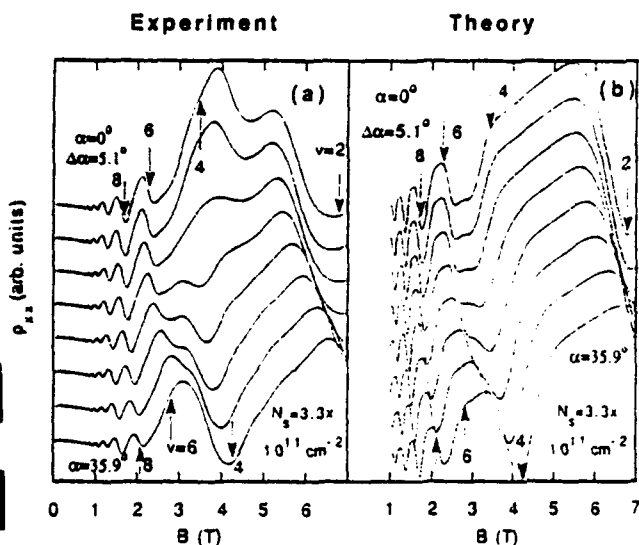


FIG. 11. (a) Experimental magnetoresistance ρ_{xx} for a series of tilt angles α at $T=2$ K. The carrier density is fixed via a suitable gate voltage so that the minimum in ρ_{xx} corresponding to filling factor $\nu=4$ is suppressed for $\alpha=0$. The curves are vertically offset for clarity. (b) Calculated magnetoresistance for the same parameter range as the experimental curves in Fig. 11(a).

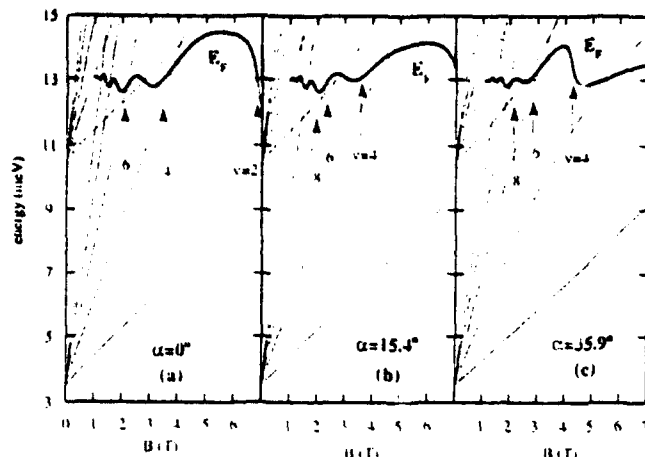


FIG. 12. Calculated energy-level structure for the same carrier density $N_s = 3.3 \times 10^{11} \text{ cm}^{-2}$ as in Fig. 11. For increasing tilt angle the energy gap at the Fermi energy for $\nu=4$ opens up resulting in the recovery of the $\nu=4$ minimum as depicted in Fig. 11.

the transport experiments in Fig. 11(a) may be interpreted as an exchange of oscillator strength between the $\nu=4$ and the $\nu=6$ state.

Figure 13 presents a comparison of three experimentally determined values for the subband separation E_{10} and the value of E_{10} from a self-consistent calculation. According to the arguments as presented in Sec. III only the suppression of the $\nu=4, 8$, and 12 state can clearly be observed in the experiment. From Fig. 11(a), which starts from a suppressed $\nu=4$ state at $\alpha=0$, the angle α and magnetic field can be deduced at which this state is recovered. With $B \cos \alpha = E_{10}$ we can extract the subband separation for this given carrier density $N_s = 3.3 \times 10^{11} \text{ cm}^{-2}$. Accordingly we find values for

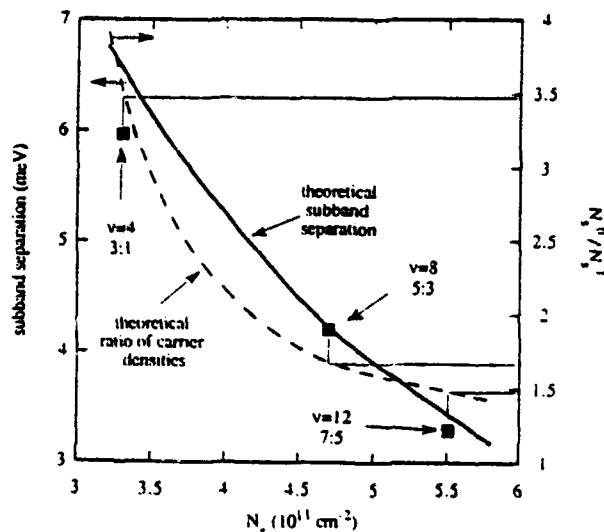


FIG. 13. The squares indicate the experimental results for the subband separation E_{10} as a function of carrier density as obtained from RS²C. The thick solid line is the result of a self-consistent calculation. The dashed line presents the calculated ratio of the carrier densities in the two subbands at $B=0$. The thin solid lines are guides to the eye as described in the text.

$E_{10}(N_s)$ for the suppressed $\nu=8$ state (Ref. 24) and the $\nu=12$ state as marked by the solid squares in Fig. 13. The full line is the result of the self-consistent calculation for $B=0$ in good agreement with the experimental results. The situation to suppress the $\nu=4$ state at $\alpha=0$ is most favorable, if the ratio of the carrier densities in the two subbands at $B=0$ is $N_s^0:N_s^1 \approx 3:1$ because then $\nu=4=3+1$ can be realized easily in a magnetic field. The dashed line in Fig. 13 marks the result of the self-consistent calculation for the ratio of carrier densities $N_s^0:N_s^1$ as a function of total carrier density. The thin solid line starting from the full square corresponding to $\nu=4$ leads vertically until it crosses the dashed line and then moves over to the right-hand scale to end at a value that is not too far off from the desired $N_s^0:N_s^1 \rightarrow 3:1$. The same is done for the $\nu=8(N_s^0:N_s^1 \rightarrow 5:3)$ and $\nu=12(N_s^0:N_s^1 \rightarrow 7:5)$ state. In all cases the calculated ratio of the carrier densities agrees roughly with the desired value for the suppression of the respective state. We conclude that there is a qualitative understanding of the processes that lead to a suppression of quantum Hall states at $\alpha=0$ and their subsequent recovery for tilted magnetic fields.

VI. DEPOPULATION OF SUBBANDS VIA IN-PLANE FIELDS

So far we have described transport techniques that allow the evaluation of single-particle energies from the analysis of Shubnikov-de Haas oscillations in tilted or perpendicular magnetic fields. A complementary technique uses in-plane fields to depopulate subbands via the diamagnetic shift. This technique has been applied by many groups.⁴²⁻⁵⁰ The band structure for in-plane magnetic fields is fundamentally different compared to situations with $\alpha \neq 90^\circ$. For $0 \leq \alpha < 90^\circ$ there is always a component of the magnetic field perpendicular to the plane of the sample that allows for a plane-wave type wave function of the levels proportional to $B_1 = \cos \alpha B$. The Shubnikov-de Haas oscillations, that rely on this degeneracy, can be observed up to tilt angles of $\alpha=89^\circ$ and more (see, for example, Refs. 27 and 48). For $\alpha=90^\circ$ the situation is fundamentally different and an additional type of magnetoresistance oscillation arises, the so-called diamagnetic Shubnikov-de Haas effect.⁴² Figure 14(a) presents results for two orientations of current flow, parallel (ρ_{xx}) and perpendicular (ρ_{yy}) to the magnetic field, that lies in the plane of the electron gas. The inset clarifies the orientation of current flow with respect to the magnetic-field direction. The voltage across the voltage probes of the Hall bars should be ideally zero in this geometry. From the finite voltage that we detect in the experiment we estimate the accuracy of the orientation to be $\alpha=90^\circ \pm 0.01^\circ$. The experiment in Fig. 14(a) clearly shows the influence of the orientation of current flow on the detailed shape of the magnetoresistance trace.

In the literature there is widespread agreement that the magnetoresistance oscillations for in-plane fields arise from the crossing of the diamagnetically shifted subband energies through the Fermi energy. The question, how-

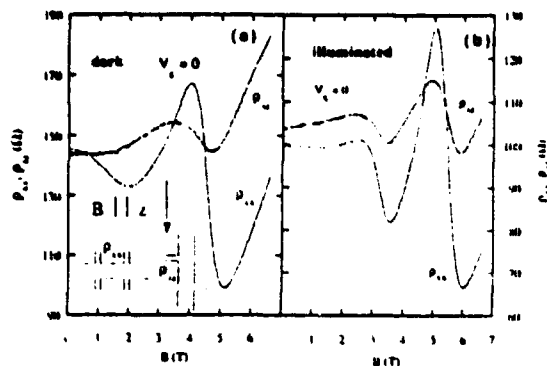


FIG. 14. (a) Magnetoresistance measured in the dark for in-plane magnetic fields at $T=4.2$ K. The resistance for current flow parallel to the magnetic field is denoted by ρ_{xx} , for the perpendicular case by ρ_{xy} . The inset clarifies this situation. (b) Experimental magnetoresistance at $T=4.2$ K after the sample has been strongly illuminated.

ever, at which point on the magnetoresistance trace (maximum, inflection point, minimum) the subband actually becomes depopulated is not satisfactorily answered so far. Furthermore, Fig. 14(a) indicates that the detailed shape of the magnetoresistance trace depends on the orientation of current flow. Most of the publications on the observation of the diamagnetic Shubnikov-de Haas effect do not mention the orientation of current flow in the experimental setup. Zrenner *et al.*⁴⁶ investigated a Si δ -doped layer in GaAs. They used a Corbino geometry and found nice agreement between the fields obtained from the maxima of $d\sigma/dB(B)$ traces and the depopulation fields from a self-consistent calculation. Kroeker and Merkt⁴⁹ did research on a InSb metal-oxide-semiconductor (MOS) structure. They found that the conductivity depends on the orientation of current flow. However the positions of the features caused by the magnetic depopulation of the subbands were independent on the orientation of current flow. The InSb-MOS structure resembles an asymmetric triangular-shaped potential for the electrons that accounts for the observed effects. In this case the electron trajectories depend on the orientation of current flow which therefore also influences the conductivity. Gwinn *et al.*⁴⁷ investigated ρ_{xx} as a function of magnetic field. The positions of the maxima in the magnetoresistance ρ_{xx} were in good agreement with the prediction of the depopulation fields according to a self-consistent calculation by Stopa and Das Sarma.⁵¹ Hopkins⁵⁰ investigated wide PQW's (≈ 500 nm) for both orientations of current flow and found pronounced anisotropies. The experimental results suggest, however, that the imperfections of the parabolic potential, that become more dominant the wider the well is, are crucial to explain the observed features.

The anisotropic band structure in the plane of the 2DEG arising from the in-plane magnetic field results in a magnetic-field-dependent effective mass perpendicular to the magnetic field of $m_x = m^* \omega^2 / \omega_0^2$. Here ω_0 is the harmonic oscillator frequency of the parabolic potential, $\omega_c = eB/m^*$ the cyclotron frequency, and $\omega^2 = \omega_0^2 + \omega_c^2$.

This mass dispersion has been experimentally observed by Batke and Tu⁵² via grating coupler-induced plasmon resonances in GaAs heterostructures. The effective mass in the direction along the magnetic field (z direction) remains unchanged. In this case there is no effective Lorentz force because the directions of the drift velocity and the magnetic field are parallel.

To investigate the influence of the mobility of the anisotropic transport behavior the sample has been illuminated with a red light-emitting diode leading to an increase of the carrier density at $V_g=0$ from 5 to $N_s = 7 \times 10^{11} \text{ cm}^{-2}$ caused by the persistent photoconductivity effect. Simultaneously the mobility has dropped from $\mu = 100,000 \text{ cm}^2/\text{Vs}$ down to $\mu = 80,000 \text{ cm}^2/\text{Vs}$. Figure 14(b) presents data for ρ_{xx} and ρ_{xy} after the sample has been illuminated. There is still a pronounced anisotropy but the positions of the maxima and minima are now closer to each other. The smaller the mobility the lower is the scattering time and the more the electrons are scattered out of their drift velocity direction. They therefore experience the band structure in all directions. We conclude that the anisotropy in ρ_{xx} and ρ_{xy} is reduced for low-mobility samples in agreement with our experimental observations [Fig. 14(a) \rightarrow Fig. 14(b)] and the results of Si- δ layers⁴⁶ and the InSb-MOS structures.⁴⁹

On the theoretical side Tang and Butcher^{53,54} have calculated the transport coefficients assuming an energy independent DOS with $D = m^* \omega / \pi \hbar^2 \omega_0$. Their model system was a PQW with $\hbar \omega_0 = 3 \text{ meV}$ and $N_s = 5.8 \times 10^{11} \text{ cm}^{-2}$. The mobility assumed in their calculation is about a factor of 20 below the mobility of our sample. In Ref. 53 they calculated ρ_{xx} and in Ref. 54 ρ_{xy} . We digitized their results and put it together in one diagram as depicted in Fig. 15. The main features are similar as observed in the experiment; however, the anisotropy is much stronger in the experimental data possibly caused by the lower electron mobility assumed in the calculation. Furthermore in the calculation the inflection point of the ρ_{xx}

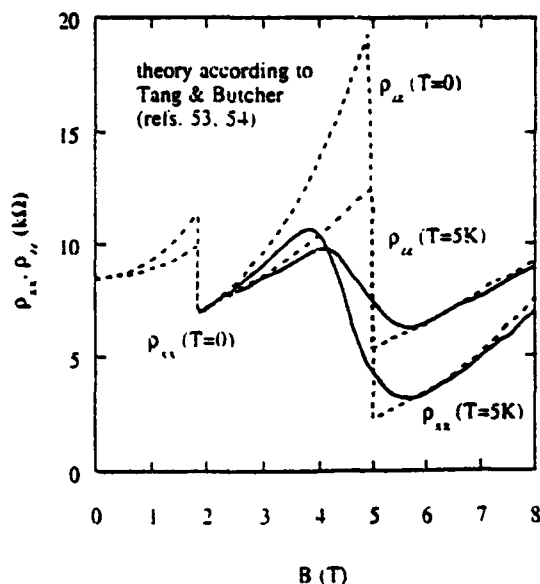


FIG. 15. Calculated magnetoresistance after Refs. 53 and 54. The dotted lines are for $T=0$, the solid line for $T=5$ K.

trace lies at lower magnetic fields compared to the corresponding feature in the ρ_{xx} trace. This is in contrast to the experimental findings [Fig. 14(a)].

Figure 16(a) presents a series of ρ_{xx} measurements for various gate voltages. For high gate voltage, $V_g = +200$ mV, two oscillatory features are observed indicating at least three occupied subbands at $B=0$. For decreasing gate bias the low-field oscillation at around $B=2.5$ T vanishes because the number of occupied subbands at $B=0$ is reduced to two. The oscillatory feature at around $B=5$ T shifts successively to lower magnetic fields for decreasing gate voltage because of the changing subband structure. Figure 16(b) shows the corresponding spectra for current flow parallel to the magnetic-field orientation. The low-field oscillation vanishes in the same way as described in Fig. 16(a). The same correspondence is true for the high-field oscillation that results from the magnetic depopulation of the E_1 subband. The overall strength of the oscillations is however much weaker for current flow parallel to the magnetic field (Fig. 17) compared to the other current orientation.

For a more quantitative analysis we have extracted the magnetic-field positions of the minima, inflection points, and maxima of the magnetoresistance oscillations ρ_{xx} and ρ_{xy} as plotted in Fig. 17. For the low-field oscillation at around $B=2.5$ T only the positions of the minima can be consistently evaluated. The data points for ρ_{xx} lie consistently about 0.5 T below the ones of ρ_{xy} as presented in Fig. 17. Following Ref. 53 a straightforward model is presented to allow a quantitative comparison of experiment and theory. The subband separation E_{10} is calculated self-consistently for $B=0$. The potential is then approximated by a parabolic potential with eigenfrequency ω_0 and $\hbar\omega_0 = E_{10}$. Therefore $\omega_0 = \omega_0(N_s)$ and the energy levels of the total confining potential are given by $E_k = \hbar\omega(k + \frac{1}{2})$ with $\omega^2 = \omega_0^2 + \omega_c^2$ and $\omega_c = eB/m^*$.^{40,41} The depopulation of subband n is then given by the condition $E_F = \hbar\omega(n + \frac{1}{2})$. With the magnetic-field-dependent density of states

$$D = m^* \omega / \pi \hbar^2 \omega_0$$

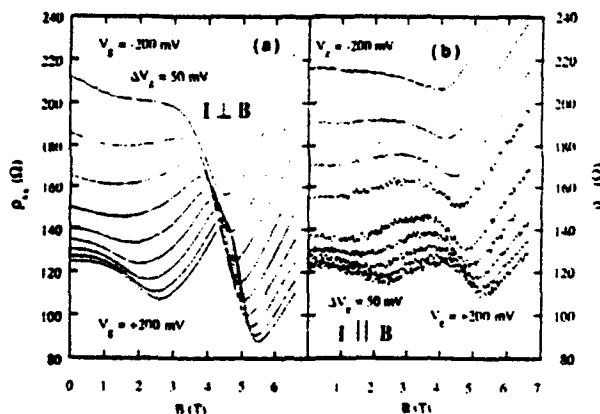


FIG. 16. (a) Experimental magnetoresistance for a series of gate voltages for current flow perpendicular to the magnetic-field orientation at $T=4.2$ K. (b) Experimental magnetoresistance for current flow parallel to the magnetic-field orientation at $T=4.2$ K.

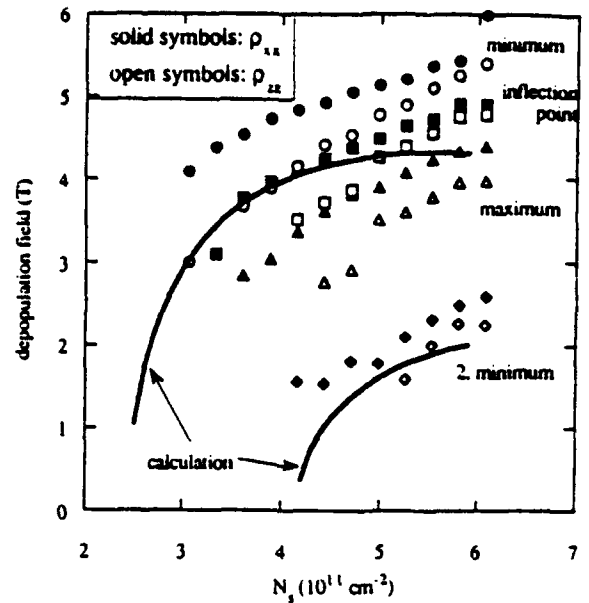


FIG. 17. Positions of the maxima, inflection points and minima along the magnetoresistance traces ρ_{xx} (open symbols) and ρ_{xy} (solid symbols) as a function of carrier density. The solid lines mark the result of the calculation as described in the text.

we get

$$N_s = \frac{m^*}{\pi \hbar^2} \frac{\omega}{\omega_0} \sum_{k \leq n} [\hbar\omega(n + \frac{1}{2}) - \hbar\omega(k + \frac{1}{2})].$$

This approximation is justified as long as the cyclotron diameter is larger than or comparable to the electronic width of the electron gas. For typical experimental conditions ($N_s = 5 \times 10^{11} \text{ cm}^{-2}$, $B = 5$ T) we obtain a classical cyclotron diameter of 47 nm. This is larger than the effective width of the electron layer at the same carrier density which is about 40 nm (see Fig. 1). For lower values of the carrier density the cyclotron orbit as well as the width of the electron layer shrink. We conclude that the assumption of an energy-independent density of states is justified. Higher magnetic fields will result in a one-dimensional-type density of states.⁴⁶ The magnetic field B_n , where subband n becomes depopulated, is then given by

$$B_n = \frac{m^*}{\hbar e} \left[\left| \frac{2N_s}{n(n+1)} \frac{\pi \hbar^2}{m^*} - \hbar\omega_0 \right| \hbar\omega_0 \right]^{1/2}.$$

The self-consistency enters via $\omega_0 = \omega_0(N_s)$ as calculated for $B=0$. The results of this calculation are depicted in Fig. 17 by solid lines. The main features of the experimental data are well explained by this model. Deviations occur for high magnetic fields, where the density of states becomes energy dependent⁴⁶ as described above.

The energy separation E_{23} is underestimated in the calculation because of the parabolic model. Intuitively Fig. 17 suggests, that the depopulation of the E_1 energy level occurs close to the inflection point of the ρ_{xx} trace. The data further imply that one has to be careful with the assignment of a depopulation field from magnetoresistance measurements on high mobility structures. The detailed influence of the subband depopulation on the magne-

oresistance traces is theoretically not well understood and requires future investigations.

VII. SUMMARY

This paper presents a series of transport experiments that allow the evaluation of the single-particle subband separation in a parabolic quantum well. The special subband structure of a PQW results in the possible occupation of several electrical subbands even at high magnetic fields applied perpendicular to the plane of the electron gas. This fact can be used to study the case where Landau levels associated with different electrical subbands are degenerate at the Fermi energy. The experiments reveal the suppression of quantum Hall states which can be recovered by a lifting of the degeneracy. This can be achieved either by a change of the subband separation via a suitable gate voltage or by a tilt of the sample with respect to the magnetic-field axis that leads to a resonant level anticrossing. Especially interesting is the case,

where for very low temperatures spin splitting of the Landau levels can be resolved. The magnetoresistance in this case is influenced by the subband dependent exchange enhancement, that leads to overshoots in the quantum Hall plateaus.

Finally an experiment is presented where, for in-plane magnetic fields, the magnetoresistance oscillations depend on whether the current flows parallel or perpendicular to the magnetic field. The positions of the oscillations are related to the magnetic depopulation of the electrical subbands. All experiments are accompanied by self-consistent subband calculations that allow for a quantitative comparison with the experimental results.

ACKNOWLEDGMENTS

We like to thank J. P. Kotthaus, U. Merkt, and A. Zrenner for very enlightening discussion. Financial support by the Volkswagen Foundation and the Air Force is gratefully acknowledged.

- ¹T. Ando, A. Fowler, and F. Stern, *Rev. Mod. Phys.* **54**, 437 (1982).
- ²See, for example, A. Pinczuk and J. M. Worlock, *Surf. Sci.* **113**, 69 (1982).
- ³A. Kamgar, R. Kneschaurek, G. Dorda, and J. F. Koch, *Phys. Rev. Lett.* **32**, 1251 (1974).
- ⁴Z. Schlesinger, J. C. M. Hwang, and S. J. Allen, Jr., *Phys. Rev. Lett.* **50**, 2098 (1983).
- ⁵G. L. J. A. Rikken, H. Sigg, C. J. G. M. Langerak, H. W. Myron, J. A. A. J. Perenboom, and G. Weimann, *Phys. Rev. B* **34**, 5590 (1986).
- ⁶A. D. Wieck, J. C. Maan, U. Merkt, J. P. Kotthaus, K. Ploog, and G. Weimann, *Phys. Rev. B* **35**, 4145 (1987).
- ⁷K. Ensslin, D. Heitmann, and K. Ploog, *Phys. Rev. B* **39**, 10879 (1989).
- ⁸K. Karrai, H. D. Drew, H. W. Lee, and M. Shayegan, *Phys. Rev. B* **39**, 10426 (1989).
- ⁹A. Wixforth, M. Sundaram, K. Ensslin, J. H. English, and A. C. Gossard, *Surf. Sci.* **267**, 523 (1992).
- ¹⁰W. P. Chen, Y. J. Chen, and E. Burstein, *Surf. Sci.* **58**, 263 (1976).
- ¹¹S. J. Allen Jr., D. C. Tsui, and B. Vinter, *Solid State Commun.* **20**, 425 (1976).
- ¹²L. Brey, N. F. Johnson, and B. I. Halperin, *Phys. Rev. B* **40**, 10647 (1989).
- ¹³K. Karrai, X. Ying, H. D. Drew, and M. Shayegan, *Phys. Rev. B* **40**, 12020 (1989).
- ¹⁴K. Ensslin, M. Sundaram, A. Wixforth, G. H. English, and A. C. Gossard, *Phys. Rev. B* **43**, 9988 (1991).
- ¹⁵K. Ensslin, C. Pistitsch, A. Wixforth, M. Sundaram, P. F. Hopkins, and A. C. Gossard, *Phys. Rev. B* **45**, 11407 (1992).
- ¹⁶M. Sundaram, A. C. Gossard, J. H. English, and R. M. Westervelt, *Superlatt. Microstruct.* **4**, 683 (1988).
- ¹⁷A. Wixforth, M. Sundaram, K. Ensslin, J. H. English, and A. C. Gossard, *Appl. Phys. Lett.* **56**, 454 (1990).
- ¹⁸H. L. Störmer, A. C. Gossard, and W. Wiegmann, *Solid State Commun.* **41**, 707 (1982).
- ¹⁹J. J. Harris, D. E. Lacklinson, C. T. Foxon, F. M. Selten, A. M. Suckling, R. J. Nicholas, and K. W. Barnham, *Semicond. Sci. Technol.* **2**, 783 (1987).
- ²⁰T. P. Smith, II and F. F. Fang, *Phys. Rev. B* **37**, 4303 (1988).
- ²¹F. F. Fang, T. P. Smith, III, and S. L. Wright, *Surf. Sci.* **196**, 30 (1988).
- ²²A. M. Kreschuk, M. Yu. Martisov, T. A. Polyanskaya, I. G. Savel'ev, I. I. Saidashev, A. Ya. Shik, and Yu. V. Shmartsev, *Solid State Commun.* **65**, 1189 (1988).
- ²³H. van Houten, J. G. Williamson, M. E. I. Broekaart, C. T. Foxon, and J. J. Harris, *Phys. Rev. B* **37**, 2756 (1988).
- ²⁴R. Fletcher, E. Zaremba, M. D'Iorio, C. T. Foxon, and J. J. Harris, *Phys. Rev. B* **38**, 7866 (1988).
- ²⁵T. P. Smith, III, F. F. Fang, U. Meirav, and M. Heiblum, *Phys. Rev. B* **38**, 12744 (1988).
- ²⁶K. Ensslin, D. Heitmann, and K. Ploog, *Phys. Rev. B* **37**, 10150 (1988).
- ²⁷R. M. Kusters, Ph.D. thesis, University of Nijmegen, 1990.
- ²⁸K. Hirakawa and H. Sakaki, *Phys. Rev. B* **33**, 8291 (1986).
- ²⁹R. R. Gerhardts, *Surf. Sci.* **58**, 227 (1976).
- ³⁰D. Weiss, V. Moser, V. Gudmundsson, R. R. Gerhardts, and K. von Klitzing, *Solid State Commun.* **62**, 89 (1987).
- ³¹K. Ensslin, D. Heitmann, R. R. Gerhardts, and K. Ploog, *Phys. Rev. B* **39**, 12993 (1989).
- ³²See, for example, E. Gornik, R. Lassnig, G. Strasser, H. L. Störmer, A. C. Gossard, and W. Wiegmann, *Phys. Rev. Lett.* **54**, 1820 (1985).
- ³³G. Gobsch, D. Schulze, and G. Paasch, *Phys. Rev. B* **38**, 10943 (1988).
- ³⁴Y. Guldner, J. P. Vieren, M. Voos, F. Delahaye, D. Dominguez, J. P. Hirtz, and M. Razeghi, *Phys. Rev. B* **33**, 3990 (1986).
- ³⁵D. G. Hayes, M. S. Skolnick, D. M. Whittaker, P. E. Simmonds, L. L. Taylor, S. J. Bass, and L. Eaves, *Phys. Rev. B* **44**, 3436 (1991).
- ³⁶See, for example, R. J. Nicholas, R. J. Haug, K. von Klitzing, and G. Weimann, *Phys. Rev. B* **37**, 1294 (1988).
- ³⁷T. Ando and Y. Uemura, *J. Phys. Soc. Jpn.* **36**, 959 (1974).
- ³⁸See C. A. Richter, R. G. Wheeler, and R. N. Sacks, *Surf. Sci.* (to be published), and references therein.
- ³⁹T. Ando, *Phys. Rev. B* **19**, 2106 (1979).
- ⁴⁰J. C. Maan, in *Two-Dimensional Systems, Heterostructures and Superlattices*, edited by G. Bauer, F. Kuchar, and H. Heinrich

- (Springer-Verlag, Berlin, 1984), p. 183.
- ⁴¹R. Merlin, *Solid State Commun.* **84**, 99 (1987).
- ⁴²W. Beinvoigt, A. Kamgar, and F. Koch, *Phys. Rev. B* **14**, 42 274 (1976).
- ⁴³Th. Englert, J. C. Maan, D. C. Tsui, and A. C. Gossard, *Solid State Commun.* **45**, 989 (1983).
- ⁴⁴H. Reisinger and F. Koch, *Surf. Sci.* **170**, 397 (1986).
- ⁴⁵D. J. Newson, K. F. Berggren, M. Pepper, H. W. Myron, G. J. Davies, and E. Scott, *J. Phys. C* **19**, L403 (1986).
- ⁴⁶A. Zrenner, H. Reisinger, F. Koch, K. Ploog, and J. C. Maan, *Phys. Rev. B* **33**, 5067 (1986).
- ⁴⁷E. G. Gwinn, R. M. Westervelt, P. F. Hopkins, A. J. Rimberg, M. Sundaram, and A. C. Gossard, *Phys. Rev. B* **39**, 626 (1989).
- ⁴⁸M. Shayegaa, T. Sajoto, J. Jo, M. Santos, and H. D. Drew, *Phys. Rev. B* **40**, 3476 (1989).
- ⁴⁹M. Kroeger and U. Merkt, *Solid State Commun.* **69**, 69 (1989).
- ⁵⁰P. F. Hopkins, Ph.D. thesis, Harvard University, 1990.
- ⁵¹M. P. Stops and S. DasSarma, *Phys. Rev. B* **40**, 10048 (1989).
- ⁵²E. Batke and C. W. Tu, *Phys. Rev. B* **34**, 3027 (1986).
- ⁵³H. Tang and B. N. Butcher, *J. Phys. C* **21**, 3313 (1988).
- ⁵⁴H. Tang and B. N. Butcher, *J. Phys. C* **21**, 3959 (1988).

Size effect in parabolic GaAs/Al_xGa_{1-x}As quantum wells

W. Walukiewicz

Materials Sciences Division, Lawrence Berkeley Laboratory, University of California, Berkeley, California 94720

P. F. Hopkins, M. Sundaram, and A. C. Gossard

Department of Materials/ECE, University of California, Santa Barbara, California 93106

(Received 13 May 1991)

We report the results of experimental and theoretical studies of the electron mobility in remotely doped, quasi-three-dimensional GaAs/Al_xGa_{1-x}As parabolic wells. We show that the electron mobility in such structures is strongly reduced by a size effect due to nonspecular scattering of electrons from rough walls confining the electron gas. The roughness of the walls results from random fluctuations of the remote-ionized-impurity concentration and/or the alloy composition. Incorporation of the size effect allows for a quantitative description of the electron mobility in these parabolic wells.

Electron scattering in metals due to the size effect has been studied for over 50 years.^{1,2} The resistivity of very thin metal films is observed to increase with decreasing film thickness. This phenomenon has been attributed to scattering of the electrons from rough surfaces of the metal film,²⁻⁴ when the electron free path l_0 is larger than the thickness of the film w_e , or $\hbar k_F \mu_b / e > w_e$, where $k_F = (3\pi^2 n)^{1/3}$ is the Fermi surface electron wave vector, n is the electron concentration, and μ_b is the bulk electron mobility. It has been suggested that a similar size effect should be observed in thin semiconductor films⁵ or in semiconductor inversion layers,⁶ although there has been no clear experimental evidence for such an effect in these systems.

Recently, a semiconductor heterostructure device, the remotely doped wide parabolic well (WPBW), has been introduced.^{7,8} These structures have been demonstrated to contain thick layers (>1000 Å) of high mobility ($>200\,000$ cm²/Vs) electron gas with roughly uniform three-dimensional (3D) electron densities.⁹⁻¹¹ The electrons in these wells form a slab of nearly constant 3D density $n(z) \approx n$ over a width w_e .

One of the objectives of the remote doping is to reduce the concentration of ionized impurities and to enhance the mobility of the electrons in the wells. Experimentally, low-temperature electron mobilities as high as 3×10^5 cm²/Vs were reported in parabolic wells with electron concentration $n \approx 10^{16}$ cm⁻³. Such mobilities are much higher than the electron mobilities in uniformly doped GaAs crystals with the same electron concentration. However, they are still at least one order of magnitude lower than mobilities of the 2D electron gas in high-quality modulation-doped heterostructures. Using typical parameters for the electron-gas layer in WPBW structures, $n \approx 10^{16}$ cm⁻³ and $w_e \approx 1000$ Å, we find that the electron mean free path will be greater than the electron slab width w_e if $\mu_b > 30\,000$ cm²/Vs. This suggests that scattering of the electrons from the slab surfaces could significantly affect the electron mobility of these structures. In this paper we present results of theoretical and

experimental studies of electron mobility in WPBW GaAs/Al_xGa_{1-x}As structures. A quantitative understanding of the experimental data is possible if the nonspecular electron scattering from the walls of the parabolic wells is included in our mobility calculations for these structures.

We have considered three previously studied¹² WPBW wafers, PB31, PB24, and PB23, which were grown by molecular-beam epitaxy with essentially identical layer designs but with different nominal parabolic well widths of 2000, 4640, and 5680 Å, respectively. The parabolic wells were grown in the form of fine (20 Å) GaAs/Al_{0.3}Ga_{0.7}As superlattice, with the average Al concentration profile varied parabolically from $x=0$ at the well center to $x=0.2$ (PB31) or $x=0.3$ (PB24 and PB23) at the edges by changing the Al shutter duty cycle under computer control.^{8,9} Si-doped Al_{0.3}Ga_{0.7}As regions set back by 200 Å (PB31) or 400 Å (PB24 and PB23) from either side of the well provide the electrons. The corresponding design densities n are 2.5×10^{16} , 0.7×10^{16} , and 0.5×10^{16} cm⁻³ for wafers PB31, PB24, and PB23, respectively. A more detailed description of sample preparation and measurement techniques is given elsewhere.¹²

Figure 1 shows the measured Hall mobility μ , as reported in Ref. 12, for the temperature range 4–300 K for the three samples PB31, PB24, and PB23. The most striking feature of the data in Fig. 1 is that the Hall mobilities of the three samples are nearly identical over the entire temperature range measured. The highest measured values of the electron mobility in PB23 and PB24 are $\mu \approx 2.4 \times 10^5$ cm²/Vs. A slightly higher value of 2.9×10^5 cm²/Vs has been measured in the PB31 sample. We have found that the low-temperature sheet densities n_s are almost temperature independent for $T < 70$ K, indicating the high quality of the low-density electron gas in these samples. The $T=4.2$ -K values of n_s for samples PB31, PB24, and PB23 are 2.3×10^{11} , 1.4×10^{11} , and 0.77×10^{11} cm⁻², corresponding to nominal electron layer widths $w_e = n_s / n$ of 900, 2000, and 1700 Å, respec-

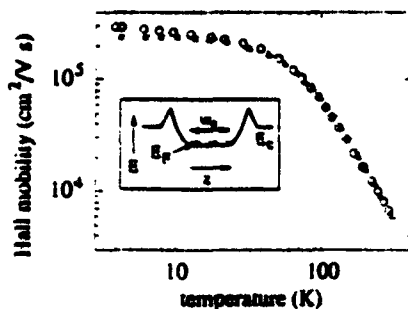


FIG. 1. Hall mobilities as functions of temperature in three parabolic well structures. A schematic representation of the conduction-band-edge energy E_c vs growth direction z is shown for a remotely doped parabolic well with electron layer thickness w_e .

tively. The widths w_e of the electron layers were determined experimentally by a comparison of transverse Shubnikov-de Haas oscillation measurements at $T = 50$ mK with local-density-functional calculations of the sub-band energies and wave functions.¹¹ These widths were in reasonable agreement with the estimated values from the Hall measurements. We have also inferred density profile uniformities for samples PB31 and PB24 from comparison of the experimental and theoretical energies.¹¹ The electron density across w_e for PB31 is estimated to be uniform to within $\sim 10\%$ of n , while for PB24 the density is uniform to within $\sim 30\%$ of n .

Since the widths of the electron gas in the samples is less than the mean free path l_e as determined from mobility measurements, a complete calculation of the mobility in these samples must include scattering of the electrons from the confining walls. In order to consider the effect of electron scattering from rough walls we use the approach originally proposed by Cottley, who found the following expression for the electrical conductivity of thin metallic films:

$$\sigma = \frac{3\sigma_b}{4} \int_0^\pi d\theta \frac{\sin^3(\theta)}{1 + l_e/l_s(\theta)}, \quad (1)$$

where $\sigma_b = ne\mu_b$ is the bulk conductivity, $l_s(\theta)$ is the effective electron mean free path associated with the electron scattering from the surface, and θ is the angle of incidence at the surface. It was shown that³

$$l_s(\theta) = -w_e / \{ |\cos(\theta)| \ln[p(\theta)] \}, \quad (2)$$

where $p(\theta)$ is the specularity parameter. Parameter p represents the probability that an electron will be specularly scattered from the surface, while $(1-p)$ is the probability for a diffuse scattering. In the diffuse scattering the angle of reflection is random and is not correlated with the angle of incidence. Soffer⁴ has calculated $p(\theta)$ for a randomly rough surface characterized by a roughness parameter α . He found

$$p(\theta) = \exp \left[- \left(\frac{4\pi\alpha}{\lambda} \right)^2 \cos^2(\theta) \right], \quad (3)$$

where $\lambda = 2\pi/k_F$ is the electron wavelength. Substituting Eq. (3) into Eq. (2) and performing the integration in (1) one obtains an analytic expression for the electron mobility,

$$\mu = \mu_b \left[c^{-1/3} \left\{ \frac{1}{4} \ln \left[\frac{(1+c^{1/3})^3}{(1+c)} \right] + \frac{\sqrt{3}}{2} \left[\tan^{-1} \left[\frac{2c^{1/3}-1}{\sqrt{3}} \right] + \frac{\pi}{6} \right] - \frac{1}{2c} \ln(1+c) \right\} \right], \quad (4)$$

where

$$c = 4l_e k_F^2 \alpha^2 / w_e.$$

For perfectly smooth surfaces with $\alpha \rightarrow 0$, or for very wide wells with $w_e \rightarrow \infty$, $c \rightarrow 0$, and, as expected, $\mu \rightarrow \mu_b$.

It should be emphasized that the size effect is a phenomenon basically different from the interface roughness scattering in 2D systems.¹³ Since the specularity parameter, given by Eq. (3), is a monotonically decreasing function of α , therefore the largest contribution to the size effect comes mostly from large size fluctuations. On the other hand, in the case of interface roughness scattering 2D electrons are most efficiently scattered by rough interfaces with $\alpha \approx \lambda/\pi$.¹³

One finds from Eq. (4) that the mobility reduction due to the size effect depends on the roughness parameter α and the electron free path l_e . A common difficulty with the microscopic description of the size effect in thin metal films stems from the poor and uncontrollable quality of thin-film surfaces. Consequently, most of the interpretations of the size effect are based on phenomenological approaches. The great advantage of the parabolic well system is that in this case the confinement walls are determined by two well-defined potentials: the electrostatic potential of the remote impurities and the conduction-band-edge potential as determined by the Al composition of the $\text{Al}_x\text{Ga}_{1-x}\text{As}$ alloy. Random fluctuations of the remote ionized impurity concentration and/or alloy composition contribute to the roughness of the walls. Small-size statistical fluctuations produce small changes in the confining potential, and as is seen from Eq. (3), contribute very little to the reduction of the specularity parameter p . On the other hand, large-size fluctuations are effectively screened by free carriers. One can thus argue that the largest contribution to the actual value of the specularity parameter comes from the fluctuations of the order of screening length, i.e., one can assume $\alpha = R_s$. Here R_s is the Thomas-Fermi screening length given by

$$R_s = \left[\frac{2\sqrt{2}e^2 m^{3/2} (k_B T)^{1/2}}{\pi \hbar^3 \epsilon_0} F_{-1/2}(\eta) \right]^{-1/2}, \quad (5)$$

where $F_{-1/2}(\eta)$ is the Fermi-Dirac integral of the order $-1/2$, $\eta = E_F/k_B T$, and E_F is the Fermi energy.

In the calculation of bulk electron mobility we assume that the electron gas confined in the wide parabolic well can be treated in the 3D approximation. In these calcula-

tions we include all the major scattering processes: background ionized impurity, acoustic-phonon deformation potential, acoustic-phonon piezoelectric, and alloy disorder scattering. Screening by the free carriers in the parabolic well is included in the calculations. Scattering by optical phonons can be safely ignored since we consider the low-temperature range $T < 50$ K.

In the parabolic $\text{GaAs}/\text{Al}_x\text{Ga}_{1-x}\text{As}$ well the composition x as well as the alloy disorder scattering¹⁴ parabolically depend on the location z in the well. To find the bulk mobility in the well we average the total microscopic relaxation time over the well width

$$\bar{\tau}(E) = \frac{1}{W} \int_0^W \tau(E, z) dz, \quad (6)$$

where E is the electron energy. Finally, the macroscopic bulk mobility μ_b is obtained from a standard averaging of the microscopic relaxation time over the electron energy.

Most of the GaAs and $\text{Al}_x\text{Ga}_{1-x}\text{As}$ material parameters are well known. Here we use GaAs parameters,¹⁵ ignoring any dependence of the parameters on the Al composition in the well. This approximation is justified because the Al concentration x in the portion of these parabolic well structures occupied by the electron gas is small, $x < 0.1$. We have adopted an experimentally determined value of 9 eV for the conduction-band deformation potential in GaAs .¹⁶ This value is close to recent theoretical determinations reported by two independent groups.^{17,18} The electron mobility in the parabolic wells is not very sensitive to the alloy disorder scattering parameter $\langle V \rangle$. Here we find that $\langle V \rangle = 0.5$ eV provides the most consistent explanation for the experimental data.

Figure 2 shows the calculated electron mobilities as functions of ionized background impurity concentration for a well with parameters identical to those of structure PB31. It is seen from the figure that incorporation of the size effect leads to very substantial reduction of the electron mobility. The measured 4-K mobility in the structure PB31 is equal to 2.9×10^5 cm²/V s. We find that this value of the mobility can be explained with the background ionized impurity concentration of $n_H = 2.3 \times 10^{14}$

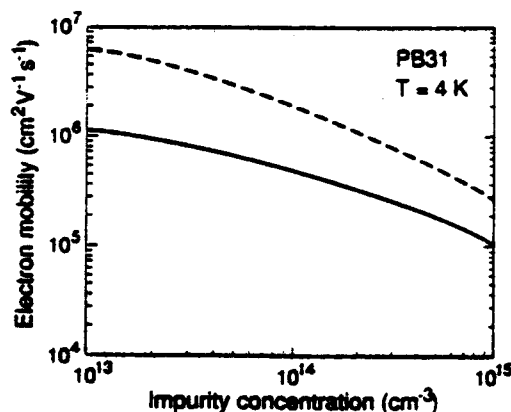


FIG. 2. Calculated bulk mobility (---) and size effect limited (—) mobility as functions of background ionized impurity concentration.

cm⁻³, which is very close to the expected contamination with carbon impurities in the well. Because of larger well widths the size effect is less pronounced in the PB24 and PB23 structures. The experimental 4-K mobilities of 2.44×10^5 cm²/V s in PB24 and 2.35×10^5 cm²/V s in PB25 can be explained with $n_H = 2.5 \times 10^{14}$ and 2.1×10^{14} cm⁻³, respectively. Thus we find that, despite a much different geometrical configuration, the residual impurity concentrations required to account for the observed mobilities are practically the same in all three studied structures.

One could argue that the low values of the experimental electron mobilities can be understood without invoking the size effect, but assuming only a higher background impurity concentration. For example, as is seen in Fig. 2 (upper curve), the 4-K experimental mobility of 2.9×10^5 cm²/V s is equal to the bulk mobility calculated for $n_H = 10^{15}$ cm⁻³. We find that such an explanation is inconsistent with a temperature dependence of the electron mobility observed in this structure. As shown in Fig. 3, incorporation of the size effect for $n_H = 2.3 \times 10^{14}$ cm⁻³ leads to the temperature-dependent mobility which is in very good agreement with the experiment. However, if one ignores the size effect, the calculated mobility (dashed line in Fig. 3) shows a temperature dependence which is in clear disagreement with the experimental data. The experimentally observed temperature dependence is a manifestation of the fact that the acoustic-phonon scattering is a major process contributing to the bulk mobility μ_b (dash-dotted line in Fig. 3). The scatter-

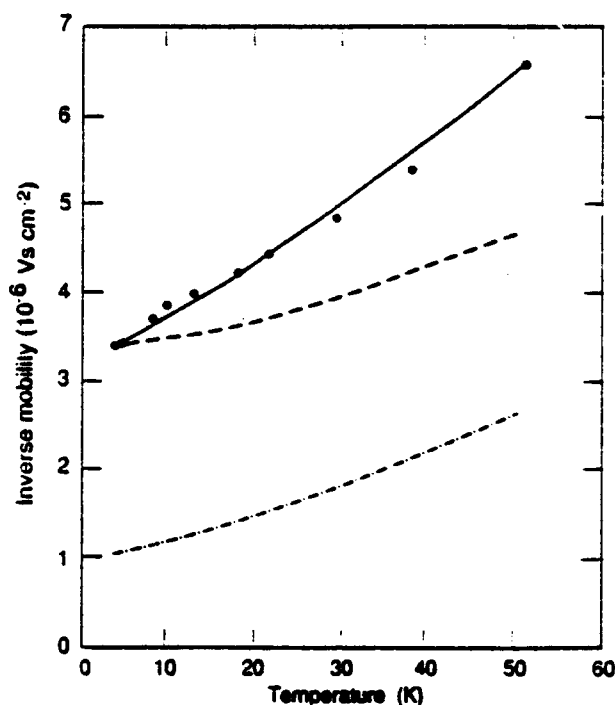


FIG. 3. Temperature-dependent inverse electron mobility: —, size effect included, $n_H = 2.3 \times 10^{14}$ cm⁻³; ---, no size effect, $n_H = 2.3 \times 10^{14}$ cm⁻³; - · - · -, no size effect, $n_H = 1 \times 10^{15}$ cm⁻³. The points represent the experimental data for the structure PB31.

ing from rough surfaces reduces the bulk mobility by an almost constant, weakly temperature-dependent factor leading to an observed temperature dependence of the total mobility.

The proposed explanation of the reduced electron mobility in the parabolic wells could be further tested by studying the dependence of the size effect on the electron concentration and thus also on the well width. It is expected that with increasing well width the effect of nonspecular scattering should be reduced, leading to an increased effective electron mobility. However, one should realize that in wider wells a portion of the well with higher Al concentration is occupied. This will result in an increased alloy disorder scattering. The additional scattering will to some degree compensate the mobility enhancement due to reduction of the nonspecular scattering. A careful analysis will be required to quantitatively evaluate relative contributions of these scattering mechanisms.

Application of an external magnetic field offers another method to reduce the interaction of the electrons with the confining walls. A magnetic field in the plane of the well

affects the trajectories of electrons moving in the direction perpendicular to the walls, increasing the electron free path between two subsequent reflections from the walls. This effect should manifest itself in a negative longitudinal magnetoresistance observed at low magnetic fields. At high fields, the effects of quantization on the electron transport will have to be considered.

In conclusion, we have shown that a nonspecular scattering of electrons from rough walls very significantly reduces the mobility of quasi-3D electron gas confined in a parabolic quantum well. The incorporation of the size effect allows for a quantitative description of low-temperature mobility in $\text{GaAs}/\text{Al}_x\text{Ga}_{1-x}\text{As}$ parabolic wells.

Discussion with L. Falicov, E. Haller, and R. Westervelt are gratefully acknowledged. This work was supported by the Director, Office of Energy Research, Office of Basic Energy Sciences, Materials Science Division of the U.S. Department of Energy under Contract No. DE-AC03-76SF00098 and Air Force Contract No. AFOSR-88-0099.

-
- ¹I. S. Appleyard and A. C. B. Lovell, *Proc. R. Soc. (London) Ser. A* 158, 718 (1937).
²K. Fuchs, *Proc. Cambridge Philos. Soc.* 34, 100 (1938).
³A. A. Cottey, *Thin Solids Films* 1, 297 (1967).
⁴S. B. Soffer, *J. Appl. Phys.* 38, 1710 (1967).
⁵F. S. Ham and D. C. Mattis, *IBM J. Res. Dev.* 4, 143 (1960).
⁶J. R. Schrieffer, *Phys. Rev.* 97, 641 (1955).
⁷B. I. Halperin, *Jpn. J. Appl. Phys. Suppl. No. 26-3* 26, 1913 (1987).
⁸M. Sundaram, A. C. Gossard, J. H. English, and R. M. Westervelt, *Superlatt. Microstruct.* 4, 683 (1988).
⁹E. G. Gwinn, P. F. Hopkins, A. J. Rimberg, R. M. Westervelt, M. Sundaram, and A. C. Gossard, *Phys. Rev. B* 41, 10 700 (1990).
¹⁰M. Shayegan, T. Sajoto, J. Jo, M. Santos, and C. Silvestre, *Appl. Phys. Lett.* 53, 791 (1988); T. Sajoto, J. Jo, M. Santos, and M. Shayegan, *ibid.* 55, 1430 (1989).
¹¹A. J. Rimberg and R. M. Westervelt, *Phys. Rev. B* 40, 3970 (1989).
¹²P. F. Hopkins, A. J. Rimberg, E. G. Gwinn, R. M. Westervelt, M. Sundaram, and A. C. Gossard, *Appl. Phys. Lett.* 57, 2823 (1990).
¹³T. Ando, A. L. Fowler, and F. Stern, *Rev. Mod. Phys.* 54, 437 (1982).
¹⁴L. Makowski and M. Glicksman, *J. Phys. Chem. Solids* 34, 487 (1973).
¹⁵G. E. Stilman and C. M. Wolfe, *Thin Solid Films* 31, 69 (1976); W. Walukiewicz, J. Lagowski, L. Jastrzebski, M. Lichtensteiger, and H. C. Gatos, *J. Appl. Phys.* 50, 899 (1979).
¹⁶D. D. Nolte, W. Walukiewicz, and E. E. Haller, *Phys. Rev. Lett.* 59, 501 (1987).
¹⁷C. G. Van de Walle and R. M. Martin, *Phys. Rev. Lett.* 62, 2028 (1989).
¹⁸M. Cardona and N. E. Christensen, *Phys. Rev. B* 35, 6182 (1987).

Reprinted from

Journal of **APPLIED PHYSICS**

Volume 73

1 January 1993

Number 1

Capacitance-voltage profiling through graded heterojunctions: Theory and experiment.

M. Sunderam and A. C. Gossard

*Department of Electrical and Computer Engineering, and Materials Department, University of California,
Santa Barbara, California 93106.*

pp. 251-260

a publication of the American Institute of Physics

AIP

Capacitance-voltage profiling through graded heterojunctions: Theory and experiment

M. Sundaram and A. C. Gossard

Department of Electrical and Computer Engineering, and Materials Department, University of California, Santa Barbara, California 93106

(Received 9 September 1991; accepted for publication 21 September 1992)

Starting from the general equations for capacitance-voltage (CV) profiling through a graded heterojunction, we obtain numerical solutions to yield thermal-equilibrium energy-band diagrams, real electron profiles, and apparent electron profiles (i.e., the profile extracted from a CV measurement) for modulation-doped square, triangular, and parabolic potential wells. Room-temperature CV measurements are performed on parabolic potential wells grown by molecular beam epitaxy in the $\text{Al}_x\text{Ga}_{1-x}\text{As}$ system, and the measured apparent electron profiles fitted to computer reconstructions whence the real electron distributions are deduced. These measurements reflect a uniform electron distribution in a parabolic well, with 3D electron density determined by well curvature. Data analysis also suggests the presence of a doping asymmetry in the modulation doping of the well. Appropriate corrections to growth conditions remove these asymmetries, as reflected in CV measurements. Besides its importance in the analysis of potential wells of different shapes, the theory presented is applicable to the determination of band offsets by the CV profiling technique where the unintentional grading of the band gap and/or doping in the neighborhood of the isotype abrupt heterojunction is known.

1. INTRODUCTION

Graded heterojunctions are an important part of the physics and technology of semiconductors. When the base of a heterojunction bipolar transistor (HBT) is graded, carrier transport across the base is enhanced, leading to improved device performance.¹ The intrinsic (*i*) region of a double-heterostructure laser, such as a graded-index-separate-confinement-heterostructure (GRINSCH) laser, is graded for better electrical confinement of the electrons and holes pumped into it from the adjacent *p* and *n* regions, as well as better optical confinement of the lasing mode resulting from the radiative recombination of the injected electrons and holes, leading to improved lasing thresholds and efficiencies.² Graded heterojunctions have also been used to realize potential wells of controlled shapes, especially in the $\text{Al}_x\text{Ga}_{1-x}\text{As}$ system where there exists a nearly linear relationship between energy band gap and Al mole fraction *x* (over a certain range of *x* values) which allows a potential well of a desired shape to be made in a graded $\text{Al}_x\text{Ga}_{1-x}\text{As}$ alloy with a graded Al mole fraction profile of the same shape.³ Modulation-doped parabolic wells have been made to realize high-mobility three-dimensional electron gases to study their electrical and optical properties.⁴ The nonlinear responses of asymmetric wells, like half-parabolic wells, have been exploited to generate second, as well as third, harmonics in the far infrared.⁵ Symmetric triangular wells and barriers are being tried as devices to achieve subharmonic mixing in mm-wave communications.⁶

A problem of particular interest in modulation-doped potential wells is the measurement of the carrier distribution at thermal equilibrium. For instance, it is required that an electron gas in a modulation-doped wide parabolic well be nearly uniform at the curvature density over a large

distance (~ 2000 Å).⁴ Transport studies, such as Hall measurements, and optical measurements, such as absorption or photoluminescence across the band gap, offer an indirect measure of this distribution at best. Techniques such as transmission-electron microscopy (TEM), scanning-tunneling microscopy (STM), or secondary-ion mass spectroscopy (SIMS) may be able to measure the variation of the Al mole fraction across the well, but do not directly measure carrier distributions.

Capacitance-voltage (CV) profiling through a graded heterojunction is a powerful and simple method of determining the free-carrier distribution in such a structure. The method has been used to determine band offsets in, among other material systems, the $\text{GaAs}/\text{Al}_x\text{Ga}_{1-x}\text{As}$ system.^{7,8} This has usually involved room-temperature CV profiling through abrupt *n-N* or *p-P* (isotype) heterojunctions, where the *n(p)* and *N(P)* regions are materials with different energy band gaps, uniformly doped right up to the interface where there is an abrupt transition from one material to the other. Unintentional grading of the band gap or doping near the interface affects the carrier distribution in its neighborhood, but still yields the correct band offset.⁹ The effects of compositional and dopant grading near the interface has been analyzed theoretically;¹⁰ dopant grading near the interface has been treated experimentally.¹¹

However, a comprehensive theory that accounts for grading of both the band gap as well as the doping in specially graded heterojunctions, such as modulation-doped wide potential wells, is yet to emerge. Tests of such a theory against experiments on real structures also need to be performed. In this article, we derive the general set of equations of the CV profiling technique and apply it to CV measurements of the carrier distribution in modulation-doped wide parabolic potential wells at room temperature.

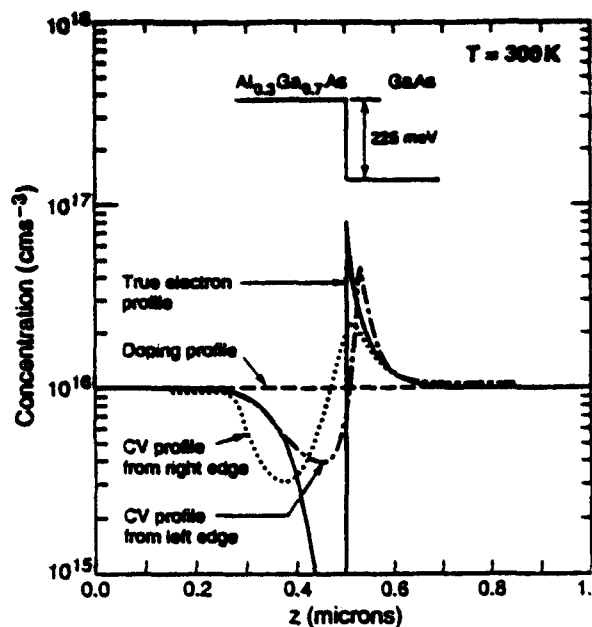


FIG. 1. The simulated 300 K electron distributions in n - N GaAs/ $\text{Al}_{0.3}\text{Ga}_{0.7}\text{As}$ abrupt heterojunction are shown. The true profile shows dipole formation at the interface with electron accumulation in GaAs and depletion in $\text{Al}_{0.3}\text{Ga}_{0.7}\text{As}$. CV (apparent) distributions profiled from Schottky gates at either edge (with an ohmic contact at the opposite edge) are also shown. CV profiles are seen to be smeared-out versions of the true profile. Note differences between and asymmetry in the two CV profiles.

II. THEORY

A. Simulation equations

It is known that the CV profiling process senses the free-carrier concentration and not the ionized-impurity concentration. Additionally, it is not the true carrier distribution that is usually measured but an apparent distribution.⁷ It is only in the case of a uniform true carrier distribution that the two are the same. The apparent profile, in all other cases, is a smeared-out version of the true profile; the smearing occurring over the order of several Debye lengths.⁷ At a single abrupt n -GaAs/ N - $\text{Al}_x\text{Ga}_{1-x}\text{As}$ heterojunction, for instance, a dipole exists, with an accumulation of electrons on the GaAs side and an equal depleted positive fixed charge on the $\text{Al}_x\text{Ga}_{1-x}\text{As}$ side. The Debye length in the neighborhood of this dipole is quite large as a result of this depletion, and the apparent profile seen by the CV profiling is a smeared-out version of the real electron distribution. This is illustrated in Fig. 1, where simulations of the true profile $n(z)$, the doping profile $N(z)$, and two apparent profiles $\tilde{n}(z)$ are shown, one apparent profile obtained by profiling from the right edge, and the other from the left edge, of a structure that has two slabs, one of n -GaAs and the other of N - $\text{Al}_{0.3}\text{Ga}_{0.7}\text{As}$ adjoining each other. It has been proved that the total charge and the first moment of the charge distribution are conserved in the profiling process, i.e., the integral of the charge distribution and the integral of the first moment of the charge distribution are the same for the true and ap-

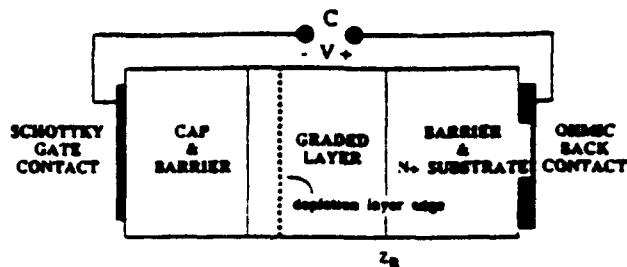


FIG. 2. The CV measurement schematic is shown. The depletion edge of the gate Schottky barrier is swept through the graded heterojunction. The capacitance between the gate and conducting substrate is measured as a function of applied bias and apparent electron profile vs depth extracted.

parent profiles.⁷ It is precisely this that causes the asymmetry in the two apparent profiles.

The CV measurement schematic is shown in Fig. 2. As the graded heterojunction is generally a very leaky diode, the capacitance of any dipole formed within it cannot be directly measured. Instead, one measures it by applying a reverse bias at an adjacent Schottky barrier and sweeping the edge of the depletion layer thus formed, through the layer.⁷ If the structure of interest is grown on a doped substrate, the substrate can be used as a back ohmic contact. Otherwise, the channel electrons may be ohmically contacted directly. If C is the measured capacitance per unit area between the Schottky barrier and ohmic contact at applied voltage V , then the apparent depletion depth z and the apparent electron concentration $\tilde{n}(z)$ at this depletion depth, are given respectively by:¹²

$$z = \frac{\epsilon_n}{C}, \quad (1a)$$

$$\tilde{n}(z) = \frac{2}{q\epsilon_n} \left[\frac{d}{dV} \left(\frac{1}{C} \right) \right]^{-1}, \quad (1b)$$

where ϵ_n is the uniform dielectric permittivity assumed in the layers.

Inasmuch as it is very difficult to deconvolve the true profile from the apparent profile, the best approach to analyzing the measured data is to compare the measured apparent profile with a computer-reconstructed apparent profile, changing design parameters as required to obtain the best fit between the two. A general theoretical analysis to obtain both the true and apparent (CV) profiles for a layer with arbitrarily variable energy band gap, carrier effective mass, dielectric constant, and doping profile, is developed below. Quantum size effects are ignored, i.e., potential wells, if present, are assumed to be so wide that the intersubband spacing is much smaller than kT where k is the Boltzmann constant and T the measurement temperature, or so narrow as to permit the assumption of an effective local band edge. Thus, only the Poisson equation need be solved. Deep donors and acceptors are neglected. The analysis is done for electrons, but the method is easily extended to the case of holes.

Consider Fig. 3. The epilayer is divided into two regions: region 1, where there is a variable conduction-band

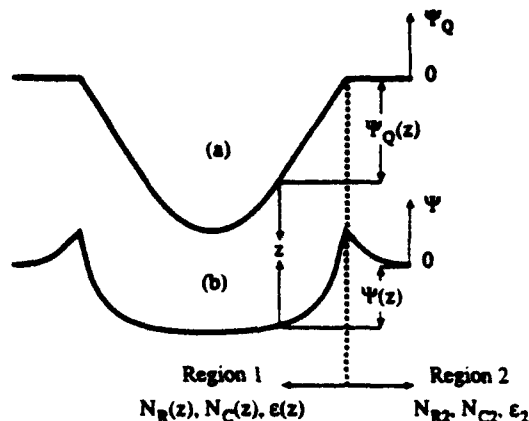


FIG. 3. The conduction-band diagrams (energy expressed in units of kT ; zero of energy in substrate) for a parabolic potential well are shown. (a) Quasiconduction-band diagram as a result of band gap grading, and (b) self-consistent band diagram when (a) is modulation doped.

energy $E_{CQ}(z)$ obtained by controlled grading of the band gap, doping density $N_R(z)$, effective conduction-band density of states $N_C(z)$, and dielectric permittivity $\epsilon(z)$; and region 2 which is the bottom layer with uniform (assumed zero, as reference) quasiconduction-band energy, doping density N_{R2} , effective conduction-band density of states N_{C2} , and dielectric permittivity ϵ_2 . Figure 3(a) shows a wide parabolic well as an example of a tailored energy band; such a graded structure could be obtained in the GaAs/Al_xGa_{1-x}As system for instance, by varying the Al mole fraction parabolically. Figure 3(b) shows the thermal-equilibrium band energy after introducing real charges in selected regions of the structure in Fig. 3(a). The essential equations are most easily constructed by defining the total energy E_C , total electric field F , and total doping density N at any point z as the sum of their respective real and quasicomponents, as follows:

$$E_C(z) = E_{CR}(z) + E_{CQ}(z), \quad (2a)$$

$$F(z) = F_R(z) + F_Q(z), \quad (2b)$$

and

$$N(z) = N_R(z) + N_Q(z). \quad (2c)$$

We further express the conduction-band energies, both real and quasi-, in units of kT as:

$$\Psi(z) = \frac{E_C(z) - E_C(\infty)}{kT}, \quad (3a)$$

$$\Psi_R(z) = \frac{E_{CR}(z) - E_{CR}(\infty)}{kT}, \quad (3b)$$

and

$$\Psi_Q(z) = \frac{E_{CQ}(z) - E_{CQ}(\infty)}{kT}, \quad (3c)$$

where

$$\Psi(z) = \Psi_R(z) + \Psi_Q(z) \quad (3d)$$

and

$$E_C(\infty) = E_{CR}(\infty) = E_{CQ}(\infty) = 0 \quad (3e)$$

is the reference energy.

The local fields and local potentials are then related to each other by:

$$F(z) = V_T \frac{d}{dz} \Psi(z); \quad F_R(z) = V_T \frac{d}{dz} \Psi_R(z);$$

$$F_Q(z) = V_T \frac{d}{dz} \Psi_Q(z), \quad (4)$$

where $V_T (= kT/q)$ is the thermal voltage.

The quasi-energy $\Psi_Q(z)$, the quasifield $F_Q(z)$, and the quasidoping density $N_Q(z)$ are related to each other by:

$$qN_Q(z) = \frac{d}{dz} \epsilon(z) F_Q(z) = V_T \frac{d}{dz} \epsilon(z) \frac{d}{dz} \Psi_Q(z), \quad (5)$$

where ϵ is the permittivity. The Poisson's equation in region 1 can now be expressed as:

$$\frac{d}{dz} \epsilon(z) F(z) = V_T \frac{d}{dz} \epsilon(z) \frac{d}{dz} \Psi(z) = q[N(z) - n(z)], \quad (6)$$

where $n(z)$ is the electron concentration and is given, in the Boltzmann approximation, by:

$$n(z) = \frac{N_2}{N_{C2}} N_C(z) \exp[-\Psi(z)]. \quad (7)$$

Inasmuch as the parameters of experimental control are the real doping density $N_R(z)$ and the quasiband-bending $\Psi_Q(z)$ (through grading), the Poisson's Eq. (6) is better expressed as:

$$V_T \frac{d}{dz} \epsilon(z) \frac{d}{dz} [\Psi(z) - \Psi_Q(z)] = q[N_R(z) - n(z)]. \quad (8)$$

In region 2, ϵ and N_R are constant, and $\Psi_Q = 0$. Using this in Eq. (7), Eq. (8) for region 2 simplifies to:

$$\frac{d^2 \Psi(z)}{dz^2} = \frac{1}{L_D^2} \{1 - \exp[-\Psi(z)]\}, \quad (9)$$

where L_D , the substrate Debye length, is given by:

$$L_D = \sqrt{\frac{\epsilon_2 V_T}{q N_{R2}}}. \quad (10)$$

Equation (9) can be solved to yield a general relationship between the local field and the local bandbending in the uniformly doped region as:¹³

$$F(z) = -\text{sign}[\Psi(z)] \sqrt{2} \frac{V_T}{L_D} \{\exp[-\Psi(z)] - 1 + \Psi(z)\}^{1/2}. \quad (11)$$

While an analytical solution exists in region 2, the Poisson's Eq. (8) in region 1 has to be numerically solved with appropriate boundary conditions. The discretization procedure for an equation such as Eq. (8) is well known.¹⁴ However, we wish to perform the discretization in this instance in such a way that the derived equations involve

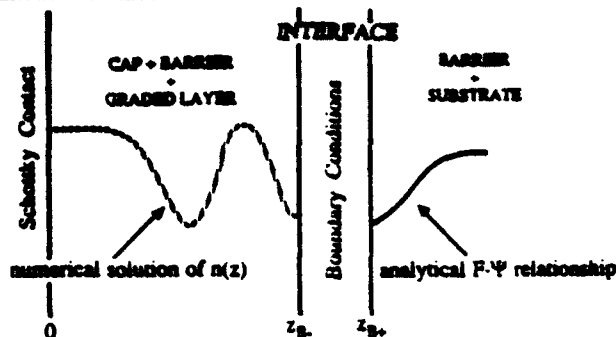


FIG. 4. The simulation schematic is shown. An analytical solution exists for the ungraded uniformly doped substrate. Starting with boundary conditions at z_{B+} , the electron density, field, and potential are calculated numerically back toward the surface ($z=0$). The potential at z_{B+} is changed by bisection till field and potential at the surface satisfy boundary conditions, indicating convergence.

variables which are not merely of numerical convenience, but are measurable and physically significant quantities; the procedure therefore bears repetition here. This is schematically indicated in Fig. 4. We divide region 1 into a grid with spacing dz , as indicated in Fig. 5. Associated with each point z is a true electron concentration $n(z)$, a total band bending $\Psi(z)$, a quasiband bending $\Psi_Q(z)$, and an effective conduction-band density of states $N_C(z)$. Also associated with each point z but defined at the middle of the gap between z and $z+dz$, are the local real electric field $F_R(z)$ and the local dielectric permittivity $\epsilon(z)$. With these definitions, the analog Poisson's Eq. (8) can be split into three digital equations, as follows:

$$n(z+dz) = \frac{N_2}{N_C} N_C(z+dz) \exp[-\Psi(z+dz)], \quad (12a)$$

$$\begin{aligned} \epsilon(z)F_R(z) - \epsilon(z+dz)F_R(z+dz) \\ = -q[N_R(z+dz) - n(z+dz)]dz, \end{aligned} \quad (12b)$$

and

$$\Psi(z) - \Psi(z+dz) = -\frac{F_R(z)dz}{V_T} + [\Psi_Q(z) - \Psi_Q(z+dz)]. \quad (12c)$$

The above equation connects Ψ and F_R at $z+dz$ with Ψ and F_R at z , and by iteration eventually to Ψ and F_R at the surface $z=0$. The boundary conditions at the right extreme of region 1:

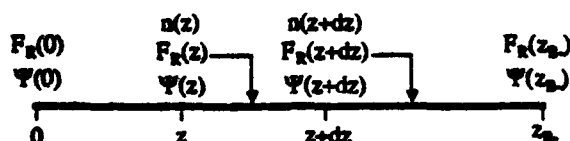


FIG. 5. The z mesh for numerical simulation is shown. Electron density n and potential Ψ are defined at z . Real field F_R associated with z is defined at midpoint between z and $z+dz$. Knowing Ψ and F_R at $z+dz$, Ψ and F_R at z can be calculated back to $z=0$.

$$\Psi(z_{B-}) = \Psi(z_{B+}) + \frac{\Delta E_{CB}}{kT}, \quad (13a)$$

$$\epsilon(z_{B-})F(z_{B-}) = \epsilon(z_{B+})F(z_{B+}) - q\sigma_B \quad (13b)$$

where ΔE_{CB} and σ_B are, respectively, the conduction-band offset and interface charge at the boundary z_B , connect Ψ and F_R immediately at the left of the interface to the corresponding values immediately to the right.

The iteration scheme involves changing $\Psi(z_{B+})$ by bisection until both $\Psi(0)$ and $F_R(0)$ approach zero, indicating convergence and yielding thermal-equilibrium real electron distributions and energy band diagrams. To simulate the CV profiling process, one changes $\Psi(z_{B+})$ by a $\Delta\Psi(z_{B+})$ and repeats the iteration of Eqs. (12) to obtain $\Delta\Psi(0)$ and $\Delta F_R(0)$. Inasmuch as the capacitance per unit area C and the apparent depletion depth z are defined as:

$$C = \frac{\epsilon_u}{V_T} \frac{dF(0)}{d\Psi(0)} \quad \text{and} \quad (14a)$$

$$z = \frac{\epsilon_u}{C}, \quad (14b)$$

the corresponding digital equations can be written as:

$$z_k = -V_T \frac{\Delta\Psi_k(0)}{\Delta F_k(0)}, \quad (15a)$$

$$\hat{n}(z_k) = \frac{\epsilon_u}{q} \frac{\Delta F_k(0)}{z_k - z_{k-1}}; \quad k > 1, \quad (15b)$$

where $\hat{n}(z_k)$ is the apparent or CV electron concentration measured at the depth z_k and k is the number of the run starting from the thermal equilibrium distribution. The above equations are handily implemented by converting Eq. (12) to a corresponding set of difference equations between the k th and $(k+1)$ th run. If the epilayer does not have the uniform permittivity ϵ_u assumed in Eq. (1) but a variable permittivity $\epsilon(z)$, it has been shown that by simply scaling all densities as:¹⁵

$$\tilde{n}(y) = \frac{1}{\epsilon_u} \epsilon(z)n(z), \quad \text{etc.}, \quad (16a)$$

where y is an equivalent depth defined by:

$$y = \epsilon_u \int_0^z \frac{d\theta}{\epsilon(\theta)}, \quad (16b)$$

the Poisson's Eq. (8) can be written as:

$$\frac{d^2}{dy^2} [\Psi(y) - \Psi_Q(y)] = \frac{q}{\epsilon_u V_T} [\tilde{N}_R(y) - \tilde{n}(y)]. \quad (17)$$

By using Eq. (1), we thus effectively measure the equivalent apparent electron density $\hat{n}(y)$ at the equivalent apparent depth y . If the ϵ_u assumed in the measurement is that of the topmost layer with a uniform permittivity and uniform carrier distribution then, $y=z$ and $\hat{n}(y) = \hat{n}(z) = n(z)$ for this layer.

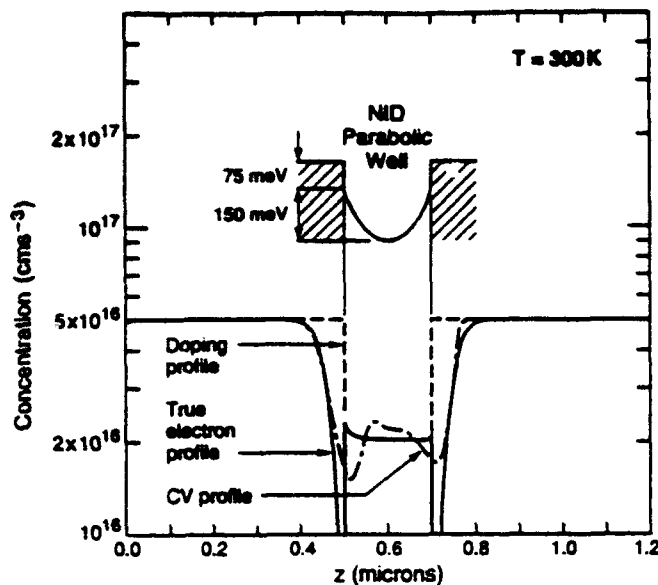


FIG. 6. The 300 K electron distributions simulated for modulation-doped parabolic well (inset) are shown. The true profile shows density in the well to be determined by the curvature of the parabola. Note the asymmetry in the CV (apparent) profile as a result of profiling through two back-to-back GaAs/AlGaAs heterojunctions.

B. Simulation results

The results of such a simulation for a modulation-doped wide parabolic potential well at 300 K is shown in Fig. 6. The doping profile shows that the structure is uniformly doped everywhere except in the well region. The true electron profile shows a uniform electron distribution in the well with a value determined by the parabolic potential curvature¹⁶ ($q^2 N_Q \omega^2 / 8\epsilon = \Delta$, where N_Q is the quasicarrier concentration corresponding to a parabolic potential of width ω and potential depth Δ). Electrons are depleted from the barrier regions bordering the well and dumped into the well. Far away from the well region, the electron distribution becomes equal to the doping distribution. The simulated apparent profile that would be seen in a CV measurement between surface gate and substrate ohmic contact is also shown. The uniform permittivity ϵ_s assumed is that of the top $\text{Al}_{0.3}\text{Ga}_{0.7}\text{As}$ layer. Note the asymmetry in the apparent electron distribution as a result of profiling through back-to-back GaAs/Al_xGa_{1-x}As heterojunctions. The apparent profile is a smeared-out version of the true profile in the region of the well, and is equal to the true profile only far away from the well where the true profile is uniform.

300 K true electron profiles are shown for four different barrier doping densities for the case of a parabolic, triangular, and square well in Figs. 7(a)–7(c), respectively. All three wells have the same potential depth below the surrounding barriers. The corresponding apparent profiles are shown in Figs. 8(a)–8(c). The differences between the apparent profiles for the different wells are sufficiently large that one can confidently expect any substantial deviation from the designed band gap grading to manifest itself in the CV measurement.

C. Conservation of charge and charge moment

Both the total charge and the first moment of the charge distribution are conserved in the profiling process.⁷ This can indeed be confirmed with the profiles in Fig. 6, where each electron profile, true and apparent, with the known doping profile contributes net zero charge and charge moment when integrated across the entire region of interest. The moment of the dipole formed at an n - n abrupt heterojunction is in fact related in a simple way to the net band offset across the heterojunction. In the symmetric modulation-doped potential wells considered above, we have two back-to-back dipoles. The two dipole moments obtained by integrating the moment of the net charge distribution from $-\infty$ to the right edge of the left dipole, and the left edge of the right dipole to $+\infty$ respectively, for both the true and apparent electron profiles, are related to the depth of the potential well below the surrounding barriers by:^{7,15}

$$\begin{aligned} \Delta E_C + kT \ln \left[\frac{\bar{n}(y_{DB}) / \bar{N}_C(y_{DB})}{\bar{n}(-\infty) / \bar{N}_C(-\infty)} \right] \\ = \frac{q^2}{\epsilon_s} \int_{-\infty}^{y_{DB}} [\bar{N}_R(y) - \bar{n}(y)] (y - y_i) dy \\ = \frac{q^2}{\epsilon_s} \int_{-\infty}^{y_{DB}} [\bar{N}_R(y) - \hat{n}(y)] (y - y_i) dy, \end{aligned} \quad (18a)$$

$$\begin{aligned} \Delta E_C + kT \ln \left[\frac{\bar{n}(+\infty) / \bar{N}_C(+\infty)}{\bar{n}(y_{DB}) / \bar{N}_C(y_{DB})} \right] \\ = \frac{q^2}{\epsilon_s} \int_{y_{DB}}^{+\infty} [\bar{N}_R(y) - \bar{n}(y)] (y - y_i) dy \\ = \frac{q^2}{\epsilon_s} \int_{y_{DB}}^{+\infty} [\bar{N}_R(y) - \hat{n}(y)] (y - y_i) dy, \end{aligned} \quad (18b)$$

where y_{DB} is the common boundary between the two dipoles, and y_i is the location of the interface that separates the positive and negative charge in each dipole.

This can readily be confirmed for the case of the parabolic well in Fig. 6. Interestingly, when the parabolic well is replaced by either a triangular well or a square well with the same net well depth below the surrounding barriers, the well depth obtained from the dipole moments (real and apparent) agree well with each other and with that for the parabolic well case despite the very different electron distributions. Specifically, for the real and apparent electron profiles for the three wells shown in Figs. 7 and 8 for the case where the barrier doping is $5 \times 10^{16} \text{ cm}^{-3}$, the well depth calculated using Eq. (18) agrees with the design well depth of 225 meV to within ± 2 meV for the parabolic well, ± 15 meV for the triangular well, and ± 20 meV for the square well, the charge conservation for all the apparent profiles also being concurrently preserved to better than $1 \times 10^{10} \text{ cm}^{-2}$.

The deconvolution of the true electron profile from the apparent profile, computer simulated or measured, is intractable. The experimental procedure that suggests itself is to extract the apparent electron profile from the measured

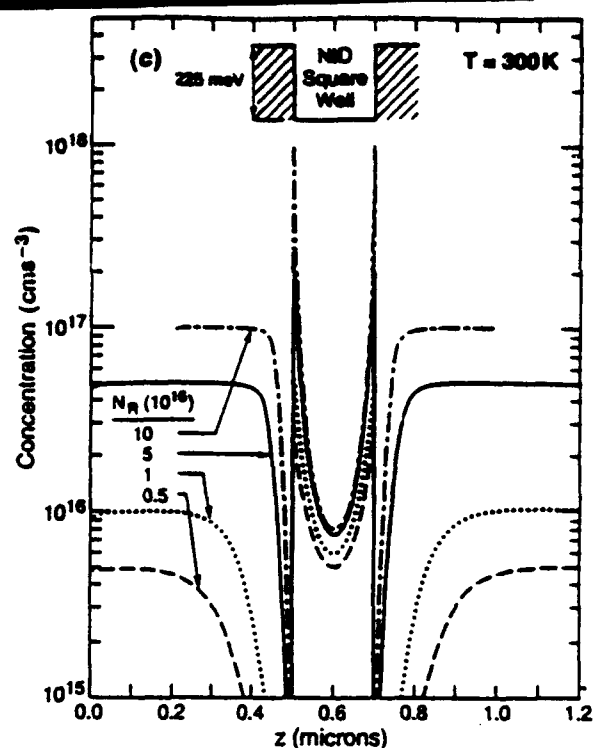
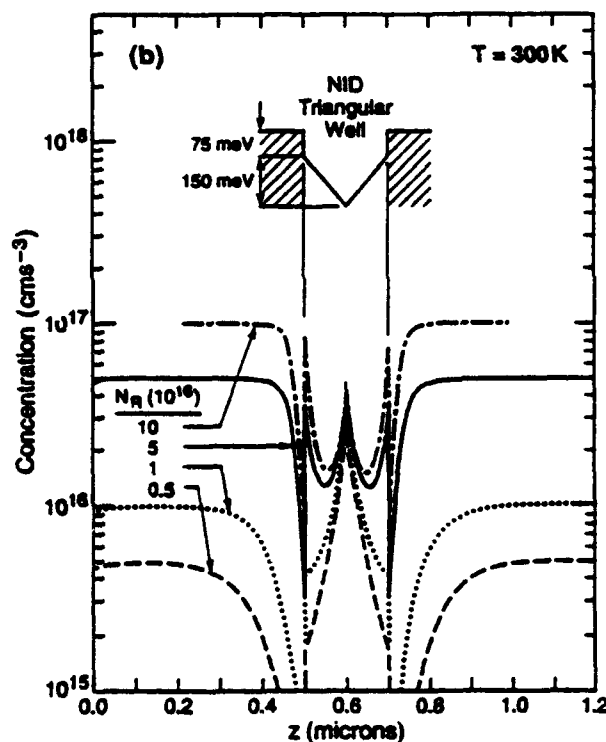
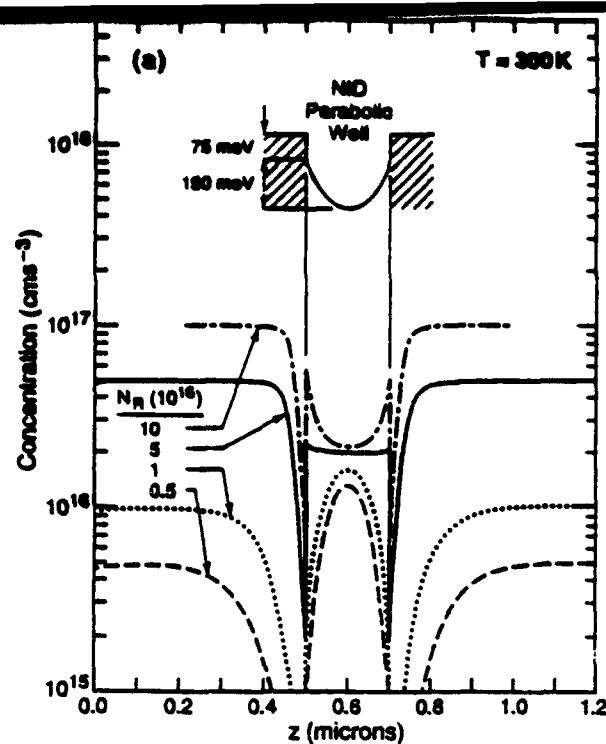


FIG. 7. The 300 K true electron profiles simulated for four different values of barrier doping for a modulation-doped parabolic well (a), triangular well (b), and square well (c), all three wells having the same width and same potential depth below the surrounding barriers, are shown. Note differences in electron distribution when the well shape is changed.

CV data using the permittivity of the barrier AlGaAs layer as ϵ_s in Eq. (1). The flat portions of the measured apparent profile on either side of the well region then directly give the uniform doping in the barrier regions. One makes a reasonable guess at the locations of the interfaces (i.e., the boundaries of the well) and assumes the doping profile to extend uniformly to these interfaces, as they are intended to be. An integral of the charge distribution reveals any excess sheet charge which can then be placed at either interface, preferably at the lower or reverse GaAs/AlGaAs interface for reasons explained below. The total dipole mo-

ment or the integral of the first moment of the charge distribution across the entire structure should ideally be zero. The dipole moment of each dipole can be used to deduce the well depth. To calculate this, both the true electron concentration at the common boundary between the two dipoles and the variation of dielectric permittivity $\epsilon(z)$ with depth need to be known. The former is assumed to be the curvature of the parabolic potential well; the latter is assumed to be linearly dependent on the Al mole fraction x of the $\text{Al}_x\text{Ga}_{1-x}\text{As}$ as:¹⁷ $\epsilon(x) = 13.1 - 3x$. The apparent profile can then be computer simulated and com-

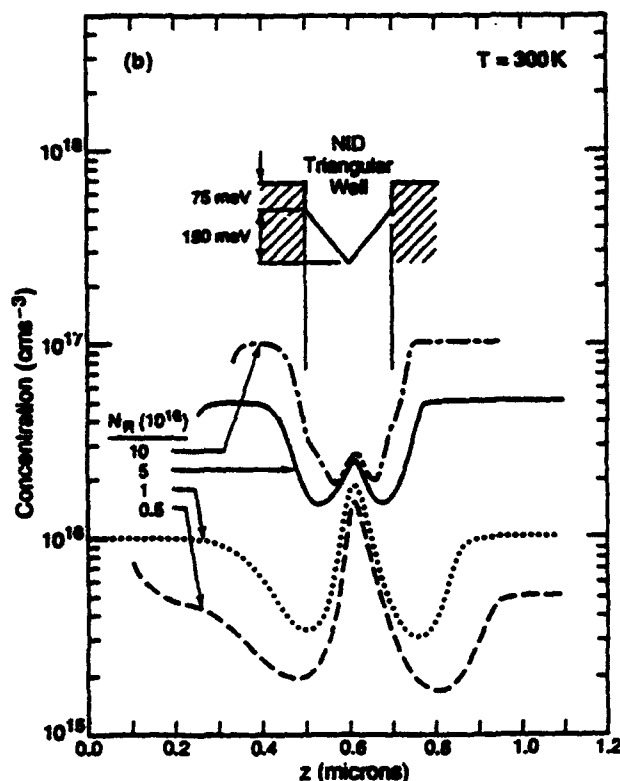
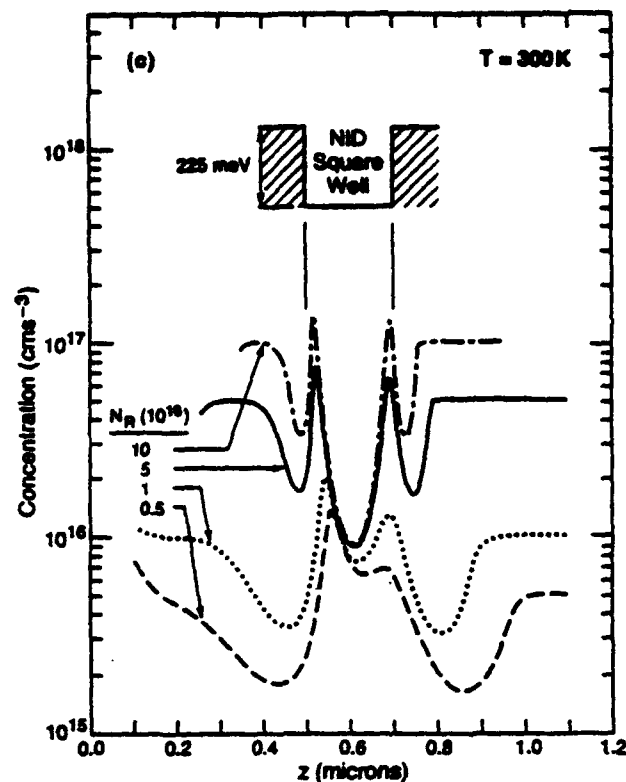
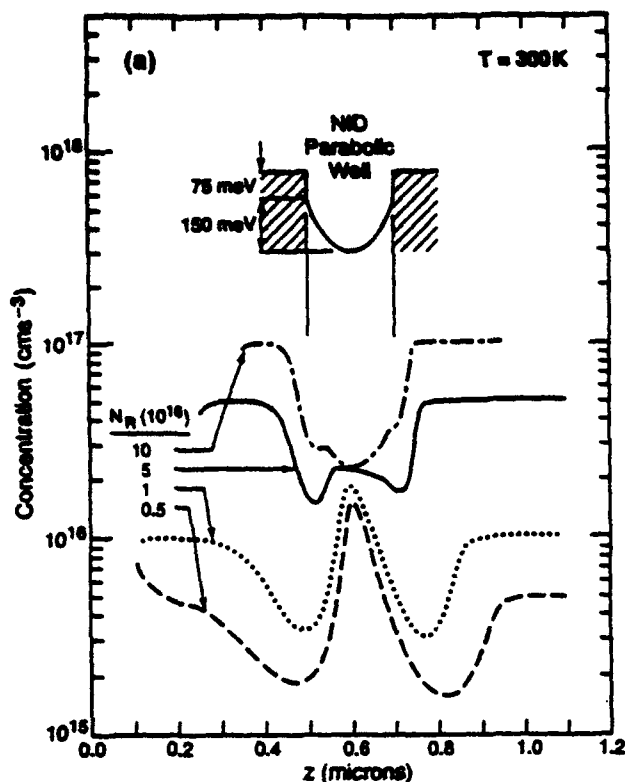


FIG. 8. The 300 K CV profiles corresponding to Fig. 7 are shown. The differences in the true electron profiles in Fig. 7 due to differences in the well shape are manifested in the corresponding CV profiles.

pared to the measured apparent profile, the curvature of the parabolic potential being used as a fitting parameter. Within reasonable variations of the curvature, the best fit is found. Appropriate corrections to the interface locations are made and the above process repeated until convergence is obtained. The true profile corresponding to the best fit then gives the real electron distribution in the graded heterojunction.

III. EXPERIMENT

Samples were grown by molecular beam epitaxy in a Varian GEN II MBE system on heavily doped *N*-type GaAs substrates. The parabolic well itself was realized as a graded $\text{Al}_x\text{Ga}_{1-x}\text{As}$ with parabolically varying Al mole fraction x by using the digital-alloy technique in a manner explained elsewhere.¹⁸

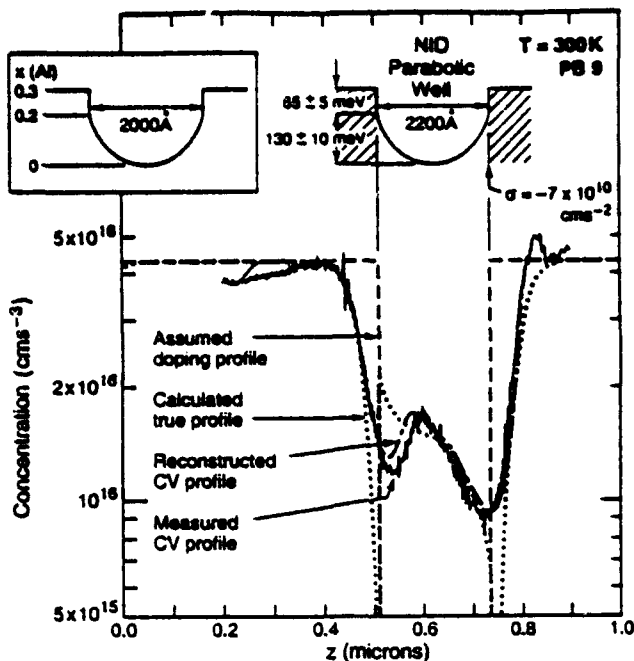


FIG. 9. Room-temperature profiles: measured CV, simulated CV, simulated true, and assumed doping, for a parabolic well (boxed inset depicts nominal design) are shown. Parameters for the best fit of measured and simulated CV profiles are shown above the well. The presence of a negative sheet charge at the lower interface is deduced; this points to an asymmetry in the doping profile and is mainly responsible for the asymmetry in the electron distributions.

Mobility measurements on similar modulation-doped parabolic potential wells grown at the same time but on semi-insulating substrates reveal^{4,18} the presence of a thick (~ 1000 Å) high-quality three-dimensional electron gas (3DEG) with low-temperature mobilities in excess of 2×10^5 cm²/V s in the well. A background ionized acceptor impurity concentration of $\sim 2 \times 10^{14}$ cm⁻³ is calculated to be present in the undoped wells.¹⁹

Due to the $\pm 4\%$ uncertainty in the determination of the growth rates of GaAs and AlAs using the RHEED oscillation method, the Al mole fraction in the $\text{Al}_x\text{Ga}_{1-x}\text{As}$ in the barriers and in the digital-alloy superlattice is uncertain to within $\pm 6\%$ for $x=0.3$. Ion-gauge measurements of the Al flux in the well show that the curvature of the parabola can vary by $\pm 10\%$ across the well, the error approaching $\pm 100\%$ at a few 100 Å about the well center due to the low x and the extremely short Al pulses there.²⁰ These flat spots in a narrow region about the well center should be effectively screened out by the electron gas at room temperature. The samples were not rotated during growth. For the substrate-oven geometry in our MBE machine, we estimate a consequent maximum variation of $\pm 6\%$ in the x of the barrier $\text{Al}_x\text{Ga}_{1-x}\text{As}$, $\pm 20\%$ in the thickness of a layer grown, and $\pm 30\%$ in the curvature of the parabola across a 2-in.-diam wafer.

Circular Ti-Au gates of different radii were evaporated onto the sample surface. The ohmic contact to the conducting substrate was made by pasting In on to it in a hot plate. The small-signal capacitance versus gate voltage be-

tween gate and substrate ohmic contact was measured with a variable frequency HP4192 impedance analyzer. All measurements were made at room temperature. The measurements were found to be independent of both bias-voltage sweep rate and small-signal ac frequency. The apparent electron profile versus depth was extracted from the CV measurement using Eq. (1), taking the dielectric permittivity of the cap $\text{Al}_{0.3}\text{Ga}_{0.7}\text{As}$ to be the ϵ_r .

Data for two wafers are presented below. The first one, PB9, was nominally designed to be the same as the one for which the simulation results were presented in Fig. 6. The substrate temperature was 600 °C throughout the growth. The measured apparent profile, the best computer-simulated apparent profile, the corresponding true electron profile, and the assumed doping profile are shown in Fig. 9. Also shown are the dimensions of the potential well that gave this best self-consistent fit. The boxed inset shows the nominal well design in terms of Al mole fraction versus depth. The well width, well height, and barrier height (measured from the bottom of the well) could all be varied over a small range while still retaining a reasonably good fit between the simulated and measured CV profiles. These values, viz. 2200 ± 50 Å in the well width (nominally 2000 Å), 130 ± 10 meV in the height of the parabolic well (x nominally going from 0 at well center to 0.2 at well edges), and 65 ± 5 meV in the height from the well edge to the top of the barrier (x nominally going from 0.2 to 0.3), sufficed to also fit the measured profiles from adjacent samples. In every case though, a negative sheet charge $\sigma \sim -7 \times 10^{10}$ cm⁻² at the lower interface of the parabolic well had to be used to ensure a complete fit. Without this interface charge, only a partial fit (over about half the parabolic well) could be obtained. Note, though, that despite the presence of this charge, the electron gas is uniform over most of the well width, its density given by the curvature of the well.

The exact origin of this interface charge at the reverse interface is unclear. It could be due to the Si and/or C and/or other impurity riding on the growing AlGaAs surface, piling up in the first period of the superlattice composing the parabolic well. The fact that there is a diffusion of the Si from the doped AlGaAs layer through the spacer layer and toward the 2DEG in reverse interface GaAs on AlGaAs heterojunctions is well established.^{21,22} The problem is somewhat mitigated by doping the AlGaAs at a lower substrate temperature²³ (so that the Si sticks and incorporates and does not ride on the growing surface) and/or by inserting a superlattice spacer layer between doped AlGaAs and 2DEG²⁴ which also serves to getter impurities away from the parabolic well.

Both these measures were adopted in the second wafer PB22, which in all other respects was identical to PB9. The doped layers and spacers (with nominal $x_{\text{avg}}=0.24$) were grown at a substrate temperature of 520 °C, while the well itself was grown at 600 °C, the temperature change occurring during the growth of the spacer layer. The results of the CV measurement and analysis are shown in Fig. 10. No interface charge is present in this sample. Excellent fits are obtained assuming well widths of 2200 ± 100 Å (nominally

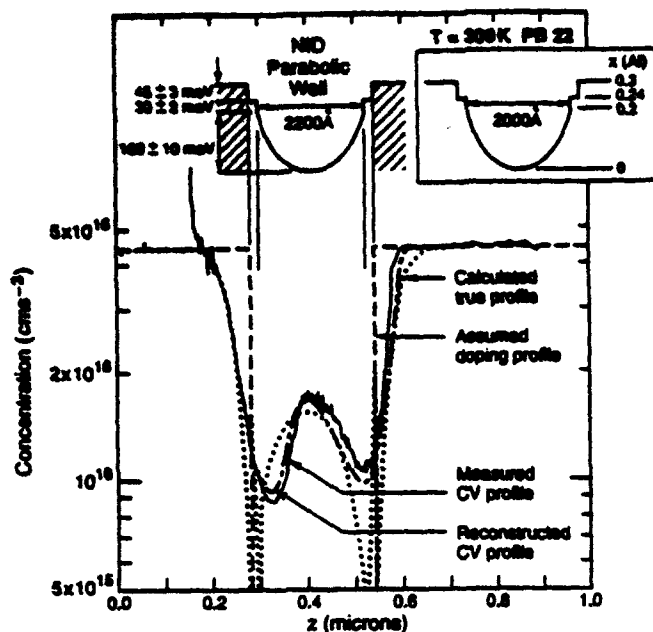


FIG. 10. Room-temperature profiles: measured CV, simulated CV, simulated true, and assumed doping, for a parabolic well (boxed inset depicts nominal design) are shown. The parameters for the best fit of measured and simulated CV profiles are shown above the well. Low-temperature doping of the barrier AlGaAs and the insertion of superlattice spacer layers reduce asymmetry in doping, as evidenced by the absence of interface charges and the good fit between measured and simulated CV profiles.

2000 Å), 160 ± 10 meV in the well height (x nominally going from 0 to 0.2), 30 ± 2 meV in the height from the well edge to the top of the spacer (x nominally going from 0.2 to 0.24), and 45 ± 3 meV in the height from the top of the spacer to the top of the barrier (x nominally going from 0.24 to 0.30). The corresponding true electron profile shows that while there are not enough electrons to fill the well completely, they are distributed almost uniformly over most of the well with a 3D density determined by the potential curvature. Using these modified growth conditions, we have been successful in obtaining high-quality 3DEGs in parabolic potential wells grown on semi-insulating substrates.⁴

Our measurements and analysis also give us the room-temperature conduction-band offsets of $\text{Al}_x\text{Ga}_{1-x}\text{As}$ with respect to GaAs, as a function of Al mole fraction x . These are plotted in Fig. 11. Each sample yields several data points, one for each potential step. The vertical error bars are the maximum allowed variations that still give reasonable fits to the measurements. The horizontal error bars represent uncertainties in the Al mole fraction due to both the uncertainty in the growth-rate measurement and the variation across a 2-in.-diam wafer. The relation: $\Delta E_C (\text{meV}) = 720x$ seems to best accommodate the data from the two wafers. Using the known¹⁷ $\Delta E_G (\text{meV}) = 1247x$ yields $\Delta E_C/\Delta E_V = 58/42$ at room temperature.

Quantum size effects appear and Debye smearing effects disappear if the measurements are done at $T = 0$ K. These have been investigated in detail and discussed elsewhere.²⁵

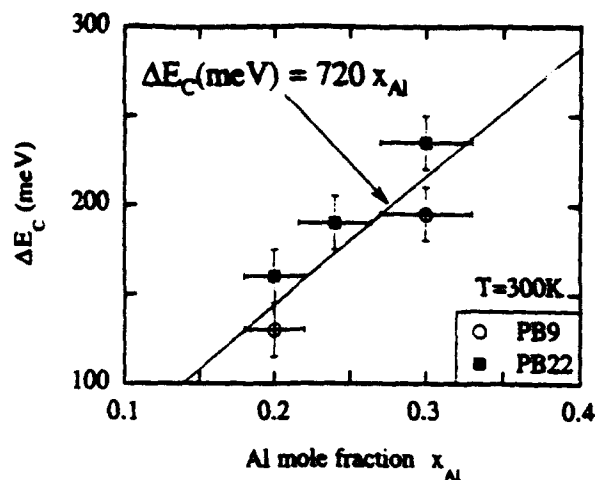


FIG. 11. The 300 K conduction-band energy offsets versus Al mole fraction x in $\text{Al}_x\text{Ga}_{1-x}\text{As}$ arrived at from simulated fits of experimental CV measurements of two parabolic wells are shown. Line shows best fit to both samples. Vertical error bars span the range of energies that give good experimental fits, and horizontal ones, the variation in x values across a 2-in.-diam wafer.

IV. CONCLUSIONS

We have presented general equations to calculate the true and apparent (CV) thermal-equilibrium carrier distributions in graded heterostructures of known band gap and dopant grading. Numerical solutions of these equations have been performed to obtain electron profiles in potential wells of different shapes at room temperature. Both the real electron profile and the profile that would be measured in a CV measurement are calculated for modulation-doped parabolic, triangular, and square potential wells. Electrons are seen to distribute themselves uniformly in a parabolic well with a density determined by the curvature of the parabolic potential. Charge and charge moment are conserved in the profiling process.

Parabolic potential wells were grown by MBE as graded $\text{Al}_x\text{Ga}_{1-x}\text{As}$ digital alloys and CV measurements performed on them. Excellent fits could be obtained to the measurements using the equations presented above. The doping asymmetry at the two interfaces, the normal AlGaAs on GaAs and the reverse GaAs on AlGaAs, manifested itself in the CV measurement as a sheet charge at the lower interface. Using a lower substrate temperature during the AlGaAs doping and inserting superlattice spacer layers between the well and doped layer succeeded in restoring symmetry to the real electron distribution.

The CV profiling technique is extremely useful in measuring carrier distributions in semiconductors if accompanied by an analysis of the type presented above. This method is also applicable in a more accurate determination of band offsets in abrupt heterojunctions if the unintentional band gap and/or dopant grading in the region of the dipole formed at the interface is independently known. For the parabolic potential wells measured, the ratio of the conduction-to-valence-band offsets $\Delta E_C/\Delta E_V$ is determined to be 58/42 at room temperature.

ACKNOWLEDGMENTS

It is a pleasure to thank A. Wixforth, P. F. Hopkins, K. Ensslin, E. G. Gwinn, and M. S. Sherwin for discussions. M.S. would like to thank J. H. English for valuable tips on MBE growth and Professor H. Kroemer for his inspiring lectures on the CV profiling technique in a graduate course. The above work is an extension of the theses work of two of Professor Kroemer's graduate students, W. Y. Chien and D. I. Babic, on CV profiling through abrupt heterojunctions. We thank L. Pfeiffer for providing us with a preprint of a paper on Si dopant migration in AlGaAs. This research was supported by the United States Air Force Office of Scientific Research.

- ¹H. Kroemer, *J. Vac. Sci. Technol. B* 1, 126 (1983).
- ²W. T. Tsang, F. S. Choa, M. C. Wu, Y. K. Chen, A. M. Sergent, and P. F. Sciortino, Jr., *Appl. Phys. Lett.* 58, 2610 (1991).
- ³A. C. Gossard, *IEEE J. Quantum Electron.* QE-22, 1649 (1986).
- ⁴See, for example, P. F. Hopkins, A. J. Rimberg, E. G. Gwinn, R. M. Westervelt, M. Sundaram, and A. C. Gossard, *Appl. Phys. Lett.* 57, 2823 (1990); T. Sajoto, J. Jo, L. Engel, M. Santos, and M. Shayegan, *Phys. Rev. B* 39, 10 464 (1989).
- ⁵W. W. Bewley, C. L. Felix, J. J. Plombon, B. Galdrikian, M. S. Sherwin, M. Sundaram, A. C. Gossard, and B. Birnir (unpublished).
- ⁶S. Giugni, T. L. Tansley, G. J. Griffiths, F. Green, C. Shue, and M. Gal, *Proc. Sixth Intl. Conf. on Molecular Beam Epitaxy*, San Diego, 1990.
- ⁷H. Kroemer, W. Y. Chien, J. S. Harris, Jr., and D. D. Edwall, *Appl. Phys. Lett.* 36, 295 (1980).
- ⁸M. O. Watanabe, J. Yoshida, T. Nakamizi, A. Hojo, and M. Masuda, *J. Appl. Phys.* 57, 5340 (1985).
- ⁹H. Kroemer, *Appl. Phys. Lett.* 46, 504 (1985).
- ¹⁰G. Gummel, *Phys. Status Solidi A* 108, 813 (1988).
- ¹¹M. Ogasawa, T. Murakami, M. Miyoshi, T. Miyoshi, and S. Shimizu, *Jpn. J. Appl. Phys.* 27, L1334 (1988).
- ¹²See, for example, D. P. Kennedy, P. C. Murley, and W. Kleinfelder, *IBM J. Res. Dev.* 12, 399 (1968).
- ¹³H. K. Gummel and D. L. Scharfetter, *J. Appl. Phys.* 38, 2148 (1967); see also C. Kittel and H. Kroemer, *Thermal Physics* (Freeman, San Francisco, 1980), 2nd ed., Chap. 13.
- ¹⁴See, for example, L. Collatz, *The Numerical Treatment of Differential Equations*, 3rd ed. (Springer, Berlin, 1960).
- ¹⁵D. I. Babic and H. Kroemer, *Solid State Electron.* 28, 1015 (1985).
- ¹⁶M. Sundaram, A. C. Gossard, J. H. English, and R. M. Westervelt, *Superlattices and Microstructures* 4, 683 (1988).
- ¹⁷H. C. Casey, Jr. and M. B. Panish, *Heterostructure Lasers* (Academic, New York, 1978), Chap. 4.
- ¹⁸M. Sundaram, A. C. Gossard, and P. O. Holtz, *J. Appl. Phys.* 69, 2370 (1991).
- ¹⁹W. Walukiewicz, M. Sundaram, P. F. Hopkins, A. C. Gossard, and R. M. Westervelt, *Proc. MRS Fall Mtg.*, Boston, 1990.
- ²⁰M. Sundaram, A. Wixforth, R. S. Geels, A. C. Gossard, and J. H. English, *J. Vac. Sci. Technol. B* 9, 1524 (1991).
- ²¹S. Sasa, J. Saito, K. Nanbu, T. Ishikawa, and S. Hiyamizu, *Jpn. J. Appl. Phys.* 23, L573 (1984).
- ²²L. Pfeiffer, E. F. Schubert, K. W. West, and C. W. Magee, *Appl. Phys. Lett.* 58, 2258 (1991).
- ²³K. Inoue and H. Sakaki, *Jpn. J. Appl. Phys.* 23, L61 (1984).
- ²⁴H. Shtrikman, M. Heiblum, K. Seo, D. E. Galbi, and L. Osterling, *J. Vac. Sci. Technol. B* 6, 670 (1988).
- ²⁵A. Wixforth, M. Sundaram, K. Ensslin, J. H. English, and A. C. Gossard, *Appl. Phys. Lett.* 56, 454 (1990).

Capacitive detection of subband structure in the electron gas in a wide parabolic GaAs/Al_xGa_{1-x}As quantum well

A. J. Rimberg, Scott Yang, Jed Dempsey, J. H. Baskey, and R. M. Westervelt
Division of Applied Sciences and Department of Physics, Harvard University, Cambridge,
Massachusetts 02138

M. Sundaram and A. C. Gossard
Materials Department, University of California, Santa Barbara, California 93106

(Received 12 June 1992; accepted for publication 18 November 1992)

Profiles of the capacitance $C(V_g)$ between a front gate and the electron gas in a wide parabolic well and its derivative dC/dV_g are used to study the subband structure and uniformity of the electron gas layer. Subband depopulation events are detected as peaks in the derivative profile dC/dV_g as the width of the electron gas is reduced by application of the gate voltage V_g . To separate depopulation events from nonuniformities in electron density, derivative profiles are repeated for increasing in-plane magnetic fields: depopulation peaks move to smaller gate voltages and disappear at characteristic fields, while nonuniformities remain fixed and are accentuated in strong fields.

Wide parabolic quantum wells (WPBWs) have received much attention in the past few years as a system in which an electron gas of variable thickness and subband structure can be studied.¹⁻³ These wells are also interesting in that they can provide an electron gas with low three dimensional (3D) density ($\sim 5\text{--}25 \times 10^{15} \text{ cm}^{-3}$) and good uniformity over wide ($\sim 2000 \text{ \AA}$) regions.^{4,5} Recently, Wixforth *et al.*² and Sundaram *et al.*³ have turned to measurements of the capacitance profile $C(V_g)$ between a front gate and the electron gas in a WPBW as a function of gate voltage V_g to probe changes in the subband structure of the system as the gas width is changed. Such measurements are difficult for two reasons. First, changes in capacitance associated with changes in subband occupancy can be quite small (\sim one part in 10^3) compared to the total capacitance, requiring high sensitivity. Second, a local variation in electron density due to imperfect well shape will give rise to a feature in $C(V_g)$ similar to a subband depopulation, but potentially much larger.

We report here the detection of peaks in the derivative profile dC/dV_g for a wide parabolic well which can be unambiguously identified with subband depopulations. An in-plane magnetic field H is used to separate peaks due to subband depopulations from features due to nonuniformities in the electron gas. The depopulation peaks move to smaller gate voltage with increasing field H , in excellent agreement with self-consistent calculations: the depopulation fields H_d at which the peaks are projected to reach zero gate voltage are also in excellent agreement with in-plane magnetoresistance measurements. In the quantum limit for which only one subband is occupied, we obtain an approximate charge density profile^{6,7} uniform to $\pm 20\%$ across the electron gas layer.

The total inverse capacitance^{2,3} of the electron gas in an ideal wide parabolic well can be expressed as the sum of geometric and quantum parts:

$$\frac{1}{C} = \frac{1}{C_{\text{geom}}} + \frac{1}{C_q} \quad (1)$$

The geometric capacitance is associated with the classical electron density profile, which we model as a uniform slab at the 3D design density of the well n_{3D} with sharp edges, giving:

$$C_{\text{geom}} = \epsilon \epsilon_0 A \left(z_0 + \frac{2\epsilon \epsilon_0 V_g}{en_{3D}} \right)^{-1/2} \quad (2)$$

Here A is the area of the gate, z_0 is the distance from the gate to the front of the slab at $V_g=0$ V, $\epsilon=12.8$ is the dielectric constant of GaAs, ϵ_0 is the electric permittivity of free space and $-e$ is the electronic charge. The inverse quantum capacitance $1/C_q$ is defined via Eq. (1) as the difference between a quantum-mechanical self-consistent calculation⁹ of the total inverse capacitance of the electron gas and $1/C_{\text{geom}}$ from Eq. (2). This difference is associated with changes in the Fermi energy E_F relative to the electrostatic potential of the geometric model: $C_q = e^2 A \partial n / \partial E_F$. The Fermi energy has two contributions: a kinetic energy term, and the difference between the true self-consistent and the simple geometric potentials.

The sample chosen for study (PB31) was grown via molecular beam epitaxy using the digital alloy technique.¹⁰ It contains a well of nominal width 2000 \AA and height 175 meV , with nominal electron density $n_{3D} = 2.5 \times 10^{16} \text{ cm}^{-3}$. Previous transport measurements in both transverse⁵ and in-plane¹¹ magnetic fields demonstrated that the density and subband energies of the electron gas are in excellent agreement with theory, and that the electron layer is 900 \AA wide with three occupied subbands. For the present work, a Cr/Au front gate was added to the sample, which caused only a small (2%) reduction in Hall sheet density to $n_s = 2.26 \times 10^{11} \text{ cm}^{-2}$. The sample was cooled in the dark inside a ³He cryostat; to change sample orientation with respect to the magnetic field, we thermally cycled and remounted it. The capacitance profile $C(V_g)$ between the gate and the electron gas was measured by applying a variable dc bias V_g with a superimposed sinusoidal oscillation (20 mV rms at 402 Hz) which induces a small ($\sim 1.7\%$) change in sheet density at $V_g=0$ V. The ac current was

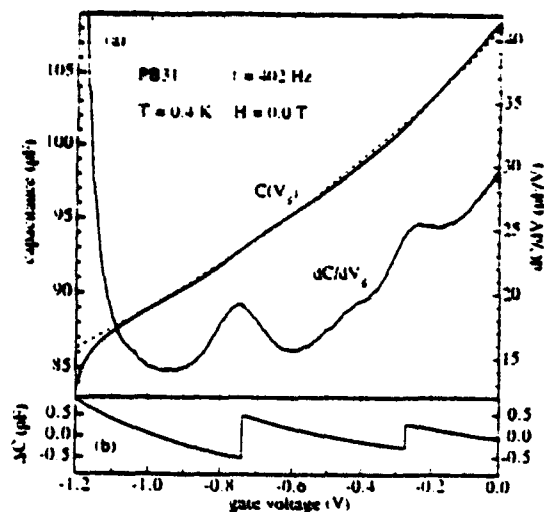


FIG. 1. (a) Capacitance $C(V_g)$ and derivative dC/dV_g profiles vs gate voltage V_g at zero magnetic field. The dashed line is a fit to the geometric capacitance from Eq. (2). (b) Theoretical quantum contribution to the capacitance $\Delta C = -C_{\text{geom}}^2/C_g$ from self-consistent calculations; steps occur in ΔC at subband depopulations.

amplified and detected using standard lock-in techniques. The derivative profile dC/dV_g was simultaneously measured at twice the fundamental frequency with a second lock-in amplifier. We found no significant change in $C(V_g)$ or dC/dV_g for oscillation frequencies and amplitudes in the range 101–1010 Hz and 10–30 mV rms. The measured impedance was purely capacitive except near pinch-off.

A typical measured capacitance profile $C(V_g)$ is shown in Fig. 1(a) for zero in-plane field H . As shown $C(V_g)$ decreases smoothly with V_g until pinch-off occurs at $V_g = -1.2$ V. The geometric capacitance C_{geom} from Eq. (2), shown as the dotted curve, provides an excellent fit to the measured profile indicating that this simple classical approximation is fairly good. The gate area $A = 3.4 \times 10^{-3}$ cm² determined by the fit is 11% less than the area measured under a microscope. The values of the other parameters z_0 and n_{3D} in C_{geom} were determined by fits to depopulation peak voltages as discussed below. Small differences between the measured profile $C(V_g)$ and C_{geom} are shown clearly as two peaks in the measured derivative profile dC/dV_g in Fig. 1(a). As demonstrated below, these two peaks are caused by subband depopulations rather than nonuniformities in the electron density profile.

To compare with theory, the change $\Delta C \equiv C - C_{\text{geom}} = -C_{\text{geom}}^2/C_g$ from Eq. (1) due to the quantum capacitance C_g was determined from self-consistent calculations⁹ for the ideal case of zero temperature and no disorder. As shown in the plot of ΔC in Fig. 1(b), each depopulation event causes a vertical step in ΔC due to a change in slope of the Fermi energy versus sheet density. Each step in ΔC corresponds to a delta function peak in the derivative profile dC/dV_g ; for experimental data these peaks are broadened by disorder and temperature. The profile ΔC shown in Fig. 1(b) is a fit obtained by varying the parameters n_{3D} and z_0 to match the voltages of the two steps in ΔC with the two peaks in the measured derivative profile dC/dV_g .

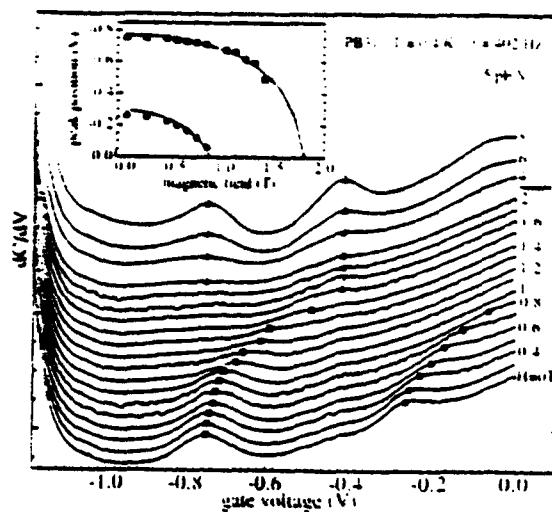


FIG. 2. Derivative profiles dC/dV_g vs gate voltage V_g offset for a series of in-plane magnetic fields $H = 0$ –8 T. From 0 to 2 T the field increment is $\Delta H = 0.1$ or 0.2 T; from $H = 2$ to 8 T, $\Delta H = 2$ T. Gate voltages associated with depopulation events (solid squares and circles) and nonuniformities (open circles) are indicated. The inset shows the field dependence of the measured gate voltages for depopulation events (solid squares and circles), together with theoretical calculations (solid lines). Depopulation fields at zero gate voltage obtained from magnetotransport measurements are also indicated (vertical dashed lines).

The best fit is for $n_{3D} = 2.4 \times 10^{16}$ cm⁻³ and $z_0 = 3600$ Å, 4% smaller and 16% larger than their nominal values assuming symmetric filling of the parabolic well above the center. Furthermore, the areas of the peaks in dC/dV_g are in good agreement with the theory: the measured areas 0.63 and 0.30 pF for the peaks at -0.75 and -0.26 V are slightly smaller than the corresponding theoretical step sizes in $\Delta C = 1.0$ and 0.54 pF. Thus a fit by three parameters n_{3D} , z_0 , and A gives excellent agreement with theory for both the geometric and quantum parts of the calculated capacitance, including the strength of depopulation peaks.

To separate subband depopulation peaks from features due to nonuniformities, a series of derivative profiles dC/dV_g were recorded for increasing magnetic fields H applied in the plane of the parabolic well, as shown in Fig. 2. In this geometry, the subbands of the well potential couple with Landau levels, and higher subbands depopulate at characteristic magnetic fields H_d for zero gate voltage. Similarly, one expects the gate voltage V_g at which higher subbands depopulate to decrease with H , and depopulation peaks in dC/dV_g to move to less negative voltage V_g as H increases, reaching zero gate voltage at H_d . This behavior is, in fact, observed for the depopulation peaks in Fig. 2, labeled as solid squares and solid circles, which move to less negative gate voltage and disappear for moderate field $H < 2$ T. The peak positions are plotted versus magnetic field H in the inset to Fig. 2, and are in excellent agreement with a self-consistent Hartree calculation¹² of the field-dependent depopulation voltages, shown as the solid lines, performed with no new adjustable parameters. The only inputs to theory are n_{3D} and z_0 from the fit above at $H = 0$ T, and the measured Hall sheet density n_s . In-plane mag-

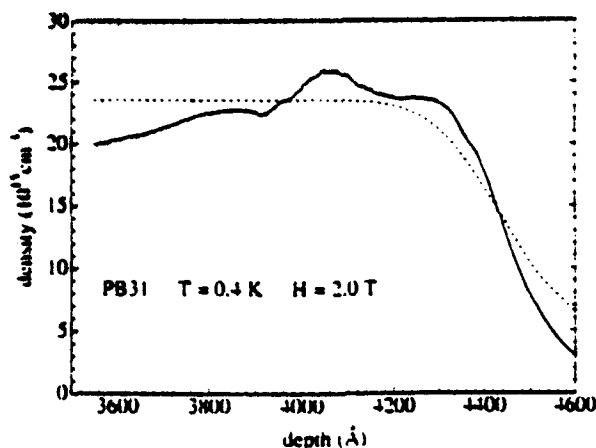


FIG. 3. Classical charge density profile $n(z)$ (solid line) and smeared rectangular profile (dashed line) modeling quantum uncertainty in the electron position.

netotransport measurements¹¹ give independent measurements of the depopulation fields $H_d \approx 0.8$ and 1.8 T at zero gate voltage for the third and second subbands of this sample, shown in the inset to Fig. 2 as vertical dashed lines, which are in excellent agreement with theory. The detailed quantitative agreement between capacitance profiles, theory, and magnetotransport measurements allows us to unambiguously identify the peaks in the derivative profile that are due to subband depopulation.

In contrast to depopulation events, features due to nonuniformities in the electron density profile remain at fixed gate voltage, and grow stronger with increasing in-plane fields H , due to electron localization as the magnetic length $\ell_H = (\hbar/eH)^{1/2}$ is reduced. Features of this type are found in the derivative profiles shown in Fig. 2 for stronger in-plane fields $H > 2$ T, and are labeled by open circles. The classical electron density profile $n(z)$ obtained from C and dC/dV_g using the geometrical model¹³ is shown in Fig. 3 as the solid line for the magnetic quantum limit ($H = 2.0$ T) for which only the lowest subband is occupied. As shown, variations in $n(z)$ are small, indicating a high degree of uniformity in the electron gas for moderate in-plane magnetic fields. The density profile $n(z)$ in Fig. 3 is smeared by quantum effects, modeled by the dotted curve in Fig. 3, which is a rectangular profile convolved with a Gaussian of variance $\ell_H^2/2$. The sheet density $n_s = \int n(z) dz$ is conserved⁷ in a quantum treatment and the integral $\int n(z) dz$

of the density profile $n(z)$ in Fig. 3 agrees with the measured Hall sheet density to within $\sim 6\%$.

In conclusion, we have detected peaks in the derivative profile dC/dV_g for the gate-to-gas capacitance in a wide parabolic well which can be unambiguously identified with subband depopulations. At zero magnetic field, a quantitative fit to theory is obtained for both the capacitance and derivative profiles which give parameter values in agreement with nominal values. An in-plane magnetic field is applied to separate depopulation peaks from features due to nonuniformities. The field dependence of the depopulation peaks is in excellent agreement with theoretical calculations using no new adjustable parameters, as well as with in-plane magnetotransport measurements. For moderate magnetic fields in the quantum limit the electron density profile $n(z)$ is found to be uniform to $\pm 20\%$.

We thank P. F. Hopkins for helpful comments. One of us (J.H.B.) acknowledges support from the Natural Sciences and Engineering Research Council of Canada. This work was supported at Harvard by NSF Grants DMR-91-19386 and DMR-89-20490 and at Santa Barbara by AFOSR Grant AFOSR-91-0214.

¹E. G. Gwinn, R. M. Westervelt, P. F. Hopkins, A. J. Rimberg, M. Sundaram, and A. C. Gossard, *Phys. Rev. B* **39**, 6260 (1989); T. Sajoto, J. Jo, M. Santos, and M. Shayegan, *Appl. Phys. Lett.* **55**, 1430 (1989).

²A. Wixforth, M. Sundaram, K. Ensslin, J. H. English, and A. C. Gossard, *Appl. Phys. Lett.* **56**, 454 (1990).

³M. Sundaram, K. Ensslin, A. Wixforth, and A. C. Gossard, *Superlatt. Microstruct.* **10**, 157 (1991).

⁴E. G. Gwinn, P. F. Hopkins, A. J. Rimberg, R. M. Westervelt, M. Sundaram, and A. C. Gossard, *Phys. Rev. B* **41**, 10700 (1990).

⁵P. F. Hopkins, A. J. Rimberg, E. G. Gwinn, R. M. Westervelt, M. Sundaram, and A. C. Gossard, *Appl. Phys. Lett.* **57**, 2823 (1990).

⁶D. P. Kennedy, P. C. Murley, and W. Kleinfelder, *IBM J. Res. Dev.* **12**, 399 (1968).

⁷H. Kroemer, W. Y. Chien, J. S. Harris, Jr., and D. D. Edwall, *Appl. Phys. Lett.* **36**, 295 (1980).

⁸T. P. Smith, B. B. Goldberg, P. J. Stiles, and M. Heiblum, *Phys. Rev. B* **32**, 2696 (1985).

⁹A. J. Rimberg and R. M. Westervelt, *Phys. Rev. B* **40**, 3970 (1989).

¹⁰M. Sundaram, A. C. Gossard, J. H. English, and R. M. Westervelt, *Superlatt. Microstruct.* **4**, 683 (1988).

¹¹R. M. Westervelt, A. J. Rimberg, P. F. Hopkins, E. G. Gwinn, M. Sundaram, and A. C. Gossard, in *Proceedings of the 20th International Conference on the Physics of Semiconductors*, Thessaloniki, 1990, edited by E. Anastassakis and J. D. Joannopoulos (World Scientific, Singapore, 1990), Vol. 2, p. 1085.

¹²J. Dempsey (unpublished); see also M. P. Sope and S. Das Sarma, *Phys. Rev. B* **40**, 10048 (1989), and L. Brey and B. I. Halperin, *Phys. Rev. B* **40**, 11634 (1989).

¹³See, for example, D. C. Look, *Electrical Characterization of GaAs Materials and Devices* (John Wiley, Chichester, 1989).

COVER. Cross section of a serpentine superlattice (100 angstrom period) and its three lowest energy electron wave functions as an example of fabrication on a small scale (see page 1326). The cross-sectional view (far right) shows the aluminum-rich regions (dark) that confine electrons to the gallium-rich regions (light) in the segregated aluminum-gallium-arsenic alloy. The most colorful portions of the wave functions (in sections to the left) are regions of maximum electron density; the reddish-brown areas indicate zero density. See the editorial on page 1277 and the special section beginning on page 1300. [Simulations by J. C. Yi of the University of California, Santa Barbara]

Reprint Series
29 November 1991, Volume 254, pp. 1326-1335

SCIENCE

New Quantum Structures

MANI SUNDARAM, SCOTT A. CHALMERS, PETER F. HOPKINS, AND ARTHUR C. GOSSARD

New Quantum Structures

MANI SUNDARAM, SCOTT A. CHALMERS, PETER F. HOPKINS, ARTHUR C. GOSSARD

Structures in which electrons are confined to move in two dimensions (quantum wells) have led to new physical discoveries and technological applications. Modification of these structures to confine the electrons to one dimension (quantum wires) or release them in the third dimension, are predicted to lead to new electrical and optical properties. This article discusses techniques to make quantum wires, and quantum wells of controlled size and shape, from compound semiconductor materials, and describes some of the properties of these structures.

THERE HAS BEEN SWIFT PROGRESS IN RECENT YEARS IN THE synthesis of artificial quantized structures. Electrons in these small structures show quantum effects that strongly modify their behavior. Progress has been especially rapid in layered quantum structures (1), which are stacks of precisely deposited thin films in which electrons show fundamentally new electrical and optical properties. These materials offer a miniature laboratory that has influenced our basic understanding of solids and has provided new

kinds of optical and electronic devices (2). Among the discoveries emerging from layered structures are the quantum Hall effect (for which the 1985 Nobel Prize in Physics was awarded), transistors with record speed, and lasers with record low threshold current for lasing. Practical application of the structures has been so rapid that they are encountered now in our daily lives. Devices currently being manufactured with layered quantum structures include most lasers in compact disc players, low noise amplifiers in direct broadcast satellite receivers, and laser sources for fiber optic communication.

Past research on quantized semiconductor structures has focused on layered structures that confine conduction electrons to two dimensions. Now, systems in which the electrons are confined to one dimension of free motion (quantum wires) are providing materials with remarkable new properties [for instance, the quantization of electrical conductance in ballistic quantum wire channels (4)]. But the challenges of fabricating these wire-like structures are greater than those for making layered structures, and extensive improvements in the fabrication techniques are needed. A starting point for the fabrication of quantum wires has often been two-dimensional layered structures that are lithographically processed to achieve lateral confinement. But higher performance will require the fabrication of smaller structures for which it will probably be necessary to actually control the lateral motion of atoms during growth of the materials. This presents a major challenge in growth technology for the next generation of quantum structures.

The authors are in the Department of Electrical and Computer Engineering, and Materials Department of the University of California, Santa Barbara, CA 93106.

Another class of quantized semiconductor structures in which new and previously unattainable phenomena are now being observed is provided by materials with wider layers in which electrons have a third degree of freedom. These materials provide an approach to a three-dimensional electron gas for which new ordered states of the electrons have been predicted and for which new behaviors in the far infrared and submillimeter wave spectral region may be investigated.

The majority of the structures discussed above have been fabricated using III-V compound semiconductors. These materials are compounds of elements from the third column (group III) and elements from the fifth column (group V) of the periodic table. Gallium arsenide (GaAs) and aluminum arsenide (AlAs) have been the two most intensely studied III-V compound semiconductors. In this article we present the design concepts, growth, and properties of the new quantized structures in the III-V compound semiconductor system.

Two-Dimensional Electron Systems—Background

The fundamental design concept that enables quantized electron structures to function is the difference in electron affinity between different materials. For example, a conduction electron has greater affinity for GaAs than for AlAs. When introduced into a stack of layers of GaAs and AlAs (called a heterostructure, as opposed to a homostructure which consists of a single type of semiconductor), the electron prefers to be in the GaAs layers, it being energetically favorable to do so. An electron is thus confined in a square potential well created by a layer of GaAs sandwiched between two layers of AlAs (Fig. 1a).

The depth of the well can be varied over a range of about 500 meV, for example by employing an alloy of AlAs and GaAs ($\text{Al}_x\text{Ga}_{1-x}\text{As}$, where x is the Al mole fraction) rather than just pure AlAs, for the barrier layers. The well-depth is proportional to the difference between the bandgaps of the barrier and well layers, and varies almost linearly with x , for x ranging from 0 to 0.45. With well-controlled epitaxial growth techniques (5) like molecular beam epitaxy (MBE) and metal-organic chemical vapor deposition (MOCVD), it is now possible to grow layered ultrahigh purity thin single-crystalline films of compound semiconductors, where the thickness of each layer can be precisely controlled down to a single layer of atoms (approximately a few angstroms thick). This control over the well depth and the well thickness enables one to engineer the microscopic operating environment for electrons in quantum structures.

As explained in basic quantum mechanics textbooks, the allowed energy states of an electron are discrete or quantized. The energy of an electron confined in a potential well that is formed by a layer of GaAs sandwiched between two layers of $\text{Al}_x\text{Ga}_{1-x}\text{As}$ is similarly quantized (Fig. 1a). The difference in energy between two quantized levels becomes larger when the width of this potential well is reduced. This difference becomes of practical use in GaAs/AlAs heterostructures when the width of the GaAs layer is reduced to less than a few hundred angstroms. It is important to bear in mind, though, that the potential well produced in the manner described above confines the electron only in one direction, namely the growth direction. The electron is essentially free in the plane of the substrate (the wafer, usually GaAs, on which the GaAs/AlAs thin film stack is grown). Hence the name: the two-dimensional electron gas or 2DEG. The electrons in this gas are distributed in a set of energy subbands, in which the bottom (the lowest energy state) of each subband is determined by the energy quantization in the growth direction; the higher energy values within each subband arise from the kinetic energy of the electrons in the substrate plane.

The electrons themselves are introduced by the technique of doping: a donor impurity such as Si is used to dope either all the layers or just selective layers (the latter technique is called modulation doping (6)). In the AlGaAs system the group IV Si atom is incorporated substitutionally onto a group III Al or Ga site, donating its extra valence electron for conduction. When only the $\text{Al}_x\text{Ga}_{1-x}\text{As}$ layers are modulation doped, the electrons fall into the neighboring potential wells and are spatially separated from the parent ionized donor atoms in the barriers. As a consequence, the scattering of the electrons by the donor atoms is drastically reduced. The benefits of this reduction are most strongly realized at liquid helium temperatures when the scattering from lattice vibrations is frozen out, and the electrons enjoy large mean free paths (the average distance the electrons travel between collisions) in the plane of the quantum well. Low-temperature electron mobilities (electron drift velocity per unit of applied electric field) in excess of 10 million $\text{cm}^2 \text{V}^{-1} \text{s}^{-1}$ have been reported in the last 2 years (7). Such mobilities and their attendant large mean free paths have enabled the discoveries of new phenomena attributed to electron-electron interactions, such as the fractional quantum Hall effect (8) in high-purity low-disorder systems, and have prompted an intense search for the 2D Wigner crystal, the lattice which the electrons are predicted to freeze into in the limit of absolute zero temperature ($T = 0 \text{ K}$) (9).

High-speed electronic devices such as the high electron mobility transistor (HEMT) and the heterojunction bipolar transistor (HBT), and optical devices such as lasers, are some of the practical applications of bandgap-engineered 2D electron systems (10). The

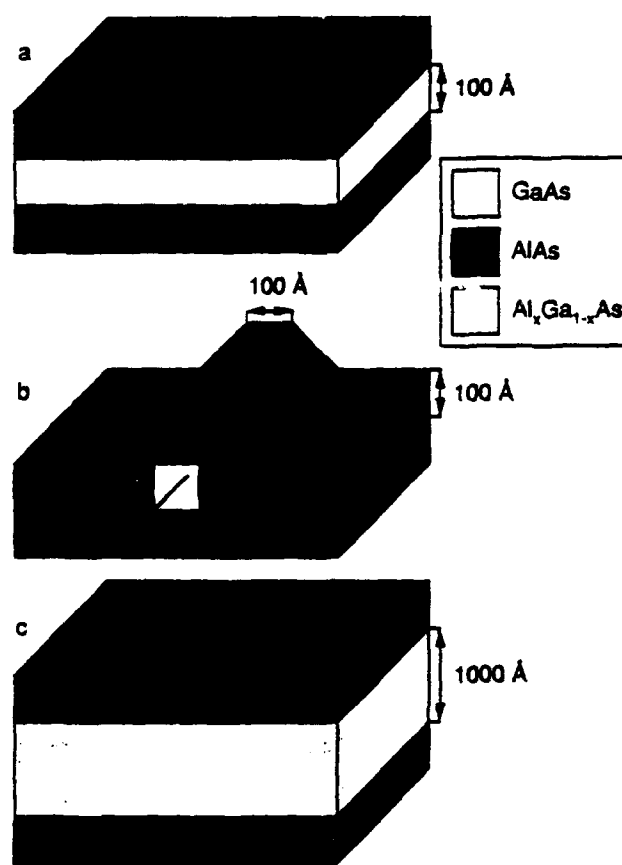


Fig. 1. Schematic sketch of layered quantized structures used to confine electrons and fabricated from stacks of precisely deposited thin films of GaAs and AlAs. (a) Quantum well that confines electrons to two dimensions. (b) Quantum wire that confines electrons to one dimension. (c) Wide specially shaped quantum wells that can be used to study effects of weakening confinement in the vertical direction.

high electron mobility resulting from modulation doping, and the consequent fast electron transport between source and drain of a field effect transistor, gives the fast switching speed and high-frequency operation of the HEMT (11). The emitter gain of a n-p-n HBT is increased by using a larger bandgap material for the emitter than for the base, which enhances electron flow from emitter to base, while at the same time inhibiting the backflow of holes from base to emitter (12). Heterostructure lasers employ larger bandgap materials in the p and n regions of a p-i-n diode, which serve to provide not only electrical confinement of electrons and holes in the lower bandgap i (intrinsic or undoped) region into which they are electrically or optically pumped, but also optical confinement of the lasing mode resulting from radiative recombination of the injected electrons and holes (13).

Approaches to One-Dimensional Structures

Fundamental new features are expected when electrons are further confined into quantum wires, so that their only degree of free motion is along the wire (Fig. 1b). The effects of scattering on electron motion are greatly changed in this case. In two and three dimensions, most of the scattering of electrons occurs by small deflections, or small-angle scattering. In quantum wires, however, this scattering is strongly reduced, and 180° direction reversals become the only energy-conserving collisions that are allowed (14). Recently, it was found that electrical conductance in ballistic wires, which are wires shorter than the electron mean free path so that electrons move in ballistic trajectories, become quantized in integral units of e^2/h (4). Energy quantization effects become even more dominant than in two dimensions, with the increased energy separation between the electron states and the redistribution in energy of these states from the constant distribution for 2D into peaks for 1D. Because of this, semiconductor lasers in ideal quantum wires should operate at lower bias currents and their performance should be sustainable to higher temperatures (15).

Technologically useful quantum wires will require lateral dimensions less than about 100 Å so that the energy separation between the quantized states ($E_n \sim n^2 \hbar^2 / 8m^* L^2$ for electrons of effective mass m^* in square wells of width L) will be greater than room temperature thermal energies, which will allow appreciable device currents to be carried. Unfortunately, precision fabrication of 100 Å scale quantum wires is proving to be a difficult technological challenge. Several methods are currently being pursued to fabricate quantum wires; all these methods use the more conventional epitaxial techniques mentioned earlier in at least some capacity (Fig. 2).

Probably the most obvious and the most common method attempted for the fabrication of 1D structures is the processing of conventional 2D quantum well structures by electron- or ion-beam writing techniques (Fig. 2a); typical processing procedures may include damaging or removing undesired regions of the quantum well, or patterning evaporated metal gates on its surface to electrically deplete certain regions. These techniques have the advantage of being very flexible with respect to the patterned features. With the use of high electron mobility 2D structures as substrate material, these structures have probed the wavelike nature of electrons in the ballistic electron transport regime. Examples of new phenomena discovered by this work include the quantized conductance of ballistic wires (4) as mentioned above, electron optics in semiconductors (16), and varied magnetic phase interference (17). Unfortunately, although features as small as 15 Å have been produced in other materials, the effective resolution of these techniques in semiconductors is at best about 300 Å because of difficulties involved with transferring patterns to the semiconductor materials

and with surface damage effects. The energy quantization effects attributable to these lateral sizes are not large compared to thermal energies at room temperature. Therefore these techniques are not presently capable of producing 1D structures that will operate above cryogenic temperatures.

A recent approach, in which conventional epitaxy is used to form 1D structures, involves cleaving a conventional 2D quantum well structure to form an edge that is perpendicular to the original layers (Fig. 2b). This cross-sectional edge is then used as a new surface to grow a second confinement layer (18). This technique is exciting because of its potential for producing small-scale 1D structures for study, but structures that exhibit 1D properties have yet to be reported. Before commercial device application becomes feasible, the challenges related to the very small active areas on the edge of the cleave and the number of procedures it takes to make the structures must be overcome.

One-dimensional structures can also be formed by epitaxially depositing atoms on prepatterned substrates (Fig. 2c) (19). The substrates are typically etched by conventional wet chemical methods so that they have an array of V-shaped grooves that are typically about 5000 Å wide and deep. When a thin layer of GaAs is deposited on this surface, the atoms preferentially migrate to the bottom of the grooves, forming a narrow crescent shaped quantum well, on top of which is grown an AlGaAs barrier layer. Lateral motion of atoms on the growth surface is thus used for wire formation. This leads to a structure with an effective lateral confinement of somewhat less than 1000 Å in width. Lasers have been made from this type of structure, but because of the relatively large lateral size, performance enhancement due to the additional confinement has been small.

A fundamentally different fabrication method that also relies on the motion of atoms on the growth surface, but has the potential to make smaller quantum wire structures (periods of less than 80 Å have been obtained), makes use of atomic steps on a crystal surface (Fig. 2d) (20). The atomic steps allow some control over the lateral placement of the atoms deposited on the crystal surface, and the formation of 1D structures without having to resort to intermediate processing steps or patterned substrates. For these reasons, our effort at UCSB in the growth of quantum wires has focused on this

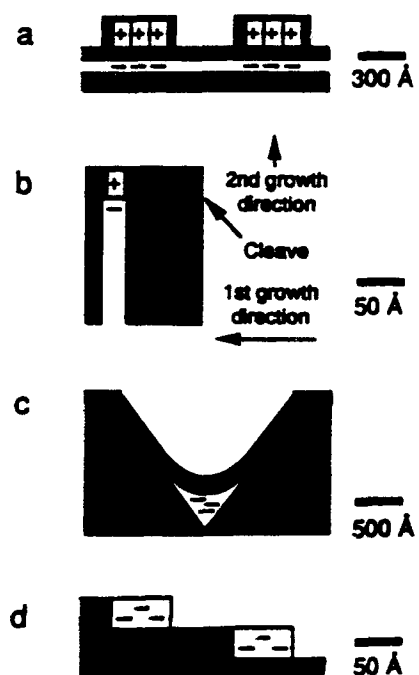


Fig. 2. Schematic illustrations of various methods being developed to fabricate quantum wire structures (vertical dimensions not to scale). (a) Patterning the surface of a conventional 2D quantum well by focused ion beam or electron beam. (b) Cleaved edge overgrowth, which forms a 1D structure by growth on the cleaved edge of a conventionally grown 2D quantum well. (c) Overgrowth of prepatterned V-grooved substrates. (d) Formation of a lateral superlattice (LSL) by growth on atomically-stepped substrate.

technique. Like the methods described above, this technique shows promise for ultimately producing high-quality 1D structures, but it too is an immature technology.

The semiconductors on which epitaxial layers are grown are crystals composed of periodic, closely spaced atomic planes. Normally, growth is performed on a surface that is cut parallel to one of the primary crystallographic planes (Fig. 3a), but if the orientation of the cut is instead slightly away from such a plane, the surface will intersect the primary atomic planes at regular intervals, resulting in a periodically stepped surface (Fig. 3b). The period, or width, of the steps depends on the angle the surface is misoriented away from the primary plane; for example, a surface tilted 2° from the GaAs (100) plane has steps with an average spacing of about 80 Å. These steps can then be used to create lateral structures with the same period, as discussed below. Under the correct growth conditions (such as substrate temperature and source fluxes), the deposited atoms can be made to position themselves at the step edges, where more atomic bonds are available per bonding site than on the step terraces. This results in a stronger bond between the deposited atoms and the substrate. If all the deposited atoms have enough thermal energy to migrate to a step edge and adhere there before bonding somewhere on the terrace, growth occurs by the propagation of the step edges, a process known as step-flow growth. The thermal energy for atom surface migration is provided by the substrate, which, in the case of GaAs growth, is typically heated to about 600°C throughout the growth. Higher substrate temperatures provide more thermal energy, resulting in larger atom surface migration lengths, and therefore a better chance for step-flow growth to occur.

Step-flow growth is important because it allows atoms to be placed on a surface in an ordered manner. To use it to form structures with very small lateral dimensions, enough material of one compound (such as GaAs) is deposited to cover a fraction of each of the step terraces (that is, deposit a fraction of a monolayer) (Fig. 3c), and then enough material of a second compound (such as AlAs) is deposited to cover the remaining area of the terraces (Fig. 3d). Because growth is by step-flow, the first compound will cover the back portion of the terraces, while the second will cover the front portion; if, during this

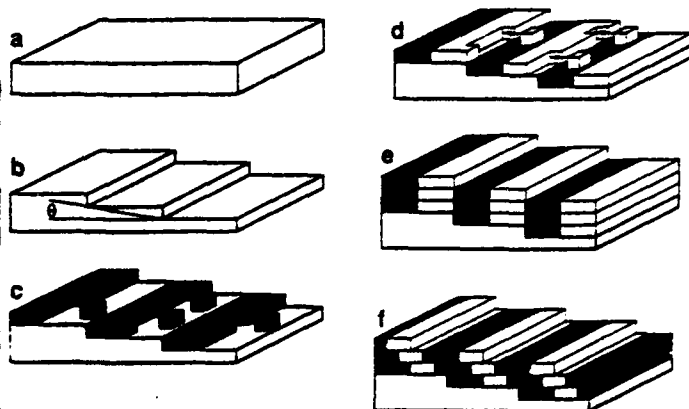


Fig. 3. (a) Nominally flat crystal surface, which is cut parallel to a primary crystal plane [usually (100)], and is used for the majority of epitaxial growths. (b) Atomically stepped crystal surface, produced by cutting a crystal at an angle θ from a primary plane. (c) The first step in forming a LSL: deposition of enough material of a compound to cover a fraction of each step terrace. Because of stronger bonds there, deposited atoms prefer to adhere to the step edges, causing these edges to propagate across the step terraces. (d) The second step in forming a LSL: deposition of a second compound to cover the remaining portions of the step terraces. If the total amounts of the two compounds deposited sums to exactly one monolayer, then the step edges will return to their original locations. (e) Formation of a thicker LSL by repeating the steps in (c) and (d). (f) Formation of a tilted LSL by depositing a sum of less than a monolayer of material each deposition cycle.

process, exactly one monolayer of material is deposited, the step edges return to their original locations. The result is a lateral structure that has a very short lateral period and that is one monolayer thick (~ 3 Å). To produce a thicker structure, this process is simply repeated as many times as necessary, stacking regions of like-compounds on top of each other, creating a lateral superlattice (LSL) (Fig. 3e). This structure can be used to confine electrons lateral to the growth surface, and can be used in combination with conventional layer growth techniques to produce 1D structures. A common name for these LSLs is tilted superlattices, because if a total of slightly more or less than one monolayer is deposited each cycle, the step edges will not return to their original locations. This causes the regions of like compounds to stack slightly displaced from the previous layer deposited, and thereby results in tilted stacks of compounds (Fig. 3f) (21). Lateral superlattices have been successfully grown in both the AlAs/GaAs material system (21, 22), and the similar AlSb/GaSb material system (23). The change of the LSL tilt with deposition amount per cycle can be directly seen and measured by cross-sectional transmission electron microscopy (TEM) (Fig. 4). With present deposition systems it is difficult to control the deposited amounts to better than about 1 to 2%, which can lead to tilt uncertainties as great as 30° . This lack of control over LSL tilt is undesirable because it leads to uncertainties in the confinement widths of the LSLs and hence in the quantized electron energy levels. It should be possible to design the next generation of MBE equipment to have improved control over deposition quantities, but until this capability is available, we will have to rely on clever structural designs to consistently grow untilted, or vertical, LSLs.

One way to guarantee a confinement region that will contain a vertical LSL is to grow what is known as a serpentine superlattice (SSL) (24), which is a LSL whose deposition amounts, and therefore whose tilt, is varied continuously from the bottom of the structure to the top. If, for example, the deposition amount per cycle is raised from 0.95 to 1.05 through the SSL growth, then the SSL tilt will vary continuously between about $+70^\circ$ and -70° . The SSL thereby contains a region in which the deposition per cycle is one monolayer and the barrier regions are vertical. In this way small uncertainties in the deposition rate will affect the beginning and final tilts, but an intermediate vertical region is guaranteed. Because the wells in the vertical region are wider than those in the tilted regions,

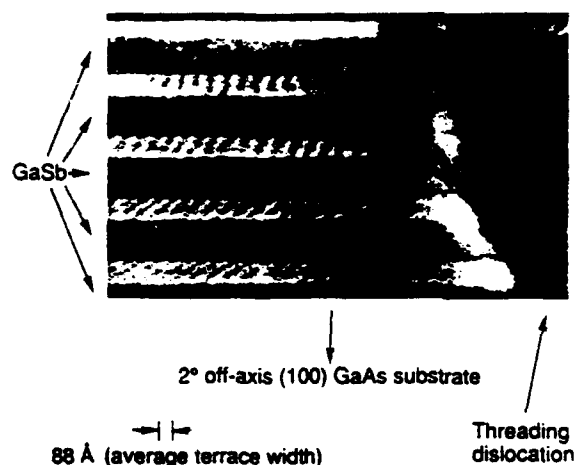


Fig. 4. Cross-sectional transmission electron micrograph of four AlSb/GaSb lateral superlattices, formed by depositing nominally 0.4 monolayers of AlSb followed by 0.6 monolayers of GaSb in each of 40 deposition cycles per LSL. The LSLs are separated by layers of GaSb, and they differ in the amount they are tilted, which is caused by each LSL having a different sum of AlSb and GaSb deposited each cycle. The sums for the layers are, from top to bottom, 1.00, 1.01, 1.03, 1.05.

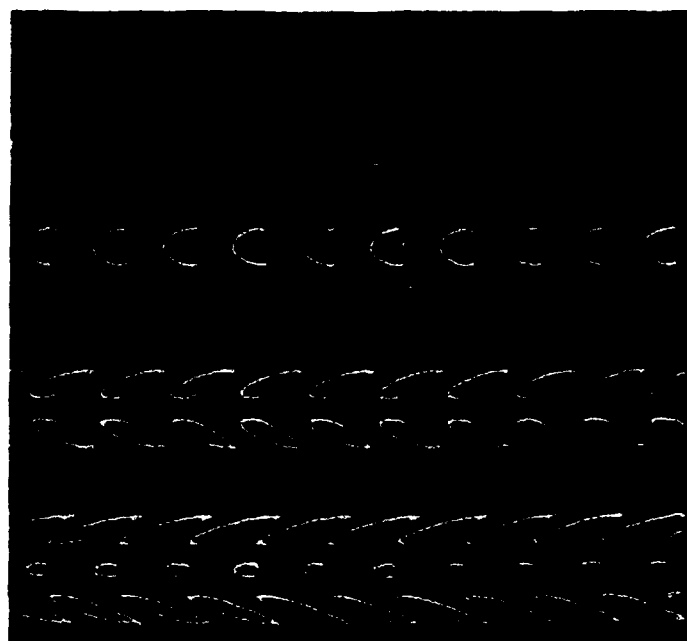


Fig. 5. Top section: schematic diagram of a serpentine superlattice (SSL), where the dark regions are AlAs barriers and the light regions are GaAs wells. Bottom three sections: the calculated three lowest energy electron wavefunctions for the SSL shown, with the ground state in top, followed by increasing energy states. Brightest regions indicate maximum electron density, dark regions denote zero electron density. The ground state has a density maximum at the SSL center, indicating 1D confinement. Higher energy states are less well confined.

electrons will have lower confinement energies and be more concentrated there, resulting in a well-controlled 1D structure. Calculations of the three lowest energy electron wavefunctions in such a structure indicate that the ground-state wavefunction has density peaks at the center of the structure, showing the 1D nature of the electrons (Fig. 5). Successive wavefunctions, which have increasingly higher electron energies, are less well confined.

While TEM images give visual evidence of the successful formation of LSLs, there are also a number of electrical and optical experiments that have supplied information on the nature of the lateral electron confinement the LSLs provide. For example, one monolayer thick LSLs imbedded in AlGaAs/GaAs 2D structures have resulted in devices that exhibit electron mobility anisotropies where the electrons are more free to move in the direction parallel to the LSLs (25). AlGaAs/GaAs HEMT structures with LSLs at the conducting interface (Fig. 6) (so-called washboard transistors) have also been demonstrated (26). These transistors exhibit a new kind of transistor action owing to a switchable interference between the conduction electrons and the LSL (26). Photoluminescence from LSL structures show polarization dependencies and energy-level shifts that are due to the lateral redistribution of electrons by the LSLs (27). These experiments were performed with simple LSL structures; in the future, when perfected, the LSL technique will allow for a wide range of possible structural geometries.

Although the above experiments suggest that LSLs are indeed modifying the electron distribution lateral to the growth plane, they have also shown that complete lateral confinement is not occurring; that is, electrons to a significant degree are able to move between different columns of the LSLs, and the structures are therefore not truly 1D. The causes of this have been attributed to two ways in which the LSL structures deviate from ideal behavior, both of which are related to their growth. One is the nonuniformity of the stepped surface, which causes the confinement regions to vary in width

laterally across the sample. Consequently, the electron confinement energies and the amount of tunneling between the 1D structures also varies. The other is the intermixing that occurs between the compounds of the LSL. Intermixing results in a reduction of the energy barrier heights between the 1D structures. The resulting spread in electron energies in the structures also reduces the usefulness in many applications, for example "single wavelength" lasers with narrow wavelength distributions.

The most common technique for determining LSL uniformity is cross-sectional TEM, which gives a side view of the LSL (Fig. 4). This view provides direct information on the widths of the terraces, the LSL tilt orientation, and compound intermixing. To get an idea of the uniformity in the growth plane, however, we need a top view of the LSL. This can be acquired by using planview TEM through a thinned sample. The image obtained is accurate only if the LSL is vertically oriented which, unfortunately, is often not the case. An alternative method for viewing the LSL structure from the top uses atomic force microscopy (AFM) to detect GaAs ridges that are left behind on surface LSL after the AlAs regions have been chemically etched away (28). AFM can produce a perspective view of these ridges (Fig. 7). This method can be extended to image large surface areas of the LSLs thereby determining their degree of nonuniformity.

Ideally, we would like to grow LSLs on surfaces with straight and uniformly spaced step edges. To prepare the stepped substrates, wafers are first cut from a crystal ingot so that they have the desired surface orientation, and are then mechanically and chemically polished to remove as much of the surface roughness as possible, because surface roughness results in a nonuniform distribution of step terrace widths. This surface roughness can be investigated with reflection high-energy electron diffraction (RHEED). RHEED is an important MBE tool which, among other things, can be used to monitor the evolution of the terrace widths while growth is taking place. It consists of analyzing high-energy electrons (~ 10 keV) that have been reflected from the sample surface at a low incident angle, typically 1 to 2 degrees from the surface plane (29). In this geometry the electrons are sensitive to the arrangement of essentially the top layer or two of atoms. When the beam is directed down the surface steps, the periodic steps result in a series of diffracted electron beams, and from their spacing and shape we can deduce the step periodicity and terrace width uniformity, respectively (30, 31). When the electron beam is directed parallel to the step edges, RHEED is also used to determine the growth conditions necessary for step-flow, which is a valuable tool when growing LSLs (30, 32), because in this geometry the shape of the diffracted beam measures the smoothness of the step terraces, rather than the step periodicity. MBE and especially MOCVD can quickly

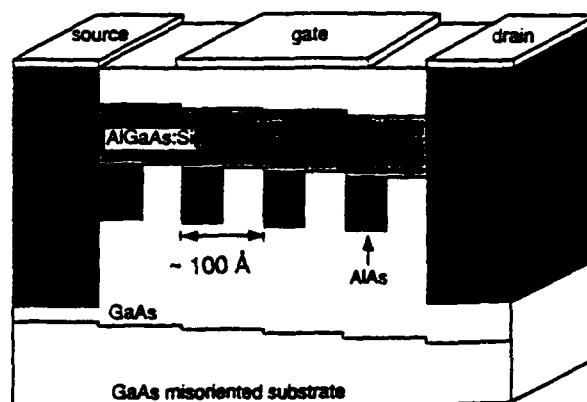


Fig. 6. Cross section of an AlGaAs/GaAs HEMT device with a LSL imbedded in the 2DEG at the conducting interface (so-called washboard transistor). By tuning the electron density with the gate, switching due to interference between the conduction electrons and the LSL can be achieved (26).

smooth the individual terraces, but the unequal terrace widths that result from the nonflat surface heal more slowly, especially for long-range roughness variations. Experimentally, a 3000 Å buffer layer grown on top of an as-polished substrate can reduce the standard deviation of the terrace width fluctuations (which we assume are roughly Gaussian distributed) from on the order of several terrace widths to about half a terrace width, as measured by cross-sectional TEM and in situ RHEED (30). Unfortunately, this remains a significant nonuniformity.

A topic of current research and possibly the most serious obstacle in LSL development is the intermixing of the LSL's two constituent compounds during growth. This intermixing raises the energy of electrons in the wells, lowers the energy of the barriers, and effectively reduces the 1D nature of the LSLs. The intermixing can be caused by the thermal diffusion of the deposited atoms from their desired positions. Unfortunately, the same hot substrate that is necessary for step-flow growth causes this thermal diffusion. Thus, LSL growth involves a trade-off: at too low a substrate temperature the deposited atoms cannot all reach the step edges, while at higher substrate temperatures there is increased intermixing. With present growth techniques, there appears to be no position in the temperature window for GaAs/AlAs LSL growth that allows for completely segregated well and barrier regions. Current research of segregated LSL growth is focused on lowering the temperature necessary for atoms to reach the step edges. This can be attempted by optimizing conventional growth conditions such as the group III atom deposition rates and the ratio of the two compounds in the structure. It can also be accomplished by a technique known as alternating-beam, or migration-enhanced epitaxy (33). This method entails depositing the group V atoms of a layer after the group III atoms; this results in greater migration lengths for the group III atoms as they have more time to move around before combining with the group V atoms to form the final compound. This technique can be used for one or both of the compounds of the LSL, and results in a reduction of the minimum step-flow temperature (by about 20 to 30°C in AlAs/GaAs LSLs) (34), and a better, though not perfect, LSL

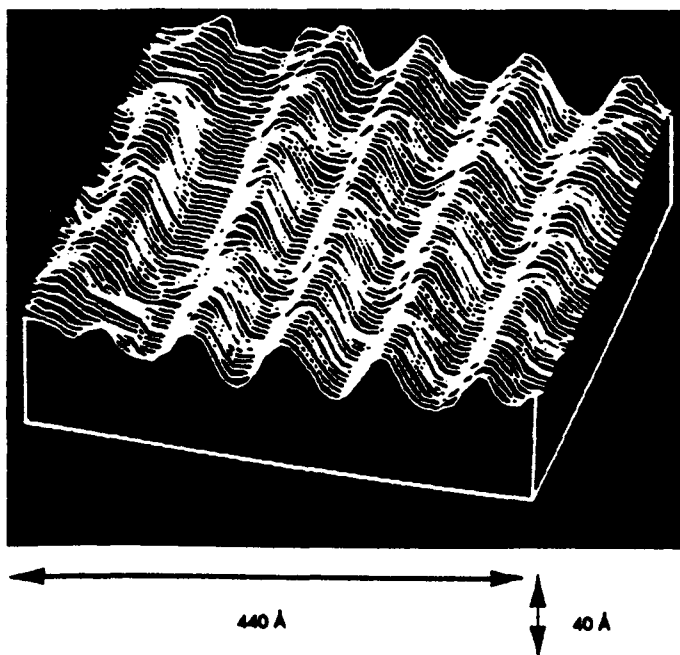


Fig. 7. Atomic force microscope image of lateral superlattice structure. GaAs ridges are formed after the AlAs columns of an AlAs/GaAs surface LSL are chemically removed. This technique can be used to study LSL uniformity in the growth plane.

segregation. For drastic improvements in LSL segregation it may be necessary to resort to nonconventional growth techniques, such as using a nonthermal energy source (such as light or particle beams), which would allow us to selectively excite migrating atoms, but not atoms already in their desired positions.

Although further advances in epitaxial technology should allow for improved growth of LSL structures, perfect segregation of LSL components may not be necessary for many applications. In any event, growth of LSL structures is revealing a great deal about atomic motion and growth on atomically stepped surfaces, and about the physics of low-dimensional structures.

Approaches to Three-Dimensional Structures

Advancement of the research on electron systems has been predominantly toward more confinement—from quantum well (2 degrees of freedom) to quantum wire (1 degree of freedom) to quantum box (0 degrees of freedom). Surprisingly, no comparable effort has been undertaken in the opposite direction, that is in the study of high-quality three-dimensional (3D) systems (Fig. 1c) in which the conduction electrons have 3 degrees of freedom. Although there has been extensive research in the study of high electron density 3D systems such as metals, our understanding of low-density 3D systems such as semiconductor structures is rather poor. There are several interesting but as yet unverified predictions for low-density 3D electron systems. For instance, in the limit of zero temperature and in sufficiently strong magnetic fields, a low-density electron gas is predicted to undergo a

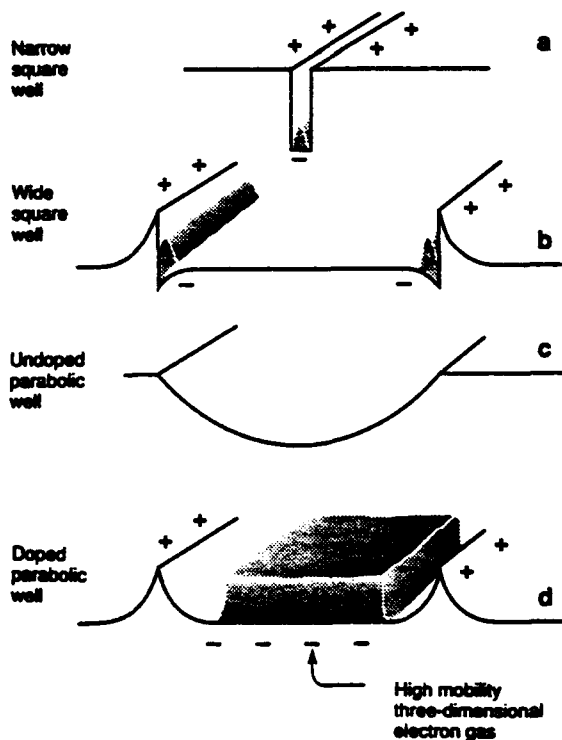


Fig. 8. Schematic of different potential energy wells for four different heterostructures, and the electron distributions (shaded) within each. The barriers surrounding the potential well are doped in order to supply electrons to the well. For a narrow square well (a), the electrons are concentrated at the well center. For a wide square well (b), the electrons repel each other and accumulate at the two interfaces. To obtain an electron gas with uniform density, the well must be graded parabolically (c) to compensate for this electrostatic repulsion. From Poisson's equation, electrons introduced into a parabolic well by doping the barriers (d) distribute themselves uniformly at a density given by the curvature of the parabola.

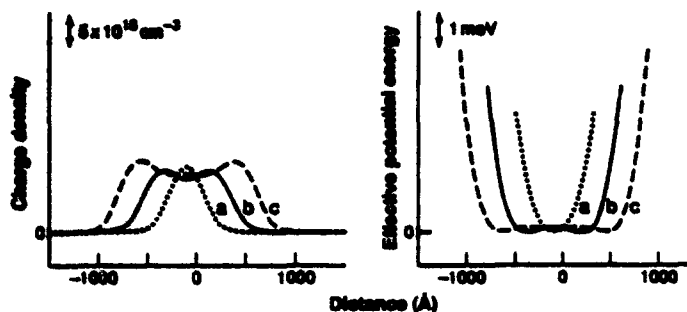


Fig. 9. Electron distribution (left) and effective potential energy (right) versus distance as the number of electrons in the parabolic well is increased. Curve a corresponds to the case when only one subband is occupied; curve b, two subbands occupied; and curve c, three. Note that the height of the charge density distributions, on the left, is preserved from curve a through curve c. The increasing thickness of the distribution accommodates the increase in the number of electrons. Note also the flattening, on the right, of the parabolic well over the region of occupation of the electrons. This flattened portion increases from curve a through curve c with increasing thickness of the electron distribution.

transition to a spin-density wave state (35), where the electron-electron interaction causes spin ordering in the ground (lowest energy) state, producing highly anisotropic electrical properties. In still stronger magnetic fields or at lower electron densities, the electron gas is predicted to form a 3D Wigner crystal. One would expect a uniformly doped semiconductor (such as GaAs doped with Si) to be a sufficient candidate for this study. But the semiconductor electron gas floats in a sea of fixed discrete background charges (of the donor ions). Electron scattering from the donor atoms inhibits observation of many effects expected for an ideal three-dimensional electron gas (3DEG).

One might expect to obtain thick electron layers of high mobility by using modulation-doped wide square wells in which the dopant atoms lie exclusively outside the conducting well channel. However, the charged electrons will repel each other and form two narrow electron layers near the walls (the GaAs/ $\text{Al}_{0.3}\text{Ga}_{0.7}\text{As}$ interfaces) of the well (Fig. 8b). Compensation for the electrostatic repulsion between the electrons must be made to create a spatially uniform 3DEG density.

In 1987, it was suggested that a parabolic grading of the conduction band edge along the growth direction of the GaAs/ $\text{Al}_{0.3}\text{Ga}_{0.7}\text{As}$ heterostructure (Fig. 8c) would provide a structure for a thicker electron gas layer (36). A parabolic potential is equivalent to a constant charge, according to Poisson's equation $\nabla^2\Phi = -\rho/\epsilon$, relating electrostatic potential Φ to charge ρ in a material with dielectric constant ϵ . Electrons introduced into a parabolic potential well are tricked into thinking that the potential is produced by a uniform positive background charge of density proportional to the second derivative (curvature) of the parabola. In an attempt to neutralize this fictitious charge and minimize the energy of the system, the electrons distribute themselves at the same density as this background positive charge. This uniform electron density in turn produces a parabolic electrostatic potential that is equal and opposite to the original parabola. The net electrostatic potential that an individual electron sees is the sum of the two and consists of the original parabola with a wide flat bottom, the flattened portion being the region where the electrons are sitting (Fig. 8d). This is what one expects classically (37).

Quantum mechanical corrections are expected to be important at low temperatures where the separations between the quantized electron energies or subbands are larger than the thermal energy (kT). Owing to the large well width (typically 1000 Å) these subbands are separated by roughly 1 meV, and are larger than the thermal energy only for $T < 10$ K. Despite this energy quantization,

quantum mechanical calculations of the electron distribution in a parabolic well at $T = 0$ K show that this distribution is still uniform at the curvature density as long as there is more than one energy level or subband occupied (38). In fact, the more subbands that are occupied, the more the gas behaves classically. When only the lowest subband is occupied, the 3D density of the electron distribution increases with increasing number of electrons in the well, as for a 2DEG. As soon as the second subband is occupied, this 3D density is essentially pinned at the curvature value. Addition of more electrons into the well only makes the electron layer thicker (Fig. 9), while retaining a constant 3D density. A few ripples are observed in the distribution due to the finite number of subbands occupied. The number of electrons in these wells can be controlled with a surface gate as in a field-effect-transistor; the electron gas can therefore be tuned to have one, two, three, or more subbands occupied, and its properties can be studied in the transitional regime from 2D (one occupied subband) towards 3D (more than one occupied subband).

This concept is general and can be used to realize carrier profiles of different shapes by introducing electrons into potential wells whose second derivatives are proportional to the desired carrier density distributions, according to Poisson's equation. Classically, in the limit of zero temperature the electron density tracks the curvature of the well exactly; quantum mechanically, the density follows the curvature fairly closely once more than one subband is occupied.

As stated in the introduction, the bandgap of $\text{Al}_x\text{Ga}_{1-x}\text{As}$ varies linearly with Al mole fraction x , over a certain range of x . A parabolic potential well in the conduction band for electrons can therefore be realized by synthesizing a graded $\text{Al}_x\text{Ga}_{1-x}\text{As}$ alloy with a parabolic mole-fraction profile. Computer-controlled MBE can be used to grow a graded alloy of $\text{Al}_x\text{Ga}_{1-x}\text{As}$ with precisely controlled Al mole fraction variation (39). This variation can itself be achieved in two ways: by pulsing the Al beam, or by varying the Al flux by controlled variation of the Al oven temperature, in the presence of constant Ga and As fluxes impinging on a GaAs

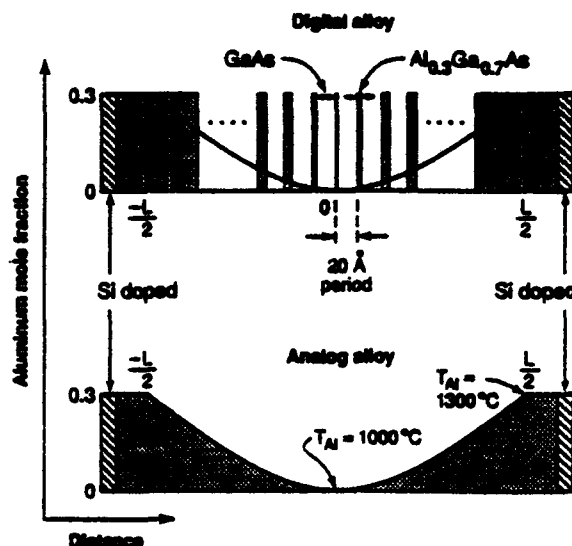
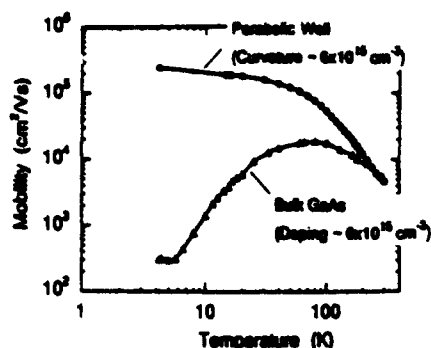


Fig. 10. Realization of a parabolic potential well by synthesis of a graded alloy of $\text{Al}_x\text{Ga}_{1-x}\text{As}$ with parabolically varying (with distance) Al mole fraction x . Computer-controlled molecular beam epitaxy (MBE) is used to make either a digital alloy (top) or an analog alloy (bottom). The digital alloy is a superlattice consisting, in the above case, of GaAs and $\text{Al}_{0.3}\text{Ga}_{0.7}\text{As}$, with a 20 Å period; the pulse duration of the $\text{Al}_{0.3}\text{Ga}_{0.7}\text{As}$ is varied parabolically so that the average Al mole fraction versus distance is parabolic (top). The temperature of the Al oven is varied continuously in the presence of constant Ga and As fluxes to obtain the graded analog alloy (bottom). The barriers are doped with Si to supply electrons to the well. The width L of the well is usually between 1000 Å and 6000 Å.

Fig. 11. Electron mobility versus temperature for a 2000 Å thick electron gas in a parabolic well (at the curvature density $\sim 6 \times 10^{15} \text{ cm}^{-3}$) and for bulk GaAs uniformly doped at the same density. The spatial separation of the donor atoms in the barriers in the well reduces scattering and enhances the mobility of the electron gas in the parabolic well to be over two orders of magnitude higher than for the bulk GaAs at low temperatures. The collision of electrons with the rough walls confining the gas may be the scattering mechanism that limits the in-plane mobility.



substrate (Fig. 10). The former is called a digital alloy, the latter an analog alloy. Parabolic wells have been grown by both techniques and show similar electrical and optical properties.

The digital alloy is essentially a superlattice (a periodic extension of a unit cell that consists of two or more different materials) with a period of typically 20 Å; each period consists of two layers: GaAs and $\text{Al}_y\text{Ga}_{1-y}\text{As}$ where y is the maximum Al mole fraction in the structure, usually the value in the barriers. The pulse duration of the $\text{Al}_y\text{Ga}_{1-y}\text{As}$ is varied parabolically by computer control. The 20 Å superlattice period is sufficiently small to permit tunneling of electrons between the layers so that the electron sees an effective average Al mole fraction that varies parabolically with distance (Fig. 10). The parabolic composition profile can be calibrated by Al flux measurements where an ion flux gauge is used in place of the substrate (40). The Al mole fraction can be controlled to within 5% of its nominal value and the curvature to within 10% by computer control of the Al oven shutter (for the digital alloy) or the Al oven temperature (for the analog alloy).

The electrons are introduced by selectively doping the barrier layers on either side of the parabolic well with donors such as silicon. As in the case of the 2DEG described earlier, the spatial separation of the electrons from the ionized donors results in a mobility for motion in the substrate plane up to two orders of magnitude higher, at temperatures $T < 100 \text{ K}$, than would be obtained in a uniformly-doped semiconductor with the same 3D density of electrons (Fig. 11). Mobilities in excess of $100,000 \text{ cm}^2 \text{ V}^{-1} \text{ s}^{-1}$ (and as high as $350,000 \text{ cm}^2 \text{ V}^{-1} \text{ s}^{-1}$ for a 3DEG with density $\sim 10^{16} \text{ cm}^{-3}$) have been obtained in a variety of 3DEGs with densities ranging from as low as $4 \times 10^{15} \text{ cm}^{-3}$ up to 10^{17} cm^{-3} (41, 42). Although this mobility is much higher than for uniformly doped materials, it is still substantially lower than the best mobilities in 2DEGs.

Low-temperature transport measurements in a magnetic field show oscillations in the resistance of the gas and the well-known quantum Hall effect (43). A Fourier analysis of the oscillations reveals multiple frequencies which are related to the occupation of electrons in individual quantized subbands. This analysis reveals the Fermi energy of the electron gas in the parabolic well to be fairly constant as the number of electrons is changed and is therefore a signature of the three-dimensionality of the gas (in the 3D limit the Fermi energy is constant for a uniform 3D density). The analysis yields the energies as well as the number of electrons in each subband, which agree with calculations to within 10%, an agreement that is rather remarkable given the fact that a well depth is the only parameter assumed. This gives us some indication of how accurately we can make a potential well today. The number of electrons in a parabolic well in a given sample can be increased or decreased by illumination of the sample or by use of a surface gate electrode. Analysis of the resistance oscillations

(in magnetic field) of the electron gas, as the number of electrons in the parabolic well is varied by either technique, show that the parabolic well fills at nearly constant 3D density, from zero thickness to thicknesses up to 2000 Å (44).

That the electrons are distributed uniformly in the parabolic well has been measured directly using capacitance-voltage profiling techniques, wherein the electron density versus depth profile is extracted from a measurement of the capacitance between a surface metal gate and the electron gas (which forms the other plate of the parallel-plate capacitor), at different gate-to-gas voltage biases. This simple measurement has been used to optimize MBE growth conditions to obtain more uniform and symmetric 3DEGs in parabolic wells (45).

These results suggest that the electron gas in a wide parabolic well is a promising candidate for the study of effects predicted for a 3DEG and of effects in the transitional regime from two to three-dimensionality. Experiments in this direction are under way by several research groups: for instance, there has been a study of the evolution of the fractional quantum Hall effect as the electron layer becomes thicker (42).

The parabolic wells also show striking optical effects. One interesting discovery occurred in the optical absorption of the electron plasma in the parabolic well (46). The plasma frequency of the 3DEG is calculated to be equal to the harmonic-oscillator spacing of the empty parabola. This frequency is in the far-infrared (FIR), typically 50 cm^{-1} (200- μm wavelength) for a density of $2 \times 10^{16} \text{ cm}^{-3}$. It was discovered that, irrespective of the number of electrons in the well, the electron gas always absorbs at this bare harmonic-

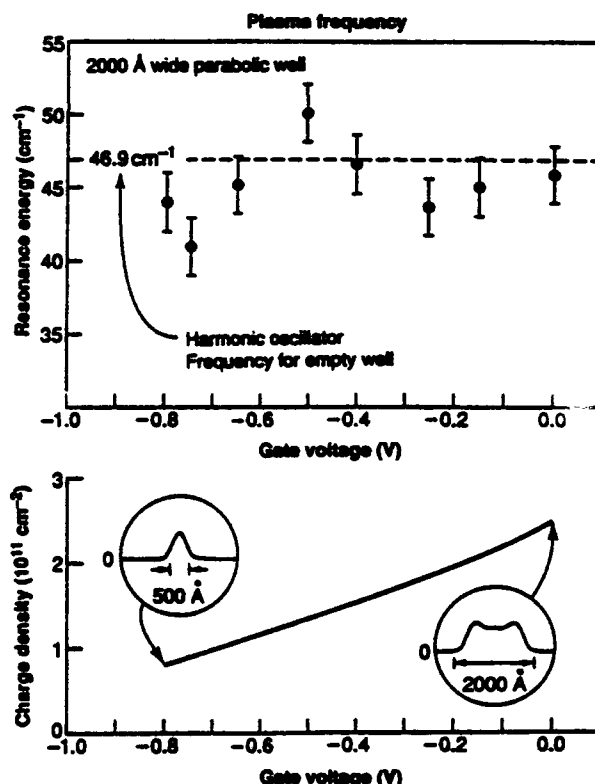


Fig. 12. Resonance energy of absorption of the three-dimensional electron gas versus gate voltage (top) shows absorption at the empty-well harmonic-oscillator frequency irrespective of the number of electrons in the well (changed by the gate voltage). This is a property unique to a ideal harmonic oscillator and is a consequence of the parabolic potential and the translational invariance of the electron-electron interaction. The bottom half shows how the number of electrons in the well is changed by the gate voltage. The insets depict how the increase in the number of electrons with more positive gate bias is accommodated by an increase in the thickness of the electron gas at constant 3D density.

oscillator frequency, as shown in Fig. 12 (47).

Recall that a single electron in a parabolic well partially filled with electrons sees a parabola with a flat bottom, the flattened region being proportional to the number of electrons in the well. Consequently, the energy spectrum of this individual electron is not the equally spaced one of a harmonic oscillator, but that of a flattened oscillator that is actually very close to a square-well spectrum. As the number of electrons is increased, the width of this approximate square well increases proportionately, with an attendant decrease in the energy spectrum spacing (for an infinitely deep square well, the energy spectrum changes inversely with the square of the well width). One would expect this change to be reflected in the FIR absorption of the 3DEG at different electron fillings. The observation that the gas always absorbs at one frequency suggests a more fundamental effect. It has been shown theoretically (48) that this is indeed a property unique to the ideal harmonic oscillator or parabolic well. The translational invariance of the electron-electron interaction (the fact that this interaction depends only on the relative distance between the two electrons) coupled with the quadratic form of the potential, when inserted in the Schrödinger equation, give the following general result: the motion of the center of mass of the 3DEG can be decoupled from the motion of the individual electron; as long as the wavelength is much larger than the thickness of the gas, the incident light simply grabs the entire cloud of electrons and oscillates it in unison. The maximum absorption is of course at the plasma or harmonic-oscillator frequency. The individual electron sees an approximate square potential well, but the ensemble of electrons sees the original parabola; applying a linear term to the parabolic potential with a gate bias does not change its second derivative and hence its plasma frequency.

This result is relevant to the case of quantum wires and boxes, where the optical absorption shows a similar independence of the number of electrons in the wire or box, a result which had puzzled researchers for a while. We now know this to be a consequence of the parabolic shape of the confining potential. Deviations from the parabolic potential, whether deliberate or unintentional, manifest themselves in the optical absorption spectra as additional structure and give clues to the modes of absorption of the individual electrons. Deviations from this generalized theorem for an ideal parabolic potential are being investigated in a systematic way in potential wells of different shapes, by several groups.

Thanks to computer-controlled MBE technology, pretty much any textbook potential well can be made. The square well and the parabolic well are the first examples. One could think of these potential wells as atoms, the shape and size of whose electrostatic potential can be controlled over a fairly large range in both distance and energy. By making these wells wide, one can access energy spectra in the FIR. Although we have so far discussed only wide symmetric (in the growth direction) wells, asymmetric wells also provide a rich field of study. For example, asymmetric wells have nonlinear optical responses. One group has recently observed second- and third-harmonic generation while subjecting electrons in a wide half-parabolic well to intense FIR radiation (49). This nonlinear response is predicted to develop into chaotic behavior in stronger driving electromagnetic fields (50).

Several groups are working on the properties of an electron gas in which the density is periodically modulated in the growth direction. Such a gas is realized by growing a modulation-doped wide (~ 2000 Å) parabolic well with a superimposed superlattice of shorter period (~ 200 Å) in the well: the slow parabolic potential ensures the uniform electron density, the superlattice then modulates this density by up to 100% (51). One technological application is a tunable FIR detector (52): in a specially shaped well, in which the local curvature varies with depth, a surface gate can be used to control the position of the center

of the electron gas in the well and thereby tune the energy spectrum of the electrons, thus changing the wavelength of light at which these electrons have resonant absorption.

Performance limits for most such electronic devices as well as the chances of observing electron-electron interaction effects are enhanced to a large extent by the electron mobility. It appears that the factor that limits the electron mobility in the parabolic well structures may be a new type of scattering mechanism known as the size effect (53), related to a similar effect seen previously in thin metal films. Nonspecular or diffuse scattering of the electrons off the rough confining walls of the thick electron gas may be the dominant scattering mechanism in these structures. However, this is a current topic of research.

Background impurities and precise control of the mole-fraction profile of the graded $\text{Al}_x\text{Ga}_{1-x}\text{As}$ are two important limitations to the growth of high-quality 3DEGs. Carbon atoms from residual gases in the vacuum system are the dominant ionized impurities in these MBE grown structures. Carbon is a shallow acceptor in GaAs, and is negatively charged in n-type material where the Fermi energy lies in the conduction band; these negatively charged acceptor ions act as strong scattering centers for electrons. Calculated fits to the mobilities for the best 3DEGs suggest carbon to be present in the alloy at the level of $2 \times 10^{14} \text{ cm}^{-3}$, a reasonable number for a clean MBE machine. It is ultimately this density, too, that limits how dilute an electron gas can be achieved with this technique: a uniform negative background charge of 10^{14} to 10^{15} cm^{-3} ionized carbon acceptors will produce a parabolic potential of the opposite curvature to the design curvature, thus altering the desired parabola. The curvature can be controlled to within 10% in these MBE-grown graded alloys. Further improvements can be made with more precise computer control (faster clock), better oven temperature controllers (analog alloy), and using electric shutters instead of pneumatic ones in front of the ovens (digital alloy).

These limits are sufficiently broad that one can access a wide range of electron densities and distributions and a broad span of infrared energies with potential wells of controlled widths and shapes. These wells and gases constitute good candidates for the study of electron-electron interactions in 3DEGs (and in the transitional regime from 2D to 3D), nonlinear optical behavior and chaos in the FIR, and for the development of novel detectors and other FIR optical devices.

Summary and Conclusions

The rapid progress in two-dimensional electron structures is now being extended to semiconductor systems in which conduction electrons are constrained (at least partially) to free motion in one dimension, or are allowed, at least partially, free motion in the third dimension. The process of formation of these structures is intimately connected to epitaxial thin film crystal growth technology that enables the motion of atoms on surfaces to be governed by surface asperities as small as atomic thickness islands and terrace steps. What emerges from these studies is increased knowledge of the atomic processes of crystal growth and new information on the dynamics and the interactions of electrons under partial confinement in the quantum size regime. The technological promise that emerges from these studies is the discovery of new routes to enhanced quantum-based electronic and electro-optic devices and the discovery of new media for device structures in the submillimeter and far infrared regimes.

REFERENCES AND NOTES

1. For a review, see V. Narayanamurti, *Science* **235**, 1023 (1987).
2. For a review, see V. Narayanamurti, *Phys. Today* **37**, 24 (October 1984).
3. For a review, see B. I. Halperin, *Sci. Am.* **254**, 52 (April 1986); and *The Quantum*

- Hall Effect, R. E. Prange and S. M. Girvin, Eds. (Springer-Verlag, New York, 1985).
4. B. J. van Wees *et al.*, *Phys. Rev. Lett.* 60, 848 (1988).
5. For a review, see A. Y. Cho, *Thin Solid Films* 100, 291 (1983); R. D. Dupuis, *Science* 226, 623 (1984).
6. For a review, see H. L. Seifert, *Surf. Sci.* 132, 519 (1983).
7. L. Pfeiffer, K. W. West, H. L. Seifert, K. W. Baldwin, *Appl. Phys. Lett.* 55, 1888 (1989).
8. For a review, see J. P. Eisenstein and H. L. Seifert, *Science* 248, 1510 (1990); H. L. Seifert and D. C. Tsui, *ibid.* 220, 1241 (1983).
9. E. P. Wigner, *Phys. Rev.* 46, 1002 (1934); for latest developments, see editorial by A. Kluza, *Phys. Today* 43, 17 (December 1990).
10. For a review, see M. H. Brodsky, *Sci. Am.* 262, 68 (February 1990).
11. For a review, see L. F. Eastman, *Phys. Today* 39, 77 (October 1986).
12. For a review, see A. F. J. Levi, R. N. Nottenberg, Y. K. Chen, M. B. Panish, *ibid.* 43, 58 (February 1990).
13. For a review, see Y. Sasaki, *ibid.* 38, 32 (May 1985); D. S. Chemla, *ibid.*, p. 57.
14. H. Sakaki, *Jpn. J. Appl. Phys.* 19, L735 (1980).
15. Y. Arakawa and H. Sakaki, *Appl. Phys. Lett.* 40, 939 (1982).
16. J. Spector, H. L. Seifert, K. W. Baldwin, L. N. Pfeiffer, K. W. West, *ibid.* 58, 263 (1991).
17. C. J. B. Ford *et al.*, *J. Phys.* C21, 1325 (1988).
18. H. L. Seifert, L. N. Pfeiffer, K. W. West, K. W. Baldwin, paper presented at the International Symposium on Nanostructures and Mesoscopic Systems, Santa Fe, NM, May 1991; L. Pfeiffer, *J. Cryst. Growth* 111, 333 (1990).
19. E. Kapon, *Appl. Phys. Lett.* 55, 2715 (1989).
20. P. M. Petroff, A. C. Gossard, W. Wiegmann, *ibid.* 45, 620 (1984).
21. J. M. Gaines *et al.*, *J. Vac. Sci. Technol.* B6, 1378 (1988).
22. T. Fukui and H. Saito, *ibid.*, p. 1373; H. Yamaguchi and Y. Horikoshi, *Jpn. J. Appl. Phys.* 28, 352 (1989).
23. S. A. Chalmers, H. Kroemer, A. C. Gossard, *Appl. Phys. Lett.* 57, 1751 (1990).
24. M. S. Miller *et al.*, *J. Cryst. Growth* 111, 323 (1991).
25. J. Motohisa, M. Tanaka, H. Sakaki, *Appl. Phys. Lett.* 55, 1214 (1989).
26. K. Tsubaki, Y. Tokura, T. Fukui, H. Saito, N. Sasa, *Electron. Lett.* 25, 728 (1989).
27. T. Fukui, H. Saito, Y. Tokura, *Appl. Phys. Lett.* 55, 1958 (1989).
28. S. A. Chalmers *et al.*, *ibid.*, p. 2491.
29. P. I. Cohen and P. R. Pukite, *J. Vac. Sci. Technol.* A5, 2027 (1987).
30. S. A. Chalmers, A. C. Gossard, P. M. Petroff, J. M. Gaines, H. Kroemer, *ibid.* B7, 1357 (1989).
31. P. R. Pukite, C. S. Lent, P. I. Cohen, *Surf. Sci.* 161, 39 (1985).
32. J. H. Neave, P. J. Dobson, B. A. Joyce, J. Zhang, *Appl. Phys. Lett.* 47, 100 (1985).
33. F. Bejones, D. Goins, L. Gonzalez, A. Ruiz, *J. Cryst. Growth* 81, 19 (1987); Y. Horikoshi, M. Kawashima, H. Yamaguchi, *Jpn. J. Appl. Phys.* 27, 169 (1988).
34. S. A. Chalmers, A. C. Gossard, P. M. Petroff, H. Kroemer, *J. Vac. Sci. Technol.* B8, 431 (1990).
35. V. Celli and N. D. Mermin, *Phys. Rev.* 140, A839 (1965).
36. The suggestion was made by A. C. Gossard and B. I. Halperin: see B. I. Halperin, *Jpn. J. Appl. Phys.* 26 (Suppl. 26-3), 1913 (1987).
37. M. Sundaram, A. C. Gossard, J. H. English, R. M. Westervelt, *Superlattice Microsc.* 4, 683 (1988).
38. These calculations solve both Poisson's equation and the Schrödinger wave equation with appropriate boundary conditions: see A. J. Rimberg and R. M. Westervelt, *Phys. Rev. B* 40, 3970 (1989); T. Sejono, J. Jo, H. P. Wei, M. Santos, M. Shayegan, *J. Vac. Sci. Technol.* B7, 311 (1989); M. P. Soaps and S. DasSarma, *Phys. Rev. B* 40, 10048 (1989); A. Wixforth, M. Sundaram, K. Enslin, J. H. English, A. C. Gossard, *Appl. Phys. Lett.* 56, 454 (1990).
39. A. C. Gossard, *IEEE J. Quant. Electron.* 22, 1649 (1986).
40. M. Sundaram, A. Wixforth, R. S. Geck, A. C. Gossard, J. H. English, *J. Vac. Sci. Technol.* B9, 1524 (1991).
41. M. Sundaram, A. C. Gossard, P. O. Holtz, *J. Appl. Phys.* 69, 2375 (1991).
42. M. Shayegan, J. Jo, W. Suen, M. Santos, V. J. Goldman, *Phys. Rev. Lett.* 65, 2916 (1990).
43. See, for example, P. F. Hopkins *et al.*, *Appl. Phys. Lett.* 57, 2823 (1990).
44. E. G. Wynn *et al.*, *Phys. Rev. B* 39, 6260 (1989); T. Sejono, J. Jo, M. Santos, M. Shayegan, *Appl. Phys. Lett.* 55, 1430 (1989); K. Enslin, M. Sundaram, A. Wixforth, J. H. English, A. C. Gossard, *Phys. Rev. B* 43, 9988 (1991).
45. M. Sundaram and A. C. Gossard, in preparation.
46. K. Karrai, H. D. Drew, M. W. Lee, M. Shayegan, *Phys. Rev. B* 39, 1426 (1989); K. Karrai, X. Ying, H. D. Drew, M. Shayegan, *ibid.* 40, 12020 (1989).
47. A. Wixforth, M. Sundaram, K. Enslin, J. H. English, A. C. Gossard, *ibid.* 43, 10000 (1991).
48. L. Brey, N. F. Johnson, B. I. Halperin, *ibid.* 40, 647 (1989).
49. W. W. Bewley *et al.*, in preparation.
50. M. Sherwin, in preparation.
51. J. Jo *et al.*, *Appl. Phys. Lett.* 57, 2130 (1990); A. J. Rimberg *et al.*, paper presented at the International Symposium on Nanostructures and Mesoscopic Systems, Santa Fe, NM, May 1991.
52. J. Maserjian and A. C. Gossard, patent pending.
53. W. Walukiewicz, M. Sundaram, P. F. Hopkins, A. C. Gossard, R. M. Westervelt, in *Proceedings of the MRS Fall Meeting*, Boston, MA, 1990 (Materials Research Society, Pittsburgh, 1990).
54. We thank the following colleagues for discussions on matters pertaining to this article: P. M. Petroff, H. Kroemer, J. H. English, H. Weman, M. Miller, A. Wixforth, K. Enslin, E. G. Wynn, R. M. Westervelt, M. S. Sherwin, B. I. Halperin, A. J. Rimberg, and M. P. Soaps. Our thanks also to J. C. Yi for calculating and preparing Fig. 5, to S. Gidir and K. Campman for critical readings of the manuscript, and to D. J. McLaren for her skillful translation of some of the authors' ideas into lucid figures.

A direct method to produce and measure compositional grading in $\text{Al}_x\text{Ga}_{1-x}\text{As}$ alloys

M. Sundaram, A. Wixforth, R. S. Geels, A. C. Gossard, and J. H. English
*Department of Electrical Engineering, and Materials Department, University of California,
Santa Barbara, California 93106*

(Received 3 December 1990; accepted 31 January 1991)

We present a method to calibrate the profile of Al mole fraction versus depth, deposited in growth of graded $\text{Al}_x\text{Ga}_{1-x}\text{As}$ alloys in a molecular-beam epitaxy machine. A computer is used to either ramp the Al oven temperature (analog alloy), or pulse the Al beam (digital alloy), with a fractional monolayer depth resolution that permits averaged alloy profiles corresponding to a range of different design profiles to be obtained. The profiles are measured in calibration runs by using a fast picoammeter to track the ion-collector current of the beam flux monitor ion gauge (facing the ovens), and integrating the ion current with time. Parabolic quantum wells are grown by either technique and the corresponding measured profiles are compared to each other and to the design profile. The ability of the digital-alloy technique to obtain almost arbitrarily varying graded-alloy profiles is illustrated.

I. INTRODUCTION

Tailoring of the energy band gap in semiconductor heterostructures is a useful technique of controlling the electronic and optical properties of carriers in devices made from these materials. Examples are the single (multi) quantum well p - i - n laser in which the intrinsic region consists of a square well(s) with parabolically graded barriers (e.g., the GRINSCH laser),¹ and heterojunction bipolar transistors (HBTs) with graded-gap base regions.² The scope of this technique is so wide that it is referred to generally as band gap engineering.³ Modern epitaxial growth techniques such as molecular-beam epitaxy (MBE) lend themselves readily to the growth of abrupt or smoothly graded $\text{GaAs}/\text{Al}_x\text{Ga}_{1-x}\text{As}$ heterointerfaces.⁴

Recently, a series of structures have been devised in which modulation doping and a graded band gap have been combined to obtain a high-mobility electron gas with a controlled static density distribution.⁵ In the structures which were studied, electrons were introduced into wide parabolic wells by remotely doping the barrier layers surrounding the well. The parabolic potential wells were themselves created by appropriately grading the mole fraction x of an $\text{Al}_x\text{Ga}_{1-x}\text{As}$ alloy layer. The electrons were found to distribute themselves across the parabolic well with the density being governed by the curvature of the design parabola, in the limit of absolute zero of temperature. These high-mobility uniform electron gases or three-dimensional electron gas (3DEGs) are the best experimental approximation to the theoretical construct of jellium, and have exhibited a number of interesting properties in transport measurements.^{6,7} Grading of the band gap allows a wide range of densities to be achieved. Modulation doping results in high carrier mobilities of these gases without low temperature carrier freeze-out.

These and other graded structures are often realized in the $\text{GaAs}/\text{Al}_x\text{Ga}_{1-x}\text{As}$ system, where there exists a nearly linear relationship between the $\text{Al}_x\text{Ga}_{1-x}\text{As}$ energy band gap

and Al mole fraction x for $x < 0.45$.⁸ Controlled variation of x results in a corresponding controlled variation of the alloy band gap. The variation of x with depth in a thin film can itself be achieved in two ways. The Al flux can be changed during growth in a controlled manner by controlling the temperature of the Al oven in an MBE machine, in the presence of constant Ga and As fluxes.⁹ We refer to the alloy obtained in this way as an analog alloy. One could alternately grow a superlattice with a constant period (sufficiently small to permit tunneling of electrons between the layers), each period being composed of two layers: GaAs and $\text{Al}_y\text{Ga}_{1-y}\text{As}$, where y is greater than or equal to the maximum Al mole fraction in the graded alloy. The duty cycle of the $\text{Al}_y\text{Ga}_{1-y}\text{As}$ is varied in a controlled manner so that the average Al mole fraction follows the desired profile.¹⁰ In other words, the Al beam is pulsed in controlled fashion by controlling the Al oven shutter in an MBE machine. We refer to the alloy obtained by the latter technique as a digital alloy.

The actual profile of Al mole fraction versus depth obtained is not easily measured directly. Its general shape is sometimes deduced from optical or electrical measurements on the resulting structures,¹¹ followed by a fitting of the data to calculations for the designed energy bandgap profile. These techniques are indirect at best. Techniques like secondary ion mass spectrometry (SIMS) have limited depth resolution, and are destructive besides.

In the present work we present a method to calibrate deposited Al mole fraction versus depth before growth with a simple, reproducible technique having reasonably high resolution and accuracy. The measurement is done in the MBE machine itself in a calibration run immediately prior to sample growth. If the variation from one measured run to another is negligibly small, the measured profile can be reasonably assumed to be the actual profile grown.

The Al flux can be measured by a beam flux monitor that consists of an ion gauge (Bayard-Alpert gauge in a Varian GEN II MBE system). The beam flux monitor gauge that is

used for this purpose can be made to directly face the ovens. The collector current (usually in the range of nA) of the ion gauge is fed to a fast picoammeter. The variation of Al flux $F_{Al}(t)$ with time is therefore measured directly. Inasmuch as actual growth occurs in the presence of a constant Ga flux, a constant collector current corresponding to the Ga flux F_{Ga} is assumed in the calculations. F_{Ga} is adjusted to be in the same ratio to a particular F_{Al} , say $F_{Al}(t=0)$, as the ratio of the corresponding GaAs and AlAs growth rates, which are in turn determined by reflection-electron-diffraction (RED) oscillations¹² immediately prior to the ion-gauge measurement. Integrating the total flux F_{total} ($F_{total} = F_{Al} + F_{Ga}$) from time $t = 0$ until time $t = T$:

$$z = \int_0^T F_{total}(t) dt, \quad (1)$$

gives us a measure of the thickness z of the graded alloy grown until time T . Integrating $F_{Al}(t)$ and $F_{total}(t)$ over a time interval ΔT centered at T , gives the Al mole fraction $x(z)$ as

$$x(z) = \left(\int_{-\Delta T}^{\Delta T} F_{Al}(t) dt \right) / \left(\int_{-\Delta T}^{\Delta T} [F_{Al}(t) + F_{Ga}] dt \right). \quad (2)$$

The variation of Al mole fraction x with depth z can therefore be measured and compared with the design profile.

The method is applicable to measuring the alloy grades of both analog and digital alloys. The Al fraction in the alloy may in places be designed to be very small. In the digital alloy technique this requires very rapid pulsing of the pneumatic shutter of the Al oven and thence of the Al beam. This causes corresponding rapid changes in the collector current of the ion gauge. Hence the need for a fast picoammeter to track the current.

II. EXPERIMENTS AND DISCUSSION

Measurements were made in a Varian Gen II MBE machine used for the growth of GaAs/Al_xGa_{1-x}As epilayers. Oven temperatures and shutter opening times are controlled by a HP-9000 Series 300 instrument controller having a time resolution of 10ms. The equation of the desired alloy profile versus depth is used by the computer program to generate a ramp of Al oven temperature with time (analog alloy), or a sequence of shuttering times of the Al oven pneumatic shutter (digital alloy), with a resolution fine enough to produce a smooth alloy gradient. The ion gauge of the beam flux monitor faces the ovens, and is situated at the same location where the substrate would be during actual growth. The collector current of the beam flux monitor is measured with a Keithley 480 picoammeter. The analog output of the picoammeter is fed back to the controller via a fast analog-digital converter. All computations are then performed by the controller at the end of the run.

Figure 1 shows measured profiles of Al flux $F_{Al}(t)$ with time, for a single pulse 0.5 s long (the command to open being issued at time $t = 0$, and the command to close being issued at time $t = 0.5$ s). The profiles correspond to measurements of the same pulse, with two different rise time settings (7 and 70 ms, respectively), corresponding to two different sensitivity scales of the picoammeter. The 70 ms

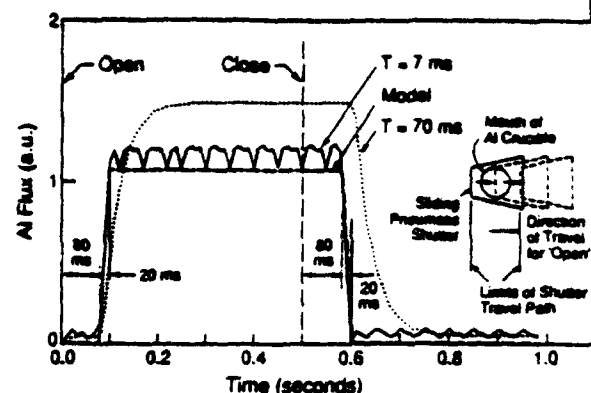


FIG. 1. Beam flux monitor (BFM) ion gauge measured flux profiles of Al pulse in an MBE machine: solid profile for a range having a 7 ms rise time, dotted profile for 70 ms rise time. The "open" command is issued to the pneumatic shutter at time $t = 0$, and the "close" command at $t = 0.5$ s. Opening and closing delays of ~ 80 ms, and ramp-up and ramp-down times of ~ 20 ms are measured. The assumed ideal flux profile (dashed) is also shown. Inset shows the finite speed at which the shutter slides across the crucible mouth as the origin of these delays. The semiperiodic interference spikes in the solid trace occur whenever the picoammeter is used to measure the ion-collector current with a fast response time setting.

response time is seen to dominate the rise and fall times of the dashed profile. The shorter response time setting of 7 ms is needed to resolve the speed of rise and fall of the actual profile, as seen by the solid line. A nearly periodic background interference signal is seen in the solid profile due to the fast rise time setting of the picoammeter. Note the opening and closing delays, and the finite times to ramp up the flux and ramp it down. The inset shows the origin of these delays. The pneumatic shutter travels for a finite distance on either side of the crucible mouth, giving rise to the open (T_{open}) and close (T_{close}) delays. Besides motion time, electronic delay, and shutter backlash also contribute to the open and close delays. The travel across the face of the Al crucible itself gives rise to the ramp-up and ramp-down times. Inasmuch as all other times involved in the measurement: ion collection time in the gauge's electric field, picoammeter and A-D converter delays, are smaller than the 10 ms clock resolution of the computer, the measured solid profile of Fig. 1 is believed to reflect the true delays of the pneumatic shutter. The open (T_{open}) and close (T_{close}) delays are thus of the order of 80 ms and both the ramping times ($T_{ramp up}$ and $T_{ramp down}$), of the order of 20 ms. The true profile is approximated by a trapezoidal profile with all these time constants incorporated (also shown in Fig. 1). The actual time that the Al oven shutter is to be opened for a given thickness of AlAs to be grown in, say, a superlattice, is automatically computed in the program taking these delays into consideration.

There are three possible scenarios for a shutter opening and closing sequence. Case 1, outlined in Fig. 1, is where the shutter moves all the way across the face of the oven and comes to rest at the other end of travel, before receiving a command to close. Case 2 is where the shutter uncovers the crucible completely, but is asked to return before it can reach the end of its travel. Case 3 is where the shutter only partially uncovers the oven, before starting on its return path.

Cases 2 and 3 are illustrated in Fig. 2. The measured flux

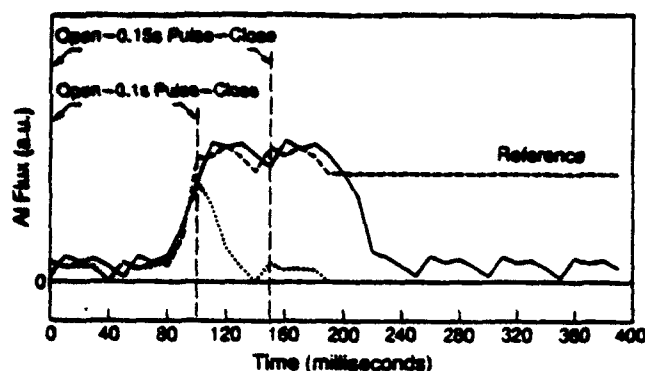


FIG. 2. Ion gauge measured flux profiles of 100 ms (dotted) and 150 ms (solid) Al pulses. In both cases, the pulse is so short that the shutter does not come to rest at the end of its travel after uncovering the crucible. It receives a command to reverse direction and close the oven, before reaching the end of its open path (regime 2). The 100 ms pulse is so short that it only partially uncovers the crucible (regime 3). The flux profile of a longer 0.5 s (dashed) (regime 1) pulse is also shown for reference. The flux profiles have the same time constants as in Fig. 1 and can be modeled as truncated trapezia of the model in Fig. 1.

profiles can reasonably be approximated by truncated trapezia with the same time constants as measured for case 1, and are used to deduce Al oven shutter open times for the correct integrated flux for extremely rapid Al pulses.

The three cases occur when the following relationships are satisfied between the four shutter time constants, the AIAs growth rate R_{AIAs} , and the AIAs layer thickness L_{AIAs} grown:

$$\text{case 1: } \frac{L_{\text{AIAs}}}{R_{\text{AIAs}}} > T_{12} \equiv \frac{T_{\text{ramp up}} + T_{\text{ramp down}}}{2} + 2T_{\text{close}}, \quad (3a)$$

$$\text{case 2: } T_{12} > \frac{L_{\text{AIAs}}}{R_{\text{AIAs}}} > T_{23} \equiv \frac{T_{\text{ramp up}} + T_{\text{ramp down}}}{2}, \quad (3b)$$

$$\text{case 3: } \frac{L_{\text{AIAs}}}{R_{\text{AIAs}}} < T_{23}. \quad (3c)$$

The mechanical inertia and free play of the pneumatic shutter, and the 60 Hz phase difference with respect to the trigger pulse, is expected to cause a certain amount of time jitter in the edges of the flux profile. This jitter is estimated to be of the order of $\Delta T_j \sim \pm 10$ ms for case 1 in Fig. 3(a), where the Al oven shutter is opened for $T = 0.5$ s in eight sequential and independent runs. The uncertainty in the thickness of AIAs grown is therefore of the order $\sim \Delta T_j R_{\text{AIAs}}$ (where, R_{AIAs} = growth rate of AIAs). Even for a growth rate of AIAs as high as $1 \mu\text{m/h}$, this is negligibly small ($\sim 0.03 \text{ \AA}$). The jitter is expected to be more pronounced for cases 2 and 3, as the forward motion of the shutter is arrested and its direction of travel reversed. This is indeed seen to be the case in Fig. 3(b) where in eight independent runs for a fast Al pulse (case 3), the shutter does not uncover the crucible mouth some of the time. The uncertainty in the Al flux deposited is $\pm 0.06 \text{ \AA}$ in this case, for $R_{\text{AIAs}} = 1 \mu\text{m/h}$. This error in the Al mole fraction can be reduced by simply going to lower GaAs and AIAs growth rates. Having a nonzero Al mole fraction minimum in the alloy so that one is always operating in the case 1 regime can also reduce

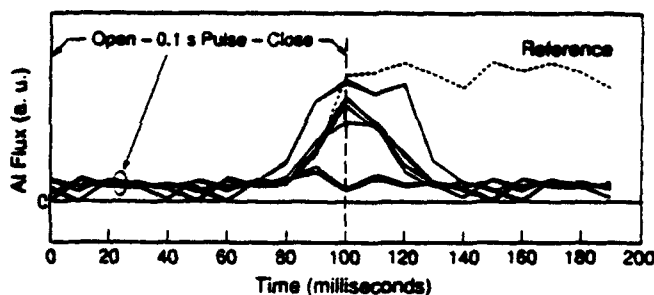
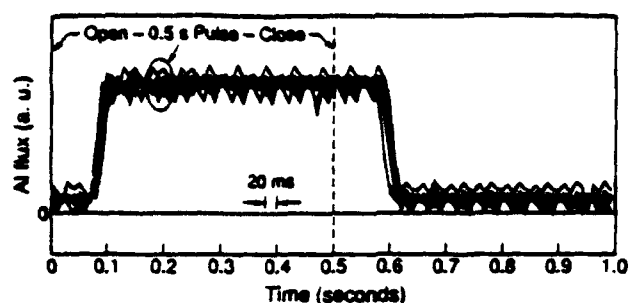


FIG. 3. Jitter in time constants observable in flux profiles of eight consecutive and independent Al pulses of 0.5 s (3a) and 0.1 s (3b) durations. The jitter is $\sim \pm 10$ ms for the longer pulse (regime 1), and ± 20 ms for the sharp pulses of the shutter operating in regimes 2 and 3.

this error. The nonzero minimum Al mole fraction is also desirable in an analog alloy in order to keep the Al oven temperature at levels where the growth rate vs oven temperature follows the behavior deduced from RED oscillations for higher oven temperatures.

The growths of two parabolic wells, one analog and the other digital, both 2000 \AA wide and with the Al mole fraction going from 0.01 (1%) at the center of the well to 0.3 (30%) at the well edges, was then run, and the corresponding ion-gauge profiles are compared to the ideal design profile in the top half of Fig. 4. The deviations Δx_{Al} , from the ideal profile are plotted in the bottom half, and are seen to be < 0.02 in the case of the digital alloy and < 0.03 for the analog alloy. The maximum Al oven temperature in either case was one that gave an AIAs growth rate of $0.32 \mu\text{m/h}$. A 1% minimum Al mole fraction at the well center ensured that the shutters were operating in the case 1 regime even at the well center for the digital alloy, and the Al oven temperature changed through no more than 200°C for the analog alloy. The superlattice period was 20 \AA for the digital alloy; for the analog alloy, the temperature of the Al oven was changed at a variable rate, each time interval corresponding to the time required to grow 20 \AA of alloy material at the particular Al oven temperature. The Al flux is measured every 10 ms and integrated so that the average Al mole fraction is plotted with the same resolution as the period, in this case 20 \AA . The picoammeter noise when integrated, has a nonzero value and consequently produces a constant offset in the measured graded profile. This offset is small (usually $< 1\%$ Al) and measurable in a simple run in which the Al oven is not opened at all. This is then subtracted from the measured profile to obtain the corrected profile.

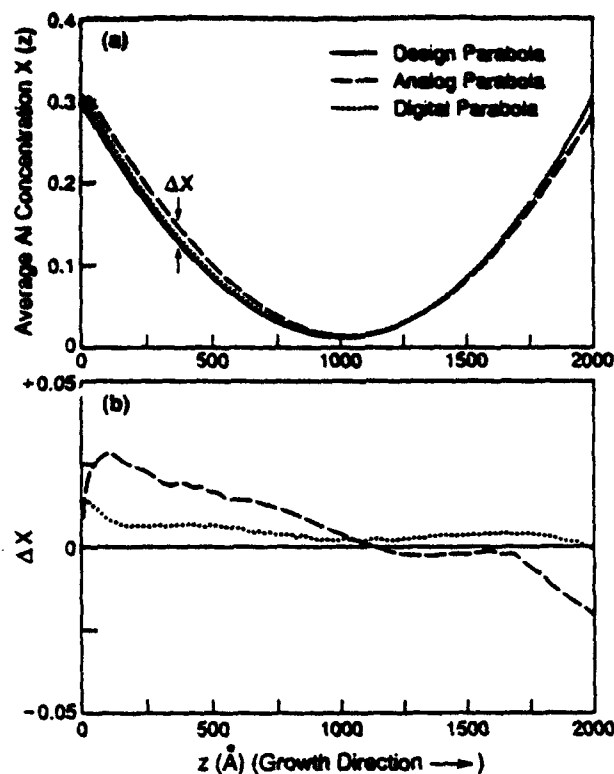


FIG. 4. Measured Al mole fraction (mf) vs depth profiles for a 2000 Å wide parabolic well with Al mf going from 1% at the center to 30% at the edges, grown with both the pulsed Al beam (digital alloy), and the variable Al oven temperature (analog alloy) methods. The design profile is also shown for comparison. A constant background GaAs growth rate of 0.75 $\mu\text{m/h}$ is assumed. Bottom half shows deviations of both measured alloy grades from design alloy.

The shift of the analog profile from the ideal profile observed is a result of the limits of cooling and heating rates of the Al charge. The Al charge is cooled simply by thermal conduction and radiation and has therefore a certain maximum cooling rate. Sufficient controllability of the negative gradient of Al mole fraction versus time is still possible even with a high constant background GaAs growth rate of 0.75 $\mu\text{m/h}$, as manifested by the measured analog-alloy parabolic well.

To accentuate the differences between the ability of the two alloy techniques to follow a desired profile, a $(\sin z)/z$ -type alloy grade profile, spread over a width of 2000 Å, and with maximum and minimum Al mole fractions of 30% and 1%, respectively, was generated. The ion gauge measured profiles are shown along with the design profile in Fig. 5. Note the considerably greater ability of the digital-alloy technique to obtain the desired alloy profile. While the analog-alloy profile does satisfy the required functional behavior, it has smaller amplitude and is broadened. One could, in principle, grow the analog alloy infinitesimally slowly so that the Al oven temperature could be changed in a more controlled manner, but this has the disadvantages of both longer growth times and possibly greater incorporation of background impurities in the growing alloy. It would also be possible to compensate for the time of oven response in the analog alloy growth by modifications in the temperature program as in Ref. 9.

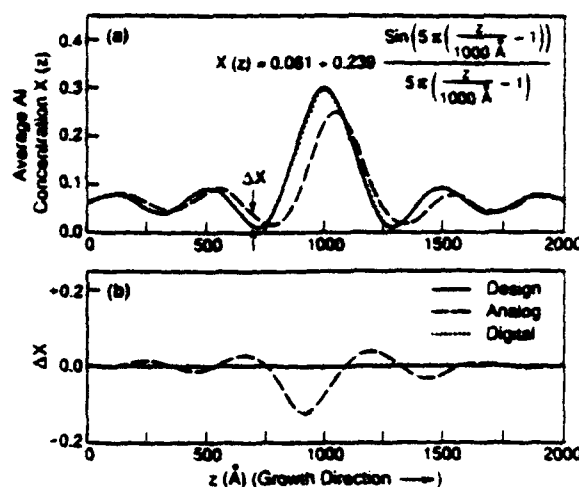


FIG. 5. $(\sin z)/z$ -type alloy grade spread over 2000 Å and with minimum and maximum Al mfs of 1% and 30%, measured for both analog and digital alloys. Note greater ability of digital alloy to produce desired profile, and the thermal lag problem in analog-alloy growth.

There is no necessity to have a nonzero minimum Al mole fraction in the alloy, especially in the digital-alloy technique. For usual AIAs growth rates, the Al mole fraction when the shutter is pulsed in the regimes of cases 2 and 3 above, is so small that deviations in the same are scarcely observable. This can be seen in the digital-alloy ion gauge measured profiles of Fig. 6, where the design alloy is a parabolic well 2000 Å wide with Al mole fraction going from 0% at the center to 30% at the edges. Five sequential and independent runs of the same design are shown, along with the ideal profile. Deviations from the design parabola are less than $\Delta x_{\text{Al}} \sim 0.03$. The largest portion of the deviation comes, in fact, from the AIAs growth rate being higher than the design value, and not from any shutter-timing-related uncertainties. The variation from run to run is also observed to be sufficiently small to permit one to predict the actual Al mole fraction versus depth grown, from an ion-gauge profile measured in a dummy run immediately prior to actual growth, to within $\Delta x_{\text{Al}} \sim \pm 0.01$.

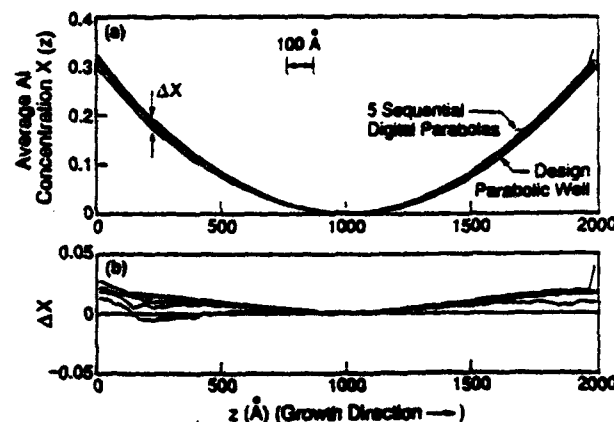


FIG. 6. Alloy profiles of five consecutive and independent digital-alloy parabolic wells, 2000 Å wide and with Al mf rising from 0% at well center to 30% at well edges, measured by ion-gauge method. Variations from run to run are small enough that a measurement made prior to actual sample growth can be taken to represent the actual graded-alloy grown.

For electron gases in wide parabolic potential wells the design parameter of interest is the well curvature, inasmuch as the carrier density profile is controlled by it. Curvature versus depth profiles calculated from the digital and analog alloy profiles measured in Fig. 4, are shown in Fig. 7 and compared to the constant design curvature. A part of the observed variation in curvature ($\sim \pm 11\%$) for the digital alloy arises from the ± 10 ms jitter in the opening and closing times of the shutter operating in regime 1. Should the Al mole fraction go to zero at the well center, the larger uncertainty in the time constants of the shutter operating in regimes 2 and 3 will cause larger (up to $\pm 100\%$) variations in the curvature. In such measurements a flat spot is sometimes observed to occur at the well center with the curvature going to zero.

If one desires to avoid the large percentage errors in the Al mole fraction resulting from the larger jitter (± 20 ms) when the shutter is operated in regimes 2 and 3 in the digital alloy technique, the minimum nonzero alloy percentage is simply

$$x_{\min 12} = \frac{R_{\text{AlAs}} T_{12}}{P}, \quad (4a)$$

in order to always operate in regime 1, and not stray into regimes 2 or 3, and

$$x_{\min 23} = \frac{R_{\text{AlAs}} T_{23}}{P}, \quad (4b)$$

in order to pulse the shutter in regimes 1 and 2, but to avoid regime 3 altogether. In the above equations, R_{AlAs} is the AlAs growth rate, P the superlattice period, and T_{12} and T_{23} are the shutter time constants defined in Eqs. (3). For $R_{\text{AlAs}} = 0.32 \mu\text{m/h}$, and a period of 20 \AA , $x_{\min 12}$ and $x_{\min 23}$ are, respectively, 0.8% and 0.09% . The percentage error in Al mole fraction at these limits are $\pm 6\%$ and $\pm 100\%$ for $x_{\min 12}$ and $x_{\min 23}$, respectively. These percentage error values are purely functions of the shutter time constants and jitter, and are ideally zero in the limit of no jitter.

Another source of deviation in Al flux from programmed values is flux transients caused by changes in the temperature of the surface of the charge in the MBE cell, upon shutter opening and closing. In our case, this can be gauged by differences in maximum Al flux values observed throughout

the growth sequence and is $< \pm 0.12 \text{ \AA/s}$, translating to $\Delta x_{\text{Al}} < \pm 0.03$ at our growth conditions.

From the jitter in the profiles measured when the Al oven shutter is pulsed in the three regimes in the digital-alloy technique, one can estimate the percentage error in the Al mole fraction at various points in a symmetric parabolic well which has 0% Al in the well center. Two critical dimensions measured from the well center z_{C12} and z_{C23} can be defined. z_{C12} is the $\pm 6\%$ error point i.e., the distance from the well center where the Al mole fraction can vary by as much as $\pm 6\%$ of the design value, and this occurs when the shutter operation moves from regime 1 to 2; likewise z_{C23} is the $\pm 100\%$ error point, this occurring when the shutter operation moves from regime 2 to 3. For the particular Al oven shutter characterized above z_{C12} and z_{C23} are given, respectively, by

$$|z_{C12}| = \frac{L_{\text{PW}}}{2} \sqrt{\frac{x_{\min 12}}{x_{\max}}} \sim 325 \text{ \AA} \left(\frac{L_{\text{PW}}}{4000 \text{ \AA}} \right) \sqrt{\left(\frac{R_{\text{AlGaAs}}}{1 \mu\text{m/h}} \right) \left(\frac{20 \text{ \AA}}{P} \right)}, \quad (5a)$$

$$|z_{C23}| = \frac{L_{\text{PW}}}{2} \sqrt{\frac{x_{\min 23}}{x_{\max}}} \sim 110 \text{ \AA} \left(\frac{L_{\text{PW}}}{4000 \text{ \AA}} \right) \sqrt{\left(\frac{R_{\text{AlGaAs}}}{1 \mu\text{m/h}} \right) \left(\frac{20 \text{ \AA}}{P} \right)}, \quad (5b)$$

where $x_{\min 12}$ and $x_{\min 23}$ are as defined in Eqs. (4), x_{\max} is the Al mole fraction at the well edges, P is the period of the superlattice grown, R_{AlGaAs} is the sum of the growth rates of GaAs and AlAs, and L_{PW} the width of the parabolic well. Similar critical dimensions for other alloy-profiles can also be derived. The percentage error in Al mole fraction will decrease approximately as z^{-2} for $|z| > z_{C12}$, is fixed at $\sim \pm 100\%$ for $|z| < z_{C23}$, and has values between $\pm 6\%$ and $\pm 100\%$ for values of z between the two critical z values. As stated earlier though, the problem can be avoided altogether by having a small nonzero minimum Al mole fraction $x_{\min 12}$ or $x_{\min 23}$ in the alloy.

The variation in the curvature of the parabolic well across a 2 in. diam wafer that is not rotated (to avoid interference between the frequency of rotation and the frequency of the shuttering in the digital-alloy case or of the temperature change in the analog-alloy case) is of interest. For the substrate/shutter/oven geometry for our Varian GEN II MBE machine we calculate a curvature variation of from $+30\%$ (at the point on the wafer farthest from the neighboring Al and Ga ovens) to -30% (at the point closest to the two ovens), 0% being at the wafer center, for both the digital and analog alloys. A further lateral nonuniformity is introduced in the digital-alloy case when the Al pulses become so sharp that the shutter only partially uncovers the oven thereby exposing the more distant points on the wafer to the Al flux for a longer time. This causes the curvature for $|z| < z_{C23}$ to vary from $+60\%$ (at the most distant point) to -100% (at the nearest point, which may not be receiving any Al flux at all) across the wafer, for our machine geometry and shutter time constants.

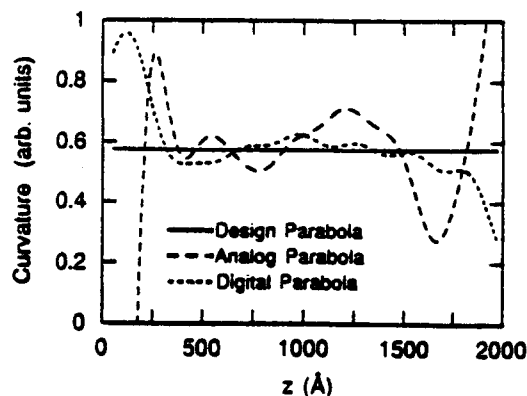


FIG. 7. Curvature vs depth of the three parabolic profiles: design, analog, and digital, shown in Fig. 4.

The ion gauge measured profiles are representative of the grown profiles only if both Ga and Al have unity sticking coefficient at the growth conditions. This is a function of substrate temperature, beam fluxes, etc.¹³ At substrate temperatures above ~670 °C and As stabilized growth conditions, Ga re-evaporation will cause changes in both the layer thicknesses and the alloy composition, and therefore the alloy profile shape. An additional complication is that Ga re-evaporation is a function of the Al flux. Under such conditions, the graded-alloy profile is perhaps best measured by monitoring the desorbed Ga signal from the substrate during actual growth by a mass spectrometer mounted in one of the furnace ports with the analyzer having a line of sight view of the substrate.^{14,15}

For our sample growth conditions (substrate temperatures of ~580 °C and As stabilized growth), the Ga and Al do have unity sticking coefficients. The growth rate of AlGaAs was measured by RED oscillations for a range of Ga and Al oven temperatures and was in all cases found to agree (within 1%) with the sum of the GaAs and AlAs growth rates, under the above growth conditions. The ion gauge measured profiles are therefore expected to be the actual alloy profiles grown.

This method can be used to calibrate the alloy grades of other ternary alloy films such as In_xGa_{1-x}As and alloys with mixed group V elements such as GaAs_{1-x}P_x and GaSb_{1-x}As_x. If the InGaAs alloy were grown as a strained digital alloy on a GaAs substrate, then the effect of lattice-mismatch strain on cation incorporation rates¹⁶ at the actual growth conditions, would have to be taken into account to deduce the grown alloy profile from the ion gauge measured profile. The measurements would also be valuable in the growth of strained graded alloys with critical composition requirements to avoid misfit dislocations.

For the alloys with the mixed group V elements, the composition of the alloy is controlled at low temperatures by limiting the amount of the element with the greater sticking coefficient and providing an excess of the more volatile species. For example, the smaller As (the preferentially incorporated element) flux supplied to the GaAs_{1-x}P_x surface to which an excess P (the more volatile element) flux is also supplied, will control the alloy fraction *x*. The ion-gauge measurement could be therefore done with the less volatile of the two group V elements. The higher vapor pressure of group V elements might complicate the measurement though.

Since the currents measured are small (nA), the resolution of this measurement technique is ultimately limited by the resolution and speed of the picoammeter in this range. The overall accuracy of the actual graded alloy grown is still limited by the ± 3% accuracy of the measurement of GaAs and AlAs growth rates by the RED oscillation method.

III. CONCLUSIONS

In conclusion, we have presented a direct technique to measure graded Al_xGa_{1-x}As alloy deposition profiles ver-

sus depth with a high degree of precision. The beam flux monitor ion gauge measured profiles are obtained in a dummy run immediately prior to actual growth in an MBE machine. Both a variable Al oven temperature technique (analog alloy) and a pulsed Al beam technique (digital alloy), have been applied to the case of a wide symmetric parabolic well. A computer is used to ramp the furnace temperature or pulse the beam with sufficient fineness to produce a smooth alloy grade, as evidenced by the corresponding ion-gauge measurements. The digital-alloy technique is further seen to be the preferable technique where changes in Al mole fraction versus depth are too rapid for the Al oven temperature to track precisely, and where reasonable growth rates are desired. Variations from run to run are small enough that one can use these measured profiles as a good indication of the actual graded Al mole fraction versus depth, grown.

The method is applicable to measuring the alloy grades of other III-V ternary alloys, especially where critical composition control is required to avoid misfit dislocations in the growth of strained graded alloys.

ACKNOWLEDGMENTS

We thank R. M. Westervelt, E. G. Gwinn, P. F. Hopkins, and A. J. Rimberg of Harvard University and P. O. Holtz, K. Ensslin, M. Sherwin, and P. Hillner of UCSB for valuable discussions. This work was supported in part by the AFOSR under Grant No. AFOSR-88-0099.

¹W. T. Tsang, *Semiconductors and Semimetals*, edited by R. Dingle (Academic, New York, 1987), Vol. 24, Chap. 7.

²H. Kroemer, *Proc. IEEE* 70, 13 (1982).

³F. Capasso, Chap. 6, *Semiconductors and Semimetals*, edited by R. Dingle (Academic, New York, 1987), Vol. 24, Chap. 6.

⁴A. C. Gossard, *J. Quant. Electronics* QE 22, 1649 (1986).

⁵M. Sundaram, A. C. Gossard, J. H. English, and R. M. Westervelt, *J. Suprat. Microsc.* 4, 683 (1988).

⁶M. Shayegan, T. Sajoto, M. Santos, and C. Silvestre, *Appl. Phys. Lett.* 53, 791 (1988).

⁷E. G. Gwinn, R. M. Westervelt, P. F. Hopkins, A. J. Rimberg, M. Sundaram, and A. C. Gossard, *Phys. Rev. B* 39, 6260 (1989).

⁸S. Adachi, *J. Appl. Phys.* 58, R1 (1985).

⁹J. P. Harbison, L. D. Peterson, and J. Levkoff, *J. Cryst. Growth* 81, 34 (1987).

¹⁰M. Kawabe, M. Kondo, N. Matsuura, and Kenya Yamamoto, *Jpn. J. Appl. Phys.* 22, L64 (1983).

¹¹R. C. Miller, A. C. Gossard, D. A. Kleinman, and O. Munteanu, *Phys. Rev. B* 29, 3740 (1984).

¹²J. J. Harris, B. A. Joyce, and P. J. Dobson, *Surf. Sci.* 103, L90 (1981).

¹³C. T. Foxon, *J. Vac. Sci. Technol. B* 4, 867 (1986).

¹⁴A. J. Spring Thorpe and P. Mandeville, *J. Vac. Sci. Technol. B* 6, 754 (1988).

¹⁵J. Y. Tsao, T. M. Brennan, J. F. Klem, and B. E. Hammons, *Proceedings of the Ninth MBE Workshop*, Purdue University, West Lafayette, IN, 1988 (unpublished).

¹⁶K. R. Evans, C. E. Stutz, D. K. Lorange, and R. L. Jones, *J. Vac. Sci. Technol. B* 7, 259 (1989).

Modulation-doped graded structures: Growth and characterization

M. Sundaram, A. C. Gossard, and P. O. Holtz¹

Department of Electrical and Computer Engineering, and Materials Department, University of California, Santa Barbara, California 93106

(Received 19 October 1990; accepted for publication 8 November 1990)

Remotely doped graded parabolic potential well structures have been grown and studied. Electrons distribute themselves uniformly in a parabolic well, the density being proportional to the curvature or quasidoping in the well. Quasidoped semiconductors are synthesized by molecular beam epitaxy in the GaAs/Al_xGa_{1-x}As system through the digital alloy technique. The analog grading produced by the digital alloy is verified by photoluminescence excitation spectroscopy. Low temperature mobility measurements show higher mobility in these quasidoped semiconductors than in similar real-doped semiconductors. Alloy-disorder scattering is suggested to be the mobility-limiting mechanism in this digital alloy system. Capacitance-voltage profiling analysis of quasidoped semiconductors has been developed, and is used to measure carrier profiles in these structures.

1. INTRODUCTION

The recently introduced concept of remotely doped graded heterostructures^{1,2} has led to the realization of a high mobility three-dimensional electron gas (3DEG). This 3DEG or jellium exhibits a number of interesting properties in low temperature transport and optical measurements.³⁻⁷

We had stated in our original introduction¹ that the concept was entirely general and could be used to realize different carrier profiles of controlled density and high mobility. We expand on this principle here. We refer to the concept as quasidoping.⁸

Both real doping and quasidoping are illustrated schematically in Fig. 1. In real doping we start with a pure semiconductor that has a flat band edge, which, on the addition of say, a uniform distribution of charged dopant impurities, results in a band edge that is parabolic (with the curvature proportional to the charge density) as per Poisson's equation. In quasidoping this equation is turned around. One starts with a graded band-edge semiconductor, say parabolic, and can subsequently think of this as being equivalent to an ungraded band-edge semiconductor that has a charged impurity distribution proportional to the curvature of the grading (constant in the case of parabolic grading). There is exact mathematical equivalence and, if quantum size effects can be ignored, the electrical properties of the quasidoped system can be deduced entirely by treating semiconductors with shallow band-edge profiles of known grading, as though they were quasidoped.

The carrier profile obtained in either case, real or quasidoping, is the same. In a real-doped semiconductor the local carrier density is due to the local charged dopant density, whereas in a quasidoped semiconductor the local carrier density is proportional to the curvature of the local band-edge grade. But the carriers in a quasidoped semiconductor, and here lies the fundamental difference between the two doping techniques, originate from a real doping of barriers that are physically remote from, and at higher potential than, the

graded region. It is in a bid to minimize the system energy and get a uniform Fermi energy level at thermal equilibrium that the carriers distribute themselves in a way that mimics the quasidoping profile. A computer simulation of the 0 K electron distribution in one half of a symmetric 2000 Å-wide parabolic well that has a curvature of $\sim 1 \times 10^{16} \text{ cm}^{-3}$, is shown in Fig. 2 for a range of barrier dopings. At a particular value of the doping, n_d , the electron distribution in the graded well is exactly uniform at the value of the quasidoping. At larger barrier dopings, excess electrons are inserted in accumulation layers at the well edges, and at smaller ones they are extracted from the edges. Over most of the well though, the electron profile tends to mimic the quasidoping profile, for a wide range of barrier dopings. This behavior is surprisingly observed at all temperatures from 0 to 300 K but the tendency towards ideality is more pronounced at lower temperatures.¹ The quasidoping density N_Q in a parabolic well of width L_{QW} and height Δ is given simply by the curvature as: $N_Q = 8\epsilon\Delta/e^2L_{QW}^2$, where ϵ is the dielectric permittivity, and e the electronic charge. For an electron gas of sheet density N_s in a parabolic well of quasidoping N_Q , the classical width of the gas is therefore simply: $w_c = N_s/N_Q$.

As the electrons in a shallow parabolic well are designed to be distributed uniformly over a thickness in excess of 1000 Å and occupy several subbands, we refer henceforth to this distribution as a three-dimensional electron gas or 3DEG.

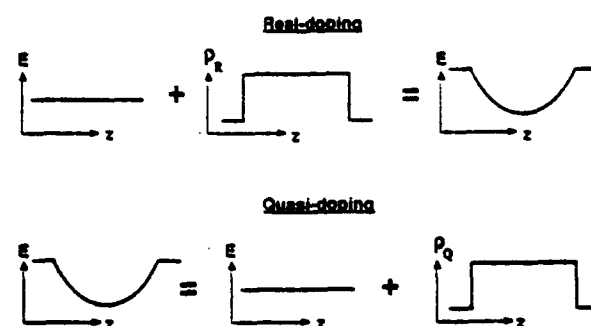


FIG. 1. Schematic illustration of real doping and quasidoping. Quasidoping is the inverse of real doping.

¹ Permanent address: Department of Physics and Measurement Technology, Linköping University, S-581 83 Linköping, Sweden.

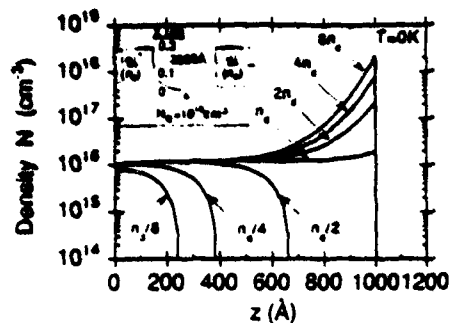


FIG. 2. 0 K Electron profiles in one half of a symmetric 2000 Å-wide parabolic well (inset) simulated for a range of barrier doping densities n_d . Well curvature $N_Q = 1 \times 10^{16} \text{ cm}^{-3}$.

II. EXPERIMENTS AND DISCUSSION

We have accomplished quasidoping in the GaAs/AlAs system through the digital alloy technique in molecular beam epitaxy. The digital alloy technique is schematically illustrated in Fig. 3. A superlattice with a constant period of 20 Å is grown. The duty cycle of the Al in each period is varied in the desired fashion, say parabolic, by computer control of the Al oven shutter in the MBE machine. The carrier "sees" an average Al mole fraction, in effect an analog alloy. Using the fact that the band gap of $\text{Al}_x\text{Ga}_{1-x}\text{As}$ has a nearly linear relationship with the Al mole fraction over a large range of x values (0–0.45), the result is a graded band gap directly proportional to the graded alloy composition. To synthesize a uniformly quasidoped semiconductor with a carrier density of $\sim 2 \times 10^{16} \text{ cm}^{-3}$ would require a 2000 Å-wide parabolic well in which the Al mole fraction went quadratically from zero at the center to 0.2 at the edges.¹ An abrupt increase in the mole fraction from 0.2 to 0.3 at the edges further provides a square well like confinement when the parabolic well is exactly filled or overfilled.

All samples in this study were grown in a Varian Gen II MBE machine, on mechanical-grade LEC semi-insulating/heavily N-doped (001) GaAs substrates, at a nominal substrate temperature of 580°C. The alloy composition was nominally 30% Al. All lower alloy compositions ($x < 0.3$), whether constant or continuously graded, were synthesized

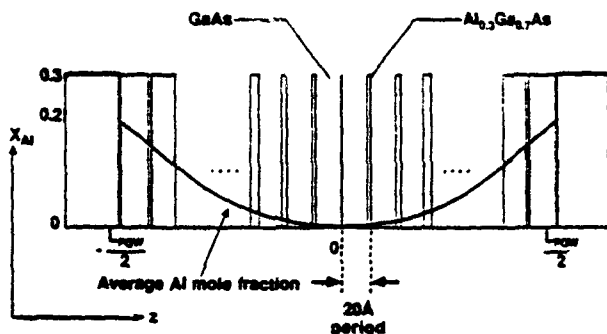


FIG. 3. Digital alloy used to realize parabolic potential well. Duty cycle of $\text{Al}_x\text{Ga}_{1-x}\text{As}$ in superlattices varies parabolically from well center to edges, resulting in parabolic variation of average Al mole fraction x , and energy band edge. L_{per} is typically between 2000 and 5000 Å.

by chopping between the $\text{Al}_{0.3}\text{Ga}_{0.7}\text{As}$ and GaAs in the manner explained above.

A. Parabolic quantum wells as a means of graded profile testing

To experimentally verify that the digital alloy technique does indeed work like an analog alloy, parabolic quantum wells were grown using this technique, and optically tested through photoluminescence excitation spectroscopy.⁹ Harmonic oscillator like exciton transitions expected to be seen in such a spectrum are shown in Fig. 4(a). nh indicates a transition from the n th electron state in the conduction band parabolic well to the n th heavy hole state in the valence band parabolic well. nl is similarly the transition to the corresponding n th light hole state. Off-diagonal transitions having $\Delta n = 2$ (e.g., $13h$) are also predicted. An excitation spectrum for a MQW sample consisting of 10 undoped 520 Å-wide parabolic quantum wells (with x going from 0 at the center to 0.3 at the edges) is shown in Fig. 4(b). Detection was 8057 Å, the position of the heavy hole free exciton in the photoluminescence spectrum (shown in the inset). The labeled peaks in the excitation spectrum reflect the harmonic oscillator like transitions between electron and hole states. Experimentally deduced energy ladder spacings are 25.2 meV for electrons, and 10.5 meV for heavy holes, which are in reasonable agreement with values calculated for ideal har-

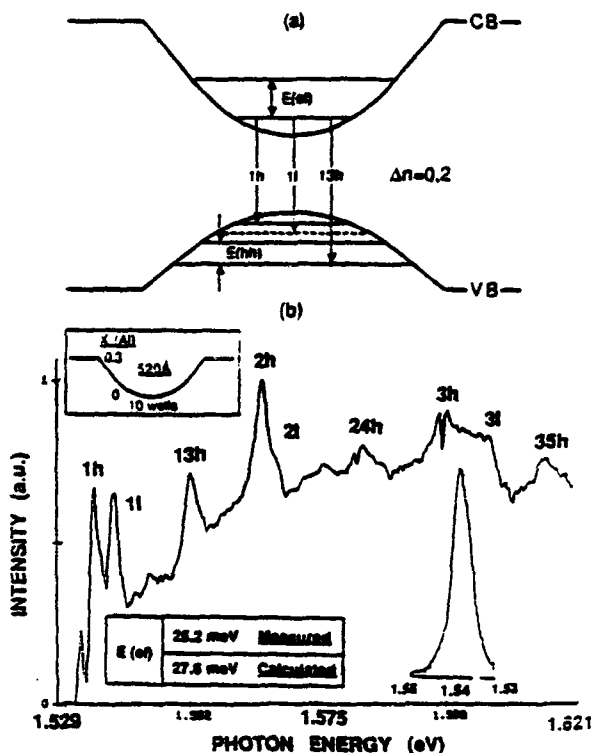


FIG. 4. (a) Harmonic-oscillator (HO)-like exciton transitions allowed between electron states in the conduction band and hole states in the valence band. Transitions are allowed for $\Delta n = 0, 2$. (b) Photoluminescence excitation spectrum of ten 520 Å-wide parabolic quantum wells, reflecting HO-like nature of the conduction and valence band parabolic wells. Exciton transitions labeled. Detection at 8057 Å, the heavy-hole exciton in the PL spectrum, shown in inset. Also shown are the measured and calculated HO energy-ladder spacings for the electrons.

monic oscillators in the conduction and valence bands (27.6 meV for electrons, and 8.7 meV for heavy holes). This effectively confirms the viability of the digital alloy technique.

The shape of the graded alloy can also be measured by monitoring the variation with time of the collector current of beam flux monitor in the growth position, in a calibration run immediately prior to actual growth, and then integrating this current with time.¹⁰ Such measurements also confirm the possibility of making alloys with controlled grades.

B. Mobility measurements

The principal advantage of quasidoping as opposed to real doping is the reduced ionized-impurity scattering and consequent mobility enhancement of the carriers in the former case. Data supporting this fact are presented below. Typical Van der Pauw (VdP) mobility (parallel to the superlattice layers) and concentration vs temperature for the 3DEG in a 4640 Å-wide parabolic well with a curvature $N_Q \sim 6.0 \times 10^{15} \text{ cm}^{-3}$ is shown in Fig. 5(a). 400 Å-wide spacer layers were inserted between the well and the doped layers in the barriers, on either side. Low temperature VdP mobilities as high as $2.5 \times 10^5 \text{ cm}^2/\text{V s}$ have been obtained in some samples. The mobility vs temperature characteristic of a sample of *n*-GaAs bulk doped to $6.2 \times 10^{15} \text{ cm}^{-3}$ is also shown for comparison. The superior mobility of the quasi 3DEG as opposed to the real 3DEG is clear, especially at low

temperatures where the reduced ionized-impurity scattering of the electrons in the modulation-doped parabolic well results in an improvement in mobility over the real-doped case by two orders of magnitude.

It is theoretically expected, and experimentally confirmed on identical samples,¹ that the electrons are distributed uniformly (at the quasidoping density N_Q) about the center of the parabolic well. In the limit of 0 K, additional electrons introduced into the well are added to the periphery of this starting distribution at a uniform 3D density. By controlled pulsing of a red LED on the sample and using the persistent photoconductivity (PPC) effect to empty DX centers in the doped $\text{Al}_{0.3}\text{Ga}_{0.7}\text{As}$ barriers, the total number of electrons N , per unit area introduced into the well can be increased and the variation of mobility μ of the 3DEG with the integrated electron sheet concentration per unit area N_s in the parabolic well, is obtained in Fig. 5(b), for a 2000 Å-wide parabolic well ($N_Q \sim 2.2 \times 10^{16} \text{ cm}^{-3}$) with 200 Å-wide spacer layers on either side. A strong decrease of μ with N_s is observed:

$$\mu \propto N_s^{-\gamma}, \quad (1)$$

where $\gamma \sim 0.76$. Mobility decreases from $\sim 9.4 \times 10^4 \text{ cm}^2/\text{V s}$ at the 2D density $N_s \sim 1.55 \times 10^{11} \text{ cm}^{-2}$ ($w_c \sim 35\%$ of the 2000 Å-wide parabolic well full at the uniform density $N_Q \sim 2.2 \times 10^{16} \text{ cm}^{-3}$) to $5.96 \times 10^4 \text{ cm}^2/\text{V s}$ at $N_s \sim 3.29 \times 10^{11} \text{ cm}^{-2}$ ($w_c \sim 75\%$ of the well filled at the same 3D density). There appears to be a peak in the mobility, $9.6 \times 10^4 \text{ cm}^2/\text{V s}$, when the well is about 37% full, and a steeper decrease to $4.58 \times 10^4 \text{ cm}^2/\text{V s}$ when the filling percentage is increased from $\sim 75\%$ to 82%. The well was saturated at this point and no more carriers could be added.

The strong decrease of mobility with concentration is a signature of the scattering mechanisms at work. Inasmuch as the effective spacer width is in excess of 200 Å when the well is partially filled (it is 200 Å when the well is exactly full or overfull), ionized impurity scattering is not expected to be the mobility limiting scattering mechanism. Alloy-disorder scattering and interface roughness scattering are expected to be the dominating scattering mechanisms for the 3DEG in a digital alloy.

A rigorous quantitative treatment of the alloy-disorder scattering in a 3DEG is complicated by the fact that as the well is filled, the electron wave functions penetrate into regions with greater Al mole fraction, consequently suffering from enhanced scattering. Added to this is the occupation of more and more subbands as the well is filled (with an attendant flattening of the parabolic well at constant Fermi energy) and the corresponding onset of the intersubband scattering terms. It is calculated that the 35% filling fraction (as cooled in the dark) corresponds to two subbands being occupied, while the 75% fraction corresponds to the occupation of four subbands. The exactly full 2000 Å-wide parabolic well has five occupied subbands. The strong decrease of mobility when the filling fraction is increased from 75% to 82% is probably due to the onset of the occupation of the fifth subband and the onset of new intersubband scattering terms.

The alloy-disorder-scattering-limited mobility μ vs N_s of the 3DEG, calculated assuming one occupied subband

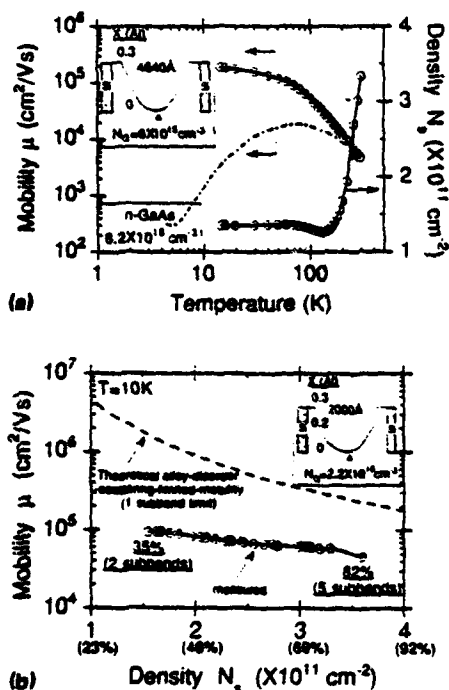


FIG. 5. (a) Mobility μ and sheet electron concentration N_s vs temperature T for 4640 Å-wide parabolic well ($N_Q = 6 \times 10^{15} \text{ cm}^{-3}$) shown in inset. μ vs T for a $6.2 \times 10^{15} \text{ cm}^{-3}$ bulk-doped *n*-GaAs also shown for comparison (Ref. 11). Note higher mobility of 3DEG in parabolic well, especially at lower temperatures. (b) μ vs N_s for 2000 Å-wide well (inset) at $T = 10 \text{ K}$. μ decreases as $N_s^{-0.76}$. Numbers in brackets along the horizontal axis indicate fraction of well filled at uniform density in classical limit. Alloy-disorder-scattering-limited mobility calculated in one subband limit, assuming a uniform (classical) electron distribution, also shown. Two and five subbands, respectively, are occupied (in the limit of 0 K) at the minimum and maximum measured N_s .

and a uniform electron distribution, is also shown in the figure.

If we use the expression¹²

$$\frac{1}{\tau_{\text{alloy}}} = \frac{m^* X (1 - X) \Omega \langle V \rangle^2}{\hbar^3} I_{\text{alloy}} \quad (2)$$

for the alloy-disorder scattering relaxation time in a random alloy, where X is the average mole fraction composition of the ternary alloy, $\langle V \rangle$ is the alloy disorder scattering parameter, Ω is the unit cell volume, m^* the electron effective mass, \hbar the reduced Planck's constant, and I_{alloy} is given, for electrons occupying the lowest subband [with wave function $\psi_0(z)$ within the alloy], by

$$I_{\text{alloy}} = \int_{-\infty}^{\infty} |\psi_0(z)|^4 dz \quad (3)$$

then using an average value for X in the parabolic well ($= X_{\text{edge}}/3$) we estimate the alloy-disorder scattering mobility limit for a 2000 Å-wide parabolic well that is exactly filled to $\sim 4.4 \times 10^{11} \text{ cm}^{-2}$, all of these occupying the lowest subband, to be $\sim 1.5 \times 10^5 \text{ cm}^2/\text{V s}$. This estimate is obtained from the calculated mobility limit for the same electron sheet concentration in the InP/In_{0.53}Ga_{0.47}As 2DEG system¹³ after appropriate scaling of parameters between InGaAs and AlGaAs (these being $m^* = 0.067$, $X = 0.2/3$, $\Omega = 4 a_0^3$ where $a_0 = 5.66 \text{ Å}$, $\langle V \rangle = 1 \text{ eV}$, for the AlGaAs alloy; and $m^* = 0.047$, $X = 0.47$, $\Omega = 4 a_0^3$ where $a_0 = 5.87 \text{ Å}$, $\langle V \rangle = 0.6 \text{ eV}$, for the InGaAs alloy). The measured mobility for the nearly filled well case is $\sim 60\%$ lower than this theoretical value. It is reasonable to attribute this lower mobility to the fact that the carriers occupy four subbands instead of one, with the attendant increase in both intersubband and intrasubband alloy-disorder scattering terms. It is interesting to note that assuming strict electron confinement to 35% of the well as cooled in the dark, the alloy-disorder-scattering-limited mobility (again assuming lowest subband occupancy) increases to $\sim 1.5 \times 10^6 \text{ cm}^2/\text{V s}$. While a part of this increase (a factor of about 2) from the filled well value, is due to the lower electron sheet concentration N_s , the main increase (a factor of 5) is due to the reduced average alloy composition, X , that the electron sees. But the assumption that the electrons are precisely confined to 35% of the width about the center of the well is not strictly valid. The wave functions penetrate beyond this width into the regions of higher Al mole fraction, resulting in lower mobility. This is especially so for the second subband which is also occupied at this filling fraction. Allowing a factor of 2 increase in the mobility, rather than 5, as a resultant of the reduced average X , and a 30% mobility reduction from the intersubband scattering when the second subband is just occupied,¹² gives $4 \times 10^5 \text{ cm}^2/\text{V s}$ as a reasonable estimate for the maximum alloy-disorder-scattering-limited mobility that the above 3DEG will have when cooled in the dark and when its three-dimensionality condition is barely satisfied, i.e., at least two subbands are occupied.

Care is in order in interpreting the results of the μ vs N_s experiment performed in the manner described above. The center of the 3DEG may not coincide with the center of the alloy parabola, to begin with. This could be due to donor

diffusion or an unequal incorporation of deep compensating impurities in the barrier layers below and above the parabolic well, unequal depletion from surface and substrate, and incomplete activation and unequal compensation of donor atoms on the two sides. Flashing a LED may cause the well to fill more from one side than the other, causing a further shift in the 3DEG distribution. The beauty of the quasidoping technique is that the 3DEG is uniform in all these cases since it only requires the presence of a parabolic potential. The calculations above for the alloy-disorder-scattering-limited mobility are valid for a 3DEG located symmetrically about the alloy parabola center. A shift in the center will cause a decrease in this mobility. Our conclusions about the μ vs N_s behavior still stand though.

Interface roughness scattering is the other important scattering mechanism in digital alloys. Monolayer fluctuations in component layer thicknesses and/or layer positions in the superlattice cause fluctuations in the quantized energies which in turn results in a scattering potential proportional to the perturbation. The roughness-scattering limited mobility μ_r can be written as¹⁴

$$\mu_r = \frac{e \langle \tau_r \rangle}{m^*} \propto \frac{1}{(V_j u)^2} \frac{g(\Lambda)}{\Lambda^2}, \quad (4)$$

where u is the mean square deviation of the roughness height in units of monolayers, Λ the lateral spatial decay rate of the roughness, V_j the quantized energy perturbation per monolayer caused by the roughness, and g a function of Λ , electron sheet concentration N_s , and temperature T .

For the lowest subband in the parabolic well, the largest fluctuation in quantized energy arises from roughness at the well center. Experimentally too this is perhaps the region of maximum roughness because of monolayer fluctuations in the very short Al pulses here. By first order perturbation theory, we get V_j to be equal to $(2/L_w) \Delta z V_0$ for an exactly filled parabolic well (and therefore a square well as seen by the individual electron), and $(1/L_{\text{HO}} \sqrt{\pi}) \Delta z V_0$ for a nearly empty parabolic well, where Δz is the small roughness, V_0 its potential height, L_w the width of the well, and L_{HO} the natural unit of length of the harmonic oscillator ($\sim 140 \text{ Å}$ for a parabolic well with a curvature of $\sim 2.2 \times 10^{16} \text{ cm}^{-2}$). For the above 2000 Å-wide well, and for one monolayer Al_{0.3}Ga_{0.7}As fluctuations at the digital alloy center, the lowest subband energy perturbations are respectively $\sim 0.7 \text{ meV}$ for the filled well, and $\sim 2.7 \text{ meV}$ for the nearly empty well. Taking $u = 0.2$ and $\Lambda = 120 \text{ Å}$ (fitting parameters deduced for 1 monolayer AlAs roughness in Ref. 14) and scaling the results for μ_r vs N_s calculated in Ref. 14, we arrive at roughness-scattering limited mobility values of $\sim 4.6 \times 10^7 \text{ cm}^2/\text{V s}$ for the nearly filled well, and $1.4 \times 10^6 \text{ cm}^2/\text{V s}$ for the nearly empty well. Once again these estimates, especially for the filled well case, should be further reduced by the occupation of several subbands. Even with this reduction, a much larger roughness than one monolayer and/or one monolayer roughness at several spots in the well would be required to account for our substantially lower measured mobility values for these two cases. Both these hypotheses, the uncontrolled insertion of a thick layer of AlGaAs at a single spot or several single monolayers at random spots, appear unrea-

sonable, given the current state of MBE technology. At any rate, the estimates for the alloy-disorder-scattering-limited mobilities for the two instances are closer to the measured values and attest to the dominance of alloy scattering as the mobility limiting scattering mechanism.

C. Capacitance-voltage (CV) profiling

CV profiling is a simple, quick, and powerful method to experimentally measure carrier distributions in semiconductors. It can, besides, be done at room temperature. We have successfully extended this technique to the study of quasidoped semiconductors.

It is well known that what the CV profiling measures is not the true carrier profile, but an apparent profile that is a *smear-out* version of the true profile, the smearing occurring over the order of a few Debye lengths. Only in a uniformly doped semiconductor are the two profiles identical. Secondly, the graded heterojunction itself being leaky it is difficult to extract the true capacitance from the measured value. It is therefore preferable to use the depletion region of an adjacent Schottky barrier¹⁵ to sweep through the carriers in the parabolic well, and measure capacitance vs voltage between gate and heavily doped substrate. Thirdly, inasmuch as it is impossible to deconvolve the true carrier profile from the measured apparent profile, a computer simulation of the CV profiling process is necessary to reconstruct the apparent profile. Measured and simulated apparent profiles are then compared and an optimum fit obtained by appropriate changes to the design parameters. Fourthly, the changes required to obtain a good fit can yield valuable information to optimize design and growth parameters.

Computer simulated profiles of the true, $N(z)$, and apparent, $N_{CV}(z)$ (the profile that would be obtained in a CV measurement), electron distributions for the nominally 2000 Å-wide parabolic well with a curvature $\sim 2.2 \times 10^{16} \text{ cm}^{-3}$, at room temperature, as also the doping profile $N_D(z)$ (graphically illustrating the fact that only the barriers of the parabolic well are doped) and the Al mole fraction profile $X_{Al}(z)$, are shown in Figs. 6(a) through 6(d). Inset in Fig. 6(e) shows the CV measurement schematic. Details of these calculation procedures will be presented elsewhere. Two features are manifest: the true electron distribution in the well is nearly uniform at the quasidoping value as expected, and the apparent profile, though mostly uniform, shows the asymmetry expected in profiling through back to back GaAs/Al_xGa_{1-x}As heterojunctions.

Figure 6(e) shows the measured apparent profile of an actual parabolic well nominally designed to be the same as the one for which the simulations in Fig. 6 were done, and grown on a heavily n^- -doped GaAs substrate. Also shown is the optimum computer-reconstructed fit, and the corresponding true electron distribution calculated for this fit. Though a reasonably good fit, especially in the top half of the well, could be obtained to the apparent profile of a purely parabolic well (the curvature being the only design parameter varied), introduction of a negative sheet charge of $-7 \times 10^{10} \text{ cm}^{-2}$ at the lower interface (towards the substrate side), gave the best fit. Silicon or oxygen segregation at the lower interface¹⁶ is the most reasonable explanation for

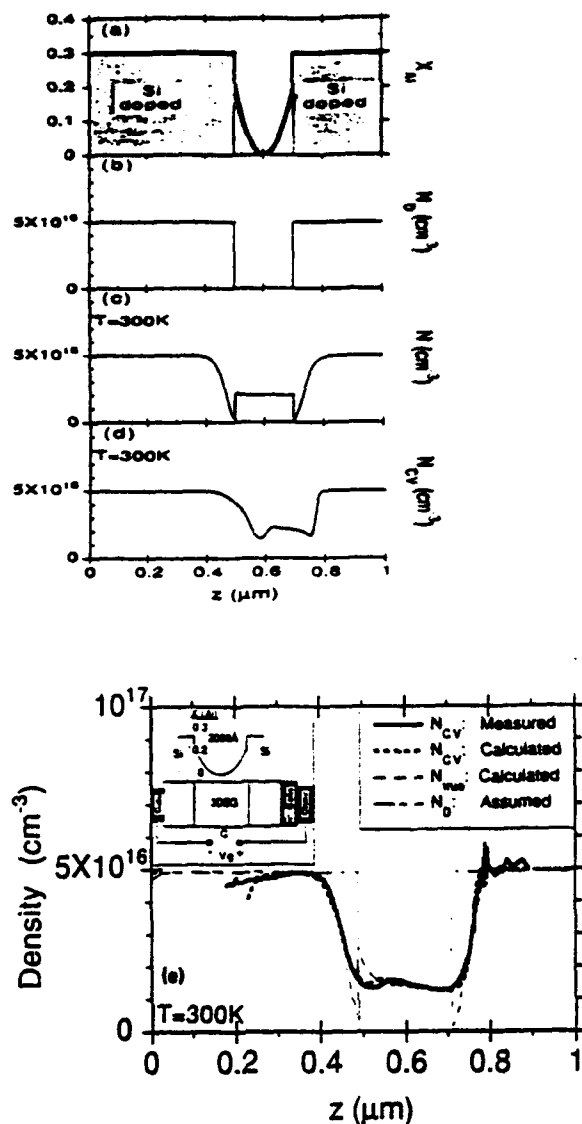


FIG. 6. (a) Al mole fraction $X_{Al}(z)$, (b) assumed real doping profile $N_D(z)$, (c) computer-simulated true electron distribution $N(z)$ at 300 K, and (d) computer-simulated apparent (CV) electron profile $N_{CV}(z)$ at 300 K, for a modulation-doped 2000 Å-wide parabolic well that is located between 0.5 and 0.7 μm below surface. Note asymmetry predicted for electron CV profile. (e) Experimentally measured CV profile for a similar parabolic well (inset shows nominal design and measurement schematic), and reconstructed fit. Also shown are the calculated true electron profile and the assumed doping profile. The presence of a negative sheet charge $\sim -7 \times 10^{10} \text{ cm}^{-2}$ is deduced, and attributed to doping asymmetries in the MBE growth of the structure. Note uniformity of true electron profile despite this doping asymmetry.

the origin of this interface charge. Improved growth techniques incorporating superlattice spacer layers and lower growth temperatures of the Si-doped AlGaAs layers should remove this discrepancy. Further details of this optimizing procedure will be presented elsewhere. Despite the doping asymmetry, note that the true electron distribution that was deduced from the measurement is uniform at the quasidoping density N_Q over most of the well, again illustrating the strong predominance of N_Q in determining the electron profile, and the relative tolerance of the technique to doping variations in the barrier layers. The data demonstrate that

uniform doping profiles can be achieved in quasidoped semiconductors.

III. CONCLUSIONS

Quasidoping of semiconductors was achieved for the first time using the digital alloy technique in the GaAs/AlAs system. A uniform three-dimensional electron gas (3DEG) was realized through remote doping of a shallow parabolic potential well. These gases exhibit high mobilities at low temperatures. Mobility measurements and first-order estimates of the same, appear to indicate the dominance of alloy-disorder scattering as the mobility-limiting mechanism in these structures. The evidence from the mobility vs electron sheet concentration is especially striking.

Capacitance-voltage (*CV*) profiling of quasidoped semiconductors has been accomplished for the first time, and preliminary results are presented. Measured room temperature electron profiles in a remotely doped wide parabolic well point to a uniform true electron distribution.

A rigorous model for alloy-disorder scattering that takes into account both intrasubband and intersubband scattering when several subbands are occupied, obviously needs to be developed. This is especially important in light of the fact that this is likely to be the mobility limiting scattering mechanism in digital alloys. The technology of MBE seems to be sufficiently advanced in growing smooth interfaces, that interface roughness scattering does not limit the mobility, at least for sufficiently shallow grades. Experimental and theoretical studies need to be done. Efforts in this direction are underway.

The *CV* profiling appears to be a powerful tool to measure deviations from the design alloy grading, as also deviations in the real-dopant distribution. Optimization of growth parameters are suggested. Preliminary studies show promising results.

ACKNOWLEDGMENTS

We thank A. Wixforth, J. H. English, K. Ensslin, and B. Halperin for valuable discussions, and R. Westervelt, E. Gwinn, and P. F. Hopkins for many discussions and mea-

surement collaborations. Our thanks to Professor H. Sakaki for making available to us his results prior to publication. We wish to acknowledge the U. S. Air Force Office of Scientific Research for supporting this research.

¹M. Sundaram, A. C. Gossard, J. H. English, and R. M. Westervelt, *Superlattices Microstruct.* **4**, 683 (1988).

²M. Shayegan, T. Sajoto, M. Santos, and C. Silvestre, *Appl. Phys. Lett.* **53**, 791 (1988).

³E. G. Gwinn, R. M. Westervelt, P. F. Hopkins, A. J. Rimberg, M. Sundaram, and A. C. Gossard, *Phys. Rev. B* **39**, 6260 (1989); E. G. Gwinn, R. M. Westervelt, P. F. Hopkins, A. J. Rimberg, M. Sundaram, and A. C. Gossard, *Superlattices Microstruct.* **6**, 95 (1989).

⁴T. Sajoto, J. Jo, L. Engel, M. Santos, and M. Shayegan, *Phys. Rev. B* **39**, 10464 (1989); T. Sajoto, J. Jo, M. Santos, and M. Shayegan, *Appl. Phys. Lett.* **55**, 1430 (1989).

⁵E. G. Gwinn, R. M. Westervelt, P. F. Hopkins, A. J. Rimberg, M. Sundaram, and A. C. Gossard, *High Magnetic Fields in Semiconductor Physics II*, edited by G. Landwehr, Springer Series in Solid State Physics, Vol. 87 (Springer, Berlin, 1989), p. 58; M. Shayegan, M. Santos, T. Sajoto, K. Karai, M. W. Lee, and H. D. Drew, *ibid.*, p. 445.

⁶K. Karai, H. D. Drew, M. W. Lee, and M. Shayegan, *Phys. Rev. B* **39**, 1426 (1989).

⁷A. Wixforth, M. Sundaram, K. Ensslin, J. H. English, and A. C. Gossard, *Appl. Phys. Lett.* **56**, 454 (1990).

⁸The terminology "quasidoping" was suggested to us by Professor H. Kroemer.

⁹R. C. Miller, A. C. Gossard, D. A. Kleinman, and O. Munteanu, *Phys. Rev. B* **29**, 3740 (1984).

¹⁰M. Sundaram, A. Wixforth, R. S. Geels, A. C. Gossard, and J. H. English (to be published).

¹¹G. E. Stillman (private communication).

¹²W. Walukiewicz, H. E. Ruda, J. Lagowski, and H. C. Gatos, *Phys. Rev. B* **30**, 4571 (1984).

¹³G. Bastard, *Appl. Phys. Lett.* **43**, 591 (1983) (see especially Fig. 3 of this paper).

¹⁴T. Noda, M. Tanaka, and H. Sakaki (to be published).

¹⁵H. Kroemer, W.-Y. Chien, J. S. Harris, Jr., and D. D. Edwall, *Appl. Phys. Lett.* **36**, 295 (1980).

¹⁶S. Sasa, J. Saito, K. Nanbu, T. Ishikawa, and S. Hiyamizu, *Jpn. J. Appl. Phys.* **23**, L573 (1984).